Bio-sensing using toroidal microresonators & Theoretical cavity optomechanics

Jens M. Dobrindt

Dissertation
an der Fakultät für Physik
der Ludwig–Maximilians–Universität
München

vorgelegt von
Jens M. Dobrindt
aus Bonn

München, den 5. Oktober 2012

Erstgutachter: Prof. Dr. T. W. Hänsch
Zweitgutachter: Prof. Dr. J. O. Rädler
Tag der mündlichen Prüfung: 5. Dezember 2012

Für meine Eltern.

Abstract

In this thesis we report on two matters, (i) time-resolved single particle bio-sensing using a cavity enhanced refractive index sensor with unmatched sensitivity, and (ii) the theoretical analysis of parametric normal mode splitting in cavity optomechanics, as well as the quantum limit of a displacement transducer that relies on multiple cavity modes. It is the unifying element of these studies that they rely on a high-Q optical cavity transducer and amount to a precision measurement of an optical frequency.

In the **first part**, we describe an experiment where a high-Q toroidal microcavity is used as a refractive index sensor for single particle studies. The resonator supports whispering gallery modes (WGM) that feature an evanescent fraction, probing the environment close to the toroid's surface. When a particle with a refractive index, different from its environment, enters the evanescent field of the WGM, the resonance frequency shifts.

Here, we monitor the shift with a frequency resolution of $\Delta\nu/\nu = 7.7 \cdot 10^{-11}$ at a time resolution of $100\,\mu$s, which constitutes a $\times\mathbf{10}$ improvement of the sensitivity and a $\times\mathbf{100}$ improvement in time resolution, compared to the state of the art. This unprecedented sensitivity is the key to real-time resolution of single lipid vesicles with 25 nm radius adsorbing onto the surface. Moreover – for the first time within one distinct measurement – a record number of up to **200** identifiable events was recorded, which provides the foundation for a meaningful statistical analysis. Strikingly, the large number of recorded events and the high precision revealed a disagreement with the theoretical model for the single particle frequency shift. A correction factor that fully accounts for the polarizability of the particle, and thus corrects the deviation, was introduced and establishes a quantitative understanding of the binding events.

Directed towards biological application, we introduce an elegant method to cover the resonator surface with a single lipid bilayer, which creates a universal, biomimetic interface for specific functionalization with lipid bound receptors or membrane proteins. Quantitative binding of streptavidin to biotinylated lipids is demonstrated.

Moving beyond the detection limit, we provide evidence that the presence of single IgG proteins (that cannot be resolved individually) manifests in the frequency noise spectrum. The theoretical analysis of the thermo-refractive noise floor yields a fundamental limit of the sensors resolution.

The **second part** of the thesis deals with the theoretical analysis of the coupling between an optical cavity mode and a mechanical mode of much lower frequency. Despite the vastly different resonance frequencies, a regime of strong coupling between the mechanics and the light field can be achieved, which manifests as a hybridization of the modes and as a mode splitting in the spectrum of the quadrature fluctuations. The regime is a precondition for coherent energy exchange between the mechanical oscillator and the light field. Experimental observation of optomechanical mode splitting was reported shortly after publication of our results.[1]

Dynamical backaction cooling of the mechanical mode can be achieved, when the optical mode is driven red-detuned from resonance. We use a perturbation and a covariance approach to calculate both, the power dependence of the mechanical occupation number and the influence of excess noise in the optical drive that is used for cooling. The result was one to one applied for data analysis in a seminal article on ground state cooling of a mechanical oscillator.[2]

In addition we investigate a setting, where multiple optical cavity modes are coupled to a single mechanical degree of freedom. Resonant build-up of the motional sidebands amplifies the mechanical displacement signal, such that the standard quantum limit for linear position detection can be reached at significantly lower input power.

[1] Gröblacher et *al.*, **Nature 460**, 724–727.
[2] Teufel et *al.*, **Nature 475**, 359–363.

Zusammenfassung

In dieser Dissertation werden zwei Themen behandelt. Im ersten Teil widmen wir uns experimentell der zeitaufgelösten Messung von Liposomen mit Hilfe eines Nahfeld-Brechungsindex-Sensors. Der zweite Teil handelt von der theoretischen Beschreibung des Regimes der starken Kopplung zwischen einem mechanischen Oszillator und dem Feld eines optischen Resonators. Des Weiteren erörtern wir ein Messschema, das es erlaubt eine mechanische Bewegung, mit Hilfe von mehreren optischen Resonatormoden genauer auszulesen. Die Gemeinsamkeit beider Arbeiten besteht darin, dass es sich jeweils um eine Präzisionsmessung einer optischen Frequenz handelt.

Im experimentellen Teil benutzen wir Toroid-Mikroresonatoren mit extrem hoher optischer Güte als Biosensoren. Dabei handelt es sich um eine ringförmige Glasstruktur, entlang welcher Licht im Kreis geleitet wird. Dazu muss eine Resonanzbedingung erfüllt sein, die besagt, dass der (effektive) Umfang des Rings einem ganzzahligen Vielfachen der optischen Wellenlänge entspricht. Ein Teil des zirkulierenden Lichts ist als evaneszente Welle empfänglich für Brechungsindexänderungen nahe der Oberfläche des Resonators. Ein Partikel, dessen Brechungsindex sich von dem der Umgebung unterscheidet, induziert beim Eintritt in das evaneszente Feld eine Frequenzverschiebung der optischen Resonanz.

Im Rahmen dieser Arbeit lösen wir relative Frequenzverschiebungen mit einer Genauigkeit von $\Delta\nu/\nu = 7.7 \cdot 10^{-11}$ und einer Zeitkonstante von $100\,\mu$s auf. Dies stellt eine Verbesserung des derzeitigen Stands der Technik um einen Faktor $\times\mathbf{10}$ in der Frequenz und einen Faktor $\times\mathbf{100}$ in der Zeit dar. Diese bisher unerreichte Empfindlichkeit der Messmethode ist der Schlüssel zur Echtzeitdetektion einzelner Lipidvesikel mit einem Radius von 25 nm. Zudem gelingt es uns innerhalb einer Messung, bis zu **200** Einzelteilchenereignisse aufzunehmen, welche die Basis für eine aussagekräftige Statistik liefern. Bemerkenswerterweise konnten wir Dank der außerordentlichen Präzision und der Vielzahl der Ereignisse eine Abweichung zur bis dato akzeptierten und angewandten Theorie feststellen. Wir ergänzen das Model um einen Korrekturfaktor, der die Polarisierbarkeit des Teilchens vollständig berücksichtigt und erlangen dadurch ein umfassendes und quantitatives Verständnis der Messergebnisse.

Im Hinblick auf biologisch relevante Fragestellungen zeigen wir eine elegante Methode auf, die es erlaubt, den Resonator mit einer einzelnen Lipidmembran zu beschichten. Wir kreieren somit eine biomimetische Schnittstelle, welche das Grundgerüst für eine spezifische Funktionalisierung mit lipidgebundenen Rezeptoren, Antikörpern oder Membranproteinen darstellt.

Des Weiteren zeigen wir, dass der Empfindlichkeit eine fundamentale Grenze durch thermische Brechungsindexfluktuationen gesetzt ist. Hierzu wird ein theoretisches Modell speziell für den relevanten niederfrequenten Bereich errechnet.

Im zweiten Teil der Arbeit beschäftigen wir uns mit der theoretischen Beschreibung eines optischen Resonators, dessen Lichtfeld an eine mechanische Schwingung gekoppelt ist. Obwohl sich die Resonanzfrequenzen der Optik und der Mechanik typischerweise um mehrere Größenordnungen unterscheiden, existiert ein Regime der *starken Kopplung*, in dem die Fluktuationen des Lichts und die mechanischen Vibrationen hybridisieren. Dies offenbart sich zum Beispiel im Phasenspektrum, wo sich das ursprüngliche Maximum der Resonanz in zwei Maxima aufspaltet. Die starke Kopplung stellt die Grundlage für kohärenten Energie- und Informationsaustausch zwischen Licht und Mechanik dar und ist daher von besonderem technischen und wissenschaftlichen Interesse. Es ist anzumerken, dass die starke Kopplung und die einhergehende Aufspaltung der Resonanz bereits kurz nach Veröffentlichung unserer theoretischen Beschreibung im Experiment beobachtet wurde.[3]

Wenn der optische Resonator (zur längeren Wellenlänge hin) verstimmt von der Resonanz angeregt wird, kann über dynamische Rückkopplung eine effektive Kühlung der mechanischen Schwingung erreicht werden. Wir berechnen die thermische Besetzungszahl der mechanischen Mode (und somit die Temperatur) mit Hilfe eines störungstheoretischen und eines Kovarianzansatzes. Dabei berücksichtigen wir sowohl ein klassisches Rauschen des optischen Feldes als auch den Einfluss der optomechanischen Kopplung auf die Grenztemperatur. Der hergeleitete Ausdruck für die finale Besetzungszahl wurde eins zu eins für die Datenanalyse in dem wegweisenden Artikel über das Kühlen eines mechanischen Oszillators in den Quantengrundzustand verwendet.[4]

Abschließend betrachten wir ein Schema, bei dem die Lichtfelder mehrerer optischer Resonanzen an eine mechanischen Schwingung gekoppelt sind. Die resonante Verstärkung der Information über die mechanische Bewegung in den optischen Seitenbändern ermöglicht es, eine durch das Standard Quantenlimit begrenzte Empfindlichkeit bei signifikant niedriger Eingangsleistung zu erreichen.

[3] Gröblacher et *al.*, **Nature 460**, 724–727.
[4] Teufel et *al.*, **Nature 475**, 359–363.

List of Publications

[1] I. Wilson-Rae, N. Nooshi, **J. M. Dobrindt**, T. J. Kippenberg, and W. Zwerger. Cavity-assisted back action cooling of mechanical resonators. *New Journal of Physics*, 10:095007, (2008).

[2] **J. M. Dobrindt**, I. Wilson-Rae, and T. J. Kippenberg. Parametric Normal-Mode splitting in cavity optomechanics. *Physical Review Letters*, 101(26):263602, (2008).

[3] **J. M. Dobrindt** and T. J. Kippenberg. Theoretical analysis of mechanical displacement measurement using a multiple cavity mode transducer. *Physical Review Letters*, 104(3):033901, (2010).

[4] **J. M. Dobrindt**, E. Rodrigo Teixeira da Silva, C. Alves, C. Oliveira, F. Nallet, E. Andreoli de Oliveira, and L. Navailles. Anisotropic brownian motion in ordered phases of DNA fragments. *The European Physical Journal E: Soft Matter and Biological Physics*, 35(1):1–11, (2012).

[5] **J. M. Dobrindt**, B. Nickel, E. Gavartin, S. Krysiak, J. O. Rädler, and T. J. Kippenberg. Time-resolved, label-free sensing of single lipid vesicles using high-Q microresonators. *submitted to Nature Nanotechnology.*

A note from the author

The essential parts of this thesis were published in the *Physical Review Letters* [2, 3] or have been submitted for publication to *Nature Nanotechnology* [5]. Parts of these manuscripts – as well as published and unpublished supplementary information – have served as the foundation of this thesis. Some paragraphs therefore appear in a similar form in the manuscripts mentioned above. In particular chapters 6 and 7 contain large parts of references [2, 3]. I confirm, however, that all text fragments used for this thesis are original work of myself.

Contents

Part I.

Bio-sensing using toroidal microresonators

1. Cavity enhanced bio-sensing

General introduction

The ultimate goal of biomedical imaging is single molecule and single particle resolution.[1] Resolving the biomechanical functioning, association and dissociation kinetics, as well as interaction between molecules and individual nanoscale particles, reveals valuable information on biological processes that cannot be obtained from ensemble averages. Prominent examples of such measurements are the movement of a kinesin motor walking along a microtubule, the functioning of myosin [7], the gating behavior of individual ion channels in a plasma membrane [8], and very recently, single lysozyme dynamics [9]. Single molecule and even single atom sensitivity was first achieved in vacuum. Experiments with trapped ions and molecules revealed remarkable results on the quantum nature of bound electrons [10, 11].
In the liquid phase, single fluorescent molecules, that passed through the focal spot of a laser beam, were identified as flashes of fluorescent photons [12, 13, 14]. However, resolving single molecules in a solid, immobilized on a substrate, or even under physiological conditions turned out to be much more difficult to achieve. Stray signal from the background and poor contrast were the main challenges.

Consequently, early experiments that strived for single molecule sensitivity followed two different roads. On the one hand, the contrast was maximized such that the background signal could be efficiently suppressed. This lead to the first single molecule traces in solid, recorded by Moerner and Kador in 1989, using an absorption modulation spectroscopy technique on pentacene in a p-terphenyl host crystal [15]. One year later, Orrit and Bernard were able to observe single molecule fluorescence in the same system [16]. These first results were, however, obtained at liquid helium temperature. In 1993 finally, Betzig and Chichester were able to collect fluorescent light from a single dye molecule on a surface at room temperature [17].
The second approach to achieve single molecule detection involved the reduction of the detection volume of the sensor to a point, where the background could be neglected. An impressive demonstration of such a method was given by Eigler and Schweizer in 1990, who used an atomic force microscope (AFM) to detect and manipulate individual Xenon atoms on a Nickel surface [18] (cf. Figure 1.1 (c)). Already in the early 1980s, a scanning tunnel microscope (STM) was used by Binning and Rohrer to image single molecules on metal surfaces [19]. The practical use for biophysical application remained, however, limited, as both STM and AFM require prepared surfaces in a highly specific environment.[2]

[1] By *particle* we shall here refer to (solid) nanoparticles with a diameter inferior to 20 nm, which are difficult to observe by light absorption and scattering. The absorption strength scales with the particle volume and the scattering cross section with the volume squared (unless interferometric

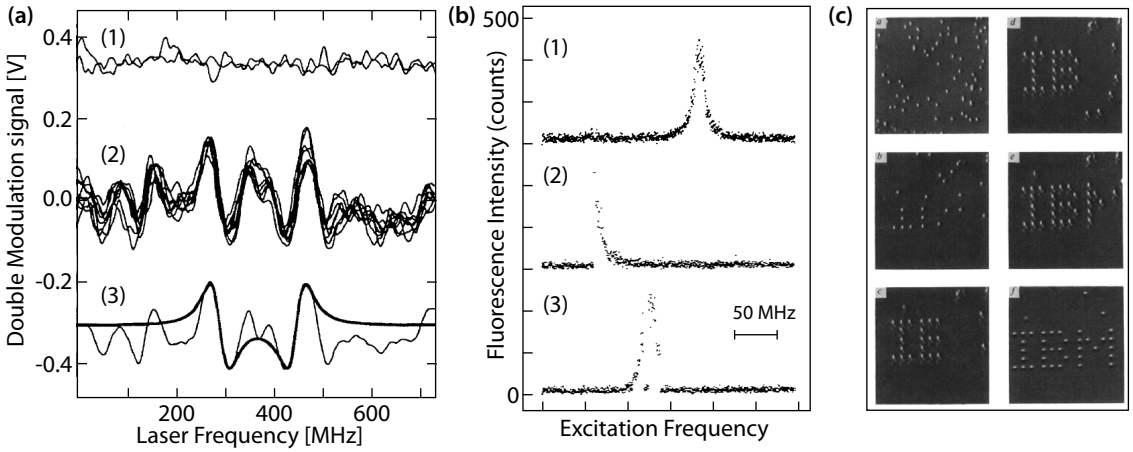

Figure 1.1.: Historical data of single molecule measurements. (a) Frequency modulation spectroscopy (FMS) data, adapted from Moerner and Kador [15], recorded from a single pentacene molecule. The upper curve (1) shows the signal far off the absorption line. Curve (2) shows eight FMS traces originating from a single molecule and curve (3) shows the average of the traces in (2) together with the simulated line shape. (b) Fluorescence data collected from a single pentacene molecule by Orrit and Bernard [16]. Curve (1) shows the fluorescent light with a line width of 12 MHz. The traces in (2) and (3) provide evidence that the light stems indeed from a single molecule (i.e., they show bleaching and a dark state). (c) Individual Xenon atoms are observed and manipulated on a Nickel surface, using an atomic force microscope [18].

It is the goal of this rather long introduction to give an overview of the broad and diverse field of sensing, different sensor types, and typical applications. The references within provide a library of influential and instructive papers that may serve as guidance for someone who is new to the field.

Applications of label-free sensing techniques

Ever since these ground breaking first measurements, experimental techniques were subsequently refined, leading to a variety of single molecule techniques that use fluorescent molecules as high contrast markers [21, 22]. In this context, super-resolution techniques, such as Stimulated Emission Depletion Microscopy (STED), Stochastic Optical Reconstruction Microscopy (STORM), or Photo-activated Localization Microscopy (PALM), have contributed pioneering work to a field that continues to expand [23]. Despite these remarkable results, there are some drawbacks associated with fluorescent methods. Just like other methods that depend on markers, labeling of the analyte prior to the measurement is required. In **clinical applications**

techniques are applied) [6].

[2] AFM tips are used in biophysical experiments for single molecule force measurements, e.g., when unfolding proteins or extracting proteins from lipid membranes. In the context of tip enhanced Raman scattering (TERS), STMs are used to measure vibrational spectra of single molecules [20].

that aim at the detection of low concentrations of a target molecule, the labeling of the sample is simply not practical. In **scientific research**, where interactions are studied on the single molecule level, an attached marker can disturb the interaction due to steric hindrance. Moreover, it is challenging to obtain quantitative results, because of the difficulty to accurately determine the binding rate of the marker to the target [24]. These considerations already indicate that there exists a broad and diverse range of application for bio-sensors, which impose particular requirements on the devices. Naturally, sensors are specifically designed for a certain task, and they can roughly be divided into two categories.

On the one hand, there are **chemical sensors that aim at the mere detection of low quantities** or concentrations of a certain target molecule, and which are employed in environmental sensing (e.g. entox, tracers), food industry (e.g. quality management), homeland security (e.g. post and airport security, sensing of explosives and drugs), military (e.g. biological and toxic weapons), epidemiology (e.g. disease surveillance, detection of bacteria and viruses), and medical diagnosis. The last field is of special interest here, as the sensor presented in this thesis has potential application in clinical research, and as there exists a large overlap between clinical and scientific research. Clinical sensors are used to detect bio-molecules in, e.g., blood samples, urine, or serous fluid, and they typically target neurotransmitters, proteins (e.g. insulin), bio-molecules (e.g. cholesterol, glucose), pathogenic bacteria, and cancer biomarkers [25]. Ideally, such sensors combine a high sensitivity, which is typically measured as the smallest detectable target mass or the lowest detectable concentration,[3] a high selectivity with respect to the target, and a short integration time (, i.e. a fast response). Moreover, a particular requirement for clinical purposes includes the possibility of multiplexing and screening for different targets in parallel [25]. For some field applications, a small packaging, robustness (also against improper use), and portability are desirable. If the development of the sensor aims at mass production and wide spread use, a low cost per unit is required [26].

On the other hand, **specialized bio-sensors are used in scientific research** to examine physiological processes on their fundamental level. Among many other applications, this involves the general functioning of the cell metabolism (e.g., detection of semiochemicals), interactions between bio-molecules (e.g. on and off binding rates), gating of single ion channels, movement and functioning of molecular motors or enzymes, and lipid membrane bound interaction. In particular the last point – membrane interactions – comprises a variety of processes that are of scientific, as well as therapeutic relevance, considering that 30% of the human genes code for membranes proteins, and about half of the approved pharmaceutics target membrane proteins [27]. Moreover, a large part of a cell‘s communication is membrane bound and involves, e.g., the interaction of lipid vesicle containers with the membrane (cf. section 3.2).

Therefore, compared to the previously described chemical detectors, scientific bio-sensors aim at much smaller quantities of a target molecule, with the ultimate goal of single molecule sensitivity. In particular, one is not only interested in the

[3] The two sensitivity figures are connected via the throughput, selectivity, and integration time.

mere presence of the target, but rather in the **interaction, which requires a much higher time resolution**. While a typical bio-detector is considered „fast“ when the the sample is analyzed within a few seconds, the step movement of a molecular motor occurs every few ms and protein binding events take place in the μs regime. The ideal sensor for scientific applications therefore features single molecule sensitivity and μs time resolution, as well as the possibility of efficient functionalization to observe specific interactions. Moreover, it is important that the sensor has a negligible influence on the target, which means that there should be no steric hindrance by markers, low sample heating (e.g., from absorption), and little exerted force (e.g., optical trapping).

These requirements motivate the development of fast, label-free sensors for scientific research at the single molecule level. The following section will give an overview of different concepts of label-free sensors that are currently under development. This is followed by a discussion of the most promising systems regarding their potential of single molecule sensitivity.

1.1. Label-free sensing techniques

In default of a marker, label-free sensing techniques are sensitive to particle properties, such as (i) the refractive index, where the real part causes a electromagnetic phase shift and the imaginary part manifests as absorption, (ii) the electronic properties of the molecule, which includes light scattering, and fluorescence, (iii) the vibrational spectrum (e.g. Raman scattering), and (iv) the particle mass. Other measurable properties, that are less often exploited, include, e.g., the magnetic moment (if present).
In early single molecule experiments, these properties were directly probed on the individual particle level, for example in direct absorption measurements or the direct observation of fluorescence. To this end, high contrast was required to distinguish the signal from the background, and consequently the first experiments were conducted at cryogenic temperatures.

To circumvent the background problem, sensors were developed that follow to a varying degree the **principle of an intermediary transducer element**: generically speaking, the transducer is a device with an attribute – such as a well defined optical or electronic resonance – that can be detected with high contrast before the noisy background [28]. When a particle interacts with the transducer, this property changes and signals the interaction. Employing such scheme, one primarily detects the attribute of the transducer, instead of the target (displaying low contrast) itself, and the difficulty of deleterious background signals is largely eliminated. In this section we are presenting a diverse selection of sensors that follows the transducer principle.

The resolution of such sensors depends on two important parameters: (i) the response of the transducer to the target, which is usually proportional to the relative

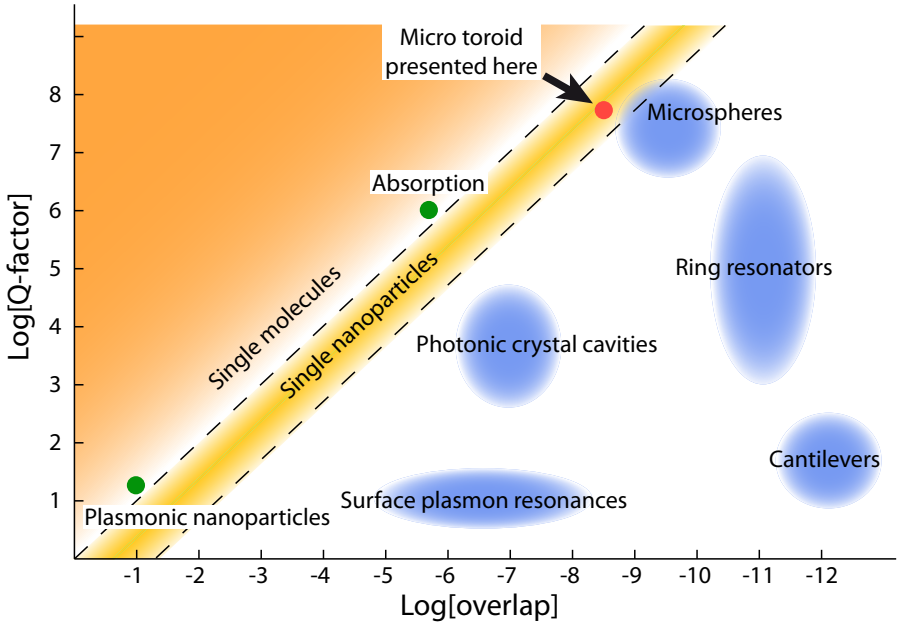

Figure 1.2.: Different label-free sensing techniques are compared with respect to their single particle sensitivity, which is plotted here as the product of the Q-factor of the resonant lever and the relative overlap of the sensor with the target. We considered sensors that operate at physiological condition (as opposed to vacuum and cryogenic temperature). The overlap on the x-axis is normalized to the volume (or mass) of a single IgG protein ($\sim 180\,\mathrm{nm}^3$) and is compared the mode volume of the sensing mode. For cantilevers, the protein mass is compared to the effective mass of the sensing mode; for the absorption measurement the cross section is compared to the focal spot and the Q corresponds to the relative intensity noise. Adding a third axis for time resolution would put the measurements presented in this thesis in front.

overlap of the target with the sensing volume, and (ii) the fidelity of the (resonant) property, i.e. the smallest relative change that can be detected. Regarding the first parameter, a large overlap is in general achieved when the design is miniaturized, and the transducer size approaches the size of the target.
For example, if a particle attaches to a vibrating mechanical cantilever, whose resonance frequency is monitored, the resonance shifts proportional to the relative increase of the effective mass. In this case it is advantageous to reduce the dimensions and thus the mass of the cantilever. A different example, a particle with a refractive index different from the environment enters the light field of an optical cavity. Then the optical resonance frequency will shift, according to the relative overlap of the particle with the optical mode. Again a smaller design and higher mode confinement will increase the relative frequency shift. These two examples reflect a general rule: the signal strength scales with the overlap of the target particle with the transducer, i.e. its active sensing volume. On the other hand, the fidelity of the sensors is best represented by the Q factor that described how well a resonance can be resolved.

$$Q = \frac{\text{resonance frequency}}{\text{full width half maximum}} = \frac{\nu_0}{\Delta\nu}$$

Apparently the smallest detectable (relative) frequency shift is proportional to Q^{-1}.

In Figure 1.2 we characterize different label-free sensor concepts with respect to their relative overlap (e.g., particle volume compared to mode volume or particle mass compared to effective mass), together with the quality factor Q .[4] We emphasize that the position on the diagram does not reflect the „usefulness“ of the design, because some of the presented schemes do not aim a single molecule sensitivity. However, the plot can give some general impression in which direction existing systems would need to evolve (i.e., to improve) to attain single molecule sensitivity.

In most cases, further reduction of the transducer size is the road to follow, as miniaturization of the design increases the response to the target. In this context, the last decade has witnessed a stunning advance in micro-fabrication that has catalyzed sensor development. New fabrication techniques have paved the way for novel designs at the mesoscale and beyond (e.g., carbon nanotube based sensors), existing techniques were integrated [30] and commercialized (e.g., Toyobo, Lenterra, Imec+Genalyte), multiplexing was achieved (e.g., DNA micro arrays), and novel classes of sensors have emerged from the adaptation of metamaterials (e.g., photonic crystal cavities) [31].

1.1.1. Toroidal microresonators

For the experiments presented in this thesis, we use toroidal microcavities that were developed in the group of Kerry Vahala at the California Institute of Technology [32]. The structure consists of a silica ring, which is supported by a silicon pillar on a silicon chip (cf. Figure 1.3 (a)). The ring constitutes an optical resonator and supports whispering gallery modes (WGM), named after the legendary whispering gallery under the dome of St. Paul‘s cathedral, London. A whisper at one point of the gallery is reflected by the circular wall of the dome and can be heard at the opposite position. Similarly, light is guided inside the transparent, circular structure of the toroidal cavity, and a resonance condition is imposed by the requirement that an integer multiple of the wavelength fits into the optical path of one round trip.

As a result of the high transparency of silica in the visible and the smooth surface of the toroid, the optical loss is low, which results in ultra-high optical Q factors exceeding 10^8, with a finesse $> 10^5$. In Figure 1.3 (c)-(e) we plot the intensity distribution of different optical WGMs in a toroid, which will be discussed in detail in section 1.2 and appendix A.1. Notably, the modes exhibit an evanescent fraction that propagates outside the ring and are therefore susceptible to the environment. A refractive index change inside the evanescent volume will cause a shift of the resonance frequency. It is this feature that constitutes the foundation for the use of WGM resonators as refractive index sensors.

The microtoroid as a refractive index sensor combines several intriguing features. Due to the high Q-factor, small relative changes of the resonance frequency, down to $\Delta\nu/\nu = 10^{-10}$, can be recorded and – in conjunction with a small mode volume

[4] A similar analysis, mostly for modeled data, is presented in reference [29].

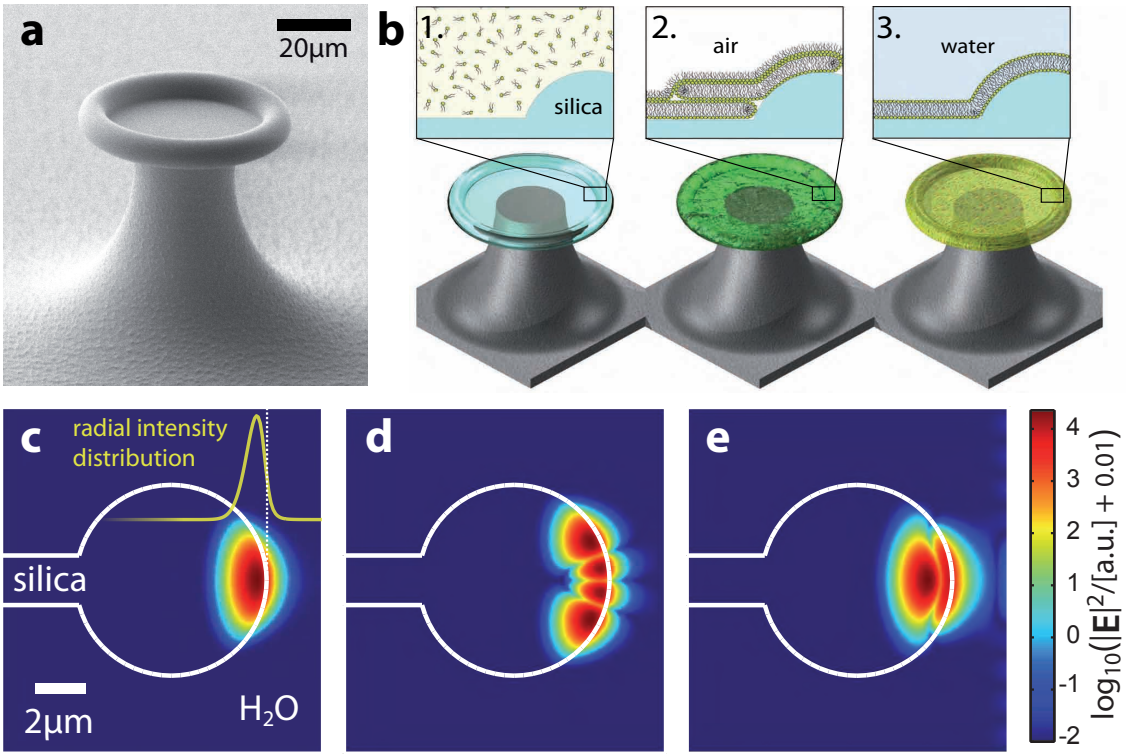

Figure 1.3.: Toroidal microresonator as a biosensor. (a) An electron microscope image of a toroidal microresonator, as it was used here for sensing. (b) The toroid is coated with a single lipid bilayer, which constitutes a universal interface for bio-sensing. Specific functionalization is achieved, when lipid-bound receptors or membrane proteins are introduced in the membrane. (c)-(e) Simulated intensity profiles for different WGMs (i.e., TM00, TM30, and TM01). The evanescent fraction is sensitive to refractive index changes and thus represents the active sensing volume.

– single molecule sensitivity is within reach (cf. Figure 1.2). Importantly the sensitivity close to the surface is the highest and the exponential decay of the evanescent field links the frequency shift to the particle's distance from the surface. As such, the sensor is ideally suited to measure interactions and motion in proximity of the surface. The possibility and importance of specific surface functionalization will be elucidated in section 1.1.3.
Compared to other sensor designs, the microtoroid profits in particular from its high optical Q, convenient handling (cf. section 2.1.3), the possibility of high fidelity readout, and a relatively large active surface area. In the following section these properties are contrasted with the most important contemporary sensor designs; an extra section – 1.1.4 – is devoted to the comparison with plasmonic antennas, which represent the fiercest competition today.

1.1.2. Other sensing schemes

There is a number of research groups that use **WGM resonance based sensors** for bio-sensing, and a variety of different structures is explored. In particular silica

microspheres have been successfully employed for sensing by the groups of F. Vollmer and S. Arnold [33, 34, 35, 36, 37, 38, 39, 40] (cf. Figure 1.4 (h)). Microspheres offer exceptional Q factors, en par with the ones of toroids, but suffer from a slightly larger mode volume, more difficult handling, and the fact that only one sphere can be integrated and tested at a time.
The groups of K. Vahala and L. Yang use toroidal microresonators for sensing and it was the former who claimed the achievement of label-free detection of single interleukin-2 proteins (and a variety of other proteins), presumably via a thermo-optic effect [41]. The results where never reproduced, and also in the context of this thesis we never observed such effects. Quite the contrary, in response to a detailed calculation of the thermo-optic effect by Stephen Arnold [42] (who came to the conclusion that the effect must be at least 400 times smaller than originally claimed), reference [41] was amended by an erratum, stating that the thermo-optic effect cannot be responsible for the discrete frequency steps observed by the authors. The paper was eventually followed up by a work, demonstrating sensitivity to single Influenza A viruses[5] via the conventional dispersive effect [43].

In contrast, L. Yang exploits the effect of mode splitting in high-Q WGM resonators and has demonstrated remarkable results on particle sizing [44, 45, 46, 47]. The mode splitting effect is presented and discussed in section 3.4. Besides the approaches relying on high-Q resonators, a number of experiments aims at the integration of WGM resonators in on-chip devices that are fabricated by lithographic means only [48] and can be combined with microfluidic systems [49, 50]. The compact design comes however at the cost of a lower optical Q, that typically lies in the range of 10^4 to 10^5, and which does not allow to attain single particle sensitivity. Nevertheless, different designs include slot waveguides and resonators (cf. Figure 1.4 (g)) [51, 52, 53], polymer ring resonators fabricated by imprinting [54], multiplexing of several resonators [55], and parallel screening for different species of biomarkers [56, 57]. Another noteworthy sensing scheme, that integrates the fluidic system, are liquid core ring resonators (LCORR), where a WGM is excited in the waist of a micro capillary and reacts to the refractive index of the fluid inside [58, 59].

The technique known as **Surface enhanced Raman scattering (SERS)** relies on the remarkable increase of Raman scattering cross section of certain molecules (cf. Figure 1.4 (d)) when they are adsorbed on metallic nanoparticles (usually silver or gold) [60, 61, 62]. The nature of the coupling is not fully understood, but it is widely agreed upon that it is dominated by electromagnetic interaction with localized surface plasmon resonances, and its strength critically depends on the position and the orientation of the molecule. To observe SERS, the surface plasmon is excited, which drives the vibrational modes of the molecule. The heating of the Raman modes manifests in the anti-Stokes to Stokes signal ratio.[6] The SERS technique only works, when the particle attaches to a so called SERS active site, which are however rare and poorly controlled.[7] Moreover, during SERS, the enhanced Raman

[5] An influenza A virus is $\sim 20,000$ times heavier than an interleukin-2 protein.
[6] As pointed out by T.J. Kippenberg, the process is reminiscent to parametric amplification of a mechanical mode in an optomechanical setting.
[7] In Tip-enhanced SERS the metallic NP is replaced by a nano-tip which gives somewhat better

modes are vibrationally driven [63], and the molecule is thus strongly affected by the measurement [64]. Evidence for a single molecule in the scattering volume is obtained, when the photon distribution changes from Gaussian to Poissonian [60].

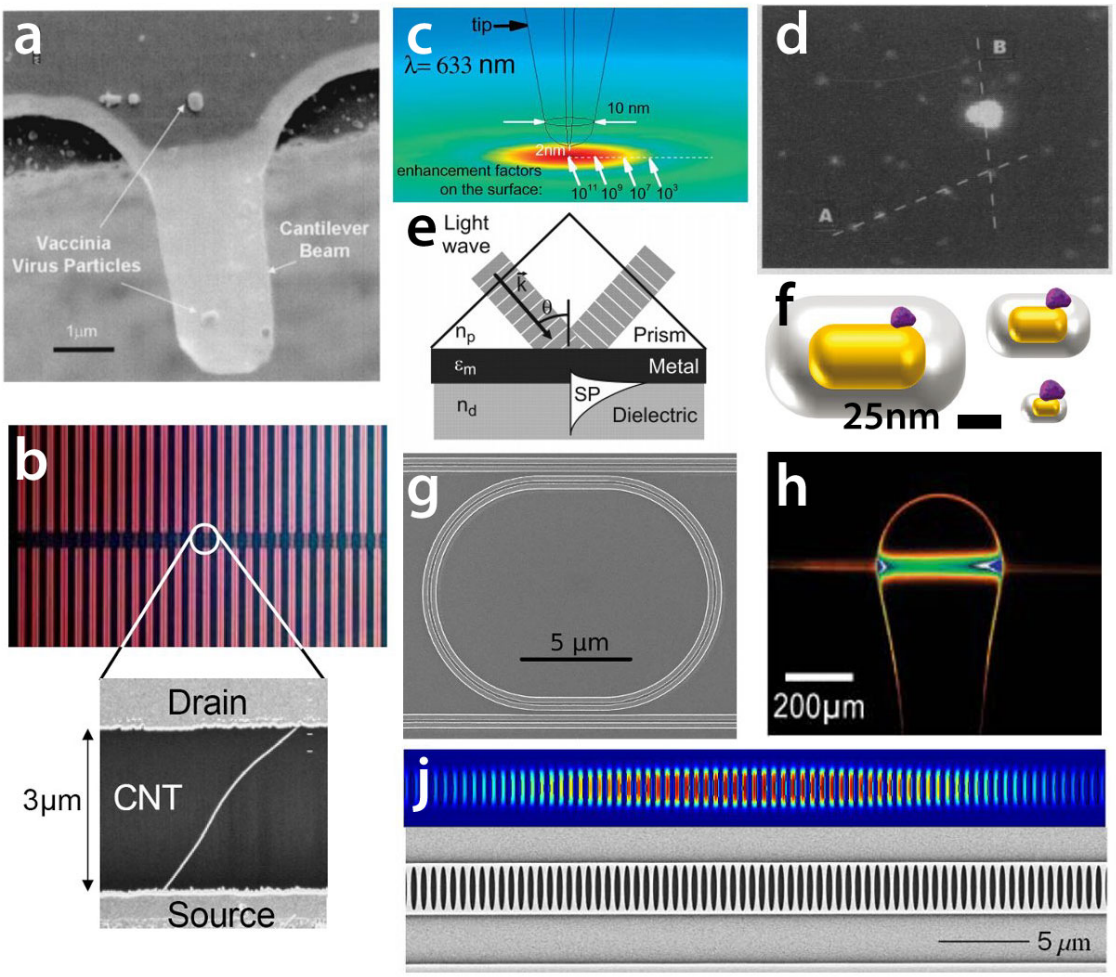

Figure 1.4.: Examples of different bio-sensors. (a) A micro-cantilever with single virus attached [65]. (b) An array of carbon nanotube (CNT) FETs. [66]. (d) The surface enhanced Raman signal from a single R6G molecule (bright spot) in direct comparison to the much weaker fluorescent signals (pale spots) [61]. (c) The principle of tip enhanced Raman scattering; the color scheme represents the enhancement factor experienced by molecules on the surface with a peak at 10^{11} [64]. (e) The principle of a surface plasmon sensor in the Kretschmann configuration, where the SPR is excited using a prism [67]. (f) Schematics of a plasmonic nano-antenna: The shaded volume around the indicated gold nanoparticle represents the sensing volume [68]. (g) A silicon slot-waveguide ring resonator, including the coupling waveguide fabricated on a chip [51]. (h) The WGM of a microsphere resonator is excited via a tapered optical fiber [34]. (j) An electron micrograph of a photonic crystal cavity used for sensing. The density plot above shows the intensity distribution [69].

control over the active site (cf. Figure 1.4 (c)).

Absorption from single molecules on a surface was among the first experiments that demonstrated single molecule sensitivity [15]. Recently several groups have succeeded in directly recording modulation free signatures of single molecules [70, 71]. In Figure 1.2 the fidelity reflects the intensity noise in the recorded signal and the overlap compares the absorption cross section to the illuminated area.

Cantilever sensors: Another class of sensors is based on micro-cantilevers [72]. These devises are usually suspended on one side only, and their dimensions range from $\sim 5\,\mu$m length up to a few mm. Cantilevers as bio-sensors are usually used in three ways: (i) a dynamic sensing method is used, where the added mass of an adsorbing particle changes the mechanical resonance frequency of the cantilever [73]. The relative frequency shift is roughly proportional to the ratio between added mass and effective mass of the cantilever. However, it depends strongly on the position where the particle attaches. Monitoring the resonance frequency of a higher order mechanical mode or a lateral vibrational mode, one can infer the absolute added mass. The resonance frequency of the beam can be accurately tracked when driving the cantilever with a piezo electric device. In Figure 1.2 the overlap parameter of a micro-cantilever was estimated using the ratio between the mass of a 150 kDa protein and the effective mass of the cantilever. In general the cantilevers suffer from a low mechanical Q in aqueous environment. However in vacuum sensitivity to single gold atoms [74] and the sizing of protein clusters [75] were demonstrated (cf. Figure 1.4 (a)). Secondly, (ii) the cantilever can be used as a static stress sensor. If one side of the cantilever is covalently functionalized, the incorporation of the target molecule or particle causes stress on the surface, which leads to a curvature of the beam. The static deflection is commonly measured via a reflected laser beam or via electro-capacitive methods. Lastly (iii), bimetallic cantilevers have been used for calorimetric measurements. Reaction heat or thermal energy uptake leads to a temperature change of the cantilever, which manifests as a deflection [65].

Sensors based on **nanowires** measure the conductance change of the wire that is associated with the adsorption of single molecules (cf. Figure 1.4 (b)) [76]. Very recently Choi and colleagues gave an impressive demonstration of the sensitivity that can be reached [9]. The authors attached a lysozyme enzyme to a carbon nanotube, which is actually much smaller in diameter than the target, and showed that the conductivity of the tube changes with the conformation of the enzyme. Strikingly they were able to observe the metabolic functioning and cutting action of the enzyme in real time.
However remarkable these findings are, the setting is specifically tailored to the task and involves the non-trivial attachment of the target molecule to the wire; it therefore falls into a different category of sensors. The goal of resolving bio-dynamics on a single particle level is however very similar.

Photonic crystals (PhC) for sensing purposes are mainly employed in two different ways. (i) Using the colorimetric technique, a PhC slab or membrane is illuminated along the surface normal with a white light source or a tunable narrow band source. The reflected and transmitted spectrum depends strongly on the hole diameter of the PhC [77, 78]. In a sensor configuration, the analyte enters the holes

of the PhC, such that the effective diameter is reduced and the reflected as well as the transmitted spectra change. Specificity is achieved, when the interior of the holes is prepared with antibodies or receptors. The second manner in which PhC are used for sensing, is in a (ii) photonic crystal cavity configuration (cf. Figure 1.4 (j)) [79, 80]. The overlap of the optical mode with the environment is maximized for PhC slot cavities [81]. The latter hold the advantage, that light can be confined to mode volumes much smaller than with conventional optical resonators. On the other hand, they suffer from low optical Q which is around $10^4 - 10^5$ in air and degrades $\sim 10^3$ in water. As PhC cavities are usually fabricated from silicon or silicon nitride, the transparency window of the material requires operation in the infrared, typically around $\lambda = 1.5\,\mu$m, which is strongly adsorbed by water. Recently, however, a PhC cavity design from low index contrast polymer has demonstrated promising results in sensing [69].

Surface plasmon resonances (SPRs) are collective charge displacement oscillations at the interface of a dielectric and a metal. Propagating, non-dissipative SPR waves were first reported by Otto [82], but it took more than a decade until SPRs were first employed for sensing by Liedberg *et al.* [83]. After this successful demonstration, the potential was recognized and SPR sensors were soon commercially developed by the company Biacore. Today SPR based methods are widely used for refractive index sensing applications in academia and industry. In the Kretschmann configuration the gold coated surface of a prism constitutes the active sensor surface in an aqueous environment (cf. Figure 1.4 (e)). A light beam, that is reflected inside the prism by total internal reflection, excites SPR waves at the interface that extend into the exterior. The dispersion relation and thus the excitation angle depends linearly on the refractive index of the environment, and typically the angle of excitation is the recorded parameter. The ease of use, robustness, and easy integration in microfluidic systems are the most prominent advantages of SPR sensors. Moreover, the technology is suited for multiplexing and arrays of sensitive spots have been developed. On the other hand, the sensitivity remains limited by the fast dephasing of the SPR (optical Q ~ 10) [6] and the relatively large excitation area. The sensitivity and range of SPR sensors is increased when long range SPRs are used that result from the constructive interference of two SPRs propagating along two metallic films, separated by a thin dielectric layer. Moreover, different SPR sensor configuration have been developed that involve gold coated tapered fibers and gratings.

Recently, sensors based on **plasmon resonances localized in metallic nanoparticles** (NPs) have been demonstrated, which constitute highly promising systems for single molecule sensitivity. Instead of a traveling surface wave, the plasmon is confined inside a nanometer scale gold or silver particle, where the excitability of the plasmon depends on the actual shape of the NP. In general cylindrical or L-shaped antennas provide the best optical properties. Typical dimensions of such plasmonic antennas are $30\,\text{nm} \times (10\,\text{nm})^2$, which is of the order of 50 mid-size proteins (cf. Figure 1.4 (f)). Therefore a molecule that attaches to the NP strongly influences its electronic properties. Recently, significant progress has been made using localized SPR with photothermal microscopy, where sensitivity sufficient to observe binding of

single mid-size proteins (streptavidin) was demonstrated [84]. A second experiment reports binding of single protein fibronectin (450 kDa) to larger gold particles ($\sim 10^4\,\mathrm{nm}^3$) by direct observation of the scattered light [68]. These techniques currently provide the highest sensitivity of all label-free single particle sensors, but suffer from other drawbacks, such as an intrinsically low quality factor (< 50) of the plasmon resonance [6]. Moreover, coupling to the plasmon is inefficient and requires high power levels of incident light to determine the resonance wavelength.

1.1.3. Biosensor functionalization

So far we have focused our discussion on the transducer elements of different sensor types. Equally important, however, is the sensor interface for target immobilization [85, 86]. Again, there are different concepts, depending on the field of application. For specific detection of target molecules, the sensor surface is usually prepared with an antibody or receptor layer [87, 88, 89]. Other methods involve unspecific particle trapping. Special attention needs to be paid to the adsorption cross section and the transport of the target. In particular mesoscale sensors, that are designed for single particle sensitivity, often display an active surface region and a depletion length that is extremely small compared to the sampled volume. This raises the important question, of how the target is transported to the sensor. If transport depends on diffusion only, it can take unrealistically long time for the target to arrive at the sensor [85]. This diffusion bottleneck is illustrated by the example of a protein, with a diffusion constant of $10\,\mu\mathrm{m}^2/\mathrm{s}$, that takes almost an hour to cover a distance of one centimeter. On the other hand, if the sensor is integrated into a fluidic system, only a tiny fraction of the flow is sampled by the sensor.
Sensors that are designed to detect low target concentration therefore posses efficient immobilization and capture schemes that serve target accumulation, while the analyte is sampled several times. In the case of DNA microarrays, the functionalized surface even constitutes the sensor itself [24, 31]. Here, we take a surface functionalization approach that goes beyond simple target immobilization. Instead the surface provides a biomimetic environment that allow us to observe the interaction of a particle or molecule with its natural counterpart. To this end, we cover the sensor surface with a lipid bilayer and hence mimic the membrane of a cell [90]. Specific functionalization is achieved by the insertion of membrane proteins or specifically labeled lipids. In a sense we reduce the natural system to its (presumably) essential constituents and build a model membrane system directly on the active sensor region [91]. The method is exemplified in Figure 1.3 (b) and presented in detail in section 4.1.

1.1.4. Advantages of high-Q cavity based sensors over plasmonic nanoparticles

We believe that the most promising sensor systems today are high-Q optical resonators, plasmonic nanoparticle antennas, and (carbon nanotube) nanowires. If

photonic crystal cavities can come up with higher optical quality in water, they could close the gap to the before mentioned systems. Figure 1.2 exemplifies that plasmonic antennas and nanowires follow an approach, where the sensor dimensions are of the order of the particle size and while sacrificing the Q-factor. As a matter of fact, the nanowire does not even rely on a resonant enhancement, but profits from a significant leverage effect of the electronic coupling. With high-Q cavity based sensors, we take the opposite approach and work with a larger mode volume, while gaining in sensitivity through the exceptionally high optical quality. Even though these approaches come from entirely different directions, a comparable sensitivity can be attained.

Despite the current success of nano-sensors, the small dimensions of the devices entail a number of difficulties and drawbacks. As discussed in the previous section, the extremely small active surface area – in the range of $10^{-3}\,\mu\mathrm{m}^2$ – makes target delivery a demanding task. Moreover, a deterministic surface preparation, which is essential for biologically relevant applications, is difficult to achieve, if not impossible for carbon nanotubes. In direct contrast, the surface area of our toroidal sensor amounts to $\sim 200\,\mu\mathrm{m}^2$, which is more that $> 10^5$ times larger. This does not only simplify target delivery, but it enables us to observe hundreds of events in a single measurement, which is required for statistical analysis and cannot be achieved with nano-sensors. In addition, we demonstrate an elegant way to create a universal bio-interface on the sensor.

Another questionable point arises from the strong (electronic) interaction of a nano-sensor with the target particle, which lays in fact the foundation for the high sensitivity. The interaction always goes two-way, and the measurement will exert a considerable influence on the molecule. It remains to be investigated, by how much this disturbs the biological functioning, i.e., of an enzyme in reference [9]. Moreover, plasmonic nanoparticles face the challenge of addressing the plasmon resonance, and typically high optical power is involved. Along this line, long integration times of several ms limit the time resolution of the measurement. Here, using the toroidal cavity, we couple light to the resonator via a tapered optical fiber, and only a few tens of nanowatts optical power enter the resonator. The measurement therefore has practically no influence on the target. A temporal resolution down to $1\,\mu\mathrm{s}$ can be achieved.

In a recent measurement, the target delivery and readout problem was addressed by an experiment where a plasmonic antenna is combined with an optical microsphere resonator [92, 93]. The particle, i.e., a virus, was optically trapped by the WGM and carried along to the nanoparticle for detection, such that the measurement itself exerts strong forces on the particle and disturbs the interaction.

Lastly, we do not want to conceal that high-Q cavity based sensors also come with drawbacks; most prominently the high Q makes them susceptible to different kinds of noise sources, i.e., thermal noise (cf. section 5.3). Therefore efficient thermal shielding is required.

1.2. WGM sensing theory

In this section we establish the theoretical background for the analysis of the experimental results. As discussed in the previous section, the frequency shift induced by a particle, and thus the sensitivity of the device, depends crucially on the geometry of the optical mode, i.e., the mode volume and the evanescent fraction. In order to compare the experimentally found results to theory, it is therefore necessary to know the exact profile of the optical mode used for sensing, which is given by the solutions to the wave equation.

$$\nabla \times \nabla \times \mathbf{E}(\mathbf{r}) - k^2 \varepsilon(\mathbf{r})\, \mathbf{E}(\mathbf{r}) = 0 \tag{1.1}$$

Here, the shape of the resonator is contained in the spatial dependence of the electric permittivity, $\varepsilon(\mathbf{r})$ and the resonance frequency is represented by the wave number $k = 2\pi\nu/c$. A silica microsphere with radius R_{major} is defined by

$$\varepsilon(\mathbf{r}) = \begin{cases} \varepsilon_{\text{silica}} & \text{, for } |\mathbf{r}| \leq R_{\text{major}} \\ \varepsilon_{ex} & \text{, for } |\mathbf{r}| > R_{\text{major}} \end{cases}$$

and, owing to the symmetry of the problem, an analytical, closed-form solutions to Equation 1.1 exists. The derivation of the microsphere solutions has been published several time before and can be found for example in references [94, 95, 96, 97]. The solutions for a toroidal geometry, which is defined by a major radius R_{major} and additionally by a minor radius R_{minor}, resemble the ones of a microsphere with some additional compression in the direction of the spatial confinement. However, a closed-form expression of the WGMs does not exist.[8] Therefore we discuss the basic properties of the modes using the solution of a microsphere, and when the exact mode profiles (within the experimental error of $< 10\%$) are required for data analysis, we rely on simulations using Comsol Multiphysics and the code developed by Mark Oxborrow [99]. In appendix A.1 the WGMs of a microsphere are presented in detail, and in appendix A.2 the analytical solutions are compared to simulation results. To provide some additional benefit to the reader, the expressions are supplemented by Mathematica code that enables the reader to plot and recalculate the modes as well as parameters that are important for sensing evaluation (e.g., mode volume, effective sensing volume, mode energy, resonant frequency). The code can directly be pasted to a Mathematica notebook.

The optical modes of a microsphere can be divided into waves of the electric type (TM polarization, electric field parallel to the excitation plane) and magnetic type (TE polarization, electric field perpendicular to the excitation plane), and they are characterized by three mode numbers $\{l, m, q\}$ that denote the polar, azimuthal, radial mode numbers, respectively. Here, m corresponds to the integer number of wavelengths fitting into the effective optical path of one round trip, and $|m - l|$ and q

[8] An analytical expression for an oblate ellipsoid that approximates the toroidal shape is given in reference[98].

are the numbers of intensity nodes in latitudinal direction and radial direction. The WGM are typically represented by the electric field vector in spherical coordinates.

$$\mathbf{E}^{\mathrm{TM}}_{lmq}(r,\vartheta,\varphi) \quad \text{and} \quad \mathbf{E}^{\mathrm{TE}}_{lmq}(r,\vartheta,\varphi)$$

Here, we normally use a the fundamental TM mode for sensing that is characterized by $q = 0$ and $l = m$, and that we denote TM00 accordingly.

1.2.1. Perturbation approach to the single particle frequency shift

The sensing principle of cavity based RI sensors relies on the effect that a refractive index change of the environment, changes the optical path length of the mode, such that the resonance frequency is shifted. In this section we follow a perturbation approach to calculate the frequency response $\delta\nu$ to a small variation of the electric permittivity $\delta\varepsilon$. We emphasize that the approach does not make any assumptions, whether the perturbation is local (i.e., a particle) or a homogeneous change of the RI. Effects that are related to the particle geometry, such as polarizability, will be included later in in section 1.3. We start with the time dependent wave equation for a field Ψ.

$$\left[\nabla^2 - \frac{\varepsilon(r)}{c^2}\frac{\partial^2}{\partial t^2}\right]\Psi(\mathbf{r},t) = 0 \tag{1.2}$$

For a monochromatic wave Ψ the time dependence can be dropped, and we assume a set of orthogonal solutions $\{E_n(\mathbf{r})\}$ to Equation 1.2 that shall represent the electric field here. Explicit expression for the electric field of a microsphere are given in appendix A.1.

$$\left[\nabla^2 + \varepsilon(\mathbf{r})k^2\right]E_n(\mathbf{r}) = 0, \qquad \forall n \tag{1.3}$$

Next, we introduce a perturbation of the permittivity $\varepsilon(\mathbf{r}) = \varepsilon^0(\mathbf{r}) + \varepsilon^1(\mathbf{r})$. In the following the dependence on the spatial coordinate $\mathbf{r}$ is implicitly assumed and shall be dropped for better readability. Taking the n^{th} mode for sensing, the perturbed mode can be written as a superposition of the unperturbed solutions.

$$E^0_n + E^1_n \;= E^0_n + \sum_j c^1_j E^0_j \tag{1.4}$$

Finally, we introduce the variation of the wave number $k_n \to k^0_n + k^1_n$ and insert the expansion 1.4 into Equation 1.3. In the next step only first order terms of the development are kept and higher order are discarded.

$$\left[\nabla^2 + \left(\varepsilon^0 + \varepsilon^1\right)\left[\left(k_n^0 + k_n^1\right)^2\right]\right]\left(E_n^0 + E_n^1\right) = 0, \qquad \forall n \tag{1.5}$$

$$\left[\nabla^2 + \varepsilon^0\left(k_n^0\right)^2 + \varepsilon^1\left(k_n^0\right)^2 + 2\varepsilon^0 k_n^0 k_n^1\right]\left(E_n^0 + E_n^1\right) \approx 0 \tag{1.6}$$

$$\left(\varepsilon^1\left(k_n^0\right)^2 + 2\varepsilon^0 k_n^0 k_n^1\right)E_n^0 + \left[\nabla^2 + \varepsilon^0\left(k_n^0\right)^2\right]E_n^1 \approx 0 \tag{1.7}$$

Now, we introduce the expansion of the field perturbation (cf. Equation 1.4) into the first order equation

$$\left(\varepsilon^1\left(k_n^0\right)^2 + 2\varepsilon^0 k_n^0 k_n^1\right)E_n^0 + \varepsilon^0\sum_{j\neq n} c_j^1\left[\left(k_n^0\right)^2 - \left(k_j^0\right)^2\right]E_j^0 \approx 0 \tag{1.8}$$

Multiplication with $(E_n^0)^*$ and integration over the entire volume, eliminates all solutions $E_{j\neq n}^0$, due to the orthogonality of the modes, and yields the expression:

$$\int dr^3\varepsilon^1\left(k_n^0\right)^2\left|E_n^0\right|^2 \approx -\int dr^3 2\varepsilon^0 k_n^0 k_n^1\left|E_n^0\right|^2 \tag{1.9}$$

$$\frac{k_n^1}{k_n^0} \approx -\frac{\int dr^3\varepsilon^1\left|E_n^0\right|^2}{2\int dr^3\varepsilon^0\left|E_n^0\right|^2} \tag{1.10}$$

The integral in the denominator is equal to the electro-magnetic mode energy U_{mode}. Moreover, we rewrite the electric permittivity in terms of the electric field constant and the relative permittivity, and reintroducing the spatial dependence, i.e. $\varepsilon^0 \rightarrow \varepsilon_0 \cdot \varepsilon(\mathbf{r})$, we write the expression for the relative frequency shift.

$$\frac{\Delta\nu}{\nu} \approx \frac{-\varepsilon_0}{2U_{\text{mode}}}\int_{V_p} d^3r\,\delta\varepsilon(\mathbf{r})\left|\vec{E}(\mathbf{r})\right|^2. \tag{1.11}$$

Here the mode energy $U_{\text{mode}} = \int d^3r\,\varepsilon_0\varepsilon_r(\mathbf{r})\left|E(\mathbf{r})\right|^2$ already contains the magnetic field contribution. Equation 1.10 represents the most general expression for the first order frequency shift. If the perturbation is non-local, i.e., $\varepsilon^1 = const$, we find that the optical mode remains unchanged, i.e. $c_j^1 = \delta_{nj}$ and $k_n^1 = -(\varepsilon^1/2\varepsilon^0)\,k_n^0$. However, this is a highly artificial case, because it requires that the refractive indices of the silica and the exterior change in the same way. More interesting is the case of a localized perturbation $\varepsilon^1(\mathbf{r}) = \varepsilon_c^1 V_p \cdot \delta(\mathbf{r} - \mathbf{r}_{\text{p}})$, with $\mathbf{r}_{\text{p}}$ being the position of the perturbation and V_p the volume of the particle. Then we obtain an expression for the single particle frequency shift.

$$\frac{\Delta\nu}{\nu} \approx \frac{-\varepsilon_0\delta\varepsilon\left|\vec{E}(\mathbf{r}_{\text{p}})\right|^2 V_p}{2U_{\text{mode}}} \tag{1.12}$$

1.3. Modification to first order perturbation theory due to particle polarization

In the previous section we have derived the single particle frequency shift, namely the frequency variation resulting from a local perturbation of the electric permittivity (i.e., the refractive index). However the calculation does not take the actual geometry of the perturbation into account. That shape matters, is nicely illustrated by an example that Richard Feynman brings up in his famous lectures. He imagines a dielectric in an external electric field and removes a thin slab from the inside. With E_0 being the electric field outside the medium, then, for a slot cut parallel to the electric field, the field inside the cavity is still equal to E_0. On the other hand, if the slot is cut perpendicular to the electric field, the field inside the slot is given by $E_0 + P/\varepsilon_0$, where P is the polarization of the dielectric. This is readily understood, because in the latter case the long face of the slot carries charges due to the polarization of the surface atoms (cf. Chapter 11 and 32 of [100]). Such geometric effects are not included in simple perturbation theory and need to be introduced separately.

Here we calculate the electric field inside a dielectric sphere, placed in an external dielectric medium, which resembles the case of a particle, i.e., in an aqueous medium. Again E_0 denotes the external field (in the dielectric) and we solve the Laplace equation for the electric field E_p inside the sphere [101]:

$$E_p = \frac{3\varepsilon_{ex}}{2\varepsilon_{ex} + \varepsilon_p} E_0$$

ε_{ex} and ε_p are the electric permittivities of the environment and of the particle respectively. The above factor was first introduced as a correction factor for the frequency shift by Teraoka and Arnold [102] and accounts for the energy of an equivalent dipole.

$$\left(\frac{\delta\nu}{\nu}\right)_{Teraoka} = \frac{\varepsilon_0}{2} \frac{3\varepsilon_{ex}}{2\varepsilon_{ex} + \varepsilon_p} (\varepsilon_p - \varepsilon_{ex})\, V_p |E_0|^2 / U_{\text{mode}}. \tag{1.13}$$

The correction is typically small, in the range of a few percent. Anyhow, Equation 1.13 failed to reproduce our measured results. Oftentimes, theory predicts a frequency shift that is about three times larger than the experimentally found values. We carefully estimated the errors deriving from frequency calibration, particle size distribution, uncertainty of the refractive index, and different mode families. The calculations were verified in the analytically accessible limit of a microsphere and backed up by simulations. Neither of these issues could explain the observed deviations.

We therefore reassess the theoretical description of the single particle shift, namely how the particle polarizability enters the equation. In contrast to Teraoka, we integrate over the full dipole field of the polarized particle – including the environment – and calculate the energy difference between the electric field with particle and the

electric field in absence of the particle. We argue that the frequency shift is proportional to the electrostatic energy shift, which was suggested before in reference [39]. Compared to the results of Teraoka and Arnold (cf. Equation 1.13) , the expected frequency shift is exactly a factor 1/3 smaller; a significant deviation that we became aware of by the precision of our own experimental results. In appendix B we show that the results published by other groups are also in agreement with the modified theoretical description.

1.3.1. Calculation of the electrostatic energy shift

In this paragraph, an alternative way to include the particle polarizability into the expression for the single particle shift is presented. A particle that enters the evanescent field of the mode leads to a perturbation of the static electric permittivity $\varepsilon \to \varepsilon + \delta\varepsilon$. According to the structure of the wave equation this corresponds to a variation of the electric potential and ergo the frequency shift (without taking particle polarization into account) is proportional to the variation of electrical energy $\Delta U/\varepsilon_0 = 1/2\varepsilon_p V_p |E_0|^2 - 1/2\varepsilon_{ex} V_p |E_0|^2$. The relative frequency shift is then given by the relative energy change $\delta\nu/\nu = -\Delta U/U_{mode}$. When a dielectric particle is exposed to an electric field, it becomes polarized, such that the electrostatic boundary conditions are fulfilled. Effectively, the particle acts as an electric dipole. Integrating over the whole dipole field and over the electric field within the particle, and subtracting the field energy in absence of the particle yields the desired energy shift.

Dielectric sphere

Here, we imagine a dielectric sphere of radius R and relative permittivity ε_p in a static electric field along the z-axis $\vec{E}(\mathbf{r}) = \vec{e}_z \cdot E_0$ in a dielectric environment with relative permittivity ε_{ex}. For simplicity a dielectric surface close to the particle, as it would be the case for an adsorbed polystyrene bead or vesicle, is not taken into account. We calculate the electric potential inside (I) and outside (II) the sphere in spherical coordinates.

$$\Phi_{\mathrm{I}}(\mathbf{r}) = -E_0 \frac{3\varepsilon_{ex}}{2\varepsilon_{ex}+\varepsilon_p} r\cos\vartheta \quad \text{for } |\mathbf{r}| \le R \tag{1.14}$$

$$\Phi_{\mathrm{II}}(\mathbf{r}) = -E_0\, r\cos\vartheta + E_0 \frac{\varepsilon_p - \varepsilon_{ex}}{2\varepsilon_{ex}+\varepsilon_p} \frac{R^3}{r^2}\cos\vartheta \quad \text{for } |\mathbf{r}| > R \tag{1.15}$$

Then the electric field inside the sphere is

$$\vec{E}_{\mathrm{I}}(r) = -\vec{\nabla}\Phi_{\mathrm{I}}(\mathbf{r}) = \vec{e}_z \cdot E_0 \frac{3\varepsilon_{ex}}{2\varepsilon_{ex}+\varepsilon_p}. \tag{1.16}$$

The expression $3\varepsilon_{ex}/(2\varepsilon_{ex}+\varepsilon_p)$ was used by Teraoka [102] to include the polarizability effect. Following the energy perturbation approach, we calculate now the energy

balance, when the dielectric sphere enters the electric field.

$$\delta U_{\mathrm{I}} = \frac{\varepsilon_0}{2}\int_{\mathrm{sphere}} d^3\mathbf{r}\left[\varepsilon_p\left|\vec{\nabla}\Phi_{\mathrm{I}}(\mathbf{r})\right|^2-\varepsilon_{ex}\left|E_0\right|^2\right] \tag{1.17}$$

$$= \frac{\varepsilon_0|E_0|^2}{2}\frac{4}{3}\pi R^3\left[\varepsilon_p\left(\frac{3\varepsilon_{ex}}{2\varepsilon_{ex}+\varepsilon_p}\right)^2-\varepsilon_{ex}\right] \tag{1.18}$$

$$\delta U_{\mathrm{II}} = \frac{\varepsilon_0}{2}\int_{\mathrm{exterior}} d^3\mathbf{r}\,\varepsilon_{ex}\left|\vec{\nabla}\Phi_{\mathrm{II}}(\mathbf{r})\right|^2-\varepsilon_{ex}\left|E_0\right|^2 \tag{1.19}$$

$$= \frac{\varepsilon_0|E_0|^2}{2}\varepsilon_{ex}\frac{4}{3}\pi R^3\left(\frac{\varepsilon_p-\varepsilon_{ex}}{2\varepsilon_{ex}+\varepsilon_p}\right)^2 \tag{1.20}$$

$$\Rightarrow \delta U_{\mathrm{I}}+\delta U_{\mathrm{II}} = \frac{\varepsilon_0|E_0|^2}{2}\left(\varepsilon_p-\varepsilon_{ex}\right)\frac{\varepsilon_{ex}}{2\varepsilon_{ex}+\varepsilon_p}\frac{4\pi R^3}{3} \tag{1.21}$$

Replacing E_0 with the electric field at the position of the particle, the relative frequency shift is expressed as

$$\frac{\delta\nu}{\nu}=\frac{\delta U}{U_{\mathrm{mode}}}=\frac{-\varepsilon_{ex}\left(\varepsilon_p-\varepsilon_{ex}\right)}{2\varepsilon_{ex}+\varepsilon_p}\frac{\varepsilon_0\left|\vec{E}(\mathbf{r}_{\mathrm{p}})\right|^2V_p}{2U_{\mathrm{mode}}}. \tag{1.22}$$

Interestingly, the result is exactly a factor $\div 3$ smaller than in Equation 1.13. We note that previously published results, i.e. by Vollmer et al. [37] and Lu et al. [43], are in agreement with the frequency shift predicted by Equation 1.22. Furthermore, we used Comsol to simulate the energy shift associated with a dielectric sphere that enters the homogeneous field of a plate capacitor, and the simulation results in Figure 1.5 exemplify that the numerical result agrees very well with Equation 1.21.

Dielectric vesicle

Next we model a lipid vesicle, considering a particle that consists of a dielectric, spherical shell with inner radius R_i and outer radius R_a. The Laplace equation is solved on three regions: (I) inside the particle, with $\varepsilon=\varepsilon_{ex}$ for $|\mathbf{r}|<R_i$, (II) the shell of the particle, with $\varepsilon=\varepsilon_p$ for $R_i<|\mathbf{r}|<R_a$, and (III) the exterior of the particle, with $\varepsilon=\varepsilon_{ex}$ for $|\mathbf{r}|>R_a$. Further we define the ratio between the particle volume and the entrapped volume $\delta=(R_i/R_a)^3$, such that the volume of the material that contributes to the refractive index contrast is given by $V_p=(4\pi/3)R_a^3(1-\delta)$. Lastly, for simplicity, we define the abbreviation $\tilde{\varepsilon}^2=2(1-\delta)\left(\varepsilon_{ex}^2+\varepsilon_p^2\right)+(5+4\delta)\varepsilon_{ex}\varepsilon_p$. Then we can write the solutions for the electrostatic potential:

$$\Phi_{\mathrm{I}}(\mathbf{r}) = -9E_0\left(\varepsilon_{ex}\varepsilon_p/\tilde{\varepsilon}^2\right)\,r\cos\vartheta \tag{1.23}$$

$$\Phi_{\mathrm{II}}(\mathbf{r}) = -3E_0\left(\varepsilon_{ex}\left(\varepsilon_{ex}+2\varepsilon_p\right)/\tilde{\varepsilon}^2\right)\,r\cos\vartheta \tag{1.24}$$

$$-3E_0R_a^3\delta\left(\varepsilon_{ex}\left(\varepsilon_p-\varepsilon_{ex}\right)/\tilde{\varepsilon}^2\right)\,\frac{\cos\vartheta}{r^2} \tag{1.25}$$

$$\Phi_{\mathrm{III}}(\mathbf{r}) = -E_0\,r\cos\vartheta \tag{1.26}$$

$$+E_0R_a^3\left(1-\delta\right)\left(\left(\varepsilon_{ex}+2\varepsilon_p\right)\left(\varepsilon_p-\varepsilon_{ex}\right)/\tilde{\varepsilon}^2\right)\,\frac{\cos\vartheta}{r^2} \tag{1.27}$$

Again, we integrate over the difference of the electric field energy density and find the total energy shift when the three contributions are added.

$$\delta U = \frac{\varepsilon_0 |E_0|^2}{2} \frac{4\pi R_a^3}{3} (1-\delta) \frac{\varepsilon_{ex} (\varepsilon_p - \varepsilon_{ex}) (\varepsilon_{ex} + 2\varepsilon_p)}{\tilde{\varepsilon}^2} \tag{1.28}$$

Notably, if we consider the limit $\delta \to 0$, such that the entrapped volume goes to zero, the result for the solid sphere is recovered. In the other extreme, $1 - \delta \ll 1$, we obtain the excess polarizability for a thin-walled particle.

$$\frac{\delta U}{\varepsilon_0 |E_0|^2 V_p} \approx 1/2 (\varepsilon_p - \varepsilon_{ex}) \frac{2\varepsilon_p + \varepsilon_{ex}}{(5+4\delta)\varepsilon_p}. \tag{1.29}$$

We will show later – in chapter 3 – that the above correction factor (instead of the equation published by Teraoka et al.) and taking the overlap of the particle with the evanescent field into account, the distribution of recorded frequency shifts is very well reproduced .
We emphasize, that the above formulas are obtained for a homogeneous, static electric field and an isotropic environment. In a realistic scenario however, the particle is close to a dielectric surface and the electric field exhibits an exponential decay. We simulated both cases, and found that the dielectric surface leads to an increase of the energy shift of $\sim 20\%$, while the field decay causes a decrease of the energy shift of $\sim 20\%$. As these two major corrections are of the same order of magnitude, but go into different directions, we did not find it necessary to include higher order terms in Equation 1.28. The error of $\sim 10\%$ can be neglected compared to other influences such as the deformation of the lipid vesicle.

1.3.2. Discussion of particle polarizability

The considerations made in the previous sections trigger important consequences and call for a second mean of verification. We therefore use Comsol to simulate the change of the electric energy density in a scenario where a dielectric particle enters a static electric field. For numerical simplification, we chose a spherical particle, placed between the homogeneously charged electrodes of a plate-type capacitor in Comsol's 2d axial symmetric mode. The resulting energy density distribution is shown in Figure 1.5 (a), where the axis of rotational symmetry cuts vertically through the sphere. Next we numerically integrate the energy density in a box around the particle, including the particle itself and calculate the energy difference compared to the setting in absence of a particle. The box size correspond approximately to the frames in panels (a)-(c). The resulting energy difference for a varying refractive index of the sphere is plotted in panel (d) and compared to the analytical result of Equation 1.21. The deviations are in the range of a few percent and thus well below the experimental error.

A full description also involves the influence of the influence of the silica surface when the sphere attaches to the resonator and a non-homogeneous, decaying electric field. Because of the involved symmetry breaking this is difficult to achieve analytically,

such that we need to rely on numerical simulations. Figures 1.5 (b) and (c) show simulations of such settings, and panel (e) of the same figure shows the corresponding (relative) energy shifts. Interestingly both effects lead to deviations of $\sim 20\%$ that go, however, in opposite directions and thus cancel. We therefore conclude that Equation 1.21 provides an accurate description of the frequency shift induced by a polarized, spherical particle. All deviations between the analytical calculation and simulations are much smaller than a factor $1/3$.

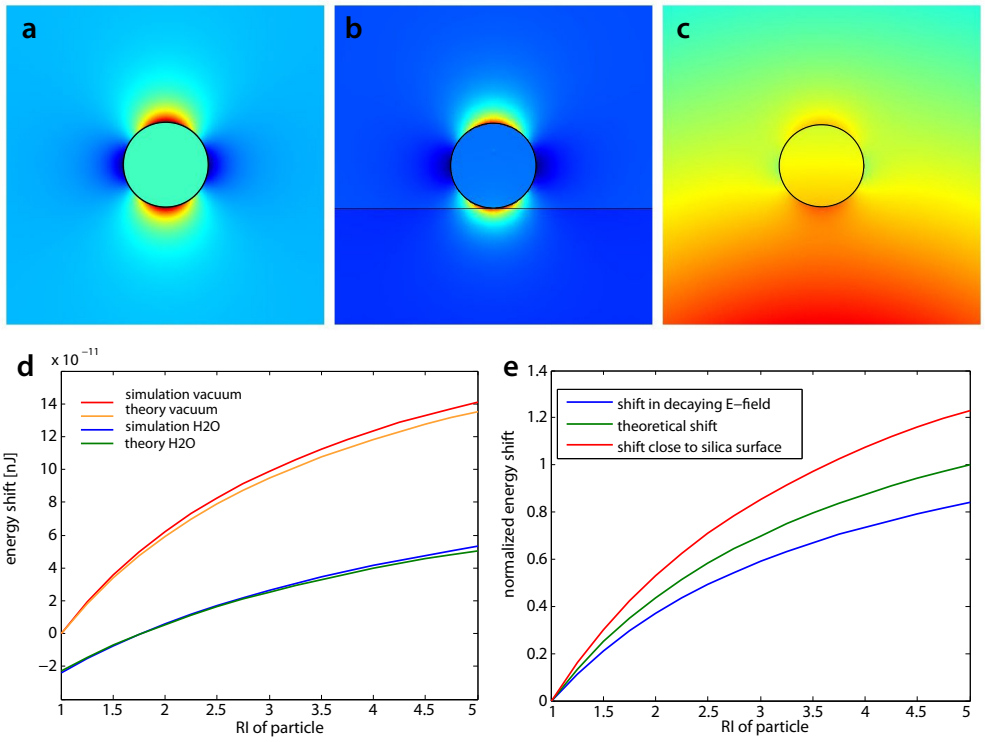

Figure 1.5.: The polarizability of a dielectric particle. The electric energy density in and around a dielectric, spherical particle in an external electric field was simulated using Comsol in its 2d axial symmetry setting. The rotation axis cuts vertically through the center of the spheroid. The color scale is arbitrary and reflects only the qualitative behavior. (a) A sphere in a homogeneous electric field. (b) A sphere on a dielectric surface in a homogeneous field. (c) A dielectric sphere in an electric field that decays with r^{-2}. (d) The change of electrostatic energy is plotted as a function of the particle's refractive index and the simulation result is compared with the theoretical value obtained from equation 1.21. Excellent agreement is found for both, vacuum and water as the surrounding medium. (e) The energy shifts for a particle in proximity of a dielectric surface and inside a decaying field are simulated. The theoretical curve is calculated for a homogeneous field (as before), with an electric field strength corresponding to the mean electric field inside the particle. Deviations of $\pm 20\%$ are observed, that go in opposite direction and largely cancel each other.

2. The experimental setup

The development of the experimental setup constitutes an essential part of experiment as it provides the stability and low noise properties that lay the foundation for the high sensitivity measurements presented in this thesis. To achieve this stability a number of particular requirements had to be met. First of all, the tracking of the resonance frequency takes place on a frequency band that ranges from DC to a few ten kHz and potentially up to a few MHz. Notably this includes building vibrations at a few Hz, the acoustic band, and prominent electronic noise sources at multiples of 50 Hz. Therefore efficient vibration isolation and filtering of electronic noise are necessary. This is in stark contrast to optomechanical experiments, where the displacement of a mechanical is monitored at a few ten MHz and the motion is restricted to a narrow bandwidth. A second distinctive feature of the setup is that the coupling to the resonator takes place in an aqueous environment. This imposes in addition requires an efficient delivery of the analyte, the ability to rinse the system, and a sample handling procedure that avoids contamination and preserves the high optical quality of the resonator in water. In the following sections we describe the setup and how the requirements stated above have been realized.

2.1. Coupling setup

The coupling setup is at the very heart of the experiment, as it is the place where the resonator, the fluidics and the optical part meet. It consist of the flow cell device (FCD), which is described in detail in the following paragraph and a positioning system to translate the sample with respect to the coupling fiber. Notably the technical advances and developments described in this chapter laid the foundation for the intriguing results presented in the chapters that follow. To preserve the extraordinary optical properties of the toroidal microresonator in aqueous environment it is absolutely necessary that the sample is not contaminated during the preparation steps as well as handling and installation. To this end a number of techniques were developed or refined. The descriptions in this chapter will often be technical and very detailed to facilitate reproduction of the results and to provide a recipe to anyone who wants to relaunch the experiment.

2.1.1. The Flow Cell Device (FCD)

The central part of the coupling and measurement setup is the flow cell device (FCD), where the coupling to the resonator takes place. The FCD is machined from

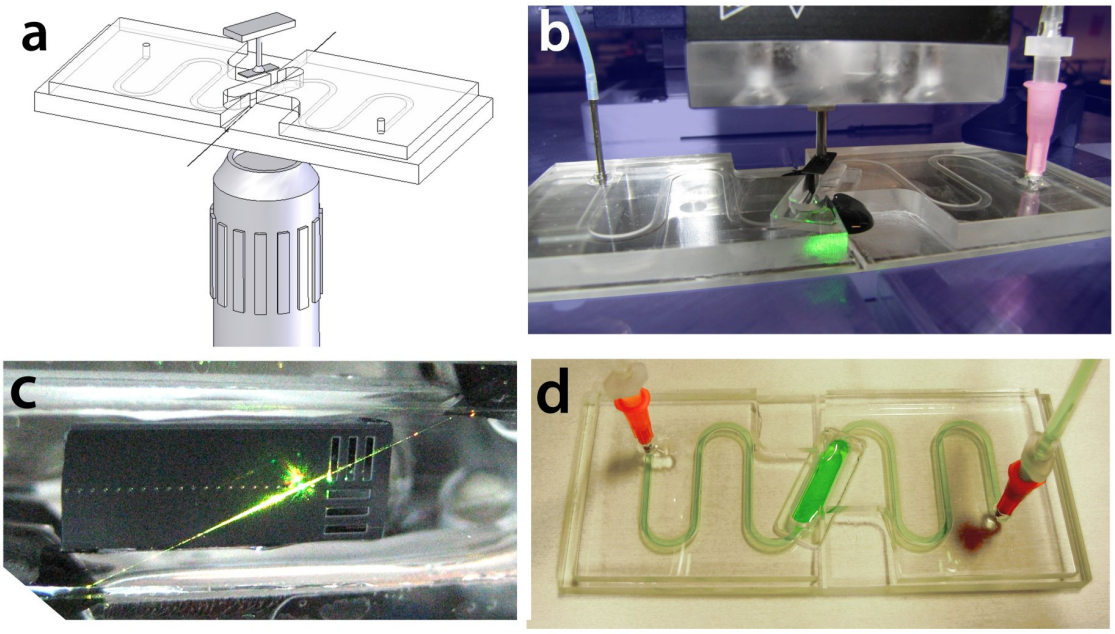

Figure 2.1.: The flow cell device. (a) Drawing of the FCD. The fiber crosses the coupling chamber at an angle of 25° through slits that are sealed with latex adhesive. The angle is a compromise between a narrow flow channel and a sufficient length of the tapered fiber. The chip that carries the resonators is glued to a mount with UV adhesive. (b) Photograph of the FCD and a sample. The sample mount is attached to a 3-axis nano-positioning system via magnets. The fluid arrives from the left through a PTFE tube and is withdrawn on the right. The fiber entry slits in the coupling chamber are sealed with latex adhesive (black material in the center). (c) A view through the bottom window shows the sample inside the coupling chamber together with the tapered fiber. Here we send $\sim 5\,\mathrm{mW}$ of power though the tapered fiber for better visibility. In a measurement around $10\,\mu\mathrm{W}$ are used. The exact coupling point on the tapered fiber (and thus the thickness) can be adjusted within the limits of lateral displacement of the chip. (d) The fluid channel and the coupling chamber are highlighted using a colorant.

acrylic glass and the sample is inserted through the open ceiling of the coupling chamber, while the coupling is monitored through a window in the bottom part of the FCD (cf. Figure 2.1 (a)). To couple to the resonator, we use a tapered optical fiber [103, 104, 105], which is firmly mounted in the FCD at an angle of 25° with respect to the coupling chamber, as shown in Figure 2.1 (c). Such design allows us to maintain a minimum length of 20 mm for the tapered region of the fiber, while at the same time minimizing the width of the coupling chamber.[1] The former avoids transmission loss at the points of entry and exit and the latter is important for efficient flushing of the coupling chamber. The fiber enters the FCD through 1 mm slits, which are sealed using a fast curing and easily removable adhesive (Microset 101RF; cf. Figure 2.1 (b)).

[1] The angle of 25° is set by the diameter and distance of the resonators on the chip, such that the fiber can pass between two neighboring cavities.

To establish a constant water or buffer flow in the FCD, we use two syringe pumps equipped with 50ml BD Plastipak syringes for fluid insertion and extraction (both Chemyx Fusion). Two supplementary pumps (New Era NE-1000) on the insertion side are used to add the analyte (cf. Figure 2.5 for a schematic layout). All pumps are computer interfaced and can be used to run synchronized insertion/flushing protocols. For valves, connectors and tubing we mostly rely on sterile medical supplies (e.g. B. Braun Discofix-3 and extensions) that are regularly exchanged. It is important to note that the flow needs to be controlled precisely to maintain a constant fluid level in the coupling chamber. Therefore, all measurements were conducted with the syringe plunger position between $15 - 45\,\mathrm{ml}$, where the plunger movement is smooth and flow is constant. Additionally, a camera was installed to monitor the fluid level in the coupling chamber. In the experiment a constant flow is important, because distortions lead to a drift of the resonance frequency, probably due to local heating.

On the mechanical side, we use a motorized xyz-translation stage (Newport Gothic-Arch 65-mm Platform) for coarse positioning of the sample. Fine alignment is achieved with an attached, inverted piezo nano-positioning system (PI, nanocube). For fast characterization of a sample, the motorized actuators are synchronized to achieve a linear movement of the chip in the coupling chamber. A translation script allows us to hop from one resonator to the next and to store absolute positions of resonators. This maximizes throughput and helps to minimized the air exposure time when the sample is mounted, as it can directly be moved to a predefined position. The whole coupling setup is installed on an optical table in a climate controlled laboratory and which is surrounded by an enclosure with sliding windows. A flow box establishes a constant air flow that prevents heat convection and ensures a constant temperature above the optical table. The syringe pumps are placed on a rack next to the optical table to grant accessibility and to decouple the vibrations from the syringe pump motors. However there is typically a temperature difference between the inside and the outside of the table enclosure, such that the fluid needs to thermalize with the environment of the coupling setup before entering the FCD. To this end we installed a thin PTFE tube (inner diameter of $0.8\,\mathrm{mm}$) of $\sim 2\,\mathrm{m}$ length, which leads to the FCD (cf. Figure 2.1 (b)) and which is taped to the surface of the optical table that serves in this case as a heat sink.

In general the inverted setup holds several advantages compared to an upright arrangement where the samples on the chip point upwards and the fiber taper is approached from the top. i) The tapered fiber does not need to be removed to exchange the sample. In practice it takes several tries to produce a fiber taper that meets the requirements for coupling in aqueous environment. Moreover an average number of $20 - 40$ resonators needs to be tested and characterized to find a high-Q optical resonance that lies within the thermal tuning range of the Nd:YAG laser. The inverted design thus allows for high sample throughput that results eventually in higher sample quality. ii) The fixed mounting of the tapered fiber leads to an increase of coupling stability. iii) The complete coupling setup is designed in a way that it fits on commercial inverted microscopes (e.g. Leica DMI3000, Nikon Eclipse MA100, Olympus GX51, Zeiss Axio Vert). (iv) Gas bubbles that could rupture

the fiber can easily escape. (v) Lastly, the sample mount itself facilitates sample handling, which will be reported on in section 2.1.3.

2.1.2. Fabrication of tapered fibers

It was already mention in the previous section that we use tapered optical fibers to achieve efficient coupling to the resonator. In this paragraph we describe the fabrication of the fiber, the transfer to the FCD and its immersion in water.
Obviously a fragile tapered fiber does not seem to be the first choice in a "difficult" environment – such as water – where surface tension might lead to rupture and impurities can deteriorate the transmission. Different coupling methods that have been reported in literature rely, e.g., on an angle cleaved fiber, prisms, or even free space coupling (to a limited degree).[2] However once the technique is mastered, the tapered fiber provides a stable way of coupling with unmatched efficiency, and it can be preserved and used for up to two weeks.

We produce a tapered fiber by pulling optical fiber (Thorlabs, 630HP) in a hydrogen torch, while monitoring the transmission at 633 nm. The position of the flame is adjusted in a way that the tapered region is shorter than 20mm. This avoids optical loss when the FCD is sealed. We estimate the thickness of the taper by manually sweeping a droplet of isopropanol over the fiber and monitoring the transmitted intensity. When the transmission drops between $50\% - 70\%$, the coupling properties have shown to be best at a wavelength of 532 nm. A total transmission loss of $< 1\%$ is frequently achieved, fibers with more than 10% transmission loss are not used.

For coupling with a thicker fiber, i.e. with a transmission drop less than 50%, it is necessary to move the fiber closer to the resonator to achieve sufficient overlap with the evanescent field. The fiber – being a dielectric itself – then induces a frequency detuning of the optical resonance and more importantly fiber vibration, e.g., due to acoustics and convection, become the dominant noise source that limits the device's sensitivity.
On the other hand, when the fiber is too thin such that the loss in the isopropanol test exceeds 70%, a broad band loss is induced when coupling to the resonator. This manifest on the one hand as a general drop of the transmission (depending on the distance to the resonator) and one the other hand by the occurrence of Fano resonances when the loss channel interferes with an optical resonance [106]. Depending on the polarization of the incident light, the typical transmission dip shape can be completely inverted. Interestingly the frequency detuning of such Fano resonance is a very sensitively with respect to the coupling gap. When approaching the resonator with the fiber, the resonance shifts by as much as 5 GHz. Interestingly one can adjust the polarization in a way, that the Fano resonance directly yields an error signal with a zero crossing at the center of the resonance (including a transmission

[2] The coupling efficiency can be enhanced, when a grating is engraved on the surface of the resonator.

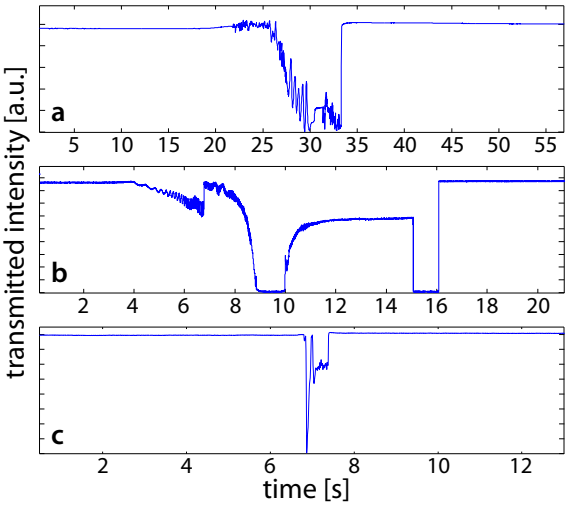

Figure 2.2: The transmission of the coupling fiber is monitored, while the FCD is filled with water. In general the transmission of the tapered fiber is not compromised. However, a water-air interface, gas bubbles, and strain due to surface tension temporarily affect the transmission properties. (a) When the water begins to wet the fiber starting from one side, typical oscillations appear, while the transmission decreases. The flow chamber is constructed such that the space beneath the fiber slowly fills up without exerting too much tension. (b) Gas bubbles arriving from the flow channel lead to a temporary loss transmission. Due to the open design of the chamber, the bubbles can escape without breaking the fiber.

offset). However due to the before mentioned delicate position dependence, faint fiber movements and vibrations directly translate into a frequency detuning.

Once a suited fiber taper has been fabricated we move to a test setup and touch the rim of a toroidal microresonator with the fiber such that it sticks to the surface. Then the fiber is pulled back until it snaps loose from the toroid. When the snap-back distance is larger than $\sim 5\,\mu$m, the fiber is tensioned and the test is repeated. Next the fiber is transferred to the FCD, which is a delicate process. We place the support with the tapered fiber on a z-translation stage and align the FCD such that the fiber is directly above the entrance slits. The fiber holder is tilted until the fiber is parallel to the FCD and finally the fiber is lowered until is touches the bottom of the grove. Here we pinpoint the fiber with two droplets of UV adhesive (NOA81, as it can be removed from the acrylic glass support) and remove the fiber from the support. Finally we seal the entrance slits with latex glue from the exterior.

Several strategies can be followed to fill the flow cell with water and in principle most of them work as the process is less critical than one would think. It is however absolutely crucial that all water that comes into contact with the taper or the sample is de-gassed before use. To this end we take fresh water from a water purification system (Millipore Milli-Q Integral) and place it into a desiccator for a few hours. Otherwise outgassing of the water will degrade the fiber transmission to $\sim 50\%$ in approximately 10 min. The optical Q of a resonator is affected as well. If the fiber transmission is accidentally destroyed by outgassing it can partially be restored by flushing with de-gassed water.

When filling the FCD surface tension of the water can break the tapered fiber. To avoid this, one can use a 20% ethanol solution to carefully fill up the coupling chamber with a syringe. The ethanol is then replaced by water from the infusion

pump. The method is very robust and the fiber is wetted immediately as surface tension is reduced by the alcohol. However when replacing the liquid, the fiber transmission frequently drops by $\sim$ 10%. This is not the case when the FCD is directly filled with water, as it is shown in Figure 2.2. To this end we insert water, using the infusion pump, and the space underneath the fiber slowly fills with water, while the fiber itself "pushes" into the surface without being wetted. It gives the impression as if the fiber would lie on a "cushion" of water. When the coupling chamber is filled such that water is extracted at the other end, we take a syringe and put a single droplet of water directly on the fiber such that it is immediately immersed and the transmission jumps back to 100%.

2.1.3. Sample fabrication and mounting

In this paragraph the fabrication of the toroidal microresonators is outlined and our method of sample handling and cleaning is introduced. The microfabrication process has been described before elsewhere [107, 108] , but nevertheless we will highlight some particular aspects here. To fabricate high-Q toroidal microresonator, we start out with commercial silicon wafers with a 2 μm oxide layer (Silicon Valley Microelectronics).[3] Briefly, we use optical lithography to define disks of varying diameters ($80 - 120\,\mu$m) and HF etching to remove excess silicon oxide (cf. Figure 2.3 (a)-(c)). In the next step the glass disks are undercut using sulfur hexafluoride. In a process developed by Emanuel Gavartin, we then use a dicing saw to cut groves that define the chips with the samples on the wafer (cf. the rectangular pattern in Figure 2.3). This way the wafer is still suited to undergo a final automated cleaning step in hot sulfuric acid in the cleanroom.

Each predefined chip has a size of 4 mm $\times$ 12 mm and carries 20 disks. To separate a single chips from the wafer it is sufficient to scribe along the grove with a razor blade or scalpel and then carefully cleave the wafer using a pair of wafer tweezers that are placed next to each other on each side of the grove. Compared to the conventional cleaving method involving a diamond scribe, the dicing method allows us the obtain well defined cleaves and samples of uniform size. The latter is particularly important, as the coupling chamber of the FCD and the sample transfer stage are laid out for a specific sample size. Moreover the method increases overall cleanliness, because of the additional cleaning step on wafer scale and because residues from scribing and cleaving remain inside the grove.

The toroidal resonator shape is obtained from the microdisk in a final laser reflow step. To this end, a CO_2 laser (Synrad 48-series, 10 W), which is strongly absorbed by silica, is focused on the disk to melt the glass. The silicon pillar provides a heat sink, such that the temperature is highest at the rim of the disk, where the liquid SiO_2 forms a ring due to surface tension. The ring shrinks towards the center, while gaining in thickness, until the cold from the pillar terminates the process and sets

[3] Oxide layers of 1 μm thickness have been tested , but the optical quality and reproducibility have shown best when using a 2 μmsilicon oxide layer.

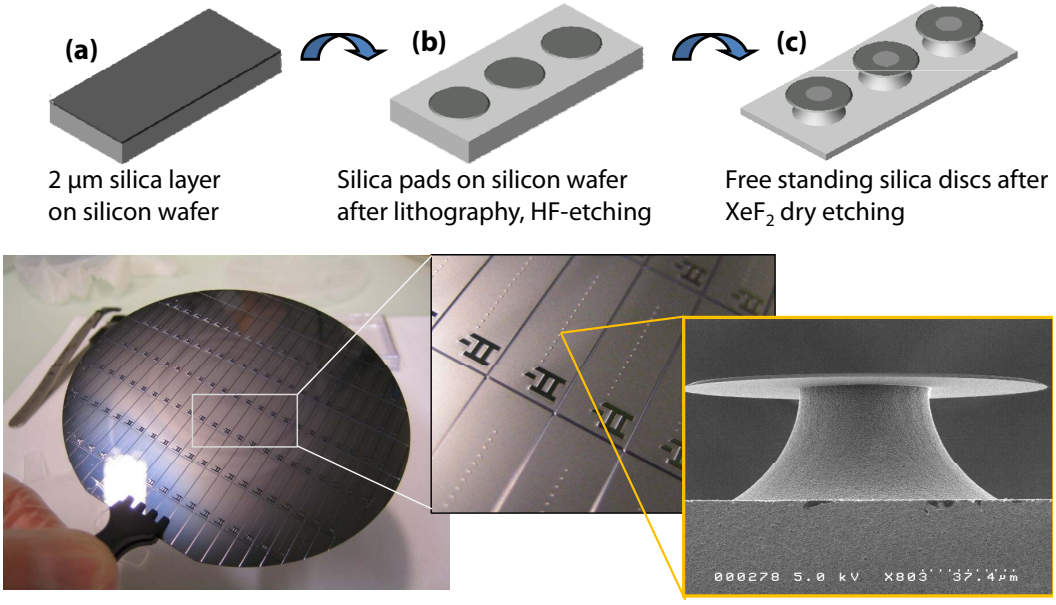

Figure 2.3.: The sample preparation at a glance. (a) Starting point of the process is a commercial 4" silicon wafer with a 2 μm oxide layer (e.g., from Silicon Valley Microelectronics). (b) The positive structures are defined using standard photolithographic methods; the excess SiO_2 is removed with a hydrofluoric acid wet etch. Typically disks with diameters from 80 μm to 120 μm are defined. (c) Next the silicon is selectively etched using either xenon difluoride of SF_6. The undercut is adjusted via the gas pressure and the number of etching cycles. The pictures at the bottom of the figure show the final wafer. The samples have been pre-diced, such that the wafer can still undergo a final cleaning step. The insets shows a magnified view of a single chip, carrying 20 microdisks and an identification/alignment structure.

the major toroid radius. There is controversy, whether a fast reflow, using a short ($10 - 100$ ms) laser pulse, or a slow reflow, by gradually increasing the laser power over a few seconds, lead to better results. Here, we found that the second method provides better control over the optical quality. However it is highly recommended that the laser power remains constant at $60\% - 70\%$, to avoid power fluctuations. To this end we work at a constant pulse width modulation and use an adjustable attenuator (ULO optics, CO2mpact attenuator with enhanced Brewster windows) to control the power.[4]

For the use with the inverted coupling setup, we designed a support that consists of a steel rod ($\varnothing = 2$ mm) attached to a PMMA block (20 mm $\times$ 8 mm $\times$ 2 mm), which is glued to a nickel plate (cf. Figure 2.4). The support is mounted in the coupling setup via magnets and can easily be handled with grooved tweezers. Figures 2.4

[4]The power level of the 10W Synrad CO_2 laser that we used for reflow is regulated via pulse with modulation (PWM). Here we set the PWM rate to the highest level (20 kHz). It is possible to control the power output fully via the PWM; however at the low power level required for laser reflow, which is typically around $10 - 15\%$ of the maximum power, we observed that the intensity fluctuates and the focal spot drifts. In particular the latter issue affects the repeatability. Moreover we found that the attenuator, which is based on a rotatable pair of Brewster plates, does not cause any visual displacement of the focal spot.

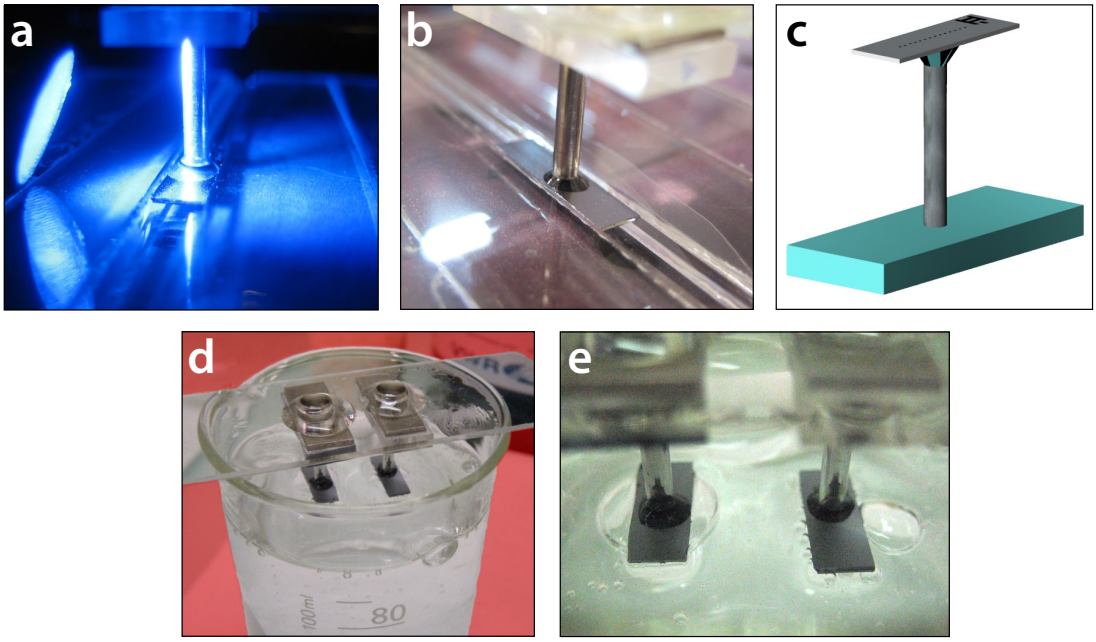

Figure 2.4.: Sample handling. The chip with the micro-resonators is glued to a support with a nickel base plate that can be attached to a magnetic holder. Nickel was chosen because of its insensitivity against a humid environment. Using grooved tweezers, the sample can be manipulated safely. A schematic view of the mount with a chip is shown in panel (c). The photograph (b) shows how the chip is aligned on a glass stage while the support is positioned using a translation stage (not in the picture) and while the glue is still wet. A groove prevents the microresonators from being damaged. (a) The adhesive is cured using a UV lamp. (d) Two samples are attached to a glass slide with matgnets and plunged in a beaker with cleaning solution. (e) A close up view shows that the sample is only wetted from the side that carries the resonators. Hence the potentially aggressive agent does not attack the glue.

(a) and (b) show how the chip is glued to the support with UV adhesive (Thorlabs, NOA-81) and how the chip is aligned on a stage assembled from microscopy slides. For sample handling and wet chemical processing, the support is attached to a glass slide with magnets (cf. Figure 2.4 (c)). This way the sample can be transferred between different cleaning and rinsing solutions without risking contamination, e.g., from tweezers.

Between two measurements the FCD is rinsed with DI water. Flushing with 4 ml of DI water has shown to be sufficient to visually remove any trace of a colorant (before a white background, cf. Figure 2.1 (d)); we flush with 30 ml to remove any residue of an analyte in between measurements. A sample that was used for a measurement can be recycled without significant degradation of its optical quality. To this end, the sample is first placed in a 65 : 25 : 1 solution of chloroform, methanol, and DI water for 20 minutes and afterward rinsed with DI water. In a second step we use SC-1 solution (5 : 1 : 1 solution of DI water, 30% hydrogen peroxide, and ammonium hydroxide at 70°C) for 10 to 20 minutes and rinse again with DI water. During the cleaning and preparation procedure the sample holder is attached to a microscope

slide, which we put on top of the beaker that contains the solution. It is an advantage of our sample mount, that the fluid level of the cleaning solution can be adjusted to a level such that the chip with the samples is only wetted from the side carrying the resonators. This avoids contamination and prevents that the UV adhesive (which is used to mount the chip) is attacked by the agent. Moreover the samples can be quickly transferred between two solutions. Following this procedure we were able to re-use a sample up to ten times. After an initial linewidth degradation from 5 MHz to 8 MHz no further loss of quality was observed. However, each recycling cycle shifts the resonance towards higher frequency by a few GHz. We believe that the SC-1 cleaning step takes off some SiO_2 material. Indeed a radius reduction corresponding to one $Si-O$ bond length shifts the frequency by roughly 3 GHz. The effect limits the total lifetime of a sample, because the resonance eventually shifts out of the laser tuning range.

2.2. The optical setup

The optical setup serves the purpose of tracking the resonance frequency of the cavity with high frequency and time resolution. To achieve this we employ two lasers, a New Focus Velocity diode laser that can be tuned over a wavelength range from 632.4 nmto 637.2 nm, and an Innolight Prometheus Nd:YAG solid state laser, operating at a wavelength of 532 nm. Figure 2.5 shows how both lasers are superposed on a dichroic mirror and can be coupled to the resonator simultaneously.
The use of two laser sources is motivated by their properties that are favorable for different applications. The diode laser has the advantage of a large tuning range that covers more than three free spectral ranges of a typical toroid resonator and a piezo sweep range of $\sim$ 40 GHz. However it suffers from a relatively broad laser linewidth of $\sim$ 300 kHz and prominent low frequency noise in the acoustic band. Dominant lines are found at multiples of 50 Hz, which give the impression of a shaking resonance when scanning the laser. We use the diode laser to record large (few GHz) frequency shifts, e.g. for ensemble measurements of streptavidin binding in section 4.2, and for the characterization of the samples. Typically a laser frequency sweep includes at least one WGM resonance that we use to align the tapered fiber with the resonator and to find a good coupling position. As we are lacking a side view on the resonator and the fiber, which can be realized for coupling setups in air or vacuum that provide better accessibility, we have to rely on the top view on the cavity for alignment.

The Nd:YAG laser on the other hand has a narrow linewidth of $\sim$ 1 kHz and features intrinsically low laser noise, which has its origin in the monolithic design of the laser cavity.[5] Here the piezo tuning range is limited to $\sim$ 800 MHz (at 532 nm) and the

[5]Indeed the laser crystal is the laser cavity. A ground facet with a dielectric coating serves as input/output coupler, while the laser beam is reflected on a closed path inside the Nd:YAG crystal via total internal reflection[109]. The crystal is clamped to a piezo for fast frequency actuation. Due to the high Young modulus of the crystal, there is little actual compression and

overall thermal tunability spans $\sim 60\,\mathrm{GHz}$, such that it is oftentimes not possible to find a suited (e.g., TM00) mode within the thermal tuning range.

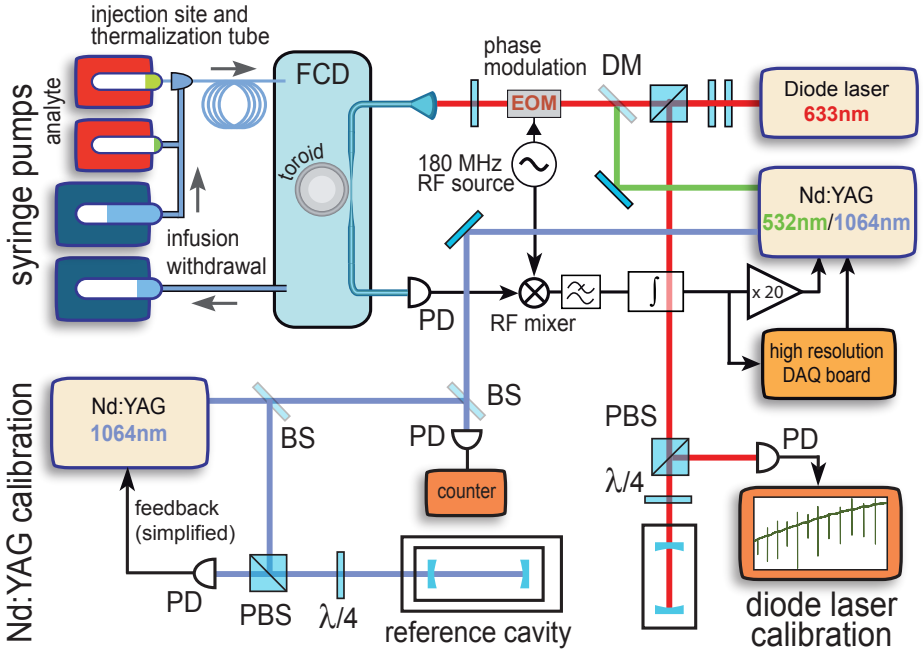

Figure 2.5.: A schematic view of the setup. The fluidic setup (indicated on the upper left side) and the optical setup come together in the FCD. On the optical side, we superpose a diode laser at 635 nm wavelength and a frequency doubled solid state Nd:YAG laser at 532 nm on a dichroic mirror (DM). Both lasers can be frequency locked to the resonator using the PDH scheme. To this end the light is phase modulated at 180 MHz using an electro optic modulator (EOM). The transmitted light is detected with a fast photodiode (PD) and demodulated with a frequency mixer to yield an error signal (cf. section 2.2.1). Using a fast PI regulator, the correction voltage is derived that is fed back to the laser piezo and that is recorded as the signal, prior to amplification.
Two schemes are implemented to calibration the correction voltage and to convert it into a frequency detuning. The diode laser is scanned over a Fabry-Pérot cavity with a free spectral range of 1.3 GHz and the minima of the reflected intensity provide frequency markers to calibrate the applied piezo voltage. For the Nd:YAG laser, we overlap a secondary Nd:YAG reference laser (Innolight Diablo) that is locked to an ultra-stable, isolated reference cavity (lower left) with the Nd:YAG laser that is locked to the sensing resonator on a beam splitter (BS). The beat frequency is recorded with a frequency counter and represents the frequency detuning between the reference cavity and the sensing resonator. As the first is much more stable than the latter (also due to their dimensions), the beat signal effectively represents the relative resonance frequency of the sensor.

displacement involved, which allows for fast actuation of up to 100 kHz (due to small charge displacement and small currents this can be handled by commercial high voltage amplifiers) at the cost of a limited frequency sweep range of $\sim 400\,\mathrm{MHz}$. Moreover the crystal is temperature controlled with an accuracy of $100\,\mu\mathrm{K}$. The laser light at the fundamental wavelength of 1064 nm is focused on a non-linear crystal for frequency doubling in a single pass configuration.

Moreover it is time consuming to scan over the whole thermal range of the laser and in practice we only search for resonances with the YAG laser after pre-characterization and alignment with the diode laser. The advantage of the Nd:YAG laser lies in its low frequency noise properties: With the diode laser the frequency resolution in a measurement is limited by laser noise, while for the Nd:YAG laser the intrinsic frequency jitter of the resonator becomes the limiting factor (on timescales faster than $\sim 1\,\mathrm{s}$).
The noise properties the resonator are discussed in chapter 5. Here we use the solid state laser for measurements that require highest sensitivity, such as the recordings of single lipid vesicles.

In the experiment we employ two different methods to track the resonance frequency of the cavity. Using the **laser scanning technique**, a saw tooth voltage is applied to the laser piezo and the wavelength is (linearly) scanned over the resonance. The transmitted intensity is recorded in parallel with the sweep voltage and the voltage corresponding to the transmission minimum is recorded. Typical scan frequencies are in the range of 10 Hz to 100 Hz. The scanning technique is used by all competitors in the field of cavity based sensing and details of our implementation are presented in section 2.2.2.
In addition we use a **laser locking method**, that relies on the Pound-Drever-Hall (PDH) technique to regulate the laser frequency to the cavity resonance. To this end a correction voltage is generated and applied to the laser piezo, such that the difference between the laser frequency and the resonator frequency is compensated. Notably frequency shifts from particle adsorption and in response to other RI changes are settled, such that the correction voltage embodies the the measurement signal (within the locking bandwidth). In the following section we introduce the PDH technique and outline the advantages of the locking method in the context of cavity enhanced sensing.

2.2.1. Pound-Drever-Hall (PDH) locking technique

The Pound-Drever-Hall technique was introduced in 1983 as a scheme to stabilize a laser to an optical resonator, such as a Fabry-Pérot interferometer, and to meet the increasing demand for ultra stable laser sources in spectroscopy and gravitational wave antennas [110, 111, 112]. The technique resembles a lock-in scheme, where the phase of the incident light is modulated and the reflected beam is detected with a fast photodiode. After demodulation with an electronic mixer or phase detector, the signal undergoes low pass filtering to obtain an error signal. A typical PDH error signal and the corresponding transmitted intensity are depicted in Figure 2.6. Within the half width of the resonance center, the error signal is proportional to the detuning between the laser and the resonator and can be used to regulate the laser frequency to match the resonance. Here we use a fast PI-regulator (Precision Photonics LB1005) to lock the laser to the resonance. Low frequency contributions, with an amplitude potentially exceeding the resonance width, are integrated (I) and fed back on the laser to correct for frequency drift; faster frequency jitter (with

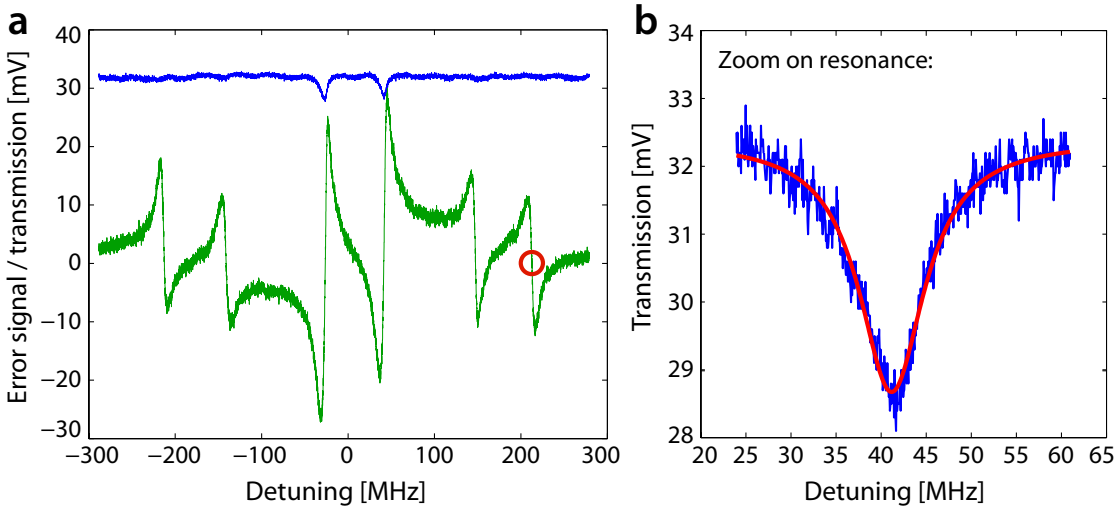

Figure 2.6.: Transmitted intensity and error signal. (a) A typical transmission signal (blue) and the generated error signal (green). Owing to the weak modulation, the sidebands are not directly visible in the transmission signal. In the error signal, however, they are well resolved and can be used for locking. Here the sidebands are detuned by ±180 MHz. The red circle indicates a locking point on the high frequency side band. The sidebands can only be observed in the error signal and are not visible in the direct transmission, due to weak modulation and undercoupling. (b) A Lorentzian fitted to the resonance. The resonance width of 8 MHz corresponds to an optical quality of $Q = 6 \cdot 10^7$.

mean zero) is proportionally (P) amplified (or attenuated) and added to the low frequency correction. The sum of these contributions is the correction signal, which is fed back on the laser. In its original sense, the scheme is used to lock a noisy laser to a stable reference. Here we take an intrinsically stable laser source to record the frequency drift and fluctuations of the resonator. It is important to note, that the locking bandwidth is not limited by the cavity bandwidth, i.e. the cavity build up time [111]. Consequently the time resolution bandwidth can exceed the typical resonance width of 5 MHz.

In our experimental setup we use a resonant phase modulator at a frequency of 180 MHz(Newport, 4001NF) that is suited for both wavelengths and which is aligned with respect to an optimized error signal (maximum amplitude and minimum undulations), which does not necessarily correspond to the alignment that maximizes the transmission. The transmitted intensity is detected with a New Focus 1801-FC-AC photoreceiver with a bandwidth of 125 MHz. Even though the modulation frequency exceeds this bandwidth, we found that the performance with respect to the amplitude and noise of the error signal is superior to the 1 GHz model and the DC coupled model of the same series of photoreceivers.

The PDH technique combines several advantages: First is ideally suited for fast sampling of the resonance frequency. Within the locking bandwidth the signal is directly obtained from the correction signal. In our current experimental setting, the locking bandwidth is limited to 100 kHz by the response time of the piezo of the

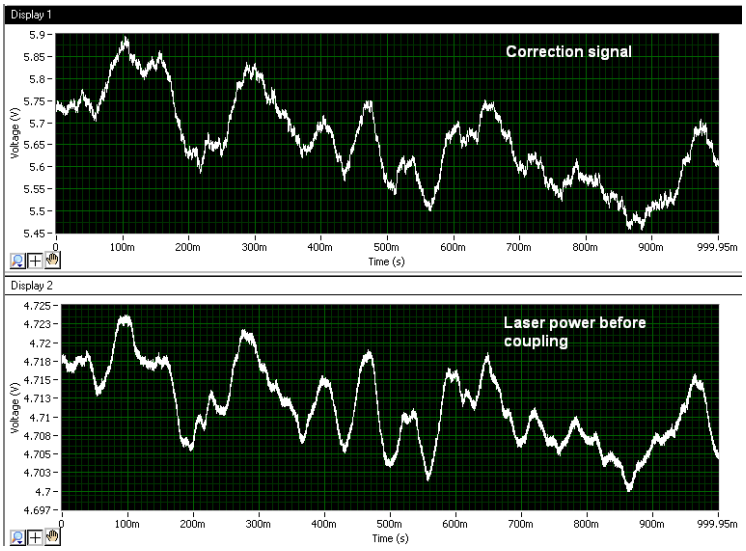

Figure 2.7: Correlation between laser intensity and correction signal. When the laser is locked to the resonance, temperature variations induced by intensity fluctuations of the laser cause a frequency drift. Here the laser intensity before coupling to the fiber is monitored simultaneously with the correction signal. A clear correlation is found.

Nd:YAG. Faster components – up to a few MHz – are contained in the error signal and can be recorded separately when the amplitude of the fast fluctuations stays within the FWHM of the resonance and thus in the linear regime of the error signal. We measure the frequency detuning of the laser as a function of the piezo voltage and use the relation to convert the correction voltage to a frequency detuning. To this end the generated sidebands provide frequency markers at a fixed detuning and give direct access to the frequency-voltage dependence. More accurate ways of calibration that we use here, are discussed in detail in section 2.2.3. Fast frequency fluctuations obtained from the error signal can be converted either by spectral overlap with the correction signal or starting from the slope of the error signal at the locking point (cf. Figure 2.6). The latter method potentially causes problems when the linewidth of the resonance and thus the slope of the error signal change during the measurement.

Another advantage of the PDH technique is the signal encoding at radio frequency (here at 180 MHz). In sensing experiments we are typically interested in a recording bandwidth from DC to a few MHz, which is susceptible to low frequency acoustic and electronic noise. Such noise is regularly picked up in the optical fiber from vibration induced stress or in cables via cross talk. Here we can efficiently block such deleterious components using high pass filters after photodetection, such that the system is only sensitive to low frequency noise after demodulation. A complete layout of the electronic components is presented in appendix C.

Lastly, it is of practical importance that the laser can be locked to a sideband, detuned from the resonance. In Figure 2.6 (a) an incident power of $\sim 12\,\mu$W is launched into the coupling fiber, which is positioned in a way that the coupling rate is much smaller than the internal loss rate (undercoupled regime[113]). On resonance, $\sim 1\,\mu$W optical power enters the cavity. In Figure 2.7 we monitor the intensity of the incident light together with the resonance frequency of the resonator (represented by the correction voltage). A clear correlation between the two recording is observed, which stems from the thermo-refractive effect that relates temperature fluctuation to a variation of the refractive index. Fluctuations of the dissipated power inside the cavity cause heat fluctuations, which translate into fluctuations of the resonance

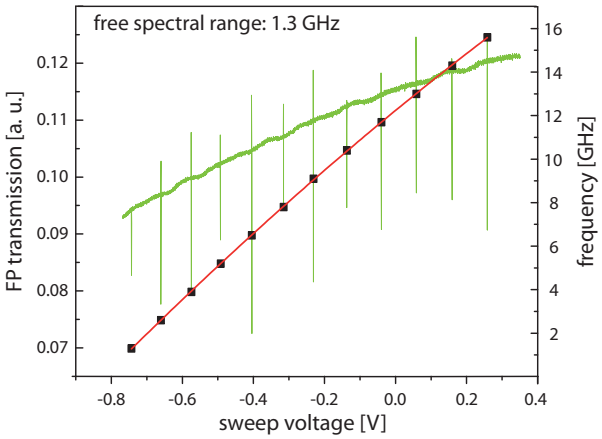

Figure 2.8: Diode laser calibration. The reflected signal (green curve, left scale) when sweeping the laser over the resonator. Two resonances are spaced by 1.3 GHz and thus provide frequency markers. We fit a polynomial to the positions of the minima and obtain a calibration curve to calibrate the piezo voltage frequency dependence of the diode laser.

frequency. This is circumvent, when the laser is locked to a frequency sideband (as indicated by the circle in Figure 2.6 (a)), such that the power entering the cavity is reduced by a factor > 20 to a few 10 nW, which practically eliminates the thermo-refractive frequency response to laser intensity fluctuations. The sideband lock is one of the main reasons why we were able to improve the sensitivity between the measurements of polystyrene beads in section 3.5 and the recordings of single lipid vesicles in section 3.3. A second reason is the optimization of the electronic setup, matching of power levels, and the strict use of low noise amplifiers.

2.2.2. Diode laser frequency calibration

We stated earlier that we use the diode laser to obtain a first impression of a resonator's optical quality and for measurements with GHz frequency shifts, which exceed the tuning range of the Nd:YAG laser. In the first case the generated sideband suffice as coarse frequency markers, when we judge the width of an optical resonance.
When it comes to a measurement, however, better means of calibration are necessary, because the dependence of the laser frequency on the piezo voltage is normally not linear and displays a slight curvature. In the experiment we scan the diode laser over the resonance and record the transmission as well as the sweep voltage in parallel. For each trace the transmission minimum is fitted with a 3^{rd} degree polynomial to find the position of the minimum. In this way 10 samples per second are acquired. We note that the stroboscopic sampling of the resonance suppresses frequency fluctuations at multiples of 10 Hz, i.e. narrow lines at 50 Hz and 100 Hz. For frequency shifts of several 100 MHz, laser noise can usually be neglected and the binding takes place on a time scale of tens of seconds, such that the 10 Hz sampling rate is not a limitation.

In addition, the scanning method allows us to monitor and to correct the coupling during the measurement, which might change during a long measurement of up to an hour, and is thus intrinsically more stable than the frequency locking methods. Using the PDH technique, we can only rely on the stray light intensity caught by the

microscope, to estimate the coupling strength, because the transmitted intensity is not a meaningful criterion when locking to a sideband. To calibrate the dependence of the frequency on the piezo voltage, we scan the laser over a Fabry-Pérot (FP) interferometer and, as shown in Figure 2.8, the reflected intensity from the FP cavity then provides a frequency ruler. We fit a polynomial to the minima of the reflected signal and obtain a conversion rule. Even when the deviation from the linear rule is weak, such calibration remains important. In particular for ensemble binding measurements (e.g. streptavidin-biotin in section 4.2), where a saturation curve is recorded, it is rather the shape of the binding curve that gives insight on the interaction (e.g., two binding time scales) than the absolute frequency shift.

2.2.3. Ultra-stable optical reference cavity

In the experiment we derive the measured signal $\nu_{meas}(t)$ from the correction voltage, which compensates for both, frequency drift and fluctuations of the laser $\delta\nu_{laser}[t]$ as well as changes of the cavity's resonance frequency. Here we separate the frequency detuning of the cavity into a contribution $\nu_{signal}(t)$ that represents the intended frequency response to refractive index changes from the analyte (e.g., single molecules), and a noise contribution $\delta\nu_{cavity}[t]$, which is due to involuntary thermal drift of the resonance or thermo-refractive frequency noise. Consequently we can write the recorded signal as the sum of these contributions.

$$\nu_{meas}(t) = \nu_{signal}(t) + \delta\nu_{cavity}[t] + \delta\nu_{laser}[t]$$

In this relation $\delta\nu_{cavity}[t]$ and $\delta\nu_{laser}[t]$ set the noise background of the measurement that determines the smallest resolvable frequency shift and thus the sensitivity of the device. The cavity noise contribution will be discussed in the course of general sensitivity considerations in chapter 5. In general $\delta\nu_{laser}$ dominates over $\delta\nu_{cavity}$ for the diode laser.

Here, we address the issue of laser noise $\delta\nu_{laser}[t]$, which can be eliminated from the recorded signal, by means of a stable frequency reference. To this end, we set up an ultra stable reference cavity, which is based on a Fabry-Pérot (FP) cavity machined from Zerodur ultra low expansion (ULE) glass. Figure 2.9 (a) shows a photograph of the FP spacer with highly reflective, low loss, mirrors attached to the end facets. The mirrors are designed for the Nd:YAG's fundamental wavelength at 1064 nm and they are clamped to the spacer with leaf springs. The assembly forms a plano-concave FP cavity and the spacer length of 115 mm corresponds to a free spectral range of 1.3 GHz. A second high finesse FP cavity at 635 nm wavelength was likewise assembled and used for the calibration of the diode laser (cf. Figure 2.5).

To achieve maximum stability against temperature changes, the cavity is placed inside a temperature controlled housing at high vacuum ($2 \cdot 10^{-7}$mbar). Photographs of the vacuum chamber and a copper cylinder with resistive wire for temperature

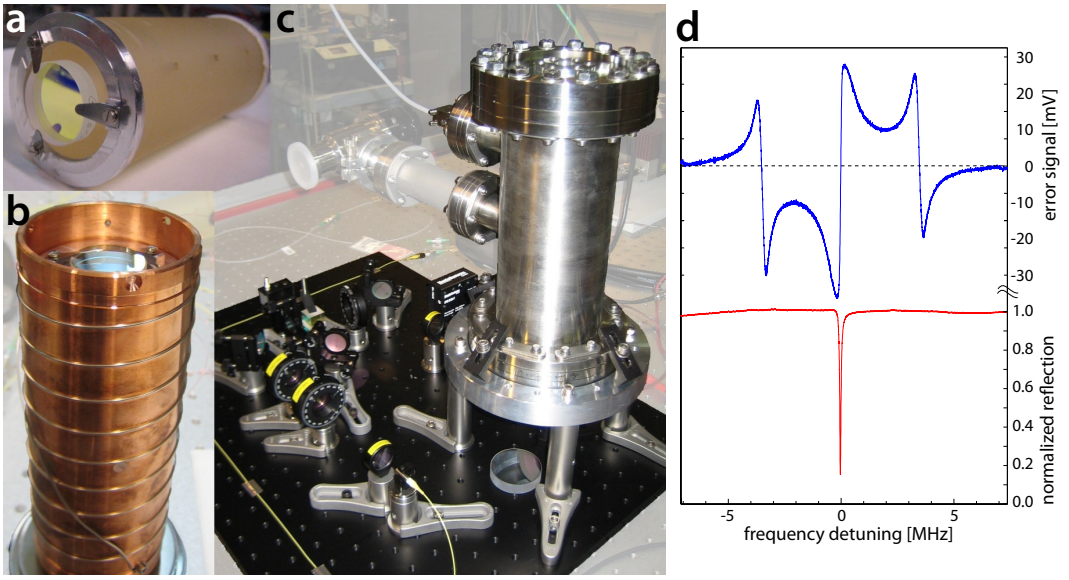

Figure 2.9.: Photographs of the ultra-stable reference cavity assembly. (a) The Fabry-Pérot cavity consists of a ultra low expansion (ULE) glass spacer and two high reflectivity low loss mirrors that are mounted with three leaf springs. (b) The cavity is placed in a temperature controlled copper cylinder, which is surrounded by two additional aluminum shieldings (not shown in the picture). (c) The full assembly with the Fabry-Pérot cavity inside the vacuum housing. A connected ion pump (Gamma Vacuum TiTan 10S) maintains a high vacuum of $\sim 2 \cdot 10^{-7}$ mbar. (d) The reflected intensity from the cavity (lower graph) and the PDH error signal that is used to stabilize the reference laser to the cavity (upper curve). The line width corresponds to a finesse of $> 10,000$ and is currently limited by the integration time of the photodiode.

actuation are shown in Figure 2.9 (b) and (c). Such isolated optical cavity experiences little exposure to temperature fluctuations of the environment provides a frequency reference which is at least two orders of magnitude more stable than the free running Nd:YAG and the microtoroid.
A second Nd:YAG laser at 1064 nm wavelength is aligned on the cavity (cf. Figure 2.5), such that intensity dip in the reflected signal is minimized for the TEM00 resonance. Figure 2.9 (d) shows the sharp reflection minimum (linewidth in the order of 100 kHz) that is observed when the laser is scanned over the resonance.

Next, we use a PDH scheme to lock the second Nd:YAG laser to the stabilized cavity, while the frequency doubled Nd:YAG laser at 532 nm wavelength is locked to a WGM of the toroid resonator. The measurement laser also features a port for the fundamental wavelength at 1064 nm, which is perfectly correlated with the measurement frequency. We overlap the two laser beams on a fast (1.8 GHz) photodiode and record the beat note. In the case, where the first Nd:YAG laser is locked to the WGM cavity, in the absence of an analyte (i.e. $\nu_{signal} = 0$), the noise characteristics of the beat note reflect purely the noise of the WGM cavity $\delta\nu_{cavity}[t]$. In section 5.1 we will show that the cavity noise is best characterized by the Allan deviation (or variance) as a measure of frequency stability.

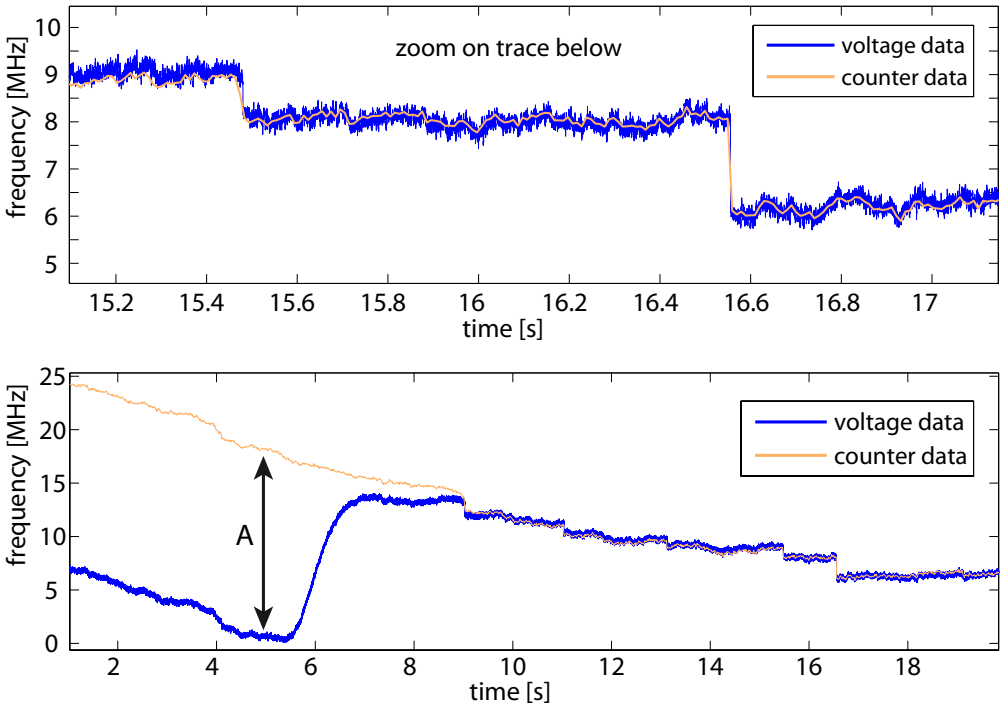

Figure 2.10.: Comparing the correction voltage to the absolute laser detuning. We measure the frequency detuning using two different schemes. The blue curve shows the calibrated signal obtained from the correction signal that is fed back on the laser piezo (before ×20 amplification). The orange curve shows the beat note between the laser locked to the resonator and the reference laser, which is stabilized to an ultra-stable Fabry-Pérot cavity. The beat signal does not require any calibration, as the counter directly issues a frequency. Moreover the beat signal does not contain laser noise, within the locking bandwidth of 30 kHz. This is well illustrated in the lower panel, where an external frequency detuning of amplitude 'A' is applied to the laser (change of crystal temperature), which triggers a compensation via the laser piezo (blue curve), but does not show in the absolute frequency (orange curve).

Indeed, it turns out, that cavity noise $\delta\nu_{cavity}$ is the limiting factor for the sensitivity on short time scale below 1 s, where it dominates over the laser noise of the Nd:YAG. On longer time scales laser drift slightly dominates over the WGM resonator drift. This is, however, only true if no analyte is added. Under realistic measurement conditions, additional temperature variations lead to an increased drift of the WGM resonator. In any case Nd:YAG laser noise does not impose a limit on the sensitivity for fast measurements, e.g. of SUV.

Recording the beat note not only permit us to measure the toroid-resonator noise, but it also provides a mean of calibration. To test the signal scaling deriving from the frequency dependence on the piezo voltage, we record the beat note in parallel to the correction signal in an SUV measurement. Counting the beat note directly provides a frequency and does not need additional calibration and scaling (besides a factor ×2 to account for frequency doubling). In Figure 2.10 we overlap the converted correction signal with the absolute beat note signal and confirm that the correction

signal indeed reflects the frequency detuning of the laser. For practical reasons it is required that the correction voltage does not exceed a certain limit. Therefore we implemented an additional slow feedback loop that acts on the laser crystal temperature and induces an opposite frequency drift when the piezo voltage becomes too large. Such a temperature correction and its effect on the laser frequency shows in the correction signal in Figure 2.10 (lower panel). The beat note is not affected by the temperature correction, as it reflects the detuning between the reference cavity and the resonator and does not contain any laser frequency drift.

3. Measuring the adsorption of single lipid vesicles

In this chapter we report on one of the main results of this thesis, the time-resolved detection of single lipid vesicles. The observation breaks ground in a double perspective. On the one hand, a sensitivity level is reached, where biologically relevant processes (cf. section 3.2) can be observed with great detail. Secondly the actual spreading of single lipid vesicles could be observed, which adds a new dimension to WGM based single particle sensing. Previously the adsorption of a single particle constituted a binary event; a sudden shift of the resonant wavelength would signal the presence of a particle. Considering that the magnitude of the shift depends on the local field intensity, a single event only has a qualitative nature and the information is thus binary. When a larger number of events is recorded, the frequency shift statistic provides a handle for calibration and turns the binary signal into a one-dimensional information. Only when the interaction can be resolved in time, a multidimensional picture is obtained, which was achieved for the first time in this thesis. Moreover we are the first to provide a meaningful frequency jump statistic that includes almost 200 events per measurement.
The chapter is organized as follows: First, the single particle sensitivity and important figures of merit are quickly reviewed. This is followed by an introduction to lipids, lipid bilayers, and lipid vesicles and their physiological as well as technical importance. Finally the experimental findings are presented, covering the adsorption of single lipid vesicles, as well as data for polystyrene beads. The effect of vesicle adsorption on optical frequency splitting is measured and critically reviewed.

3.1. Single particle sensitivity

The sensitivity to a localized change of the refractive index, as it is the case for a single particle, depends on slightly different criteria than the sensitivity to a bulk change of the refractive index of the environment. In the latter case the evanescent fraction, i.e. the totality of the evanescent field (which is typically around 3%, c.f. section 4.3), provides a meaningful figure of merit. Single particles, however, only occupy a small fraction of the evanescent field and the signal strongly depends on the local field intensity. In practice one records only a few events with maximum amplitude that correspond to an interaction at the point of highest evanescent intensity (for a TE/M00 mode this is at the equator of the toroid). It is these events that reveal the largest amount of detail and that provide the benchmark for the sensitivity. Supposed *cherry-picking* is not only justified, it is absolutely correct, as long as the events are not selected with respect to some exceptional "quality" of the

interaction, but only with respect to the amplitude of the signal. As the local field intensity does not influence the interaction (cf. section 2.2.1), the subgroup of large amplitude events includes all potential interactions.

Therefore we define the single particle sensitivity with respect to the maximum of the evanescent fields $\left|\vec{E}(\mathbf{r}_{\text{evan}})\right|_{\text{max}}$ and introduce the effective sensing mode volume V_s as a figure of merit for single particle sensing in reminiscence to the mode volume (,which was discussed earlier in section 1.1). Here we define

$$V_s = U_{\text{mode}}/\varepsilon_0 \left|E(\mathbf{r}_{\text{evan}})\right|^2_{max} , \tag{3.1}$$

such that Equation 1.11 turns into an expression for the maximum frequency shift that is potentially induced by a particle.

$$\Delta\nu_{max}/\nu_0 \approx -\frac{\alpha}{2}\left(n_p^2 - n_{ex}^2\right) V_p/V_s. \tag{3.2}$$

Obviously the signal, and thus the single particle sensitivity, is proportional to the inverse of the sensing mode volume V_s and typical values are in the order of $V_s^{-1} \sim 10^{-4}\,\mu\text{m}^{-3}$. (It is noteworthy that a similar figure of merit was introduced in the supplementary information of reference [47], where the authors refer to the "maximum of the field distribution on the resonator surface".) The optical resonance that was used for the single lipid vesicle measurements presented in section 3.3, has a sensitivity of $V_s^{-1} \approx 6.42 \cdot 10^{-4}\,\mu\text{m}^{-3}$, which is obtained from simulations using Comsol Multiphysics (cf. appendix A).

The effective sensing volume depends on the geometry of the resonator, represented by the minor and major toroid radii (R_{minor}, R_{major}), the polarization of the mode, i.e. TE and TM, and the resonant wavelength λ. We simulate V_s for different parameter sets and plot the results in Figure 3.1. Fitting the simulated values, we obtain a proportionality $V_s \propto R_{major}^{2.288}\lambda^{0.51}$; numbers that have previously been reported by Vollmer *et al.* for microsphere WGM resonators [37]. The dependence on the minor toroid radius and on the polarization are more complex, but at the same time less pronounced. An analytical approximation of the influence of the minor toroid radius can be extracted from reference [98], where the toroidal geometry of the resonator is modeled by an oblate ellipsoid.
Indeed the sensitivity is dominated by the major toroid radius and it is strongly advantageous to chose a resonator as small as possible. However, a lower limit on the toroid radius is set by the radiation loss cutoff, which defines an optimum radius for a given wavelength. Further increase of sensitivity can only be achieved by moving to shorter wavelength.

3.1.1. Geometric correction factors

To estimate the maximum frequency shift from a single particle, it is convenient to integrate the polarizability and the overlap of the particle with the evanescent field

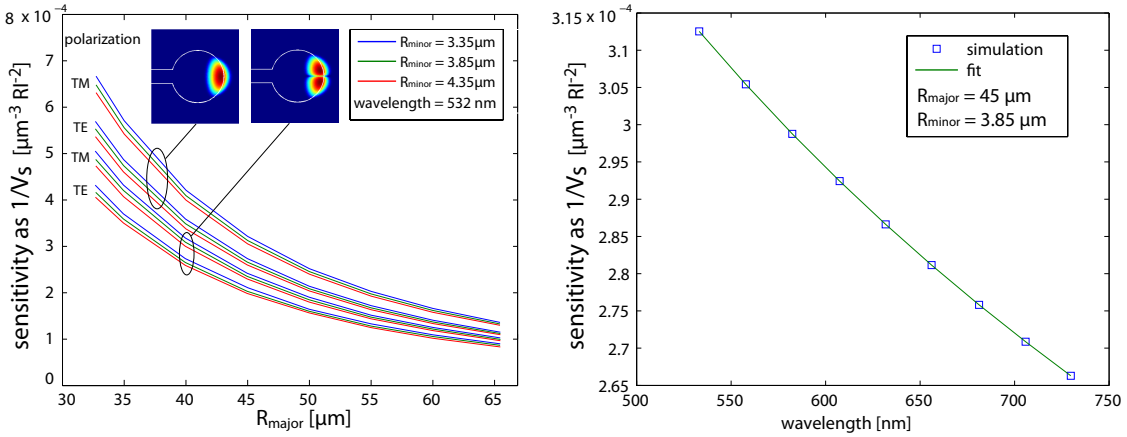

Figure 3.1.: The single particle sensitivity as a function of the major cavity radius and the wavelength. We use Comsol to simulate the peak intensity of the evanescent field and the mode energy, to compute the sensing mode volume V_s (cf. Equation 3.1) for different toroid geometries and wavelengths. In panel (a) the inverse of the sensing mode volume, V_s^{-1}, serves as a measure for the single particle sensitivity, and it is plotted here as a function of the major toroid radius for different mode families, minor radii, and polarizations. All curves can be fitted with a rational decay function $\propto R_{major}^{-2.288}$. (b) The inverse sensing mode volume V_s^{-1} is plotted as a function of the wavelength. The fitted curve is proportional to $\propto \lambda^{-0.51}$.
For many of the data that are presented in this thesis, a resonator with a major radius of $\sim 32.7\,\mu$m and a minor radius of $\sim 3.85\,\mu$m at a wavelength of 532 nm was used, which will frequently be referred to as a point of reference. The corresponding inverse sensing mode volume of the resonator is $V_s^{-1} \approx 6.42{\cdot}10^{-4}\,\mu\text{m}^{-3}$ and, for comparison, a microsphere with the same major radius exhibits a sensitivity of $V_s^{-1} \approx 3.6{\cdot}10^{-4}\,\mu\text{m}^{-3}$.

in a single parameter ξ. Hitherto, we normalize the overlap integral to the particle volume and define the geometric factor

$$\xi = \int_{V_p} d^3\mathbf{r}/V_p\,\alpha_0(\mathbf{r})\left|\bar{E}(\mathbf{r})\right|^2, \tag{3.3}$$

where $\bar{E}(\mathbf{r})$ is the evanescent field, normalized to its maximum value, and α_0 is the zeroth order correction factor due to particle polarizability that was derived in section 1.3. Here, we assume that the refractive index does not vary within the particle volume, i.e., we consider some effective "dry" volume, as it is usually done for simplification, when dealing with complex geometries such as proteins. To obtain an analytical solution for ξ, we use the parametrized form of the evanescent field of a TE/M00 mode, i.e., $\left|\bar{E}(\mathbf{r})\right|^2 = \exp(-z/\lambda_r)\cdot\exp(-4\log(2)\,x^2/\sigma^2_{\text{FWHM}})$, to approximate the overlap integral. When the particle diameter is much smaller than the latitudinal width σ_{FWHM} of the mode (i.e. $R < 500\,\text{nm}$) one can omit the x-dependence and obtains a simple expressions for ξ. For a vesicle with outer radius R_a and an inner radius R_i we express the volume ration by $\delta = (R_i/R_a)^3$ and obtain the relation:

$$\xi_{\text{vesicle}} \approx \frac{\varepsilon_{ex} + 2\varepsilon_p}{(5+4\delta)\,\varepsilon_p}\left(\frac{\lambda_r}{R_a}\right)e^{-R_a/\lambda_r}\sinh\left(\frac{R_a}{\lambda_r}\right). \tag{3.4}$$

Concomitantly the overlap of a solid sphere with radius R_a is given by:

$$\xi_{\text{sphere}} \approx \frac{\varepsilon_{ex}}{2\varepsilon_{ex}+\varepsilon_p}\frac{3}{2}\left(\frac{\lambda_r}{R_a}\right)^2\left(1-{}^{\lambda_r}/_{R_a}+e^{-\frac{2R_a}{\lambda_r}}\left(1+{}^{\lambda_r}/_{R_a}\right)\right). \tag{3.5}$$

Notably, the quantity $V_p\,\xi_{\text{sphere}}$ grows with R_a^3 for $R_a \ll \lambda_r$ and is proportional to R_a for $R_a \gg \lambda_r$. This is in contradicts the relation published in reference [37], where the overlap is found to be proportional to $R_a \exp(-2R_a/\lambda_r)$.[1] Moreover, it is interesting to note that the curvature (e.g. described by the dependency on R_a) was not taken into account by the authors of reference [43], which is reflected by the straight trend line in Figure B.2 (cf. appendix B), i.e., when going to smaller particle radii.

Using this geometric factor, the maximum frequency shift for a particle is easily estimated using the relation

$$\Delta\nu_{\max} = {}^1/_2\,\xi\,\delta\varepsilon\;(V_p/V_s)\;\nu_0. \tag{3.6}$$

Most of the data that are presented in this thesis were taken with a resonator with major radius $R_{\text{major}} = 32.72\,\mu\text{m}$ and minor radius $R_{\text{minor}} = 3.85\,\mu\text{m}$. We obtain the mode intensity distribution from Comsol simulations and find that the evanescent intensity distribution of the TM00 mode can be parametrized by a Gaussian with full width half maximum of $\sigma_{FWHM} = 1.44\,\mu\text{m}$ in latitudinal direction and by an exponential decay $\sim \exp(\cdot/\lambda_r)$ with $\lambda_r = 84\,\text{nm}$ in radial direction. Then typical values of ξ for a solid spheres in water with radii of $R_a = 25\,\text{nm}$ and $R_a = 50\,\text{nm}$ and a refractive index of $n_{\text{SOPC}} = 1.46$ are $\xi_{\text{sphere}} = 0.24$ and $\xi_{\text{sphere}} = 0.18$, respectively. For a vesicle with the same properties and a wall thickness of 4 nm values of $\xi_{\text{vesicle}} = 0.30$ and $\xi_{\text{vesicle}} = 0.21$ are found. We note that the evanescent field of a frequency split mode exhibits an intensity modulation along the azimuthal direction which is modeled by the factor $\left|\bar{E}(\mathbf{r})\right|^2_{\text{split}} \propto 2\,\cos^2\left(y \cdot M_{mode}/R_a\right) \times \left|\bar{E}(\mathbf{r})\right|^2_{non-\text{split}}$. The factor $\times 2$ accounts for a peak evanescent intensity that is twice as large compared to the one of the non-split mode. Likewise the maximum signal and thus the sensitivity of a split mode is two times larger. However differences in the frequency shift distribution arise from a changed intensity profile, which will be discussed in section 3.3.

3.2. Properties of lipid bilayers and lipid vesicles

In this section, a short overview on the properties of lipid bilayers and lipid vesicles is given, to motivate both, the lipid membrane functionalization method and the use of small unilamellar lipid vesicles as test bodies for the sensor. We provide examples of biological processes and applications that disclose the abundance of *things going on* on the length and time scale that is now accessible with our sensor.

The term *lipid* describes a vast class of biomolecules that is best characterized by a symptomatic insolubility in water. At the root of this macroscopic behavior lies

[1] The authors introduce the decay length L which is approximately equal to $\lambda_r/2$.

a common hydrocarbon chain that repels polar solvents. A particular important category of lipids are phospholipids that consist of a polar head group, such as choline, and two fatty acid tails.

Phospholipids are ubiquitous in nature and represent an integral component of biomembranes. When suspended in water, due to their amphiphilic nature, they spontaneously arrange in stable bilayer sheaths, with the polar heads pointing towards the outside [114]. These *lipid bilayers* can form spheroidal superstructures that were first reported by Alec Bangham in 1964 [115] and that were later termed *liposomes* by Gerald Weissman [116], which are – by definition – artificially created vesicles that consist of one or more lipid bilayers [117]. The more general expression "lipid vesicle" therefore includes liposomes and both term are used equivalently here. Liposomes exist in different forms and sizes and they are accordingly referred to as, e.g., small unilamellar vesicles (SUV) with a size inferior to 1 μm and a shell consisting of a single lipid bilayer. Other frequently used terms comprise large multilamellar vesicles (LMV) on the lower μm scale and giant uni- or multilamellar vesicles (GUV and GMV) with diameters up to 200 μm.

Lipid bilayers form the plasma membrane of a cell, together with embedded membrane proteins and glycolipids. The cell membrane constitutes the barrier that separates the cell from its environment and it is supported by the cytosceleton. As such it is responsible for the regulation of cell transport, which can roughly be divided into three pathways. (i) Small molecules, i.e. gas molecules in solution, can diffuse through the cell wall. (ii) Secondly, membrane channels actively controls the passage of specific ions and small molecules. The state of the channel (open or closed) can hereby depend on a variety of parameters, i.e. the transmembrane electric potential or the presence of messenger molecules. (iii) Lastly, proteins, hormones, and other mid-size molecules are transported via vesicle exo- and endocytosis. Both are complex processes that involve a considerable number of membrane proteins and that are of particular interest here, because they fall well within the sensitivity range of our sensor.
Exocytosis describes a secretion process where molecules, such as neurotransmitters (that are engulfed in innercellular liposomes) are released from the cell to the extra cellular environment. Briefly the vesicle is transported to its engagement site (trafficking), e.g. along the axon towards the synaptic gap. There it loosely binds (tethering) until a messenger initiates the docking process, followed by vesicle fusion with the cell membrane, where the cargo is released [118]. The process involves a variety of membrane proteins and is subject to ongoing research [119]. For example different pathways of vesicle fusion have been observed [120], including a process where the liposome fully merges with the membrane to be recycled elsewhere [121], as opposed to an incomplete release, where a fusion pore opens and closes again after partial release of the cargo (*kiss-and-run*). The reverse process, endocytosis, involves the formation of a vesicle from the cell membrane, the uptake of the target, and finally a cleaving process that detaches the newly created transporter from its host. As an example, the former can be initiated by the polymerization of clathrin, which attaches to and curves the membrane to form a negative of the vesicle [122, 123]. However other mechanism of vesicle formation and retrieval have

been reported and many details of the processes remain to be solved [120].

Next to their physiological role, the potential of **liposomes as model membrane systems** was recognized right from their discovery [117, 114]. In many cases biological systems are enormously complex, and researchers turn towards artificial, reduced systems with a limited number of constituents [124]. For example GUVs can be aspired with a micropipette [125], a technique that allows to control and measure membrane tension at the same time and, e.g., study phase transitions of a lipid bilayer. Furthermore, starting from a single GUV, the interaction and functioning of isolated molecules can be observed without interfering signals from other physiological processes that one would encounter *in vivo*. Such a biomimetic system was, for example, established by A. Roux *et al.* to study the polymerization and hydration dynamics of dynamin and its role in vesicle fission [126, 127]. Small unilamellar vesicles were recently used to study the interaction of a single virus with a lipid membrane [128].

In **therapeutic applications** liposomes are used as carrier vessels for drug delivery. Hereby the pharmaceutic agent is enclosed in a unilamellar or multilamellar vesicle before application [129]. Liposomal drug delivery holds several advantages compared to the direct injection of the free drug [130]. First of all the agent is protected against degradation and a circulation time of up to two days has been reported, holding the potential of gradual drug release and avoiding high initial concentrations. Moreover, the lipid material of the vesicle is *a priori* bio-compatible and does not run the risk of triggering an immunoreaction. Lipoplexes and liposomes for non-viral gene delivery have been extensively studied [131]. Finally, when specific targeting can be achieved [132] using specially designed receptors, the total amount of the drug can be drastically reduced, avoiding side effects and leading to a diminishment of the overall stress on the immunosystem.

For the totality of these reasons, there is plentiful scientific and medical interest in lipid vesicle as drug carriers. In the following we will show that we are able to observe single lipid vesicles with a time resolution in the μs-regime, which is sufficient to resolve the adsorption and spreading dynamics of distinct vesicles. Such sensitivity opens up a broad range of applications and experiments that belong to the class of processes described above.

3.2.1. Preparation of lipid vesicles

A variety of different methods to prepare lipid vesicles has been reported, for example fast immersion of lipid emulsion in ethanol or sonication of large multilamellar vesicles that are formed by simple hydration of a lipid film. Giant unilamellar vesicles with diameters exceeding 100 μm are efficiently prepared using electroformation on platinum electrodes [133, 134] or on ITO (indium tin oxide) coated coverslips [91]. Here we focus on the extrusion method, where the lipid is hydrated, and the emulsion is forced through a polycarbonate membrane, whose pore diameter determines the final size of the vesicles. In particular we use the Avanti Mini-Extruder,

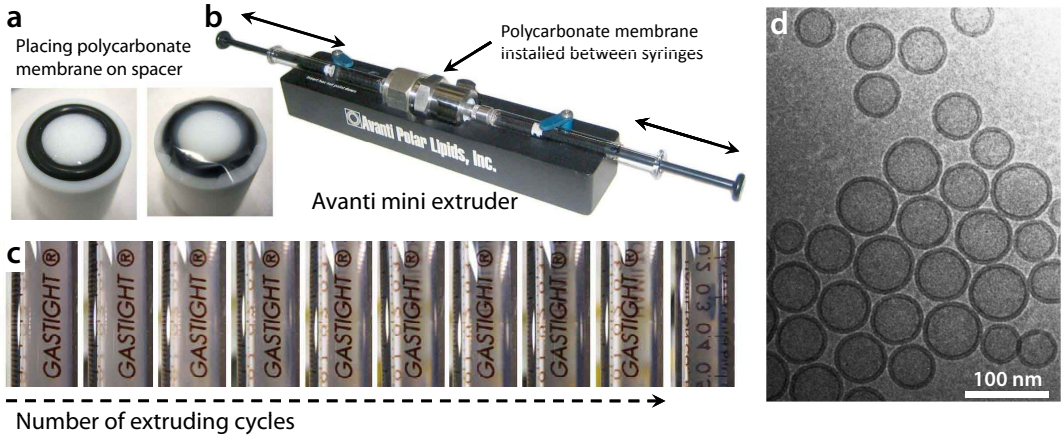

Figure 3.2.: Extrusion of lipid vesicles using the Avanti Mini-Extruder. (a) A lipid emulsion is forced through a polycarbonate membrane with pore size $\sim 100\,\mathrm{nm}$. The picture on the left shows a teflon support with an O-ring. The polycarbonate membrane is placed on the O-ring (right picture) and clamped with a second teflon support. The membrane is wetted during installation, and care is taken to avoid air bubbles. (b) The assembly is mounted and strained in a stainless steel housing. Two gastight syringes (1 ml, Hamilton) are inserted to the channels on either side. The emulsion is then inserted on one side and pushed through the membrane into the second syringe. For a 100 nm pore size and a $1\,\mathrm{mg/\,ml}$ SOPC emulsion, an initial force of $\sim 50\,N$ is required to sustain a flow of $\sim 10\,\mu\mathrm{l/s}$. (c) With each extruding cycle, the originally dull emulsion clears up. In the photo series, the imprint on the backside of the syringe becomes more and more visible. Typically $11 - 15$ cycles are performed. (d) A cryo electron micrograph of extruded lipid vesicles from reference [137]. The bilayer structure of the lipid membrane manifests in the contrast of the vesicle walls.

shown in Figure 3.2 (b), which allows us to produce lipid vesicles of deterministic size, with a relatively narrow size size distribution [114, 135, 136]. Moreover, the process does not require expensive equipment and can readily be adopted in a physics laboratory. In the following paragraph we will give a detailed description of the vesicle preparation process that addresses anyone who aims at repeating the process.

Protocol: Lipid vesicle preparation

The phospholipid *1-stearoyl-2-oleoyl-sn-glycero-3-phosphocholinein* (SOPC, Avanti Polar Lipids) is dissolved in chloroform to yield a concentration of $20\,\mathrm{mg/\,ml}$ and is stored at $-20°C$. Glass vials with a volume of four milliliter and matching lids with PTFE fittings are cleaned using a mixture of 65 parts of chloroform, 25 parts of methanol, and 1 part water. The ingredients of the cleaning solution are mixed and filled into the vials and lids. After $\sim 4\,\mathrm{min}$ the solution is disposed and the cleaning cycle is repeated one or two more times. Stirring, shaking, or wiping is not necessary.

Portions of 100 μl (or 2 mg) of the lipid solution are allotted to the vials. Then the chloroform is carefully evaporated in a weak nitrogen flow. To this end, we hold the vial in an almost horizontal position and gently blow nitrogen gas in the opening (at an angle) using an air gun, while slowly turning the vial. Ideally, after drying, the walls of the vial are covered to a great extend with lipid. It is noteworthy that the air gun is connected to an expansion bottle that prevents sharp blows of nitrogen gas and helps filtering particles that might arrive from the gas bottle. Finally, the vials with the dried lipid and the lids are placed in a desiccator over night at $\sim$ 1 mbar. Afterward, the vials are tightly closed and sealed with Parafilm. They are stored at $-20°C$.

To prepare the lipids for extrusion, they are thawed and hydrated with de-gassed, high grade water to a concentration of 1 mg/ml (cf. section 2.1.2). The emulsion is then mixed using a vortex shaker. For the the preparation of SUVs with a size smaller than 100 nm, several freeze-thaw cycles are applied before extrusion. Prior to their use, all extruder parts and syringes are disassembled and cleaned in a 20% ethanol solution, then rinsed in pure water and finally dried. We assemble the Avanti Mini-Extruder according to the manual and install a polycarbonate membrane with a pore size of either 200 nm, 100 nm, or 50 nm. Figure 3.2 (a) shows how the polycarbonate membrane is installed on the teflon spacer of the extruder. We remove any air bubbles from the extruder by pushing pure water back and forth through the membrane, before loading one syringe with the lipid solution. The emulsion is passed through the membrane at least eleven times. Figure 3.2 (c) shows how the originally diffuse color of the lipid emulsion clears up when the vesicles approach a mono-disperse size distribution. In subfigure (d) a micrograph of extruded vesicles is shown. For the preparation of 50 nm vesicles we apply three freeze and thaw cycles to the lipid emulsion and extrude the mixture using a 200 nm pore size, before moving to the 50 nm polycarbonate membrane. In addition, we gently heat the metal block of the extruder to $\sim 40°C$ to ensure that the lipid is in its liquid phase.[2]

3.3. Single lipid vesicle measurements

We prepare small unilamellar vesicles (SUVs), according to the protocol described in the previous section.[3] Here, we use polycarbonate membranes with pore size radii of 50 nm and 25 nm. After extrusion, we take the 1 ml Hamilton syringe (the one that contains the vesicles) from the extruder and exchange the short needle that connects to the teflon fittings against a long ($\sim$ 100 mm) one. Approximately 100 μl of the solution are disposed, such that the needle is filled with vesicle solution, and the syringe is introduced into the injection site of the fluidic system, such that the needle is co-linear with the PTFE tubing leading to the FCD. The syringe is

[2] An excellent review dealing with the different phases of lipid bilayers in found in reference [138].

[3] To promote vesicle adsorption, the resonator surface is rendered hydrophilic using an SC $-$ 1 cleaning solution (1 : 1 : 5 mixture of ammonia, 30% H_2O_2, and DI water at 70°C during 10 minutes).

placed on the optical table and left for thermalization for a couple of minutes, while a steady water flow of 8 ml/ h is maintained. We observed that a constant water or buffer flow is crucial for temperature, and thus frequency stability. In the absence of flow, the resonance frequency displays fluctuations, which are most likely due to temperature drift and convection resulting from local heating. These fluctuations are even more pronounced, when the analyte is directly injected in the coupling chamber and concentration gradients lead to additional convection. Therefore, measurements with highest precision require a constant flow and mixing prior to the measurement site.

On the other hand, there exists a tradeoff; when the flow in the FCD is too elevated, which is in our case > 20 ml/ h, adsorption events seem to be perturbed and occur less frequent, or are completely suppressed. Such behavior can be explained when the drift velocity of the particle is too high and short range adhesion forces cannot capture the particle anymore (i.e., the depletion length becomes shorter). For comparison, a total flow of 10 ml/ h corresponds to an average flow velocity of $\sim 150\,\mu$m/ s inside the coupling chamber, such that the vesicle passes through the evanescent field within a few ms. An exact calculation of local flow and forces would require a complex simulation of the coupling chamber with the sample and the toroids inside. A simple dimensional analysis suggests, however, that the Reynolds number is of the order unity, and assuming a laminar flow close to the chip surface (,which is not disturbed by the microtoroids), we estimate a flow velocity of $\sim 20\,\mu$m/ s in the region of the resonator.

When the syringe has thermalized, we (manually) inject $\sim 30\,\mu$l of vesicle solution with $\sim 10\,\mu$l/ s and immediately start recording. During injection the resonance frequency reversibly shifts by a few 10 MHz, due to increased flow, but equilibrium is reestablished a few 10 s later. The vesicles now pass through the PTFE tubing, whose length and diameter have been chosen to ensure complete mixing of the analyte with the water carrier, merely by diffusion. Around 700 s after injection, we observe events as discontinuous jumps of the signal (cf. Figure 3.3 (b)).

A short video clip [139] shows the PDH error signal, while the laser is scanning over the WGM resonance (i.e. the blue detuned sideband). Discrete steps signal adsorption events of single particles. The footage was taken in the course of an aborted 50 nm vesicle measurement, where the analyte was contaminated, probably due to a failed extrusion process. Occasional frequency jumps of a few 10 MHz would throw the laser out of lock, but besides these unwanted signals, a number of smaller events can be observed in the video that fall into the frequency range expected for 50 nm vesicles.

A typical trace with raw data is shown in Figure 3.3 (b). The delay between injection and the appearance of the first event is reproducibly found in all measurements and constitutes a good indicator that the signals indeed stem from the analyte. Recording is stopped, when the event occurrence rate fades. To analyze the data, we scan manually through the raw recordings and identify discontinuities in the frequency trace. With the limited number of events a visual judgment is more

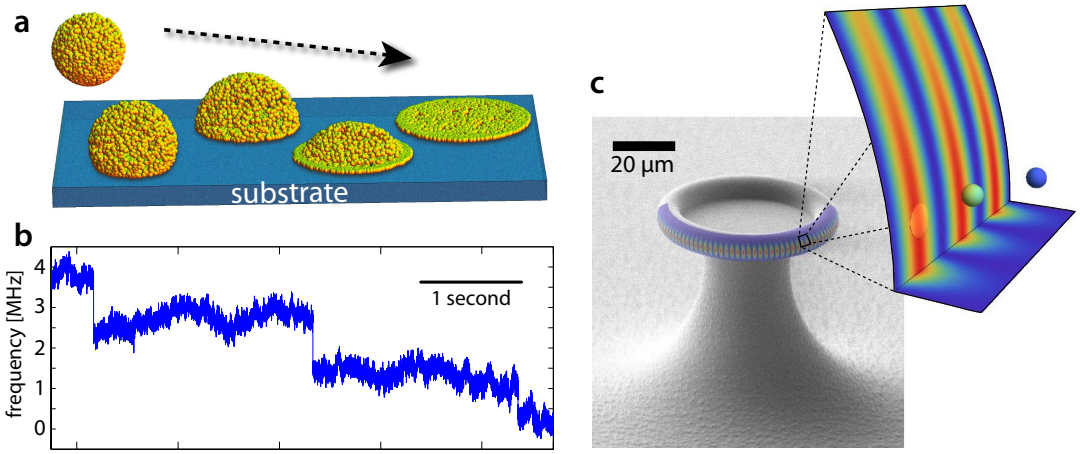

Figure 3.3.: Spreading of lipid vesicles: a schematic view. (c) An SEM image of the microresonator, covered with an image overlay that represents the evanescent intensity on the sensor surface and in radial direction. Notably, the intensity distribution corresponds to a split mode (cf. section 3.4), which manifests as intensity nodes. The magnification illustrates, at scale, how a 50 nm vesicle approaches the surface. The coloring represents the the field intensity on the particle surface. (a) A schematic view of a lipid vesicle adsorbing and spreading on a surface. The spreading itself depends strongly on the surface adhesion forces and on interaction with other vesicles (e.g. crowding). (b) A typical trace of raw data, as it appears on the oscilloscope, when single particles attach to the toroid surface.

efficient than automatic treatment of the data. Each of the events is fitted with a Sigmoid function plus a linear background to extract the exact event time and the step height. The fit parameters are plotted in Figure 3.4 (a) and (b) for the 50 nm and 25 nm vesicles. In the two measurements 172 and 165 distinct events were identified, respectively. The time intervals between the events are on the order of a few seconds and depend on the local vesicle concentration, the particle size, and the flow velocity in a complex fashion. Indeed, the initial vesicle concentration and the amount of analyte that are necessary to observe a decent number of events, that are yet well separated in time, were determined experimentally.

Number of recorded events

From the total number of events we can estimate the detection efficiency of the sensor. Starting from the Stokes-Einstein equation, we calculate a diffusion coefficient of $D \approx 4\,\mu\text{m}^2/\,\text{s}$ for a 50 nm vesicle. The circumference of the toroid is $\sim 200\,\mu\text{m}$, such that we can estimate an interaction length of $\sim 100\,\mu\text{m}$ for a split mode, which corresponds – using the previously calculated average flow velocity – to an average interaction time of $t_{int} = 5\,\text{s}$. Following the line of reasoning in reference [85], we obtain a depletion depth of $\sqrt{D \cdot t_{int}} \approx 5\,\mu\text{m}$. Together with the latitudinal width of the mode profile, we obtain a capture cross section of $\sim 10\,\mu\text{m}^2$ and, in combination with the reduced flow at the resonator, the capture probability of a 50 nm vesicle

passing through the coupling chamber is $\sim 9 \cdot 10^{-8}$.
On the other hand we can estimate the total number of vesicles that were injected, starting from the initial lipid concentration of 1 mg/ ml and the vesicle volume, which yields some $2 \cdot 10^{11}$ particles. Together with the capture probability this results in an expected number of 27,000 events; nearly 200× more than we actually observed. This deviation can be explained, if we assume that the majority of the vesicles is already lost on their way to the resonator and that the vesicle concentration at the detection site is much smaller than the initial vesicle concentration. Especially on their way through the PTFE tubing, the vesicles experience a large surface area, compared to the actual volume of the tube. Again, we can estimate this influence. The average flow inside the tube is 4.4 mm/ s, and the depletion length over the course of one mm is approximately 1 μm. Making the rough assumption that all vesicles that come into contact with the wall will stick, and using the tube radius of 400 μm, we find that only 0.7% of the SUV pass the tubing, and that $\sim$ 190 events should be observed at the sensor.

This number comes of course with a large error, and the resemblance with the actually measured event numbers is mere coincidence. So far we have not considered that some lipid material will already be lost in the extrusion process (which decreases the initial concentration), and neither we have taken into account that the interaction with the side wall does not always lead to a particle adsorption and material loss. However, the correct order of magnitude suggests, that the dominant processes of the vesicle interaction have been identified and that the estimate of the depletion length and interaction time probably falls into the correct order of magnitude.
It is important to note that no adsorption events are observed for the same initial concentration when a silicone tube is installed before the FCD instead of a PTFE tube. It is possible that the adhesion between the siloxane groups and the lipid is stronger than for PTFE, such that the vesicle concentration at the flow cell drops below any detectable level. The detection probability for a single particle can be increased by reducing the dimension (i.e. the cross section) of the coupling chamber and by reducing the flow velocity.

Statistical analysis

It is important to emphasize that – for the first time using a cavity enhanced RI sensor – a few hundred events per distinct measurement run were recorded.[4] Such large number of individual adsorption events enables us to extract meaningful statistical information from the data. To this end, we plot the jump size histograms for the 50 nm and 25 nm vesicles in Figure 3.4 (c) and (d) and compare the measured distribution to a theoretical model.

[4] In reference [43], for example, less than one event per measurement was recorded for the smallest particle. For larger particles 2 – 3 "identifiable binding events were observed" per measurement run. The data in reference [37] suggests that up to 35 events in a single measurement were recorded for polystyrene beads with a radius of 250 nm, which is however much larger (both in contrast and size) than the lipid vesicle observed here.

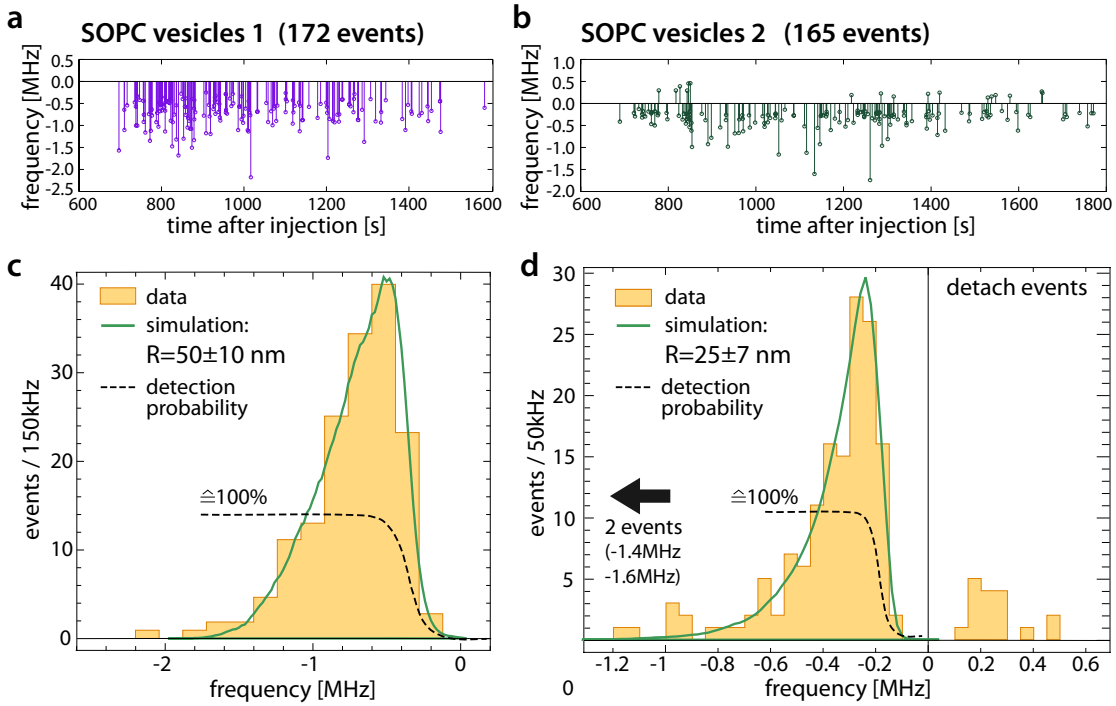

Figure 3.4.: Lipid vesicle statistics. (a,b) Frequency steps from vesicle adsorption events are plotted as a function of the measurement time. Here $t = 0$ corresponds to the time when the vesicle solution was injected into the teflon tube leading to the FCD. For measurement 1 (a), vesicles were prepared by extrusion, using a membrane with 100 nm pore size. In the second measurement (b) a pore size of 50 nm was used. (c,d) The size distribution of the events depicted in (a,b). The solid curves represent the theoretical distribution of frequency shifts for sticking, spherical vesicles that follow a log-normal size distribution. The diameter of the vesicles is centered on the pore size of the extrusion membrane and the standard deviation is chosen to fit the data. Here the detection limit is reflected by a cutoff function, which is centered around ~ 380 kHz and ~ 190 kHz, respectively. Besides the standard deviation of the radius and the cutoff function no free parameters appear.

For point-like, monodisperse particles that randomly sample the evanescent field (i.e., the binding is not influenced by the local electric field), the jump size histogram reflects the intensity profile of the evanescent field. In a realistic scenario, the lipid vesicles are not monodisperse and exhibit a size distribution, which can, for example, be measured by light scattering. In literature the "mean radius" distribution of extruded vesicles is found to follow a log-normal function, centered on the pore size of the polycarbonate membrane used in the extrusion process [136, 135]. Referring to the "mean radius" is owed to the situation that lipid vesicles are not always spherical and they have been reported to take on a prolate or oblate shape in isotonic media [136]. In our experiment, we work in a hypotonic environment and the vesicles are therefore expected to swell to a spherical shape.

The recorded histograms in Figure 3.4 (c) and (d) represent the convolution of the vesicle size distribution with the mode intensity profile, and additionally, involve

the overlap integral between the evanescent field and the particle geometry. The numerical access to the analytical description of this problem is not straight forward, such that we chose to simulate the expected jump size distribution for different sets of parameters. To this end, we start from the parametrized expression of the evanescent field (cf. Equation A.14) and numerically calculate the overlap with the particle. We differentiate between a split mode, i.e., with intensity maxima along the equator, and a non-split mode. Moreover, we investigate two modes of interaction: (i) a spherical vesicle sticking to the surface, and (ii) a spread out vesicle, forming a unilamellar, circular "pancake" with twice the radius of the original vesicle (i.e., having the same volume). We do not model any deformation of the vesicle when it attaches to the surface of the toroid, as we already discussed their expected rigidity, and considering that the presumably subtle effect would be difficult to resolve anyway.

On the other hand, the difference between a split and a non-split mode can be resolved with great detail. Not only is the maximum evanescent intensity of a split mode two times large (cf. section 3.1), but also the changed geometry – namely the modulation of the intensity along the equator – has a strong influence on the expected jump size distribution. The flat top of a Gaussian profile (, which dominates the geometry of a non-split mode) leads to a local maximum in the histogram around the position of the maximum signal. In contrast, the profile of a split mode is governed by field gradients of both, the Gaussian in latitudinal direction and the $\cos^2$ modulation in equatorial direction, and the expected jump size distribution is therefore marked by an exponential drop (with a step-like cutoff corresponding to the maximum signal). In our case the measured distributions in Figure 3.4 can clearly be attributed to a split mode that is "smeared out" by the finite size distribution of the vesicles.[5]

We use the computer algebra program Mathematica to simulate $\geq 100,000$ events for each parameter set, consisting of the mode profile (split or non-split), the kind of interaction (spreading or sticking), and a variance of the vesicle radius. Justified by the good initial fit, we leave the mean of the radius distribution locked to the radius of the pore of the extrusion membrane (i.e., 50 nm and 25 nm). For each simulated event, we generate a random radius and a random position and integrate (numerically) the overlap with the evanescent field. Finally, we apply a low frequency cutoff to the data set that reflects the detection probability due to noise, and that we approximate by an error function to suppress event below a certain size.
In Figure 3.4 (c) and (d) we plot only the simulated curves that represent the best fits to the data, and we find size distributions characterized by log-normal functions with 50 ± 10 nm and 25 ± 7 nm for the 50 nm and 25 nm vesicles, respectively. Notably the relative deviation of the radius is larger for the 25 nm vesicles, which is reflected by the rather concave shape of the distribution when dropping towards higher frequency.

The cutoff function, which is indicated by the dashed curve in Figure 3.4, was individually adjusted for the two measurements and represents the average sensitivity

[5] Indeed, a split mode was used for the measurement, such that the finding rather confirms the model instead of providing new insight.

during the measurement. For the 50 nm vesicle measurement, the cutoff is centered at 380 kHz, while for the 25 nm vesicle measurement the frequency resolution is 190 kHz. In both cases the standard deviation of the corresponding Gaussian is $\sim$ 100 kHz, which reflects varying background noise. The different center position (and thus different sensitivity) derives from the fact that, in the first case, we recorded the beat with the stabilized reference laser in parallel, which increased the overall difficulty of the experiment, and therefore some frequency resolution was sacrificed at the benefit of an increased overall stability.

In principle the cutoff function also reflects the judgment of the author, who identified the binding events in a rather conservative manner. Typically a signal to noise ratio of $3-5$ was required for an event to pass the visual threshold and enter the statistics. Defining a mathematical criterion for an event is very difficult, because the signal fluctuations and noise before and after the event need to enter, which results in a considerable number of parameters for time intervals and weights. Eventually such model would amount to the attempt to cast the visual judgment into some formula, and we belief that the reverse way, to simply measure the judgment with a cutoff function, is less obscure.

Time-resolved single lipid vesicles

In this paragraph we focus on distinct vesicle adsorption events, and we show that additional knowledge about the interaction (, which cannot be accessed by ensemble measurements) is gained from the analysis on a single particle level. In fact the statistical analysis of the frequency steps yields only a one-dimensional information on the average of the interacting vesicles, and there exist arguably better methods to measure the radius distribution of extruded vesicles. The power and the richness of our sensor is revealed, when we analyze time-resolved features of the interaction. Here – for the first time – we extract information from a single particle adsorption event that goes beyond the mere frequency step.

In Figures 3.5 and 3.6 we highlight a number of frequency jumps at a time resolution of 100 μs to give an impression of the fidelity of the measurement. We emphasize that all data shown here are raw data that did not undergo filtering. This is all the more important, as filters, in the best case, sacrifice time resolution at the benefit of an improved signal to noise ratio (SNR) and, in other cases, especially when non-linear filters such as median or percentile filters are used, even pronounce step-like features in the signal, which can lead to misinterpretation of the data. Moreover, we choose to plot a larger number of single particle frequency steps (instead of selecting and showing only a few) to demonstrate that we do not need to rely on *cherry-picking*.

Figure 3.5 (c) shows the smallest identifiable events for 25 nm vesicles, with an amplitude of $\sim$ 200 kHz, which represents, to the best of our knowledge, record sensitivity and record time resolution in dispersive particle sensing. For a 25 nm

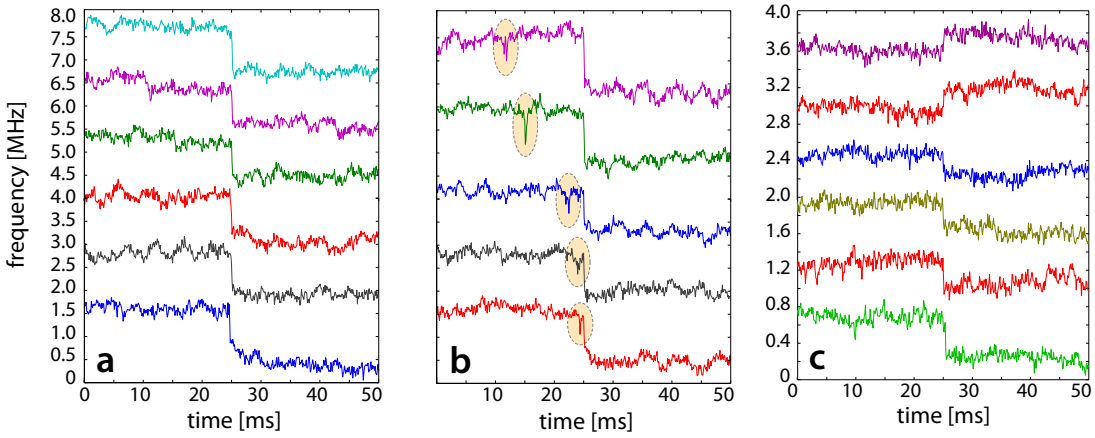

Figure 3.5.: Typical lipid vesicle adsorption events. (a) Frequency steps resulting from the adsorption of single 50 nm vesicle were recorded with high frequency resolution. Hereby, a step is associated with a vesicle that enters the evanescent field of the optical mode and is then immobilized on the surface, due to short range adhesion forces. (b) Frequently, the jump of the resonance frequency is preceded by a dip, as if the particle were to probe the field without adhering. Considering that a split mode was used for sensing, one can hypothesize that the trajectory of the particle crosses an intensity maximum before attaching in the neighboring one. These dips were also observed by other groups, who referred to them as "probing events". However they were never resolved at a ms time scale. (c) In this panel we show the smallest events that we could unambiguously resolve and which result from 25 nm vesicle adsorption events (note that the scale is stretched by a factor $\times 2$). Interestingly we observe detach events – where the frequency step goes towards larger frequency – for some of the small vesicles. This might be owed to the higher rigidity and reduced contact area of smaller vesicles.

vesicle that attaches at the equator, we calculate a signal to noise ratio (SNR) of 8 on a 1 ms time frame. Furthermore, these events give an impression of the authors visual judgment criteria that were subject to the concluding remarks of the previous subsection. We could certainly find smaller frequency steps in the trace, but this would at the same time raise the false-positive error rate, which we tried to minimize here. Also the net gain of information from an event with a SNR ~ 2 is limited to the expansion of the step size histogram to smaller frequency. On the other hand, an event with a SNR of 10 provides information that go beyond the mere frequency shift, because we are able to resolve sub-features and details.

Indeed, the high time resolution permits us to identify the fast dynamics of the events. Figure 3.5 (b) shows a selection of frequency jumps that are preceded by a dip-like feature up to 20 ms before adsorption. We have seen before in Figure 3.4 that the average time delay between distinct events is on the order of seconds, and we can therefore conclude that the dip, and the adsorption shortly after, stem from the same particle. In fact, such dips have been observed by other groups, who referred to them as *probing events*, which appeals to the notion that the par-

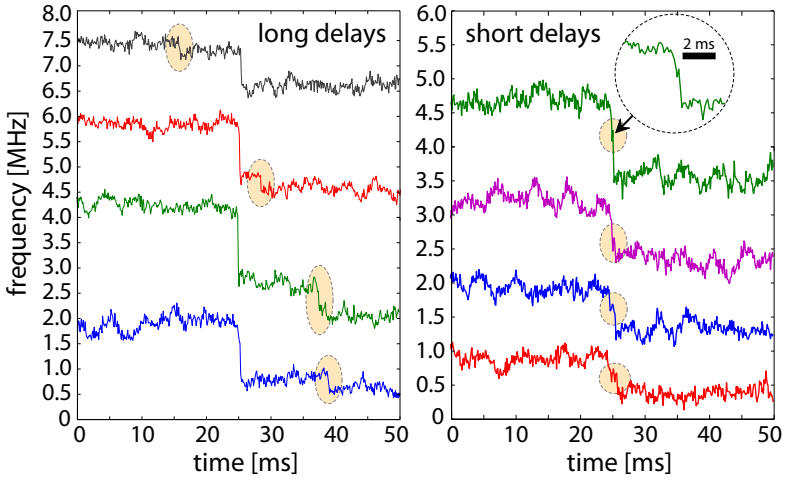

Figure 3.6.: Lipid vesicles manifesting a characteristic double step. For $\sim 15\%$ of the 50 nm vesicles we observe characteristic double steps as they are show in the panels (a) and (b). Typically, the average time between two adsorption events in on the order of a few seconds, such that we can assign the double step event to a single particle. We believe that $> 30\%$ of the vesicles show this behavior, taking the smaller steps into account, where the second jump could not be observed, if it were there. One plausible explanation for the double stepping is the spreading of lipid vesicles, where the adsorbed vesicle bursts open and forms a lipid patch on the surface. As the overlap with the evanescent field increases during spreading, a frequency jump is expected. Vesicle spreading is regularly observed on silica surfaces and is even used to form supported bilayers.

ticle probes the evanescent field and leaves again before it finally attaches. Unlike the short frequency dips observed here, these probing events occurred on a longer timescale and manifested as frequency fluctuations rather than a dip.
In section 3.5 we discuss data from polystyrene beads, where we also observed fluctuations that take place also during one second before final adsorption. Moreover, we can find evidence that the frequency fluctuation derive from the movement of an optically trapped bead in the evanescent field.

Here, the situation is less clear, because we observe only a single dip on a ms time scale, and the optical force is orders of magnitude too weak to lead to optical trapping (i.e., locking to a sideband). Frequency dips that do not lead to adsorption are also observed, but significantly less often, which brings up the question, why a probing event with high probability leads to absorption. Here, we come up with a hand waving geometric reasoning and imagine that the particle is caught in a laminar flow, diffusing around its trajectory. The toroid will most likely be approached from the front, and a particle that has gotten close enough to probe the evanescent field is very likely to be *pushed against the surface* and escape seems unlikely.

A second class of events, shown in Figure 3.6 is characterized by a distinctive double-step, where the adsorption is followed by a second (usually) smaller event up to

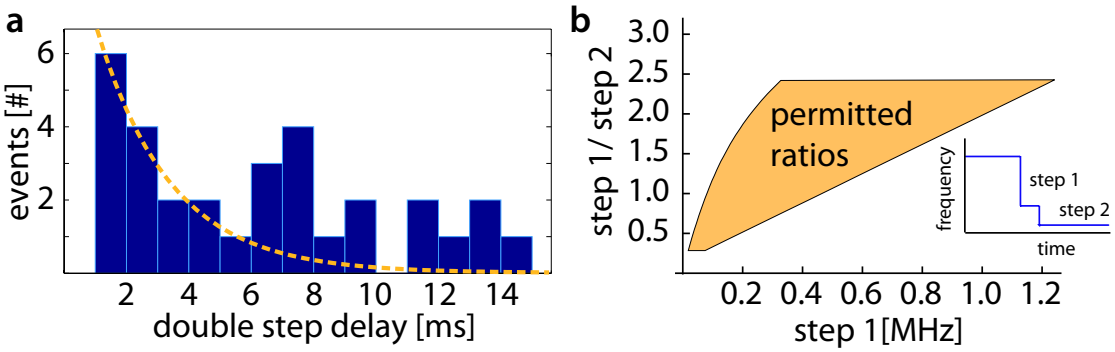

Figure 3.7.: Double step statistics. (a) For 31 of 172 adsorption events we could observe a double step feature and record the delay between the first and second step. The delay distribution shows an exponential-like drop with a decay time of ~ 2 ms. The effect could be attributed to thermally activated spreading. However, a number of vesicles manifests a longer life time of up to 15 ms, with some bunching around $7 - 8$ ms. This finding suggests that there exists either a precondition of the vesicle or a certain way of adsorption that renders the adsorbed vesicle more stable. (b) We calculate the ratio between the first step and the second step in the idealized situation that the adsorbed vesicle describes first a perfect sphere and then spreads out at the same position to form a circular patch of uniform thickness. Sampling the toroid surface, and thus the field distribution, yields a region of possible and thus permitted ratios, which are plotted here as a function of the height of the first step. In reality the borders of this region are very likely blurred out. Still the calculation shows that the observed ratios are of the order that the calculation predicts and, moreover, we learn that events where the second step is larger than the first one are allowed. An example for such an event is shown in figure 3.6 (a).

20 ms later. This behavior can be interpreted as a vesicle attaching to the surface, followed by rupture and spreading shortly after [140, 141, 142], which is schematically depicted in Figure 3.3 (a). Lipid vesicle spreading on hydrophilic surfaces is in fact a commonly observed effect, which is taken advantage of for the formation of artificial supported lipid bilayers. Indeed, the fusion process does not depend on activation by protein, but the basic mechanism is mediated by lipid-lipid interaction [143]. When liposomes attach to a surface, the adhesion force depends mainly on the charge of the surface and the lipid head groups. In literature different mechanisms of vesicle fusion on a silica surface are discussed [144]. If the surface adhesion force and the corresponding deformation of the vesicle induce sufficient stress on the vesicle, it can rupture by itself (or rather by thermal activation). On the other hand, if the initial stress is insufficient, additional forces that are exerted by neighboring attached vesicles (i.e., vesicle crowding) can initiate spreading. Once an incomplete lipid film has formed on the surface, the membrane edges (, which are unfavorable from an energetic point of view) can fuse with sticking vesicles and thus cause rupture.

We plot the distribution of the time delay between double-step in Figure 3.7 (a), and find indications for two pathways of vesicle spreading. On the one hand there is a fraction of vesicles that displays fast spreading, with a life time that decays exponentially over 2 ms. On the other hand, there appears to be a fraction of long

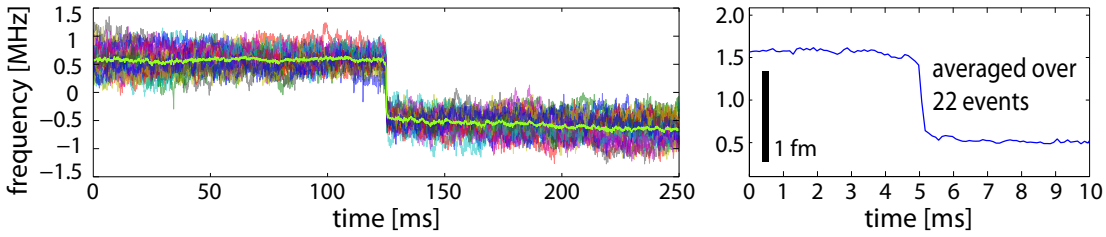

Figure 3.8.: The average of selected frequency step events. The left panel shows the overlay of 22 adsorption events, with the average curve shown in the foreground. The right hand side of the graphic magnifies a 10 ms frame around the actual step. The noise level is dramatically reduced to ~ 10 kHz, resulting in a signal to noise ratio of **100**. Here averaging is possible, because the step events are well defined in time and they can be phase locked to half of their step height. However, other details of the interaction, such as the double steps are lost, because of their non-coherent nature. For better comparison with literature, we added a wavelength scale bar.

lived vesicles. Following our hypothesis of spreading vesicles, it seems likely that first group displays thermally activated spreading, while vesicles of the latter group spread after interaction with already deposited lipid material. The notion of sticking, long-lived SUV is also supported by the observation of detaching events shown in Figures 3.4 and 3.5 (c).

We challenge our hypothesis and calculate the range of permitted step size ratios. To this end, the frequency shift for a 50 nm spherical vesicle sticking to the surface, and for a circular "pancake" at the same position, are computed numerically (cf. also appendix A.2) and their ratio is calculated. Using this position dependent relation we map the surface of the toroid onto a region of permitted frequency steps in Figure 3.7 (b). We find that the predicted ratios agree well with the plotted events in Figure 3.6. Interestingly, we also confirm that (for a split mode) there exist positions on the toroid surface where the first step resulting from the attaching particle is expected to be smaller than the second step from the spreading. In reality the borders the plot in Figure 3.7 (b) will not be sharp, but rather blurry, because our idealized and simplified model takes neither a radius size distribution of the vesicles, nor a non-circular lipid patch after spreading into account.

Out of curiosity we superpose 22 events with respect to the "center" of the frequency jump and plot the average curve together the original traces in Figure 3.8. The background noise is drastically reduced, which goes, however, along with the loss of any additional information and feature. Such averaging could only be used to improve the SNR of events that are reproducible.

With the demonstration of high temporal resolution, we have opened a promising road to pursuit in cavity enhanced RI sensing. Already in this section on single particle data analysis, the temporal resolution of the events adds a couple of pages to the discussion, and new questions are raised that cannot be addressed with conventional ensemble measurement techniques. We believe that high time resolution, in combination with high sensitivity on the low-contrast nm scale, is likely to become a unique feature of high-Q cavity based sensors.

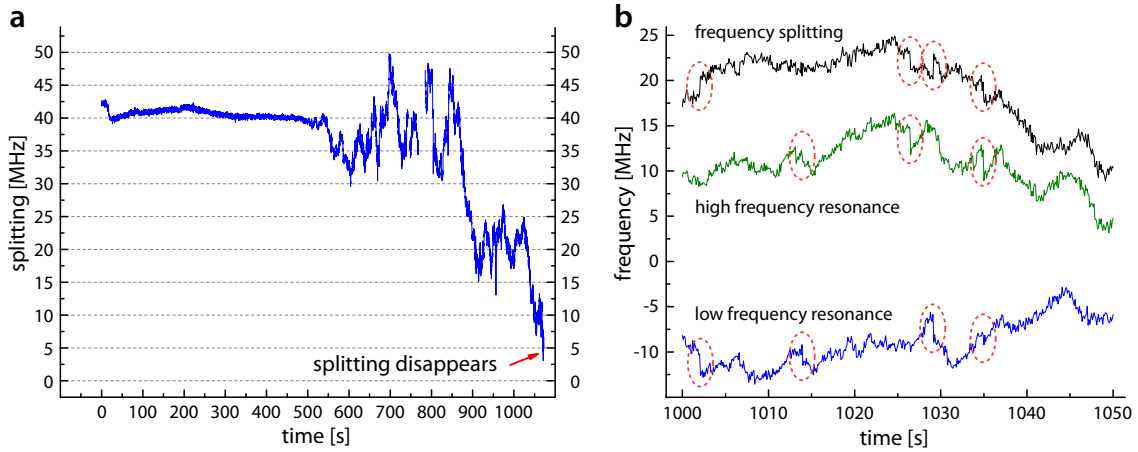

Figure 3.9.: Change of the frequency splitting in response to lipid vesicle adsorption. (a) The frequency splitting, i.e., the frequency spacing between a pair of split resonances, was monitored after $R_{\mathrm{major}} = 50\,\mathrm{nm}$ vesicles were added (at $t = -100\,\mathrm{s}$). When the vesicles arrive at the sensor, the splitting starts to fluctuate and decreases. Eventually the resonances merge, and when the splitting reaches the width of the resonances (here $\sim 5\,\mathrm{MHz}$), tracking is not possible anymore. Importantly, we did not observe any degradation of the optical Q and broadening of the linewidth while the splitting changed, which is in stark contrast to the observations by Zhu *et al.* . (b) A magnified view of a portion of the trace in panel (a) shows the frequency shift contributions from the high and low frequency resonances, as well as the difference signal. Frequency step events are observed in either trace. Interestingly the signal to noise ration is similar for all curves, and the effect of common noise cancellation, which is expected for the difference (split) signal, does not appears.

3.4. Frequency splitting

Frequency splitting in WGM resonators appears when frequency degenerate clockwise and counterclockwise modes strongly couple, and normal mode splitting occurs [145]. The coupling is induced by surface backscattering, which is frequently encountered with high-Q resonators in water. A pair of split resonances is shown in Figure 2.6. The normal modes form a standing wave inside the resonator (cf. Figure 3.3 (c)), and it has been suggested that monitoring the mode splitting instead of the resonance position, leads to an improvement of the signal to noise ratio. Moreover, Zhu *et al.* recorded the splitting and the linewidth broadening of the resonance in response to the adsorption of single polystyrene beads [44]. As both properties, the frequency splitting and the line width, depend differently on the scattering strength, their combination yields information on the particle size, independent of its position on the resonator and the local field strength.

The technique keeps the intriguing promise that the clockwise and anticlockwise modes experience common resonator noise and common frequency drift. Such common noise is canceled when the frequencies of the modes are recorded relative to each other. Only fast, thermal RI fluctuations, usually faster than 1 MHz, on a length scale of the wavelength and shorter, will affect the normal modes differently.

In our experiment we implement the split resonance scheme, to compare its performance with the results obtained via the PDH method. To this end, we continuously scan the diode laser over a pair of split resonances and fit the minima with 3rd order polynomials to calculate the position of the minimum. We chose a laser scanning frequency of 10 Hz to take advantage of the stroboscopic effect that eliminates prominent laser noise peaks at multiples of 50 Hz. Figure 3.9 (a) shows the evolution of the frequency splitting over the course of an SUV measurement. Before the arrival of the analyte, the frequency splitting remains relatively constant at 40 ± 1 MHz during 8 min, and the drift of the laser and the resonator is effectively eliminated. When the vesicles arrive at the sensor, the frequency splitting displays strong fluctuations over a gradual decrease and finally disappears. In contrast to the results reported by Zhu and co-workers, the linewidth of the resonances did not change in our case [44]. When the splitting approached 5 MHz, approximately matching the resonance linewidth, the frequency difference could not be resolved any longer, and we switched to the PDH technique. Then, single adsorption events could be clearly resolved.

In Figure 3.9 (b) we highlight a characteristic portion of the trace and plot the contributions from the two resonances individually. We notice that events (steps) are contained in both, the high and low frequency signal. Moreover, the difference signal (splitting) does not lead to any improvement of the signal to noise ratio. This is rather surprising and might be owed to the scanning speed and laser frequency noise.

We summarize this section with a critical review of the advantages and disadvantages of the method. In our experiments, we could not observe an improvement of the signal to noise ratio in the split signal. An improved optical setup that allows locking of two lasers or locking of a sideband could solve this issue.
On the other hand, we experienced an important drawback. When the frequency splitting is recorded the effect that leads to the reduction of the splitting interferes with the dispersive frequency shift and renders the method non-quantitative. Moreover the disappearance of the splitting can limit the total number of observable events in a measurement. Indeed, we were still able to record events in the PDH correction signal after the splitting had vanished.
We hypothesize that the fluctuations in the splitting are due to the varying scattering properties of the deposited material. It is likely that adsorbed vesicles will drift over the surface and that lipid patches resulting from spread vesicles will flow and reorganize. The splitting eventually decreases and disappears when surface impurities are covered with lipid and the RI contrast is washed out, or when too many randomly distributed scattering centers interfere.

3.5. Polystyrene beads

Among the first single particle measurements that we performed using the reactive sensor, were the recordings of single polystyrene beads with a radius of 50 nm. The

refractive index of polystyrene at 532 nm is $n_{ps} = 1.5986$, which gives a contrast that is more that twice as high compared to lipids. The frequency resolution of these early measurements was nearly a factor ten lower than the resolution that we achieved for the later measurements, because the laser was locked to the main resonance instead of the sideband, such that amplitude fluctuations translated into frequency noise via the thermo-refractive coupling mechanism. In addition the fine tuning of the electronic setup and the introduction of our Falco Systems low noise amplifier lead to considerable noise reduction (cf. appendix C). Nevertheless the results obtained with the PS beads exhibit some interesting features.

Figure 3.10 shows two events where a single polystyrene bead interacts with the field of the cavity and finally adsorbs. Interestingly we do not observe a singular step of the resonance frequency, as it is the case for the lipid vesicles that are immediately immobilized on the surface. Instead the interaction displays fast jitter that can be interpreted as an on-off switching behavior and that prevails for approximately one second until the frequency is "caught" in the down-state. A similar behavior can be seen in the traces of references [37] and [43] who detected polystyrene beads as well. We will later identify this behavior as optical trapping of the particles in the evanescent field of the resonator. Before, we show that the measured absolute frequency shift is congruent with our modified theory.

We work with a toroid that has a major diameter of about 90 μm, which corresponds to a sensitivity figure of $V_s^{-1} \approx 3.2 \cdot 10^{-4}\,\mu\text{m}^{-3}$. From the size of the bead and its refractive index, we calculate a geometric factor (cf. Section 3.1) of $\xi = 0.166$. The maximum expected frequency shift is then given as

$$\Delta\nu_{\max} = 0.166 \cdot \frac{n_{ps}^2 - n_{\text{water}}^2}{2} \frac{4\pi}{3} \frac{(50\,\text{nm})^3}{V_s} \nu_0 \approx 5.7\,\text{MHz}.$$

The maximum theoretical shift is consistent with the experimental findings an thus confirms the polarization correction factor that was introduced in section 1.3. In a second measurement we reduce the input power by a factor ÷4 and the nature of the interaction changes. A typical event is depicted in the lower panel of Figure 3.11. Again the presence of the particle is signaled by frequency fluctuations, which terminate however in the off state, indicating the absence of the particle. We attribute these events to particles that pass through the evanescent field, but do not adsorb on the surface.

The power dependence of the behavior supports the notion that the particles are optically trapped [39]. For further verification we calculate the trapping potential, starting from the expression that relates the relative frequency shift to the relative change of electrostatic energy. Then we replace the mode energy by the circulating power multiplied with the cavity photon lifetime.

$$\delta U \quad = \quad \frac{\delta\nu}{\nu} U_{\text{mode}} = \frac{\delta\nu}{\nu_0} \frac{P_{\text{in}}}{2\pi\nu_{\text{FWHM}}} \tag{3.7}$$

We note that the trapping potential depends on the input power, unlike the frequency shift induced by a particle. Thus the frequency shift of the passing bead

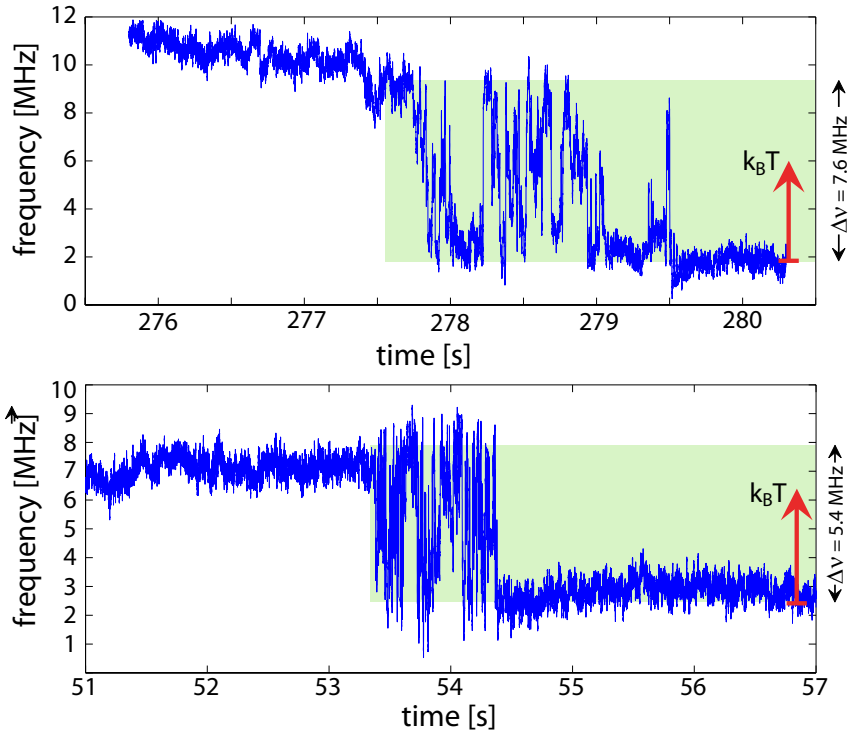

Figure 3.10.: Optical trapping of polystyrene (PS) beads. Both panels: a PS bead enters the evanescent field of the resonator, which leads to a characteristic step in the frequency detuning. We evaluate the depth of the optical potential for an optical mode with $Q \approx 4 \cdot 10^7$ and for an input power of $\sim 20\,\mu$W and compare it to the thermal energy. Here the dispersive optical force is sufficient to trap the particle. This is best illustrated when the thermal energy $k_B T$ is expressed as a frequency (cf. Equation 3.7). Figure 3.11 shows the interaction of a PS bead with the evanescent field at reduced input power such that the particle is not trapped.

is of the same order as in the previous measurement, whereas the optical potential is lowered by a factor four. For better comparison we introduce a scale bar corresponding to the thermal energy $k_B T/2$, which now corresponds to $\sim 16\,$MHz. The thermal energy exceeds the depth of the optical potential and the particle is lost. A congruent observation was made by Arnold *et al.* [39].

To learn more about the interaction of the pass-by events, we take advantage of the high time resolution and perform a spectral analysis of the frequency jitter. To this end we calculate the Fourier transform on a sliding 250 ms window. The upper panel of Figure 3.11 shows the frequency components of the signal that were normalized to the background spectrum. Clearly a tenfold enhancement of frequency components around $\sim 30\,$Hz is observed. Starting from this dominant frequency, we can speculate about the nature of the interaction. On the one hand it seems possible that the particle is temporally trapped inside an intensity maximum of the split WGM, whose dimensions are defined by a polar width of $\sim 100\,$nm and a latitudinal width of $\sim 1500\,$nm. From the curvature at the point of peak intensity we calculate the force gradient and finally the characteristic trap frequencies, which lie in the kHzregime. Even if we assume an overdamped, thermally driven motion, that

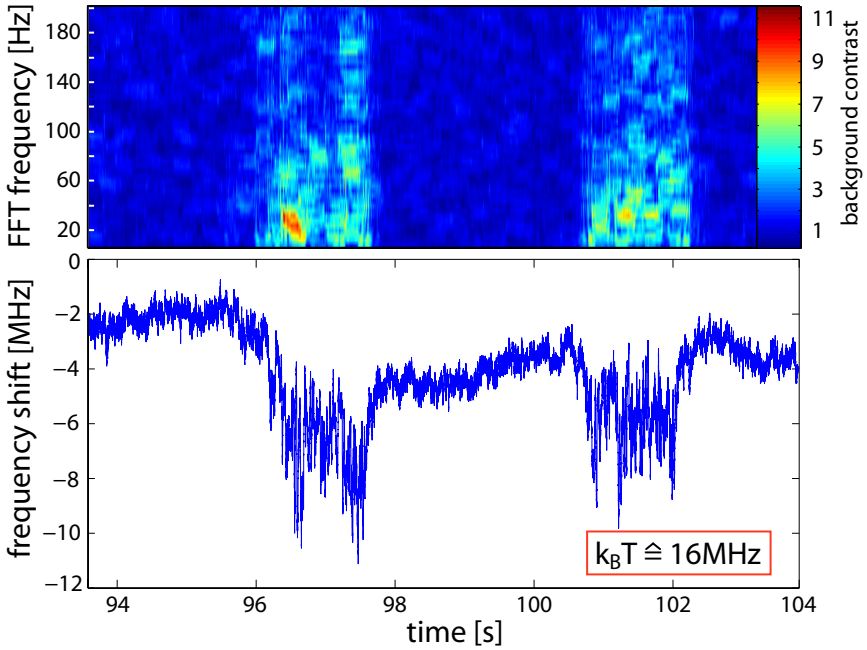

Figure 3.11.: The interaction of a passing PS bead with the evanescent field. (Lower Panel) Temporary fluctuations of the resonance detuning towards smaller frequency indicate a particle that interacts with the evanescent field but does not adsorb. Compared to the adsorption events in Figure 3.10, the input power was reduced by a factor $\div 4$ to $\sim 5\,\mu$W. In this case the depth of the dispersive optical potential is much smaller than the thermal energy such that the PS bead is not trapped. The upper panel shows a plot of the Fourier frequency on a 250 ms sliding window, which has been normalized to the background fluctuations (i.e. $t \in [98\,\text{s}, 100\,\text{s}]$). The interaction is dominated by frequencies below 100 Hz

shifts the resonance peak towards lower frequency, this hypothesis does not explain our finding. The time scale set by the $30 - 40$ Hz maximum in Figure 3.11 rather suggests, that the particle moves through the intensity maxima of the split WGM. Two adjacent maxima are spaced by 200 nm, which results in a particle velocity of $6 - 8\,\mu$m/ s and which is in the order of the estimated average flow derived in section 3.3.

When the particle is located exactly between two intensity maxima, there is still an overlap with the electric field and we compute the ratio between minimum shift and maximum shift to be around 1 : 7. Indeed the frequency jitter in Figure 3.11 does not completely go back to the background level (i.e., off state) and the offset of ~ 1 MHz fits the model of a particle moving along and probing the intensity maxima of a split WGM. The analysis exemplifies that even in a simple, non-specific case of a PS bead, the high time resolution yields a more detailed insight into the nature of the interaction.

Optical trapping of polystyrene beads was reported before in reference [39], where the authors observed a trapped particle traveling around the equator of a microsphere and which they termed WGM carousel. In a follow-up work the microsphere

sensor was combined with a plasmonic antenna that locally enhances the sensitivity [92]. To overcome the bottleneck of the strongly reduced sensing surface, the carousel effect was proposed as a mechanism to collect the target and to deliver it to the nanoparticle sensor for detection.

4. Lipid membrane functionalization

In the previous chapter, we presented single nanoparticle measurements that underlined the exceptional qualities of the WGM based sensor on the transducer side. In this chapter, we will demonstrate how this intriguing progress is complemented by an elegant, yet effective way of surface functionalization, which turns the transducer into a veritable biosensor [87]. The importance of such interface was outlined in section 1.1.3.
Surface functionalization in principle aims at general immobilization of the target and further at the observation of specific interaction. The former was achieved in the lipid vesicle measurements by rendering the surface hydrophilic and thus creating an adhesion force. Here we move beyond plain physisorption and coat the microtoroid with a lipid bilayer to create a biological interface that is suited to host complex, lipid bound receptors. In particular, we demonstrate the versatility of the functionalization technique by measuring specific interaction of streptavidin with membrane bound biotin. Streptavidin is a mid-size protein, consisting of four 15 kD sub-units, which possesses four binding sites that connect to biotin[1] with exceptionally high affinity [146]. With a dissociation constant of $10^{-15} - 10^{-14}$ the link (even though of non-covalent nature and mediated by hydrogen bonds and van-der-Waals forces only) is practically irreversible and the compound is therefore widely used in diagnostic assays.

4.1. Lipid membrane functionalization

Techniques for surface functionalization range from simple physisorption of an antibody onto a surface, to sophisticated methods of covalent binding of receptor molecules. The former method is straight forward to apply, suffers, however, from poor quantitative control of the bound antibody and is in general prone to unspecific binding. Covalent surface preparation methods are wide spread, and a large number of protocols exists, i.e., for frequently used sensor materials such as silica, silicon or gold [88, 147]. Typically the methods involve an initial hydroxilation (i.e., silica), followed by amination with a suited linker molecule [148, 87]. In a final step, specific receptor molecules are bound to the functional amino groups of the newly formed organic layer. Idle groups can be passivated to prevent unspecific interaction. Despite the remarkable success and diversity of covalent sensor surface functionalization and the advantages that go along with a mature technology, there is one major drawback to the method when applied to high-Q resonators. The large number of

[1] biotin structure (source Wikimedia Commons):

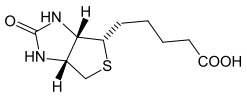

wet chemical steps, together with cleaning, baking, and general handling, puts the supreme optical properties at stake and risks the degradation of the resonator's Q factor [149].[2]

Here, we utilize a method where the the surface is covered with a single lipid bilayer that creates a universal interface for labeling with various kinds of receptor or antibodies. The method falls into the category of self assembled (mono)layer functionalization that includes a number of self organizing molecules. Here the lipid membrane coating method appeals for at least two reasons. First, it can easily be applied in a physics laboratory, without the need for expensive and bulky equipment. Additionally, one needs to master only one coating step as the specificity derives from lipid bound receptors that can be either bought or are supplied from elsewhere. Secondly, we create a biomimetic interface that resembles the natural environment of many proteins, i.e. membrane proteins. In particular when we are interested in the dynamics of a target's interaction, the coating method provides a model membrane system where membrane processes can be studied *in vitro* with a limited number of constituent and thus with reduced physiological background noise [124].

In fact the method is an established technique and is widely used as supported lipid bilayer (SLB) interface [150]. SLBs that are assembled directly on a glass slide, are easily accessible by microscopy, while granting accessibility (from the other side) at the same time. There exist different ways to attach a lipid layer on a surface [151]; in the simplest case, the surface adhesion force is sufficient, such that the bilayer will directly adsorb and stick. Otherwise, i.e., for a metallic surface, an intermediary (organic) sandwich layer or lipid anchors need to be bound to the surface first. For silica this is however not the case and SLBs are known to auto-assemble directly on the substrate. Even for strongly curved silica nanoparticles with a diameter as small as 100 nm a uniform coverage has been achieved (cf. reference [152] for impressive cryo-TEM images). To form the bilayer, different ways of lipid delivery are employed. Among the most widely utilized methods is lipid vesicle spreading, where liposomes crowd on the surface, spread and re-arrange to a single, supported layer [144, 141, 153]. Here, we use a faster methods that involves the spin coating of the structure, followed by hydration of the lipid [154].

To promote adhesion, we render the surface of the toroid resonator hydrophilic, using SC-1 cleaning solution (1 : 1 : 5 mixture of ammonia, 30% H_2O_2, and DI water at 70°C during 20 minutes) [3] before the lipid bilayer is applied. Again we will narrate the steps of the process in greater detail, for possible reproduction of the results. After the SC-1 step the sample is rinsed and stored in a Millipore water bath, while the lipids are prepared for spin coating. We thaw a vial with 2 mg of the frozen, dehydrated lipid (cf. section 3.2.1) and add 2 ml of isopropanol to obtain

[2] Apart from the reported deterioration of the optical Q during functionalization, the results reported in reference [149] are incorrect. We will therefore not consider the article as a reference for the biotin-streptavidin measurements.

[3] In practice it is recommendable to heat the water to 100°C before adding the ammonia and the hydrogen peroxide at ambient temperature.

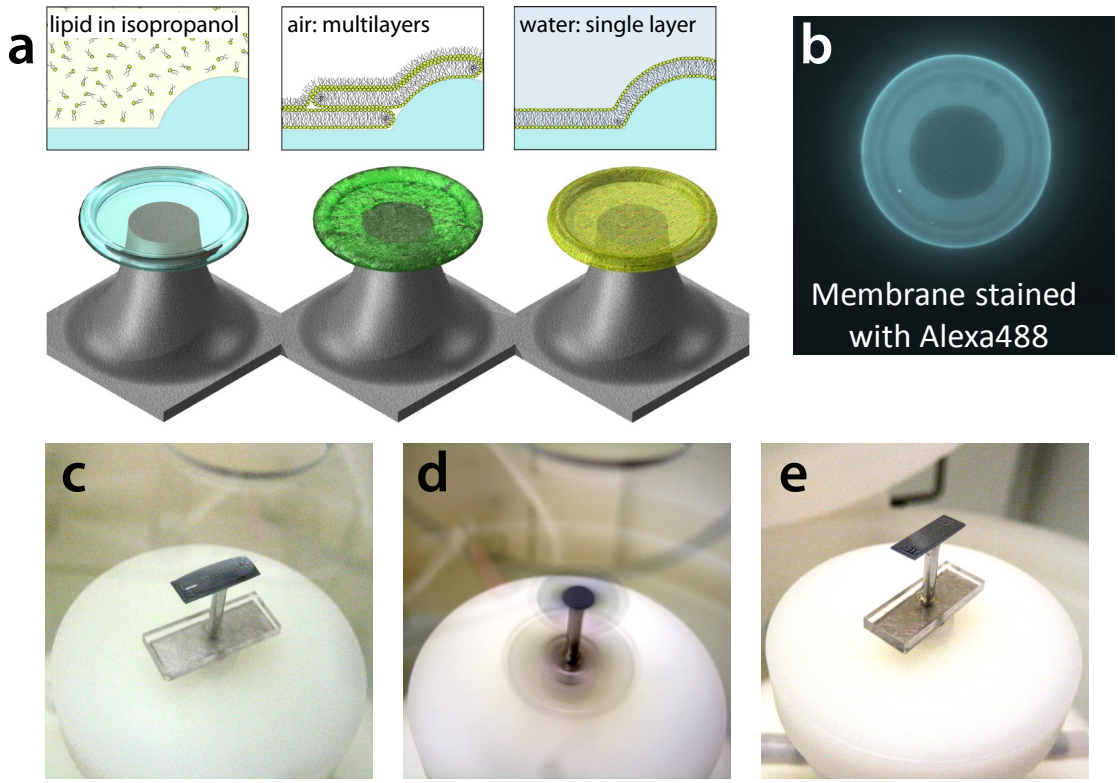

Figure 4.1.: The process of lipid membrane coating. (a) A schematic illustration of the process: First the sample is covered with the lipid solved in isopropanol, which forms, after evaporation and spinning, a diffuse multilayer film. The sample is then immersed in water, where the single lipid bilayer forms with the rearrangement of the lipid over the course of several hours. Excess lipid material is removed by rinsing. (b) A fluorescent micrograph of a toroid that has been coated with a lipid bilayer, doped with the fluorescent marker Alexa 488. A uniform intensity distribution signals an even coverage of the toroid. (c)-(e) The sample is mounted inside the spin coater and covered with the lipid. After spin coating the isopropanol has evaporated.

a concentration of 1 mg/ml. The solution is mixed using a vortex shaker. Next we carefully blow dry the sample using a nitrogen gun. Here it is advantageous to leave the sample attached to its microscope slide support and to gently blow the water along the chip such that the majority of the liquid falls of in a droplet. Then we take the support and install it on a spin coater, as shown in Figure 4.1 (c)-(e). We use an Eppendorf pipette to fully cover the chip with $50 - 70\,\mu$l lipid solution and immediately start the spinning process before the solvent evaporates. The spin-coating normally lasts 2 minutes at 3000 rpm. Then the sample is rinsed again under the directed water jet from a wash bottle and placed in a water or buffer reservoir where the membrane is allowed to settle for at least 10 hours. After settling the chip is rinsed one more time using a wash bottle.

The optical Q of a membrane coated toroid typically degrades by a factor $\div 2$ compared to the uncoated resonator in water, and values of $Q = 2-3\cdot 10^7$ are frequently achieved. Values of up to $5 \cdot 10^7$ were observed. It is important, however, to verify that the toroid is indeed covered with a single membrane layer. To obtain a visual

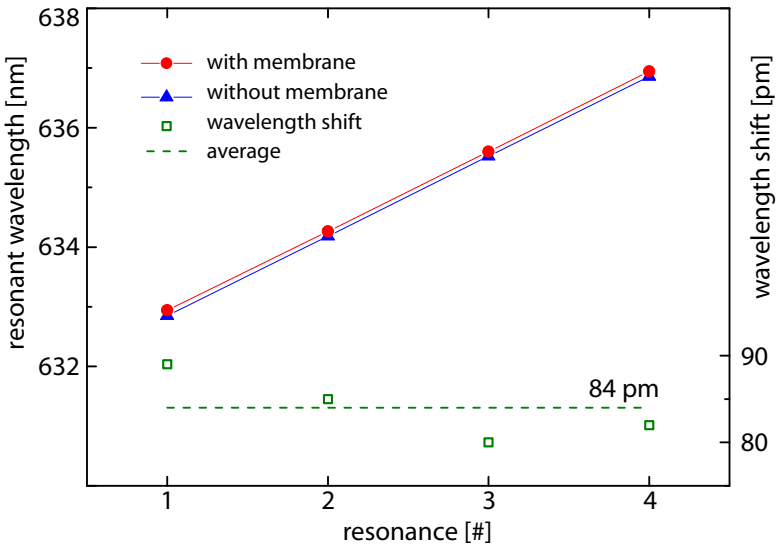

Figure 4.2.: The resonance shift after membrane coating. The resonance wavelength of the TM00 as a function of the azimuthal quantum number m. The modes are spaced by one free spectral range ($\sim 1.34\,\mathrm{nm}$). Once the resonator is coated with the lipid layer, the resonances shift towards longer wavelength. The difference between the data points is plotted below and the dashed line indicates the average frequency shift.

feedback we stain the lipid with 0.5 mol% of the lipid bound colorant Texas Red (TR-DPPE, Molecular Probes) and take fluorescence micrographs. Figure 4.1 (b) shows uniform fluorescent intensity that confirms uniform coverage with the lipid. The undercut region between the pillar and the ring appears brighter compared to the area above the pillar and the intensity ratio suggests that the undercut silica disk is coated from two sides, with additionally light shining through from the silicon chip. A quantitative analysis is difficult, because the errors of the absorption/reflection of the glass an the fluorophore are largely unknown.

Next, we determine the mobility of the lipid via continuous bleaching and fluorescence recovery measurements [155]. To this end a geometrically well defined portion of the fluoropohore is bleached by illumination with a strong laser, and the recovery of the fluorescent intensity due to diffusion is monitored . Comparison with analytical models [156, 4] yields diffusion coefficients ranging from $1 - 4\,\mu\mathrm{m}^2/\,\mathrm{s}$, which are in close agreement with values obtained for supported phospholipidic bilayers [157, 158, 159]. Furthermore we can confirm a mobile fraction of lipids of $> 90\%$.

Finally, we confirm that the amount of lipid material deposited on the resonator corresponds indeed to a single lipid bilayer. To this end, the frequency shift induced by the added material is measured, and the thickness of the lipid layer is inferred from the effective increase of the radius. We couple to a resonator with $66.4\,\mu\mathrm{m}$ diameter and scan the diode laser wavelength over a few nanometer. Then we record the resonant wavelength of a well identifiable mode family, using a wave-meter with

an instrumental resolution of 0.1 pm.[4] As the tuning range of the laser covers several free spectral ranges of the microresonator, we can measure the resonant wavelength for different azimuthal mode numbers (cf. Figure 4.2). Next we remove the resonator from the setup and coat the chip with SOPC lipid, following the previously described procedure. Reassessing the optical mode spectrum we find that the resonances have shifted towards longer wavelength with an average of 84 ± 5 pm. The error is estimated from the temperature inconsistency between the two measurements and correspond to $\pm 1\,^{\circ}\mathrm{C}$. Given that the refractive index of lipid nearly matches the RI of silica at 635 nm wavelength ($n = 1.457$), we can directly access the increase of the cavity radius from the relation $\Delta R/R = \Delta\lambda/\lambda$ and find a mean increase of radius $\Delta R = 4.4 \pm 0.26$ nm. The value is in good agreement with the thickness of a single SOPC bilayer on a silica support, which has been reported to be 4.8 ± 0.1 nm [160]. There again we can use the recorded wavelength shift to calculate the effective RI of a 4.8 nm layer, which yields $n = 1.446 \pm 0.007$, a value that is much closer to the one of the hydrocarbon backbone of the lipids ($n = 1.444$) [161].[5]

From the totality of the above findings, the evenness of the fluorescence, the fluidity of the lipids, and eventually the layer thickness, we conclude the the toroid is indeed covered with a functional lipid bilayer.

4.2. Biotin-streptavidin measurements

To observe specific interaction with a functionalized microresonator, we coat the sensor with a mixture of SOPC lipid (Avanti Polar Lipids) and varying content of biotinylated DOPC (DOPC-X-biotin, Invitrogen) [162]. In particular, we chose biotin concentrations of 1 mol %, 0.5 mol %, 0.1 mol %, and a blind sample with 0 mol % biotin. Once installed in the FCD, the sample is kept under a constant flow of phosphate buffered saline (PBS) with 10 mM HEPES. As we expect frequency shifts of the order of GHz on a slow timescale ($\gg$ s), we use the diode laser to track the frequency. To this end we scan the laser at a rate of 10 Hz and record the transmission as well as the sweep voltage. The transmission minimum is fitted on the fly with a 3$^{\mathrm{rd}}$ order polynomial, and the sweep voltage corresponding to the minimum is stored.

It is important to note that we chose the coupling point (i.e., we adjust the fiber position) such that a small displacement of the fiber does not change the resonance frequency more than the noise level. When the fiber is produced according to section 2.1.2, this is normally achieved when under coupling and setting the transmission on resonance to $50\% - 90\%$. During a measurement of one hour the coupling might slightly change, which is then signaled by the transmission without influencing the frequency signal, and we are able to correct the coupling point while the experiment is running.

[4] The experiment was performed by Bastian Schröter during his Diploma thesis.

[5] Eventually it does not make big of a difference whether we use a lower RI and an increased membrane thickness for our analysis.

During the first 5 to 10 minutes after sample installation, the resonance frequency regularly displays a drift over a few GHz. Once the signal has stabilized, we start injecting streptavidin solution (10 mg/ml in PBS + 10 mM HEPES, Sigma Aldrich) at a rate of 2 ml/h, which mixes with the buffer (6 ml/h) at the injection site to yield an overall concentration of $\sim$ 40 nM at the resonator. Figure 4.3 shows how the resonance frequency shifts when the streptavidin binds to the biotin. Around 700 s after injection the analyte arrives at the sensor, and the frequency starts to shift. During $\sim$ 50 s the shift accelerates until the streptavidin concentration has arrived at its full extend and the dilution effect has paled out (cf. also section 4.3). Then the frequency shift follows an exponential saturation curve until a plateau is reached. An exponential background (cf. section 4.3) that is fitted to the "flat" parts of the curve before and after the binding, was subtracted. While the total frequency shift is proportional to the biotin concentration in the membrane, the time scale on which the binding occurs does not change significantly. Flushing the FCD with buffer solution shows that the frequency shift is irreversible and confirms permanent binding. (Figure 4.3 (a) also shows a curve that is labeled with "unknown biotin content" and displays a total frequency shift of $\sim$ 12.2 GHz. Originally the lipid was prepared with 1% biotinylated DOPC in SOPC, but there are indications that the calculations where done for a total amount of 2 ml lipid solution, while we ended up with one milliliter. The resulting biotin concentration should therefore be around 2%, but eventually we cannot be certain about it.)

To analyze the data, we calculate the sum of single streptavidin frequency shifts and commence by estimating the effective volume of streptavidin, starting from a typical density of protein of 0.73 ml/gr and a refractive index of $n_{\text{protein}} = 1.5$ [163]. For a 60 kDa molecule this yields a volume of 73 nm^3 and with an effective sensing volume of $4.42 \cdot 10^{-4}\,\mu\text{m}^{-3}$ we expect a maximum single particle shift of 1.15 kHz.[6] With an area per lipid (in a monolayer) of 0.666 nm^2 [136, 164] and an effective sensing surface area of 397 μm^2 (70 μm resonator, $\sigma_{\text{FWHM}} = 1.61\,\mu$m) we obtain $5.96 \cdot 10^6$ (binding sites/mol %). When every site connects to exactly one streptavidin, we expect a total shift of 6.85 GHz/mol %. Considering that the value sets an upper boundary, that neglects binding of two biotin to one streptavidin, we obtain excellent agreement with the measured 6 GHz/mol %. Moreover we reject the hypothesis that biotinylated lipids, pointing towards the silica surface of the toroid, might swap and contribute to the streptavidin binding.

In Figure 4.4 (a) we compare the total frequency shift per mol % biotin to the theoretical shift and find that the fractional coverage decreases with increasing biotin concentration. The percentage number can be viewed as the average number of streptavidin molecules per biotin in the outer membrane layer. Notably, a streptavidin molecule possesses four active sites that can connect to biotin, and with increasing biotin concentration in the membrane the probability of double bindings increases. For the lowest biotin concentration we find that every streptavidin molecule binds on average to one biotin in the membrane. At a biotin concentration

[6] Here again we take explicitly the polarizability of a solid, spherical particle into account.

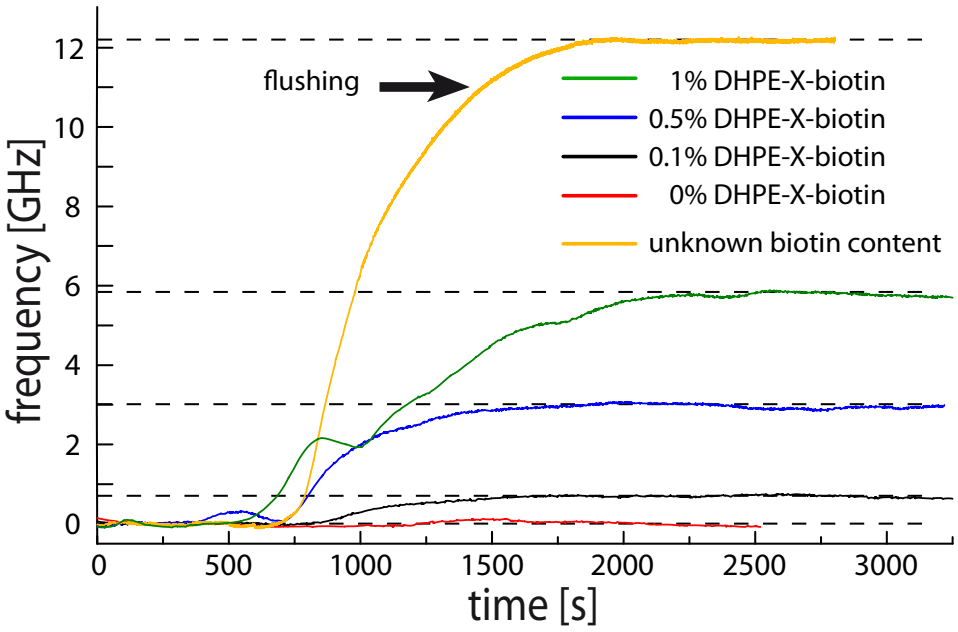

Figure 4.3.: Specific binding of streptavidin. (a) Binding of streptavidin to resonators, that were functionalized with different concentrations of biotinylated lipid, is observed. The total frequency shift is proportional to the biotin content in the membrane. For an unlabeled SOPC membrane no significant frequency shift in the presence of streptavidin is observed. Flushing with buffer solution confirms that the binding is essentially non-reversible. The curve 1 mol % displays a kink that originates from a stuck plunger of the insertion syringe and exemplifies how sensitive the resonance frequency reacts to variations of the flow in the FCD.

of 1 mol %, the value increases to an average of 1.17 links. Contrariwise, it is possible that some biotin molecules are blocked by bound streptavidin and further binding is sterically hindered. In this case we estimate that it takes only a few μs of diffusion time until the biotin connects to the blocking streptavidin molecule. We expect a fully covered surface and occupation of all binding sites only at much higher biotin concentration > 5 mol %.

A similar behavior was reported in reference [165], where the binding of FITC-avidin (66 kDa) to a lipid monolayer containing different amounts of biotin-X-DPPE was investigated. Likewise the number of adsorbed avidins per biotin decreased with increasing biotin concentration.[7] Moreover, the authors also worked with a avidin concentration of 10 μg/ ml and observed $1/e$-binding times ranging from 90 s to 200 s, which is of the same order of binding times that we observe here. Much faster binding times on the order of a few seconds or faster were observed in experiments where the biotin is covalently bound to the surface of a resonator [33] or cantilever [76], which might derive from a much higher biotin density. Nevertheless these findings illustrate that there exists a considerable difference in biological accessibility and interaction between a highly artificial system and a biomimetic interface.

[7] The results are not directly comparable, because, due to a lack of flow, the measurement in reference [165] suffers from unspecific adsorption, which is expressed, e.g., by 0.3 biotin per adsorbed avidin at a biotin concentration of 0.17 mol%.

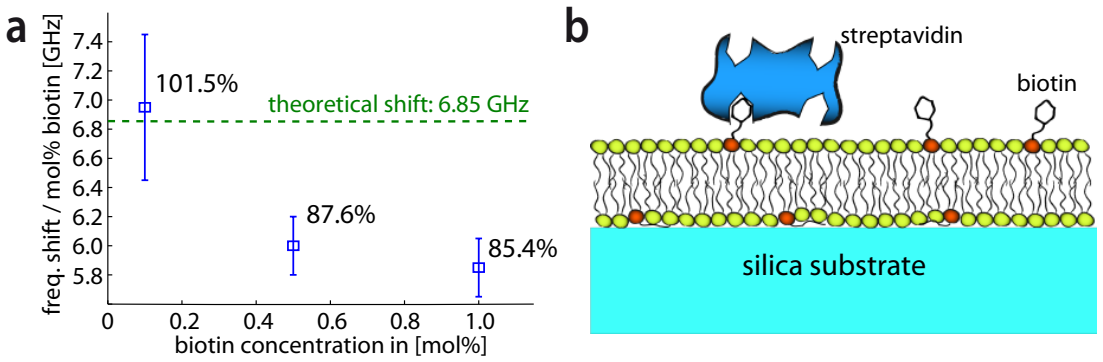

Figure 4.4.: Streptavidin surface density. (a) The frequency shift per mol % biotin in the membrane is in very good agreement with the theoretical value when each biotin binds exactly one target molecule. When the biotin concentration increases the average number of streptavidin molecules per biotin slightly decreases, which is attributed to streptavidin molecules that bind two biotin molecules. The error bars correspond to the estimated frequency fluctuations after the binding had completed. (b) A schematic view of a streptavidin molecule bound to a biotin, which is approximately at scale for a biotin concentration of 1%.

We therefore conclude that our functionalization method indeed enables us to observe specific, membrane bound interaction and is moreover suited for quantitative analysis. This is all the more remarkable, as many functionalization methods suffer from incomplete or partially dysfunctional binding of the receptor [24, 166].

4.3. Ethanol calibration measurement

In this section we describe a supplementary experiment where the resonance is tracked, while the refractive index of the exterior is changed by means of a varying ethanol concentration. The well defined boundary conditions of the measurement allow us to accurately determine the evanescent fraction of the WGM and to compare to the theoretical values. Moreover, we receive an impression of the time scales and the mixing in the fluidic system.

We prepare a solution containing 2.5% ethanol, and we track the resonance frequency of the toroid in a constant water flow at 10 ml/ h. The ethanol solution is loaded to a second syringe pump, which is connected to the insertion site. Then the flow ratio between the pumps is stepwise changed by 10%, such that the ethanol concentration is increased by 0.25% with each step, while the overall flow remains constant. Again the higher initial concentration of the ethanol solution and the mixing serve temperature stability. When the ethanol arrives at the detector, the resonance frequency shifts. Instead of a frequency jump, we observe a convoluted step, which accounts for the diffusion of the solution inside the tubing. We note that our open design enables us to prepare a sharp transition between different analytes when we inject a tiny air bubble between two species. The air bubble escapes when it

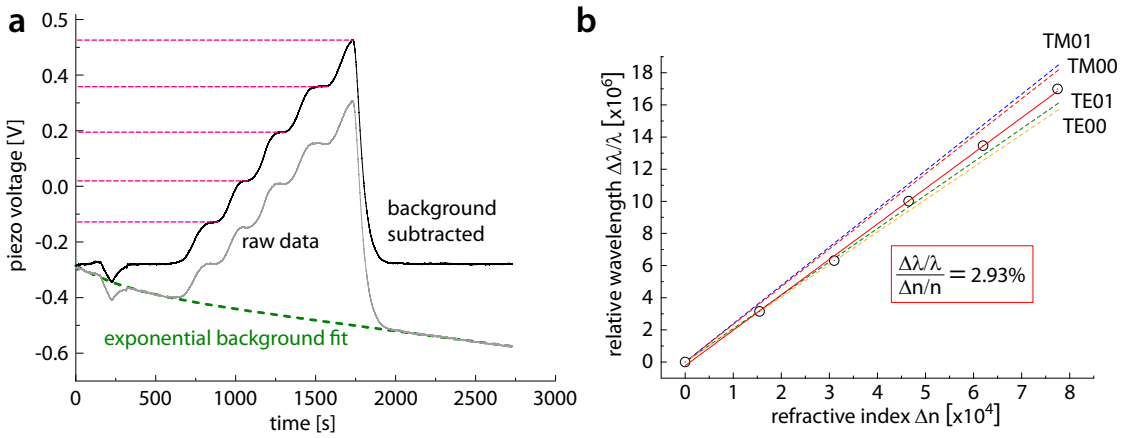

Figure 4.5.: The reactive frequency shift in response to ethanol. (a) The resonance frequency is recorded, while ethanol solution is injected. The ethanol concentration is step-wise increased by 0.25%. To minimize the impact temperature, we start from a 2.5% solution and mixing takes place inside the tubing leading to the FCD. The raw data shown in the gray curve are on top of a background drift. We fit an exponential to the portions of the curve, before and after the presence of the ethanol, and subtract the background. We then convert the step heights to a frequency and plot the shift as a function of the refractive index. The slope compares favorably to the theoretical result obtained from simulations.

enters the coupling chamber, where the mixing takes place in this case. Even though such separation is possible, it has not proven practical, as mixing always involves strong fluctuations of the refractive index and convection, which finally manifests as low frequency noise or "shaking" of the resonance.

After five augmentations of the ethanol concentration, we inject pure water (without changing the overall flow) and the resonance frequency shifts back to its original level. Here we continue recording to obtain sufficient background. Figure 4.5 (a) shows a trace of the recorded raw data, where the signal from the ethanol solution sits on top of an exponential frequency decay. We fit an exponential function to this background, which is subsequently subtracted from the data. The background presumably derives from temperature drift, probably due to evaporative cooling, and its amplitude over one hour typically correspond to a temperature change of less than 1°C.[8]

Next, we extract the step heights from the background corrected data and convert the piezo voltage shift to a frequency (cf. section 2.2.2). Figure 4.5 (b) shows the relative wavelength shift as a function of the RI change. We simulate the wavelength shift for different modes and polarizations and find excellent agreement with the measured data. The mismatch can be accounted for by an uncertainty in the ethanol concentration of the initial solution and an error of the measured cavity radius. The slope of the curve is closely related to the evanescent intensity fraction, even though it is not fully equivalent.

[8]The thermal temperature drift in water at a wavelength of 635 nm is 3.1 GHz/K.

5. Refractive index spectroscopy

In the two previous chapters, we discussed clearly resolvable frequency shifts, resulting from both, single particles and ensembles of molecules. Here we move beyond the resolution limit, set by the frequency fluctuations, and focus on the properties of the frequency noise instead. Even when the frequency shift from a single particle cannot be directly resolved, the noise spectrum potentially reveals information on single particle properties, such as on and off binding rates, or dwell times.
In this chapter, we start out with a characterization of the toroid's frequency noise and we introduce the Allan deviation as a sensitivity measure that takes the time scale on which a binding event occurs into account. Then we present a measurement of IgG protein, where the presence of the molecule manifests in the noise spectrum. The autocorrelation function and the Allan deviation are discussed regarding their application for frequency noise analysis, in particular in the presence of frequency drift. Finally, we identify thermo-refractive noise as a factor that limits the frequency resolution and thus the sensitivity of the device at short time scale (below 1 ms).

The chapter can partially be viewed as an outlook on promising measurements and possible experiments. In particular the noise spectroscopy will directly profit from even higher time resolution, which requires less effort than an improvement of the frequency resolution and therefore constitutes a canonical direction of future sensor development. The chapter concludes with a detailed outlook and a summary of what has been achieved so far.

5.1. The Allan deviation as a sensitivity measure

Sensitivity measures for refractive index sensors are frequently stated in terms of refractive index units (RIU, meaning the smallest resolvable RI variation), the minimum detectable concentration of a target molecule in the environment, or an accumulated mass of the target on the sensor [167]. For single particles the sensitivity is often referred to by the smallest individual particle that can be resolved before the noise background. However, these measures fail to reflect the time dependence of the event, i.e., the time scale on which the RI change occurs or the target binds. A fast event, such as an adsorbing vesicle, experiences a different detection limit than an ensemble measurement taking place during several minutes, which competes with frequency drift. To overcome this drawback, we introduce the Allan deviation $\sigma_\nu(\tau)$ as a measure for the frequency resolution on different time scales. The Allan deviation and its square, the Allan variance, are established quantities to

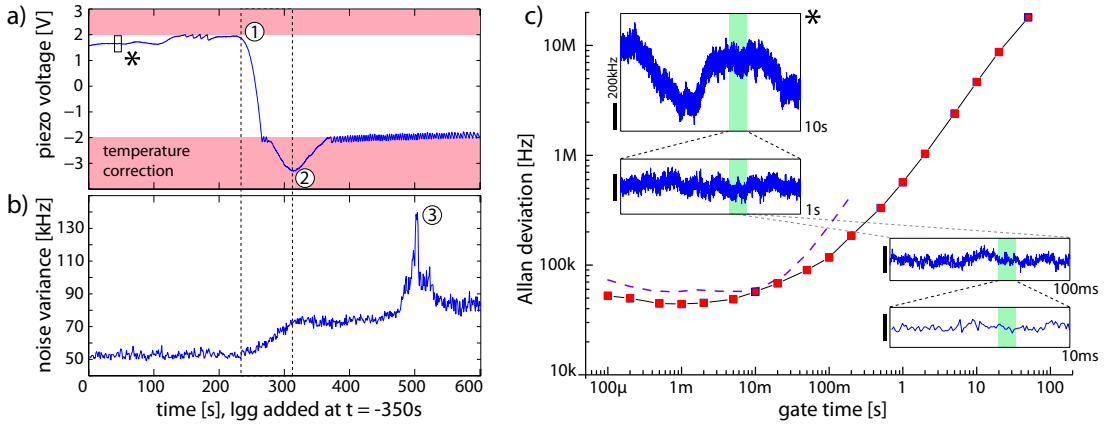

Figure 5.1.: Frequency noise during a measurement. (a) Raw data from a measurement of IgG protein. The arrival of the molecules (1) is signaled by a frequency drift, most likely due to a temperature difference of the target solution. Here 1 V corresponds to a temperature difference of $\sim 20\,\mathrm{mK}$. When the piezo voltage (before $\times 20$ amplification) exceeds $\pm 2\,\mathrm{V}$, the wavelength is adjusted via the laser crystal temperature. (b) The data point distribution on a 1 s time frame is always given by a Gaussian within the standard error. We plot the width of the Gaussian during the measurement. Its value before the arrival of the protein corresponds to a standard deviation of 42 kHz a record frequency resolution of $\Delta\nu/\nu = 7.7 \cdot 10^{-11}$. (c) The Allan deviation is plotted as a function of the gate time τ and the insets illustrate that the AD is a suited measure to describe the sensitivity towards a frequency shift taking place during a time τ.

express frequency stability of an oscillator in frequency metrology [112].

$$\sigma_\nu = \sqrt{\frac{1}{2}\left\langle (\bar{\nu}_{n+1} - \bar{\nu}_n)^2 \right\rangle_n} \tag{5.1}$$

In the above definition of the AD, one data point $\bar{\nu}_n$ corresponds to the frequency signal, averaged during the gate time τ. The AD is thus a time scale dependent quantity. In the context of sensing, a frequency shift that occurs during a time τ can be distinguished from the background noise when it is larger than $\sigma_\nu(\tau)$. In the absence of frequency drift, one can in principle recover the frequency shift by sufficient averaging and filtering of high frequencies, which comes however at the cost of reduced time resolution. Then the achievable time resolution corresponds approximately to the time where the AD equals the signal amplitude. The link between the Allan deviation and the smallest resolvable signal is illustrated in Figure 5.1 (c), where the AD is plotted next to noise traces on different time frames.

To record the Allan deviation and to characterize the frequency noise of the resonator only, it is important to eliminate laser phase and frequency noise. To this end we utilize an optical heterodyne scheme and compare the frequency of the Nd:YAG laser, locked to the resonator, to a second Nd:YAG laser, which is stabilized to an ultra-stable reference cavity (cf. section 2.2.3). In this case the signal reflects purely the resonator noise, contrary to the correction signal that also contains laser noise. Figure 5.1 (a) shows a trace that was recorded during a measurement of IgG protein

and which will be analyzed in detail in the following section. Here we focus on the part of the curve before the target arrives, i.e. on the portion inside the rectangle tagged with the asterisk. In panel (c) of the same figure a magnified view of the sub-trace is shown and with further zooming in on ever shorter pieces of the curve, one obtains an impression of how the frequency resolution increases with decreasing time scale. Furthermore we show a plot of the Allan deviation that was partially recorded from the beat note and recorded with a frequency counter. Other values were inferred from the correction signal and again the overlapping of the traces (not shown here) confirms the correct frequency calibration. It becomes apparent that a frequency shift $\sigma_\nu(\tau)$ during a time τ is related to the minimum resolvable signal. In our case the resolution is limited by phase and frequency noise at short time ($< 10\,\mathrm{ms}$), whilst on a longer time scale ($> 100\,\mathrm{ms}$) frequency drift - which is identified by its characteristic linear dependence on τ - becomes the limiting factor. For frequencies above 1 kHz, thermo-refractive noise of silica, which is discussed in detail in section 5.3, sets the fundamental detection limit.

5.2. Refractive index correlation spectroscopy

In this chapter, we go beyond the measurement of clearly resolvable frequency shifts, as they have been discussed in the two previous chapters. When the shift from a single particle is "smaller" than the noise background, it cannot be resolved anymore, which is also confirmed by statistical tests with simulated data. The reason for this derives from the fact that a frequency step displays a broad, flat frequency spectrum and additionally the events occur at random time. Therefore we cannot gain any insight from linear filtering or averaging. The presence of single particle is however contained in the noise itself, and one can access single particle properties, such as dwell times and binding rates, from a statistical noise analysis.

5.2.1. Fluorescence correlation spectroscopy (FCS)

With increasing availability of high resolution confocal microscopes and sensitive photo detectors, fluorescence correlation spectroscopy (FCS) has become a powerful technique for measurements of concentration, diffusion and molecular interaction [168]. The technique is considered as one of the milestones of light microscopy by Nature magazine [169]. For FCS the analyte is labeled with a fluorescent marker and fluorescent light is collected within the confocal excitation and detection volume. The fluorescent intensity is typically sampled around 100 kHz to 1 MHz. From the autocorrelation of the fluorescent intensity $F(t)$ one can obtain information about the number of molecules, diffusion time and binding constants.
In our system we perform a refractive index correlation spectroscopy (RICS) analysis. Here the refractive index contrast plays the role of the fluorescence intensity and the integration volume is given by the evanescent field instead of the confocal

point spread function. In this case the autocorrelation function $G(\Delta t)$ is computed from the resonance frequency fluctuations $\delta\nu(t)$ instead of the intensity signal.

$$G(\Delta t) = \frac{\langle \delta\nu(t)\delta\nu(t+\Delta t)\rangle}{\langle \delta\nu(t)^2\rangle}$$

It is an advantage of RICS, that no tedious labeling of the analyte is necessary. The key requirements for RICS are a small detection volume and fast frequency sampling. Both are realized in our system. Here, we consider only the frequency signal within the locking bandwidth. Frequencies that exceed this bandwidth are obtained from the error signal, after passing an additional high pass filter. If the amplitude of the high frequency fluctuations is smaller than the resonance width, such that the signal stays within the linear part of the error signal close to the locking point (cf. Figure 2.6), the signal is directly proportional to the frequency fluctuations. Additional calibration and conversion to frequency detuning is not required, because the autocorrelation function is normalized. The resolution bandwidth is in principle limited by the phase modulation frequency, and a time resolution below one $1\,\mu$s can be achieved.

We note that such measurement was already performed using polystyrene beads and a microsphere resonator [36]. The author tuned the laser to the side of a resonance fringe and analyzed the intensity fluctuation of the transmitted light.

5.2.2. Drift and background subtraction

In contrast to a typical FCS measurement, we encounter signal drift, which requires background subtraction, such that the fluctuation signal is given by

$$\delta\nu(t) = \nu(t) - \langle\nu(t)\rangle_T\,. \tag{5.2}$$

This can be achieved, by averaging the signal over a time interval T to obtain the drift contribution

$$\langle\nu(t)\rangle_T = \frac{1}{T}\int_{-T/2}^{T/2}\nu(t+t')dt'. \tag{5.3}$$

To separate the drift from the fluctuations, the time interval T is typically chosen in the order of the time scale where frequency drift starts to dominate over other noise terms, which occurs, in our experiment, between $1-10\,$ms. (cf. Figure 5.1 (c)). However, such simple background subtraction artificially introduces a correlation in the smoothed signal $\langle\nu(t)\rangle_T$ and thus in $\delta\nu(t)$. Calculating the auto-correlation function for smoothed and previously uncorrelated white noise, we find that an artificial linear offset proportional to $1-\Delta t/T+2\cdot\Theta(T/2-\Delta t)$ is produced for a delay $\Delta t < T$ (here $\Theta(t)$ denotes the Heaviside step function). For a fluctuating signal that is already self-correlated, the offset shows a non-trivial dependency on the correlation time and cannot be corrected simply by subtraction. To cope with this problem, we chose a percentile filter to determine the drift background and calculate the median frequency on a time window around each data point.

$$\langle\nu(t)\rangle_T = \text{median}\left\{\nu(t')\,|t'\in[t-T/2,t+T/2]\right\} \tag{5.4}$$

We still observe a linear offset, which is however much weaker than for linear filtering. In the analysis of the recorded data, we circumvent the difficulty by calculating the difference between the autocorrelation of the background (in absence of the target) and the frequency noise in presence of the target. A third possibility of background removal that we utilized in the noise analysis is piecewise fitting of a linear background, typically on time frames of 10 ms.

5.2.3. Experimental result: IgG measurement

We chose the protein immunoglobulin G (IgG) as a test body to explore the capabilities of single molecule RICS using high-Q toroidal microresonators. A single IgG molecule weights $\sim 150\,\mathrm{kDa}$ and is expected to yield a maximum frequency shift of $\sim 5.3\,\mathrm{kHz}$, which is about eight times smaller than the standard deviation of the frequency noise at 1 ms. A single adsorption event can therefore not be observed directly. We prepare an aqueous solution of the protein with a concentration of $50\,\mu\mathrm{g/\,ml}$ and render the surface of the toroid hydrophilic using the SC-1 cleaning procedure. It has been observed by Vörös that IgG physisorbes on hydrophilic surfaces without the need of specific functionalization [170]. The protein solution is extruded with a 50 nm pore size membrane to filter clusters and aggregates of proteins. A previous measurements without extrusion showed large frequency jumps up to a few MHz.

In the experiment we inject $\sim 40\,\mu\mathrm{l}$ of the protein solution and we observe that the arrival of the protein is accompanied by a strong drift and broadening of the noise by $\sim 40\%$ (cf. Figure 5.1a/b). Such effect could be attributed to a decrease of the optical quality (i.e., line width broadening) and an increase of uncertainty of the laser lock. To exclude this effect, we scale the autocorrelation function to its variance. Next we calculate the auto-correlation function $G(t, \Delta t)$ on time intervals of 1 s and plot its value for fixed delays as a function of the measurement time t. Figure 5.2 (a) demonstrates how the arrival of the analyte coincides with an increase of self-similarity. When the flushing of the FCD continues during the measurement, the auto-correlation decreases and approaches its original level. At this point one can ask a couple of questions, some of which will remain unanswered. One can hypothesize whether the correlation of the background originates from thermal noise or whether it is an artifact coming from some low pass filter. Moreover, we observe an increase of the auto-correlation which is doubtlessly due to the protein and display a peak around 700 s. After reaching its maximum, the curve decreases during $\sim 30\,\mathrm{s}$ and reaches a plateau with a much slower decay constant that we estimate around $200 - 300\,\mathrm{s}$. From the ethanol and streptavidin it is know that an initially singular portion of the target is broadened due to diffusion and passes the sensors during $\sim 50\,\mathrm{s}$, a time scale that matches the width of the peak. The remaining increase of signal correlation – namely the plateau around 800 s in Figure 5.2 (a) – could then be attributed to some noise increase due to adsorbed protein and the slow decrease could be the result of detaching molecules on a longer time scale. This is however highly speculative and calls for experimental verification.

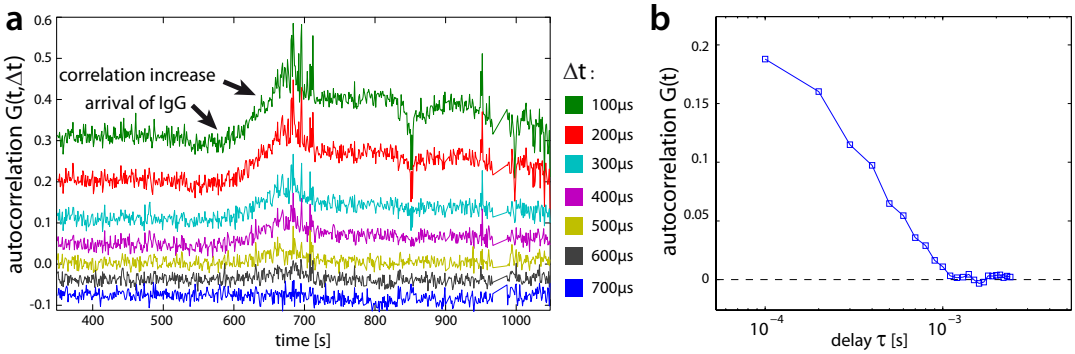

Figure 5.2.: The auto correlation function for noise analysis. (a) The auto-correlation function, normalized to the noise variance, is calculated on consecutive 1 s time frames and its values for fixed delays is plotted. The background was removed using a thirty point median filter. (b) The difference between the autocorrelation function in presence of the protein and the background correlation, i.e. $t < 500\,\mathrm{s}$, is plotted as a function of the delay time. The graph can be viewed as the *peak height* at 700 s with respect to the background around 400 s.

To gain quantitative insight we average the auto-correlation function during its peak at $t \in [650s, 700s]$ and subtract the correlation background averaged during the time interval $t \in [400s, 500s]$ before the protein arrives. The difference, i.e., the background corrected IgG auto-correlation, is depicted in Figure 5.2 (b). The curve shows a characteristic drop towards longer delays and decays proportional to $\propto \exp(-\tau/115\,\mu\mathrm{s})$. On this time scale, diffusion dominates and the particle travels around $\sim 60\,\mathrm{nm}$, a length that is in the range of the azimuthal extension of an optical node ($\sim 100\,\mathrm{nm}$) as well as the decay constant of the evanescent intensity ($\sim 84\,\mathrm{nm}$).

We do not want put too much interpretation into the result, but it can clearly be seen, that the arrival of the IgG alters the noise properties of the signal, and that the correlation is a function of the delay time τ. Moreover, the correlation signal approaches its original level, when the IgG concentration decreases with continued flushing.

Switching between different filters and smoothing methods for the removal of the frequency drift, as well as simulations, shows that the filtering method strongly influences the shape of the auto-correlation trace. The difficulty derives from the fact that one cannot easily distinguish between different noise sources in time domain. We therefore resort to the Allan deviation as a noise analysis tool that does not rely on post processing of the data. Here we compute the AD on 25 s time frames and evaluate its dependence on that gate time. At short time scale, in the TRN regime, we observe a slope change that coincides with the arrival of the IgG protein at the sensor. When the agent is removed, i.e., its concentration is reduced by flushing the FCD with buffer solution, the slope approaches its original level. In contrast to the correlation spectra, the curve is obtained without any filtering, i.e., background and drift removal, on the data. The drift term remains unaffected during the measurement (cf. Figure 5.1 (a)), but in the noise minimum (around

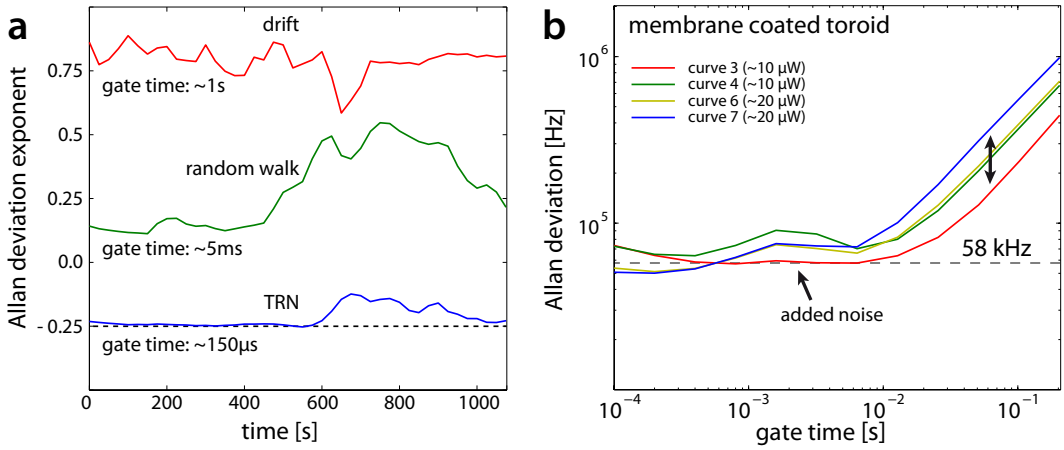

Figure 5.3.: The Allan deviation for noise analysis. (a) We calculate the Allan deviation (σ_{AD}) on consecutive 25 s time frames and plot the power dependency on the gate time (i.e. $\left(\sigma_{AD}(\tau) \propto \tau^{\beta}\right) :\rightarrow \beta$ for different gate times. The frequency drift remains unaffected during the measurement. (The expected slope of 1 is slightly altered because a straight line between the first and last data point of each portion of the trace was subtracted.) (b) The difference between the autocorrelation function in presence of the protein and the background correlation, i.e. $t < 500$ s, is plotted as a function of the delay time. The graph can be viewed as the *bump height* when the IgG arrives in Figure 5.2 (a). Panel (b) shows the Allan deviation, recorded trom a toroid coated with an (SOPC) lipd membrane at ambient temperature. Between the different curves, the input power and the gain settings of the frequency lock were changed. Most strikingly, the curve reveals that the membrane coating only leads to a minot deterioration of the frequency resolution (cf. Figure 5.1 (c)). Moreover, we observe added noise around 500 Hz, which could result from membrane undulation, and which is a promising starting point for future experiments.

$1-10$ ms) a novel noise term $\propto \tau^{1/2}$ appears. The exponent suggests a random walk noise contribution, which is expected for particles entering and leaving the field at random time.

Finally we record the noise spectrum of a lipid bilayer coated toroid and calculated the Allan deviation from the frequency noise trace. Figure 5.3 (b) shows four different traces that were taken at different input power and different gain settings of the PDH lock. Primarily, the data confirm that the lipid membrane coating technique does not compromise the frequency resolution of the sensor. This is in stark contrast to most functionalization techniques, where surface functionalization degrades the optical quality, often by more than one order of magnitude. In our case the preservation of the Q is most likely a consequence of the matching refractive indices of the lipid and the glass substrate. Impurities, scattering centers, and other surface defaults that lead to optical loss are engulfed by the lipid and abrupt changes of refractive index are faded out.
Moreover, the measurement shows that frequency drift is stronger for higher input power, as one would expect due to increased temperature. On the other hand, higher input power results in lower noise at short time scale < 1 ms, which is a result of a stronger PDH error signal and a steeper slope on resonance. Lastly, there seems to

be a resonant peak centered around 500 Hz, whose varying intensity correlates neither with the drift nor with the high frequency noise. One can hypothesize whether such feature could result from membrane undulations [171], and the effect certainly deserves future attention and verification, all the more as it is a straight forward measurement.

We conclude the IgG and noise spectroscopy measurements by summarizing the results that are certain, and with an outlook on promising experiments. We have clearly shown that the presence of molecules with a single particle shift $\div 8$ smaller than the standard deviation of the frequency noise can be detected in the altered noise properties. Moreover, we have demonstrated that an additional membrane layer for surface functionalization does not lead to a significant deterioration of the frequency resolution. On the other hand, the quantitative results are limited so far. For a more profound, deterministic analysis one requires a higher temporal resolution and possibly an active temperature control of the FCD and the inserted fluid, to minimize frequency drift. As described earlier in section 2.2.1, both measures are straight forward to implement, and future experiments could, e.g., set out to measure the plateau of the auto-correlation function at short time scale $\propto 1\,\mu$s or the noise associated with a phase transition of a lipid bilayer when scanning the temperature [138]. These experiments do not even require sophisticated locking technology and further noise reduction in the electronic setup, because it is usually sufficient to manually tune tze laser to a resonance and to record a one second trace with high time resolution.

5.3. Thermo-refractive noise (TRN)

In this section, we derive the thermo-refractive noise (TRN) spectrum for a toroidal microresonator and discuss its implications on the frequency resolution and sensitivity of the sensor. Thermal noise is ubiquitous in physics and its origin lies in the energy distribution among the degrees of freedom of an statistical ensemble at thermal equilibrium. For a canonical ensemble, the energy variance is expressed as $\langle(\Delta E)^2\rangle = k_B T^2 \cdot \partial_T \langle E\rangle$, where k_B is the Boltzmann constant, T the mean temperature of the environment, and $\langle E\rangle$ the expected energy of the ensemble. Dividing by the heat capacity squared $(\partial_T \langle E\rangle)^2$, yields the expression for the fluctuations of the mean temperature.

$$\left\langle(\Delta T)^2\right\rangle = \frac{k_B T^2}{\rho c_p V} \tag{5.5}$$

Here, the heat capacity of the ensemble was replaced by the product of ρ the density of the material, c_p the specific heat capacity, and V the volume occupied by the ensemble. The deviation from the mean temperature is linked to fluctuations of the refractive index via the coefficient of thermal refraction dn/dT (cf. Table 5.1) and the thermal fluctuation thus translate into frequency noise of the resonator. For

		fused silica	water
density	ρ	$2200\,{}^{\mathrm{kg}}/_{\mathrm{m}^3}$	$998\,{}^{\mathrm{kg}}/_{\mathrm{m}^3}$
specific heat capacity	c_p	$740\,{}^{\mathrm{J}}/_{\mathrm{kg\,K}}$	$1480\,{}^{\mathrm{J}}/_{\mathrm{kg\,K}}$
coeff. of thermal refraction	${}^{dn}/_{dT}$	$1.3 - 1.45 \cdot 10^{-5}\,\mathrm{K}^{-1}$	$-9 \cdot 10^{-5}\,\mathrm{K}^{-1}$
thermal diffusivity	D	$0.75 - 0.85 - 0.95\,{}^{\mathrm{mm}^2}/_{\mathrm{s}}$	$0.143\,{}^{\mathrm{mm}^2}/_{\mathrm{s}}$
thermal conductivity	k	$1.38 - 1.4\,{}^{\mathrm{W}}/_{\mathrm{K\,m}}$	$0.6\,{}^{\mathrm{W}}/_{\mathrm{K\,m}}$

Table 5.1.: Important material constants for silica and water at room temperature. Sources: Wikipedia, http://accuratus.com, and http://www.valleydesign.com. Multiple values or parameter ranges reflect the discrepancy between different sources.

microsphere resonators TRN was calculated and measured by Gorodetsky and Grudinin who reported a characteristic frequency dependence $\propto \omega^{-1/2}$ and the existence of a corner frequency beyond which thermal fluctuations are suppressed with ω^{-2}. However, the equations published by the authors do not fully apply to WGM in toroidal resonators, and they poorly reflect the TRN at low frequency. Here, we will show that the TRN in this regime is governed by a term $\propto \log[1/\omega]$, which implies that the thermal noise is less intense than suggested by the $\propto \omega^{-1/2}$. Importantly the $\log[1/\omega]$ dependence enables us to integrate and normalize the spectrum, and comparison with Equation 5.5 enables us to calibrate the spectrum.

In the following sections, we first consider the one-dimensional problem, where the temperature fluctuations are averaged over different envelop-functions, and we will learn how the actual shape influences the spectrum or the TRN. With some insight gained, we move on to the three-dimensional case and derive the TRN for a geometry that resembles the fundamental WGM of a toroidal resonator. Finally, we discuss how thermal noise limits the frequency resolution of a WGM sensor, and how the TRN limit can be avoided.

5.3.1. TRN in one dimension

The physics behind TRN is simple, once the underlying mechanism is identified. This fundamental work is well described in a manuscript by Voss and Clarke that deals with fundamental voltage fluctuations of thermo-resistive origin in a thin metal slab [172]. The authors nicely demonstrate that temperature diffusion is the predominant thermal transport mechanism, and they rule out other possible mechanisms, such as temperature conductance. We express a local deviation from the mean temperature by the function $u(x,t)$ and write the diffusion equation.

$$\partial_t u(x,t) = D\partial_x^2 u(x,t) + \partial_x F[x,t] \tag{5.6}$$

A driving noise term $F[x,t]$ establishes the equilibrium properties. It is important to note that the temporal change of temperature is driven by the local gradient of the heat fluctuations. In the Markovian limit, the drive $F[x,t]$ is δ-correlated white noise with

$$\langle F[t,x]F[t',x']\rangle \equiv F_0^2 \cdot \delta(t-t')\delta(x-x') = 4k_B T^2/c_p\rho \cdot \delta(t-t')\delta(x-x') \tag{5.7}$$

We solve the diffusion equation according to the books and introduce the definition of the Fourier transform.

$$u(x,t) = \int \frac{d\omega}{2\pi} \int \frac{dq}{2\pi} u(q,\omega) e^{-i\omega t} e^{-iqx} \tag{5.8}$$

Next we multiply Equation 5.6 with $\exp[i\omega t + iqx]$, integrate, and solve for the Fourier transform of the temperature fluctuations $u(q,\omega)$.

$$\begin{array}{rl} -i\omega u(q,\omega) = & -Dq^2 u(q,\omega) - iqF[q,\omega] \\ u(q,\omega) = & \frac{-iq}{Dq^2 - i\omega} F[q,\omega] \end{array} \tag{5.9}$$

Then the spectral density of the thermal fluctuations is given by a Lorentzian

$$S_u(q,\omega) = \int \frac{dq'}{2\pi} \int \frac{d\omega'}{2\pi} \langle u(q,\omega)u(-q',-\omega')\rangle = \frac{q^2}{D^2q^4 + \omega^2} F_0^2 \tag{5.10}$$

(For a detailed definition of noise operators in Fourier space and the 2π-balance refer to section 7.2.1.) The thermal fluctuations have a maximum at $\omega = D/q^2$, which can be interpreted as a dispersion relation of thermal waves in the medium. In the next step, we take the finite measurement volume into account, which is in our case, defined by the spatial profile of the WGM, and we average the thermal spectrum within this volume. In the one dimensional case the volume is replaced by a "window" or spatial gate function $w(x)$ and we will now assume three different geometries to explore the effect of the window shape on the TRN spectrum. In particular, we consider (i) a Gaussian profile, as it is typically found with WGMs, (ii) a rectangular profile, and (iii) and an exponential decay that is cut off at one side to resemble an evanescent field. In all cases, the characteristic length will be σ, and it shall already be mentioned that the characteristic length leads to a corner frequency $\sim D/\sigma^2$ in the TRN spectrum. A thermal fluctuation with a wavelength shorter than the geometric width of the window averages to zero, and the associated frequency is suppressed.

For better intuition we start out with a real space and time definition of the average temperature within the detection (normalized) window $\bar{u}(t) = \int w(x) \cdot u(x,t)\, dx$. Explicitly we write for the three geometries:

$$\bar{u}(t) = \begin{cases} \frac{1}{\sqrt{2\pi}\sigma} \int dx\, \exp[-x^2/2\sigma^2] \cdot u(x,t) \\ \frac{1}{2\sigma} \int dx\, 1_{[-\sigma,\sigma]} \cdot u(x,t) \\ \frac{1}{\sigma} \int dx\, \mathbb{1}_{[0,\infty[} \exp[-x/\sigma] \cdot u(x,t) \end{cases} \tag{5.11}$$

We replace $u(x)$ by its Fourier transform and we switch the order of the $x-$ and the $q-$integral. Then the real space integral can be evaluated and yields the Fourier transform of the window function.

$$\begin{aligned}\bar{u}(\omega) &= \int dx\, w(x)\cdot u(x,\omega)\\ &= \int \frac{dq}{2\pi}\int dx\, w(x)\cdot e^{-iqx}\cdot u(q,\omega)\\ &= \int \frac{dq}{2\pi}\, w_\sigma(-q)\cdot u(q,\omega)\end{aligned}$$

As a reminder we put the window width σ as an index of its Fourier transform. Explicitly we find:

$$w_\sigma(q) = \begin{cases}\exp[-q^2/2]\\ \frac{\sin[q]}{q}\\ 1/(1+iq)\end{cases} \tag{5.12}$$

Finally we calculate the temperature spectral density from the autocorrelation. Note that the δ-functions consume $(2\pi)^{-1}$ each.

$$\begin{aligned}S_{\bar{u}}(\omega) &= \int \frac{d\omega'}{2\pi}\,\langle \bar{u}(\omega)\cdot\bar{u}(-\omega')\rangle\\ &= \int \frac{d\omega'}{2\pi}\int\frac{dq}{2\pi}\int\frac{dq'}{2\pi}\, w_\sigma(-q)\cdot w_\sigma(q)\,\langle u(q,\omega)\cdot u(-q',-\omega')\rangle\\ &= \frac{F_0^2}{2\pi}\int dq\,|w_1(\sigma q)|^2\frac{q^2}{D^2q^4+\omega^2}\\ &= \frac{\sigma F_0^2}{D}\int\frac{dq}{2\pi}\,|w_1(q)|^2\frac{q^2}{q^4+(\omega/\omega_x)^2}\end{aligned} \tag{5.13}$$

Here we defined the corner frequency $\omega_x = D/\sigma^2$. The integral is now dimensionless and the spatial gate function behaves as a cut off at $|q|\approx 1$. The integral over the fluctuations yields

$$\int\frac{d\omega}{2\pi}\,S_{\bar{u}}(\omega) = \frac{\sigma\omega_c F_0^2}{4\pi D}\int dq\,|w(q)|^2 = k_BT^2/\rho c_pV. \tag{5.14}$$

We define the thermal volume $V_{th}^{-1}\equiv\int dq/2\pi\,|w_\sigma(q)|^2$ and such that the integral over all positive frequencies ω reproduces the temperature variance expected for a volume V_{th} (when $F_0^2 = 4k_BT^2/c_p\rho$).

Figure 5.4 (a) shows that the thermo-refractive noise spectral densities for different averaging windows $w(x)$ display different behavior at high frequency beyond the cutoff. While the Gaussian window drops proportional to ω^{-2}, as reported by Gorodetsky and Grudinin, the slope of the one sided exponential and the square window show a slope $\propto\omega^{-3/2}$, as it was observed by Voss and Clarke. The behavior is directly understood from the shape of the gate function in Fourier space

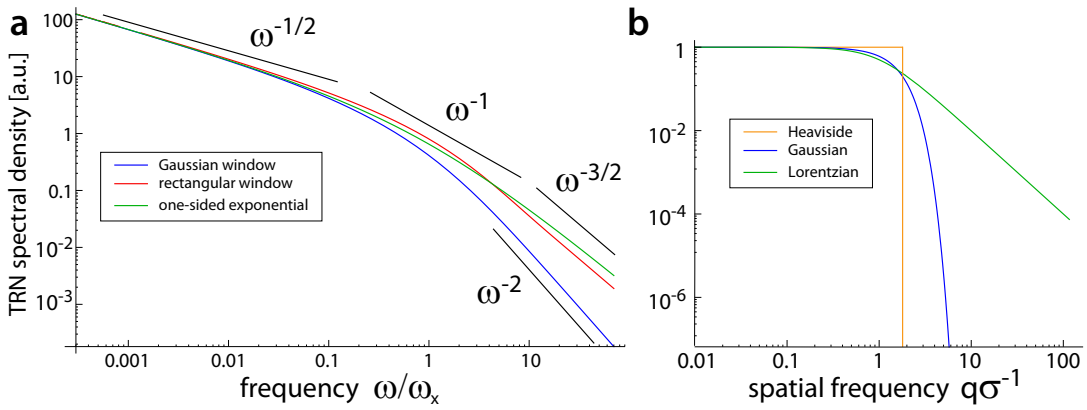

Figure 5.4.: The TRN spectral density for different geometries. (a) The TRN spectrum for frequencies $\omega < \omega_x$ is proportional to $1/\sqrt{\omega}$, independent of the shape of the averaging volume. For high frequencies, exceeding the cut off, the TRN within a Gaussian window is proportional to $1/\omega^2$, while the average over a rectangular window and the one-sided exponential display an asymptotic behavior $\propto \omega^{-3/2}$. (b) This characteristic difference is understood from the suppression of high spatial frequencies in Fourier space. Here the Gaussian provides a much sharper cutoff than the sinc-function (not shown) and the Lorentzian that approach q^{-2} and thus include higher frequency components. In the following section we make use of this intuition and approximate the cutoff by a Gaussian with a Heaviside step function, cutting spatial frequencies at $\sqrt{\pi}\sigma^{-1}$.

$|w(q)|^2$; the Gaussian case shows a sharp drop at σ^{-1} and higher spatial frequencies are rigorously suppressed. On the other hand, the Lorentzian and the sinc-function have an asymptotic tail $\propto q^{-2}$ to include higher frequencies of the discontinuity (in real space). Consequently higher spatial frequencies give rise to the appearance of higher temporal frequencies in the spectrum. Such sharp transitions at an interface are naturally much better realized in a metal film. It remains an unanswered question, whether sharp transitions and discontinuities in an optical resonator systems, e.g. originating from largely different thermal diffusivity of water and silica or from a lipid membrane layer, give rise to an $\omega^{-3/2}$ TRN spectrum.

5.3.2. TRN in three dimensions

Following up on the discussion of the general properties of thermo-refractive noise, we move to three dimensions and average the temperature fluctuations $u(\mathbf{r}, t)$ over the mode profile of a fundamental WGM. In the last section it was shown that spatial constraints lead to corner frequencies that are – in the case of a Gaussian window function – approximated by the expression

$$\nu_{\text{cut off}} \approx \frac{\log 2}{2} D \cdot \sigma_{\text{FWHM}}^{-2}. \tag{5.15}$$

For a microtoroid we encounter the situation, where the mode width in the radial and the polar direction ore similar and the associated corner frequencies are therefore

closely spaced. The table below lists typical dimensions of a fundamental WGM (the value in parentheses represents is the decay length of the evanescent field) and shows the corresponding cut off frequencies in silica and water.

direction	length (FWHM)	$\nu_{\text{cut off}}$, silica	$\nu_{\text{cut off}}$, water
x: radial	650 nm(84 nm)	700 kHz	7 MHz
y: polar	1435 nm	140 kHz	24 kHz
z: azimuthal	$\sim 200\,\mu$m	7 Hz	1 Hz

By convention, we name the directions $\{x, y, z\}$ in ascending order from short to long and denote the characteristic lengths with $\{\sigma_x, \sigma_y, \sigma_z\}$ (, which are not necessarily the full width half maxima). In our calculation we will show that the TRN spectrum shows a different ω-dependence within each interval defined by the corner frequencies. Indeed it was shown by Gorodetsky and Grudinin that the TRN at frequencies exceeding the $\nu_x$cutoff is proportional to ω^{-2} [173]. Below, they found a $\omega^{-1/2}$ dependence and it is interesting to note that the result display pathological behavior when $\sigma_y \to \sigma_x$, which could be realized in a microtoroid or a wedge resonator.[1]

In our analysis, we extend the approach and explicitly take the frequency corner set by ν_y into account. We find that the TRN spectrum in the frequency range $[\nu_y, \nu_x]$ is described by a term $\propto \omega^{-1/2}$. For lower frequency, in the interval $[\nu_z, \nu_y]$ the noise "flattens" and is given by a $\log[1/\omega]$ that approaches a constant DC value. The finding suggests that thermal noise at low frequency is less intense than predicted by the $\omega^{-1/2}$ law, which is all the more important for sensing purposes as the relevant time regime is slower that ν_y^{-1} in silica.

As starting point we chose Equation (9) from reference [173].

$$S_{\bar{u}}(\omega) = \frac{4k_B T^2 D}{\rho c_p} \int \frac{d^3\mathbf{q}}{(2\pi)^3} \frac{q^2 \left|G(\mathbf{q})\right|^2}{D^2 q^4 + \omega^2} \tag{5.16}$$

Here $G(\mathbf{q})$ is the Fourier transform of the normalized mode intensity profile.

$$G(\mathbf{q}) = \int d^3\mathbf{r}\ \left|E(\mathbf{r})\right|^2 \exp[i\mathbf{q}\cdot\mathbf{r}] \tag{5.17}$$

Integration over all positive frequencies has to go conform with with the temperature variance inside the averaging volume, given by Equation 5.5.

$$\int_0^\infty \frac{d\omega}{2\pi} S_{\bar{u}}(\omega) = \frac{k_B T^2}{\rho c_p} \int \frac{d^3\mathbf{q}}{(2\pi)^3}\ \left|G(\mathbf{q})\right|^2 \tag{5.18}$$

Hence the effective thermal volume is defined by

$$V_{th}^{-1} = \int \frac{d^3\mathbf{q}}{(2\pi)^3}\ \left|G(\mathbf{q})\right|^2 = \int d^3\mathbf{r}\ \left|E(\mathbf{r})\right|^4 \Big/ \left(\int d^3\mathbf{r}\ \left|E(\mathbf{r})\right|^2\right)^2. \tag{5.19}$$

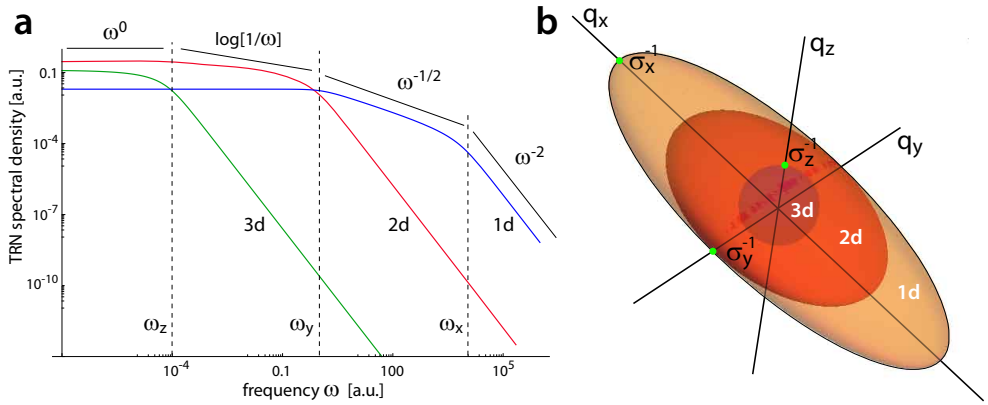

Figure 5.5.: Dimensional analysis of TRN. (a) The solution to the diffusion equation is integrated over the reciprocal mode volume (squared). (b) The mode volume in Fourier space can typically be represented by a flat ellipsoid, when one direction of the mode volume is much larger than the other two, i.e. $\sigma_z \gg \sigma_x, \sigma_y$. As the frequency dependence of the solution to the integral depends critically on the symmetry of the integration volume, we split the ellipsoid into three part, i) a sphere with radius σ_z^{-1}, ii) a disk in 2d with radius σ_y^{-1} and thickness $\propto \sigma_z^{-1}$, and iii) a 1d cigar with length σ_x^{-1}. (a) The solutions display a different dependency on ω according to the dimension of the integral, which becomes important for sensing with microtoroids as the 1d $\leftrightarrow$ 2d transition falls right into the kHz regime. Indeed the flattening of the log-function towards lower frequency, eventually leads to a lower thermo-refractive noise floor on the time scale of interest.

In the following, we try to find an approximation to the integral in Equation 5.16, as it is too complex for direct evaluation. To facilitate Fourier transformation and following our physical intuition, we approximate $|E(\mathbf{r})|^2$ with an ellipsoid. It was shown above that the actual shape of the averaging volume plays a minor role if we consider only a time scale slower than the high frequency cutoff. We therefore write the normalized mode profile

$$|E(\mathbf{r})|^2 = (2\pi)^{-3/2}\,\sigma_x^{-1}\sigma_y^{-1}\sigma_z^{-1}\exp\left[-x^2/2\sigma_x^2 - y^2/2\sigma_y^2 - z^2/2\sigma_z^2\right] \tag{5.20}$$

without any further specification. Then the Fourier transform stays a Gaussian with

$$|G(\mathbf{q})|^2 = \exp\left[-\left(q_x^2\sigma_x^2 + q_y^2\sigma_y^2 + q_z^2\sigma_z^2\right)\right] \tag{5.21}$$

$$\Rightarrow \int d^3\mathbf{q}\,|G(\mathbf{q})|^2 = \frac{\pi^{3/2}}{\sigma_x\sigma_y\sigma_z} \tag{5.22}$$

We now approximate $|G(\mathbf{q})|^2$ with a Heaviside step function, which is justified by the a similar cutoff behavior as it can be seen in Figure 5.4b.

$$|G(\mathbf{q})|^2 \approx \frac{3\sqrt{\pi}}{4}\mathbb{1}_{\left\{q_x^2\sigma_x^2+q_y^2\sigma_y^2+q_z^2\sigma_z^2\leq 1\right\}} \tag{5.23}$$

[1]The experimental results shown in reference [173] use WGM with $|m-l| \geq 3$ in microsphere resonators, such that σ_y (polar extension) is significantly greater than σ_x (radial extension).

Strictly speaking a Gaussian $\propto \exp\left(-x^2/2\sigma^2\right)$ is best approximated by a $\Theta\left(\sqrt{\pi}\sigma - x\right)$, such that it would be more accurate to replace the length parameter by $\sigma_i \rightarrow \sqrt{\pi/2}\sigma_i$. In fact it is this relation, that we used for the approximation of the cut off frequencies in Equation 5.15. Here we keep the calculation simple and therefore do the replacement at the very end of the analysis. Yet we chose a prefactor $3\sqrt{\pi}/4$ to preserve the thermal mode volume V_{th}.
The integral over the blurry Gaussian ellipsoid has now been transformed to an integral of $u(q,\omega)$ on a "solid" ellipsoid. The analytical solution is however still ridiculously complex and requires further simplification. We will see however that the frequency behavior of the integral depends critically on the dimension of the integration volume and it already was already pointed out by Voss and Clarke that the voltage noise in thin metal films on a glass substrate (2d) differs strongly from the one found in bulk material (3d) [172].

Figure 5.5 (b) schematically shows the elliptic integration volume, which is usually flat for a toroid as $\sigma_z \gg \sigma_x, \sigma_y$. To catch the entire behavior of the solution we calculate the integral in Equation 5.16 as the sum of the 3d integral, the 2d integral, and the 1d integral. To this end we divide the (inverse) integration volume into parts displaying 3d and 2d symmetry and the rest (˜1d) respectively. We start out with the approximation and extract the largest volume with three dimensional symmetry from the ellipsoid and integrate thus over a sphere with radius $\sim \sigma_z^{-1}$.

$$I_3 = 4\pi \int_0^{\sigma_z^{-1}} \frac{q^4}{q^4 + \omega^2/D^2}\, dq \tag{5.24}$$

$$\approx 4\pi\sigma_z^{-1}\left(1 + {}^7\!/_{3}\omega/\omega_z\right)^{-2} \tag{5.25}$$

For the first part of the solution we obtain the TRN spectrum of a bulk volume (with blurry edges) that consists of a plateau and a frequency cutoff $\propto \omega^{-2}$. In the next step we integrate over a two dimensional isotropic volume, which consists in our case of the largest disk (with thickness σ_z^{-1}) that fits inside the elliptical integration volume, excluding the interior. Consequently the integral covers radii from σ_z^{-1} to σ_y^{-1}.

$$I_2 = 2\pi\sigma_z^{-1} \int_{\sigma_z^{-1}}^{\sigma_y^{-1}} \frac{q^3}{q^4 + \omega^2/D^2}\, dq \tag{5.26}$$

$$= {}^{\pi}\!/_{2}\sigma_z^{-1} \log\left[\frac{\omega_y^2 + \omega^2}{\omega_z^2 + \omega^2}\right] \tag{5.27}$$

Finally it remains the one dimensional part, where the TRN spectrum is integrated between $[-\sigma_x^{-1}, -\sigma_y^{-1}]$ and $[\sigma_y^{-1}, \sigma_x^{-1}]$

$$I_1 = 2\sigma_z^{-1}\sigma_y^{-1} \int_{\sigma_y^{-1}}^{\sigma_x^{-1}} \frac{q^2}{q^4 + \omega^2/D^2}\, dq \tag{5.28}$$

$$\approx 2\sigma_z^{-1}\left(1 - \frac{\sigma_x}{\sigma_y}\right)\left(1 + \alpha_1\omega/\omega_y\right)^{-1/2}\left(1 + \alpha_2\omega/\omega_x\right)^{-3/2} \tag{5.29}$$

The approximation of the last integral is optimized when the two tuning parameters are chosen $\alpha_1 = 8/\pi^2$ and $\alpha_2 = \left(3\pi\sigma_x^{-2}(\sigma_x^{-1} - \sigma_y^{-1})/(\sigma_x^{-3} - \sigma_y^{-3})/\sqrt{8}\right)^{3/2}$. For simplicity we consider $\alpha_1 = \alpha_2 = 1$ here and the replacement is only done when computing absolute values of TRN. Notably the asymptotic behavior of the solution is $\propto \omega^{-2}$ resulting from the similar cutoff properties of the Gaussian and the Heaviside function.
In Figure 5.5 (a) the contributions of all three part-integrals are plotted – the full TRN spectrum would be given by their sum – and it becomes apparent that the 2d integral I_2 dominates for small frequency $\omega < \omega_x$, while the 1d integral I_1 determines the behavior at larger frequency and the contribution from the 3d integral can usually be neglected. Therefore we consider only I_1 and I_2 in the approximated temperature spectrum.

$$S_{\bar{u}}(\omega) = \frac{k_B T^2}{\rho c_p D} \frac{3\sqrt{\pi}}{8\pi^3} \left[I_2 + I_1\right](\sigma_x, \sigma_y, \sigma_z, \omega) \tag{5.30}$$

In the above approximation a number of crude approximations on the integration volume were made. For example the 1d integral was simply multiplied by σ_y^{-1} to account for the y-extension of the volume, even though the effective width of the ellipse is $\pi/4\sigma_y^{-1}$. On the other hand the overlaying volume from the sphere with $q_y < \sigma_y^{-1}$ was not included in the integral at all. We can estimate the total error of the approximation when calculating the effective thermal volume and comparing to $\int d^3\mathbf{q}/(2\pi)^3 \, |G(\mathbf{q})|^2$, which results in the evaluation of the expression.

$$\zeta_{\mathrm{TRN}} = \frac{3\sqrt{\pi} \int_0^\infty d\omega/2\pi \, \left[I_2 + I_1\right](\sigma_x, \sigma_y, \sigma_z, \omega)}{D \int d^3\mathbf{q} \, |G(\mathbf{q})|^2} \tag{5.31}$$

In contrast to the TRN spectrum in reference [173] the integral over $[I_2 + I_1](\sigma_x, \sigma_y, \sigma_z, \omega)$ converges and obtain a handle to calibrate the spectrum, which results in more accurate absolute values of TRN. To this end we use expression 5.31 as a correction or scaling factor in Equation 5.30 for more accurate calculations as it is required to preserve the total temperature fluctuations. Then, e.g. for comparison with a toroidal microresonator, the inverse mode profile has to be recalculated as the Gaussian approximation in z-direction is not ideal. In particular for a toroid we calculate $\int d^3\mathbf{q} \, |G(\mathbf{q})|^2 = \pi/R_{\mathrm{toroid}}\sigma_y\sigma_x$, with the σs defined according to expression 5.20.

5.3.3. Detection limits for cavity based RI sensors

In this section we discuss the practical implications of thermo-refractive noise on the sensitivity of the sensor. To this end we convert the noise spectral density to an Allan variance using a relation from reference [174], which corresponds to an average of the frequency signal within a rectangular gate function.

$$\sigma_t^2(\tau) = \pi^{-1} \int_0^\infty S_{tt}(\omega) \frac{\sin^4(\omega\tau/2)}{(\omega\tau/2)^2} \, d\omega \tag{5.32}$$

Then the TRN takes a form that can directly be related to a frequency resolution of the sensor. For a better physical understanding, we convert the TRN spectral density piecewise for each frequency interval. Here we start with

$$S_{\bar{u},2}(\omega) = \frac{k_B T^2}{\rho c_p D} \frac{3\sqrt{\pi}}{8\pi^3} \frac{\pi}{2\sigma_z} \zeta_{\mathrm{TRN}}^{-1} \log\left[\frac{\omega_y^2+\omega^2}{\omega_z^2+\omega^2}\right] \tag{5.33}$$

$$\approx \frac{k_B T^2}{\rho c_p D} \frac{3\sqrt{\pi}}{8\pi^2\sigma_z} \zeta_{\mathrm{TRN}}^{-1} \log\left[\frac{\omega_y}{\omega}\right] \tag{5.34}$$

From the noise spectrum, we obtain the Allan variance by integral transformation with a rectangular gate function of temporal width τ , according to Equation 5.32.

$$\Rightarrow \sigma_{\bar{u},2}^2(\tau) = \frac{k_B T^2}{\rho c_p D} \frac{3\sqrt{\pi}}{8\pi^2\sigma_z} \zeta_{\mathrm{TRN}}^{-1} \frac{\pi}{2} \frac{\log(\pi\tau\nu_y) + \gamma_e - 1}{\tau} \tag{5.35}$$

Here γ_e is the Euler constant with the approximate value $\gamma_e \approx 0.577$. From the Allan variance of the temperature with in the mode volume we calculate the Allan deviation of the resonance frequency according to the expression

$$\sigma_{\delta\nu} = n^{-1} \frac{dn}{dT} \sqrt{\sigma_{\bar{u}}^2}\, \nu_0 \tag{5.36}$$

Following the same steps as before we obtain the expression for the TRN at frequencies exceeding ν_y.

$$S_{\bar{u},1}(\omega) = \frac{k_B T^2}{\rho c_p D} \frac{3\sqrt{\pi}}{8\pi^3} \frac{2}{\sigma_z} \zeta_{\mathrm{TRN}}^{-1} \left(1 - \frac{\sigma_x}{\sigma_y}\right) (1 + \omega/\omega_y)^{-1/2} \tag{5.37}$$

$$\approx \frac{k_B T^2}{\rho c_p D} \frac{3\sqrt{D\pi}}{4\pi^3\sigma_y\sigma_z} \zeta_{\mathrm{TRN}}^{-1} \left(1 - \frac{\sigma_x}{\sigma_y}\right) \frac{1}{\sqrt{\omega}} \tag{5.38}$$

And again we transform to the Allan variance.

$$\Rightarrow \sigma_{\bar{u},1}^2(\tau) = \frac{k_B T^2}{\rho c_p D} \frac{3\sqrt{D\pi}}{4\pi^3\sigma_y\sigma_z} \zeta_{\mathrm{TRN}}^{-1} \left(1 - \frac{\sigma_x}{\sigma_y}\right) \frac{4\sqrt{\pi}\left(\sqrt{2}-1\right)}{3} \frac{1}{\sqrt{\tau}} \tag{5.39}$$

$$= \frac{k_B T^2}{\rho c_p \sqrt{D}} \frac{\left(\sqrt{2}-1\right)}{\pi^2\sigma_z\sigma_y} \zeta_{\mathrm{TRN}}^{-1} \left(1 - \frac{\sigma_x}{\sigma_y}\right) \frac{1}{\sqrt{\tau}} \tag{5.40}$$

To compare the theoretical results to the noise levels that we recorded with the microresonator, we numerically evaluate the scaling factor defined in Equation 5.31.

$$\zeta_{\mathrm{TRN}} = 5\,\mathrm{MHz} \cdot \sigma_{\mathrm{z}}^{-1} \mathrm{R}_{\mathrm{toroid}} \sigma_{\mathrm{y}} \sigma_{\mathrm{x}} / \mathrm{D}\pi$$

Inserting the values for the toroid dimensions and the corner frequencies that were defined earlier, we find excellent agreement with the recorded noise curves and a smooth transition between the 2d and 1d TRN contributions.[2] In Figure 5.6 we plot the TRN contributions next to the measured Allan deviation. At the relevant

[2] The σ_y coming from the original integration is replaced by $\sqrt{D/2\pi\nu_y}$, the more accurate corner frequency.

time scale for lipid vesicle adsorption ($\sim 1\,\mathrm{ms}$) we find a noise floor of 20 kHz, which decreases to 7.7 kHz at 10 ms. This noise floor constitutes a fundamental limit in a best case scenario and corresponds to a protein weight of $\sim 220\,\mathrm{kDa}$. Single molecule detection is therefore only possible at a time scale $> 10\,\mathrm{ms}$, where the TRN contribution drops below 10 kHz.

We note that theory suggests that the thermal noise floor is lowered for WGM with $\sigma_x \approx \sigma_y$ by nearly a factor 2. Higher mode confinement, i.e., shorter σ_x, σ_y, does not influence the noise floor in the $\log[1/\omega]$ regime.

A question that remains unanswered so far – and that we are not going to answer here – concerns the correlation between the temperature in the resonator, e.g. in silica, and the temperature fluctuations inside the volume occupied by the evanescent field. The physical experience of a cold window suggests that the thermal contact resistance of a silica water interface is rather low and that there should be considerable correlations. As the coefficient of thermal refraction in water is negative such correlation could even lead to an overall reduction of TRN. On the other hand heat convection and water flow could destroy the correlation. The problem becomes all the more important as the thermal fluctuations in water are considerable. The calculation would however go far beyond the scope of this thesis and we leave it as a starting point for future considerations on the sensitivity limits of cavity based RI sensors.

Noise cancellation scheme

As it was just mentioned, single molecule sensitivity requires a scheme that detects and eliminates TRN. To achieve this one could implement a scheme based on a differential measurement between a sensing mode with a significant evanescent fraction and a blind mode that is located deeper inside the toroid. Recording the frequency difference between the two modes will cancel the common noise. The cancellation can be achieved, because kHz frequency fluctuation in silica typically extend over the geometric width of the optical mode and one therefore expects significant noise correlations, even if the modes do not fully overlap. In the hypothetical case that the thermal RI fluctuation in silica could be completely canceled by a differential measurement, the TR noise in water would still impose a limit on the sensitivity. We use the relation $(\delta\nu/\nu) = 3\% \cdot (\delta n/n)$, where the 3% reflect the responsivity to a bulk refractive index, to estimate the influence of thermo-refractive fluctuations in water. For $\tau = 1\,\mathrm{ms}$ we find a noise floor of 3.2 kHz which corresponds to the maximum shift of a protein with mass $\sim 90\,\mathrm{kDa}$. This is a conservative estimate, however. Under realistic conditions, one would account for a factor $\times 1.5 - 2$ that is found with small resonators and one would require a signal to noise ratio of at least 3 to identify a single particle event.

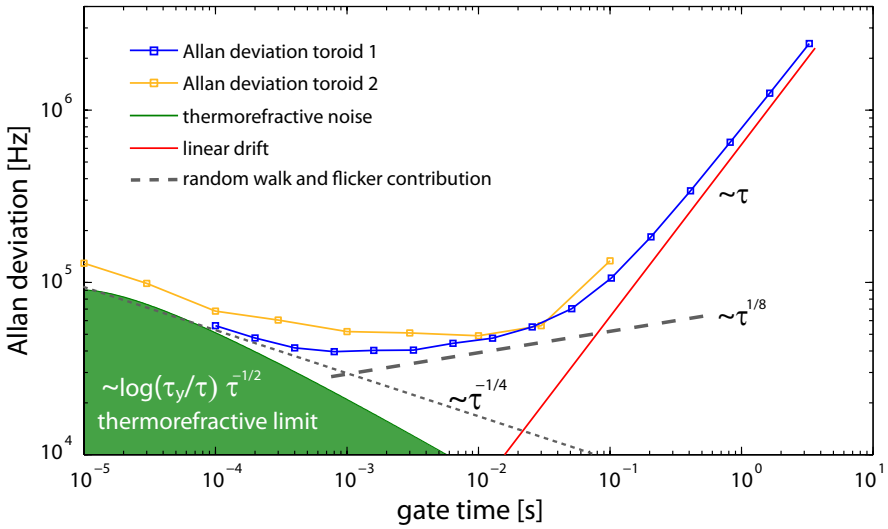

Figure 5.6.: The resolution limit set by thermo-refractive noise. We analyze the high and low frequency components of the cavity noise. On long time scale, the noise is dominated by linear drift. Below 1 ms, the noise rises again, which is an indication for thermo-refractive noise (green curve), proportional to the newly calculated expression 5.35. The dashed line indicates the $\omega^{-1/2}$ law (Equation 5.40), which is however not valid at this time scale and starts to dominate at frequencies exceeding 100 kHz. The blue curve represents data that were taken with the sample used for the IgG measurements. For a different sample we recorded the Allan variance down to a gate time of 10 μs, which illustrates the proportionality to the thermo-refractive noise. The drift contribution (red curve) was manually fitted to the data and does not constitute a fundamental limit. It can be reduced by improved thermal insulation and active temperature control, such that it might be possible to attain single molecule sensitivity at a time resolution of 10 ms. The term proportional to $\tau^{1/8}$ corresponds to the difference between TRN and drift and has yet to be identified. We note that the TRN contribution is normalized to the total temperature fluctuations and that the absolute values should be rather exact.

5.4. Outlook and Summary on Bio-sensing

In summary, we have presented a considerable number of exciting new measurements in cavity based bio-sensing, with unprecedented precision, and which are complemented by the development of a refined theoretical framework that matches the accuracy of the data.
The successful experiments are rooted in a careful development of the experimental setup that was designed from scratch. Milestones of the technical advance include the design of the inverted flow cell device, the transfer of the tapered fiber to the FCD, and the convenient technique of sample handling. Further, a fluidic system, consisting of four interfaced and automated syringe pumps, was installed for deterministic target delivery to the coupling chamber. On the optical side, we set up a reference laser system to eliminate laser noise from the signal, enabeling measurements with highest precision. Efficient vibrational shielding and decoupling, as well as the use of low noise electronics, culminate in a record-shattering resonant wavelength resolution of $\Delta\lambda/\lambda = 7.7 \cdot 10^{-11}$ in the acoustic band for a toroidal microcavity in water.

With such fine-tuned experimental setup at hand, we were able to observe, for the first time, the temporally resolved absorption and spreading of 25 nm lipid vesicles on a silica surface. The measurement constitutes $\times\mathbf{10}$ improvement in frequency resolution and $\times\mathbf{100}$ improvement in temporal resolution, compared to the state of the art. Moreover, we were able to observe hundreds of events during one measurement, which laid the foundation for a meaningful statistical analysis.

To gain a quantitative understanding of the measured frequency shift, and to bring our data into agreement with the theoretical model, we found it necessary to introduce a correction factor of $1/3$ into the existing single particle theory. So far all the experimental results presented in this thesis are in excellent agreement with the correction, and moreover, the model withstands re-evaluation of data published by other groups (cf. appendix B). The theoretical model is universal in a sense that it applies to other sensor types that rely on the reactive mechanism, and as such it potentially has a profound impact on the field of sensing.

In another experimental effort, we turned the sensor surface into a bio-compatible interface by coating it with a single lipid bilayer. Strikingly, we could show that such functionalization only leads to a minor deterioration of the resonators optical quality, which is in stark contrast to conventional methods. The applicability and potential of the technique was demonstrated in a measurement where streptavidin molecules selectively bind to biotinylated lipids in the membrane, and a quantitative understanding is gained from comparison of the ensemble frequency shift with the theoretical model.

Eventually we show that the presence and possibly the dynamics of single molecules, that are too small to be resolved individually, alters the properties of the frequency noise during the measurement. In the experiment we observe an increase in the noise correlation when IgG protein interacts with the evanescent field of the sensor.

Moreover we show that the frequency resolution of the sensor at different time scales is reflected by the Allan deviation of the frequency noise in absence of an analyte.

Our understanding of the resonator's noise properties is corroborated by an in-depth analysis of the thermo-refractive noise for a toroidal resonator geometry at low frequency and we found that a previously neglected term dominates TRN in this regime. Furthermore we confirm that the sensitivity of the device is currently limited by TRN and frequency drift and we are able to give a well-founded estimate on the absolute resolution limit.

Taking a step back and viewing our results in the larger field of label-free single molecule sensing methods, we notice that recently some research groups have turned towards ever smaller transducers – such as metallic nanoparticles or carbon nanotube wires – and demonstrated impressive experimental evidence of single molecule resolution. In fact the size of the transducer approaches the size of the target, and the high sensitivity is founded on an ever smaller mode volume, which comes, however, at the cost of low optical (or electronic) quality.
Here, we took the opposite approach of a larger mode volume and a high-Q resonance, and we gave a clear demonstration that such sensors likewise hold the potential of single molecule resolution, assuming a precisely controlled experimental setup and diligent working habits. The results might encourage others to direct their research in this direction.

Indeed, we believe that our approach will outplay the nano-transducer method on the long run, as it features a number of critical advantages compared to, e.g., plasmonic antennas. Importantly, our sensor features a more than 10^5 times larger active surface area, which abates the difficulty of target delivery. The surface can be functionalized without compromising the optical quality, and a biomimetic interface is established, when the resonator is covered with a single lipid bilayer. In addition, it is important that our method involves only nanowatts of dissipated power and therefore exerts little perturbation, which stands in flagrant contrast to plasmonic and photothermal detection methods, where milliwatts of incident power are involved. Finally, we are able to realize a temporal resolution in the μs-regime, which has not been demonstrated for nanoparticle transducers.[3]

As a matter of fact, we have shown that high time resolution – without the need of several ms to s integration time – turns the one-dimensional information of a single frequency step into a multi-dimensional picture of the particles movement inside the detection volume. It is the authors opinion that this is the path to follow, leading away from proof-of-principle measurements, towards the generation of knowledge in real-world biological applications.

Already today, a large number of biologically relevant questions can be tackled, utilizing our high-Q resonator, even without single molecule resolution. One has to

[3] We explicitly exclude highly specific experiments of the type demonstrated in reference [9], describing the dynamics of a single enzyme attached to a carbon nanotube, which constitute in fact a class of sensors of their own.

bear in mind that an improvement of several orders of magnitude compared to the state of the art, is an immense step forward and does not only allow for more precise measurements, but it makes a whole new range of experiments accessible. Possible measurements include binding and spreading of lipid vesicles onto a supported lipid bilayer, or resolving the interaction of a single virus with a membrane bound receptor. A signal to noise ratio in excess of **100** for an Influenza A virus could reveal previously invisible details of the binding dynamics.
In addition, the frequency noise spectroscopy technique provides a tool for investigation of noise in biological systems. A straight forward to realize measurement could aim at the observation of membrane undulations, possibly as a function of its phase or in the presence of a second constituent.

At the same time, further improvement of the frequency resolution is possible, all the more as we have disclosed that thermo-refractive noise at a time resolution of 10 ms does not impose a limit on single molecule sensitivity. It is the authors opinion that a resolution $< 10\,\mathrm{kHz}$ ($\hat{=} 300\,\mathrm{kDa}$) can be achieved in the next few years.

Part II.

Theoretical cavity optomechanics

6. Cavity opto-mechanics

With this chapter we herald the second part of the thesis. While the first part dealt with a high finesse optical cavity for the detection of biological targets, we now study the coupling of an optical cavity mode to a mechanical degree of freedom. A straight forward implementation of such scheme consists of a Fabry-Pérot cavity with a movable, harmonically suspended back-mirror. Obviously the length of the cavity and thus its resonance frequency depends on the position of the mirror. Reminiscent to the sensing work, the mirror's motion/displacement is monitored via tracking of the resonance frequency, however here at much higher frequency. Typically we deal with mechanical frequencies of a few 100 kHz to some 10 MHz and even up to the low GHz regime [175]. Compared to a bio-sensing experiment, where the interaction is monitored over a relatively broad frequency band ranging from DC to a few 10 kHz (with a few MHz being envisaged), the significantly lower noise level at high frequency changes the nature of the measurement profoundly.

Secondly we consider the effect of backaction. Not only does the resonance frequency of the cavity depend on the mirror position, but the reflected light exerts a force on the mirror. In a photon picture this force can be viewed as a momentum exchange of $2\hbar k$, each time a photon is reflected. Together with the circulating power $P_{\circlearrowleft}$ and the angular frequency of the light ω_p, we calculate the radiation pressure force F^{rp}.

$$F^{\mathrm{rp}} = 2\hbar k \frac{P_{\circlearrowleft}}{\hbar\omega_p} = 2P_{\circlearrowleft}/c$$

Here, c is the speed of light, and we further note that the Planck constant $\hbar$ cancels, suggesting that the effect has a classical origin. This is indeed true and there exist a number of different ways to view radiation pressure, e.g., as the change of stored electromagnetic energy in response to a small mirror movement or as the Lorentz force acting on electrons on the mirror surface. Now we can write down the classical interaction Hamiltonian of the optomechanical system that essentially describes the energy change associated with a mirror displacement x.

$$H_{\mathrm{int}} = x \cdot F^{\mathrm{rp}} = \frac{\hbar\omega_p}{L}\, x \cdot \bar{n}_{\circlearrowleft}$$

We replaced $P_{\circlearrowleft}$ with the stored energy inside the resonator divided by the round trip time in a cavity with length L. The stored energy is expressed in terms of the average number of circulating photons $\bar{n}_{\circlearrowleft}$, which illustrates that the coupling has a non-linear character.
In this chapter, we explore the nature of this *parametric coupling Hamiltonian*, and we will show that it entails a variety of effects, such as the manipulation of the mechanical motion via the light field (namely cooling and heating of the mode). Moreover, a regime of strong coupling exists, where the mechanical mode and the optical cavity field hybridize, despite their vastly different frequencies.

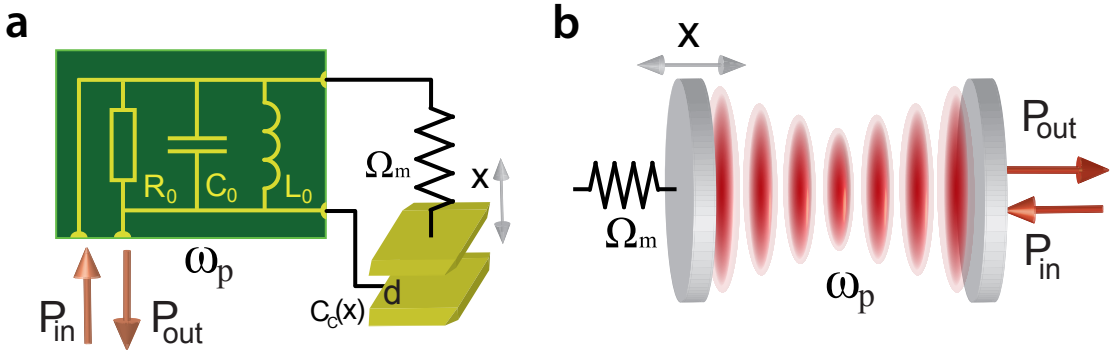

Figure 6.1.: Generic opto- and electro-mechanical schemes. (a) A typical optomechanical scheme consists of an optical cavity with an harmonically suspended back mirror. For small mirror displacements, the resonance frequency depends linearly on the position of the mirror. On the other hand, radiation pressure exerts a force on the mirror that is proportional to the circulating power. (b) An equivalent scheme in the electromechanical domain is given by a capacitor with a movable plate.. Inserted in an LC-circuit, the resonance frequency of the device depends on the distance between the plates. Here backaction results from the attractive force between oppositely charged plates.

6.1. The optomechanical scheme

During the last couple of years, cavity optomechanical systems that parametrically couple a driven high-frequency mode to a high-Q, low-frequency mechanical mode have been subject to increasing investigation [176, 177]. They have been implemented in multiple ways (cf. Figure 6.1). Optomechanical systems have been demonstrated or proposed that couple the mechanical motion to an optical field directly via radiation pressure build up in a cavity [178, 179, 180, 181, 182], or indirectly via quantum dots [183] or ions [184]. On the other hand, in the electromechanical domain, this has been realized or proposed using devices such as (superconducting) single electron transistors [185, 186], LC circuits [187], a sapphire parametric transducer [188], Cooper pair boxes [189, 190], or a stripline microwave resonator [191].

Importantly, the parametric coupling can not only be used for highly sensitive readout of mechanical motion [178] but also by virtue of *dynamical backaction* be used to cool the mechanical oscillator. The effect was predicted decades ago by Vladimir Braginsky [178, 192] and cooling is achieved when the cavity is driven red-detuned from the resonance, i.e., $\Delta = \omega_p - \omega_0 < 0$. In the so called Doppler regime, where the electric field inside the cavity decays faster that one mechanical oscillation period, such detuning leads to a phase lag between the mechanical motion and the radiation pressure force, in a way that F^{rp} counteracts the movement of the oscillator and effectively leads to damping. Notably the phase lag can be turned around when pumping blue detuned from the resonance (i.e., $\Delta > 0$), which results in parametric amplification [179].

However this simple picture cannot be sustained for high-Q optical cavities that feature photon life times in excess of 100 ns, such that a photon inside the cavities experiences on average several cycles of the mirror motion. Then the notion that the resonance frequency follows the mirror displacement does not apply anymore and one needs to switch to a picture where the oscillating mirror modulates the phase of the reflected photon and creates frequency sidebands, displaced by the mechanical resonance frequency $\pm\Omega_m$. Correspondingly this regime where the photon lifetime is longer than the mechanical oscillation period, is referred to as the resolved sideband (RSB) regime [193, 176]. Here cooling is achieved when the cavity is driven on the red-detuned sideband, i.e., $\Delta = -\Omega_m$ [194, 195]. As the frequency detuning matches the mechanical resonance frequency, the anti-Stokes process, where a pump photon consumes a phonon and becomes a resonant photon, is greatly enhanced over the reverse process.

$$\begin{aligned} \hbar\omega_p + \hbar\Omega_m &\overset{\text{anti-Stokes}}{\Longrightarrow} \hbar\omega_0 \\ \hbar\omega_p &\overset{\text{Stokes}}{\rightarrow} \hbar\left(\omega_0 - 2\Omega_m\right) + \hbar\Omega_m \end{aligned}$$

The imbalance between the Stokes and anti-Stokes scattering rates results in net cooling of the mechanical mode [181, 180, 182]. The ultimate goal – cooling a mechanical oscillator to its motional ground state – has recently been achieved by Teufel et al. and Chan et al. [196, 197]. For both electro- and optomechanical systems, it has been shown that ground state cooling is only possible in the resolved sideband regime (RSB) where the mechanical resonance frequency exceeds the bandwidth of the driving resonator [198, 199]. This result is analogous to the laser cooling of ions in the "strong binding" regime [200].

Here we show that the cooling of mechanical oscillators in the RSB regime at high driving power can entail the appearance of normal-mode splitting (NMS). NMS — the coupling of two degenerate modes with energy exchange taking place on a timescale faster than the decoherence of each mode — is a phenomenon ubiquitous in both quantum and classical physics. A prominent realization occurs when atoms are coupled to a cavity field, which leads to the splitting of the cavity transmission into a doublet [201]. In addition to atom-photon interactions, NMS also arises in exciton-photon and phonon-photon interactions [202]. NMS has also been observed with "artificial atoms" in circuit QED [203] and single quantum dot cavity QED [204] settings. In these examples the NMS corresponds to a splitting in the energy spectrum of the coupled two-mode system which may be accessed via linear response.

In contrast, the optomechanical NMS studied here involves driving two parametrically coupled modes of vastly different frequencies. Hence, as will be discussed further below, only in a "shifted" [198] rotating-frame representation does the Hamiltonian become analogous to the one characterizing the aforementioned examples. Concomitantly, the splitting, rather than appearing directly in the cavity transmission, manifests itself in the *fluctuation* spectra. This scenario is reminiscent of the single trapped ion realization of the Jaynes-Cummings model [205] with the role of the pseudo-spin now played by the optical (or electrical) mode. Since this type of normal-mode splitting occurs during RSB cooling, we analyze how the onset of NMS

affects and limits cooling in the RSB regime.
Importantly, NMS coincides with the strong coupling regime, where the energy transfer rate between the optical field and the mechanical oscillator exceeds the decoherence rate. As such the regime is prerequisite for studies of non-classical states of motion or entanglement in mechanical objects [184, 206, 207, 208, 209].

The strong coupling regime and observation of NMS was recently achieved by several research teams [210, 211, 212, 213]. Some of these experimental results are highlighted in section 6.2.1.

6.1.1. Theoretical model

We start our analysis from the rotating-frame Hamiltonian

$$\hat{H}' = -\hbar\Delta'\hat{a}_p^\dagger\hat{a}_p + \hbar\Omega_m\hat{a}_m^\dagger\hat{a}_m + \hbar x_0 G\hat{a}_p^\dagger\hat{a}_p(\hat{a}_m + \hat{a}_m^\dagger) + \hbar(s_+\hat{a}_p + s_+^*\hat{a}_p^\dagger)$$

which provides a unified treatment of both a coherently driven optical and electrical resonator (frequency ω_0) coupled to a mechanical oscillator (frequency $\Omega_m \ll \omega_p$). Here $x_0 = \sqrt{\hbar/2m_{eff}\Omega_m}$ is the zero point motion of the mechanical mode, m_{eff} its effective mass, Δ' the detuning of the drive from ω_0, and $\hat{a}_m$ ($\hat{a}_p$) is the annihilation operator for the mechanical (optical or electrical) mode. The dependence of the resonant frequency ω_0 on the mechanical oscillator's deflection x determines the strength of the coupling via $G = \frac{d\omega_0}{dx}|_{x=0}$. The driving rate is given by $|s_+| = \sqrt{P/\hbar\omega_p\tau_{\text{in}}}$, where P denotes the launched input power and τ_{in}^{-1} is the input coupling rate.

We derive the Heisenberg equations of motion for the canonical variables and introduce noise operators $\hat{\xi}_m(t)$ and $\hat{\xi}_p(t)$ weighted with the rates Γ_m and κ that characterize, respectively, the dissipation of the mechanical and optical (or electrical) degree of freedom. Subsequently, we shift the canonical variables to their steady-state values (i.e. $\hat{a}_p \to \alpha + \hat{a}_p$ and $\hat{a}_m \to \beta + \hat{a}_m$) and linearize to obtain the following Heisenberg-Langevin equations[199, 207, 214] :

$$\begin{aligned}\dot{\hat{a}}_p &= \left(i\Delta - \frac{\kappa}{2}\right)\hat{a}_p - i\frac{g_m}{2}\left(\hat{a}_m + \hat{a}_m^\dagger\right) + \sqrt{\kappa}\hat{\xi}_p(t)\,, \\ \dot{\hat{a}}_m &= \left(-i\Omega_m - \frac{\Gamma_m}{2}\right)\hat{a}_m - i\frac{g_m}{2}\left(\hat{a}_p + \hat{a}_p^\dagger\right) + \sqrt{\Gamma_m}\hat{\xi}_m(t).\end{aligned} \tag{6.1}$$

Here, Δ is the detuning with respect to the renormalized resonance and $\Delta < 0$ leads to cooling [198]. The optomechanical coupling rate is given by

$$g_m = 2\alpha x_0 G\,,$$

which is positive by an appropriate choice for the phase of s_+, and $|\alpha|^2$ gives the mean resonator occupation number. A detailed derivation of the coupled quantum Langevin equations is given in section 7.3.
In the case of the mechanical degree of freedom, the rotating wave approximation in

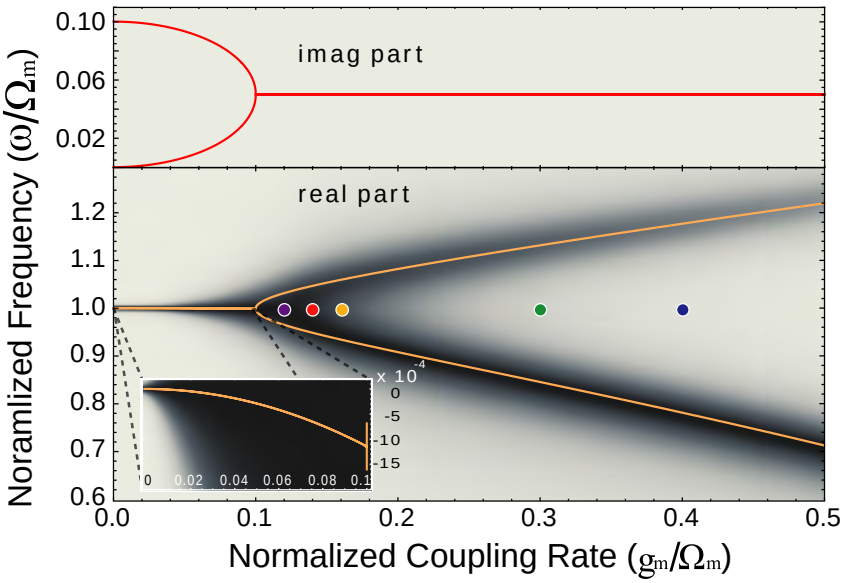

Figure 6.2.: The real and imaginary parts of the eigenvalues are plotted as a function of the optomechanical coupling rate g_m (cf. Equation 6.4 and 6.5). Here the effective detuning and the energy decay rate are $\Delta = -\Omega_m$ and $\kappa/\Omega_m = 0.2$. At the bifurcation, i.e. $g_m = \kappa/2$, the real part of the eigenvalues split into two branches, signaling the appearance of a double peak spectrum. In contrast, the imaginary part takes a constant value of $Im[\omega_\pm] \approx \kappa/4$, which goes along with a saturation of the cooling rate. The inset magnifies the resonance shift before the mode splitting. The background corresponds to the normalized classical displacement spectrum (contribution $\propto n_m$, cf. Equation 6.2) and the broadening of the "shadow" indicates the increased damping of the mechanical mode. Again the saturation of the cooling in the NMS regime can be observed. The colored dots indicate the coupling rates where the spectra in Figure 6.3 were taken.

the coupling to its environment implied by Equations 6.1 is only warranted for high Q values (and small g_m/Ω_m)[207] — conditions that are satisfied in the parameter regime of interest for ground state cooling. The latter also requires $\Gamma_m \ll \kappa$, which we will assume throughout our treatment. Equations (6.1) and their Hermitian conjugates constitute a system of four first-order coupled operator equations, for which the Routh-Hurwitz criterion implies that the system is only stable for $g_m < \sqrt{(\Delta^2 + \kappa^2/4)\,\Omega_m/|\Delta|} \approx \Omega_m$ (if $\Omega_m \gg \kappa$ and $|\Delta| \approx \Omega_m$).

Here, we follow a semi-classical theory by considering *noncommuting* noise operators for the input field, i.e., $\langle \xi_p(t) \rangle = 0$,

$$\langle \hat{\xi}_p^\dagger(t')\hat{\xi}_p(t)\rangle = \bar{n}_p\delta(t'-t),\ \langle \hat{\xi}_p(t')\hat{\xi}_p^\dagger(t)\rangle = (\bar{n}_p+1)\,\delta(t'-t)\,,$$

and a *classical* thermal noise input for the mechanical oscillator, i.e. $\langle \hat{\xi}_m(t)\rangle = 0$, $\langle \hat{\xi}_m^\dagger(t')\hat{\xi}_m(t)\rangle = \langle \hat{\xi}_m(t')\hat{\xi}_m^\dagger(t)\rangle = \bar{n}_m\delta(t'-t)$, in equation 6.1. The quantities $\bar{n}_m$ and $\bar{n}_p$ are the equilibrium occupation numbers for the mechanical and optical (or electrical) oscillators, respectively. We transform to the quadratures (i.e., $\hat{x}/x_0 = \hat{a}_m + \hat{a}_m^\dagger$) and solve the Langevin equations in Fourier space [199]. Thus we recover

a steady-state displacement spectrum [214] given (for $\bar{n}_p = 0$) by

$$S_{xx}(\Omega) = \frac{x_0^2}{2\pi}\Omega_m^2 |\chi_{eff}(\Omega)|^2 \left[\Gamma_m \bar{n}_m - \frac{\Delta^2 + \Omega^2 + \kappa^2/4}{2\Delta\Omega_m}\Gamma_s(\Omega)\right]$$

with the effective susceptibility

$$\chi_{eff}^{-1}(\Omega) = \Omega_m^2 + 2\Omega_m\Omega_s(\Omega) - \Omega^2 - i\Omega\left[\Gamma_m + \Gamma_s(\Omega)\right] \tag{6.2}$$

$$\Omega_s(\Omega) = \frac{g_m^2}{4}\left[\frac{\Omega+\Delta}{(\Omega+\Delta)^2+\kappa^2/4} - \frac{\Omega-\Delta}{(\Omega-\Delta)^2+\kappa^2/4}\right]$$

$$\Gamma_s(\Omega) = \frac{g_m^2}{4\Omega}\left[\frac{\Omega_m\kappa}{(\Omega+\Delta)^2+\kappa^2/4} - \frac{\Omega_m\kappa}{(\Omega-\Delta)^2+\kappa^2/4}\right]. \tag{6.3}$$

This spectrum is characterized by a mechanical susceptibility $\chi_{eff}(\Omega)$ that is driven by thermal noise ($\propto \bar{n}_m$) and by the quantum fluctuations of the radiation pressure (quantum backaction). The latter will be discussed in detail in chapter 7. In linear cooling theory the susceptibility is approximated by evaluating the terms $\Gamma_s(\Omega)$ and $\Omega_s(\Omega)$ at the (bare) mechanical frequency [180, 182, 215]. Then $\Gamma_s(\Omega_m)$ coincides with the cooling rate and is linear in the input power ($g_m^2 \propto P$). In Equation 6.3 the cooling rate is written in a way that highlights its origin as the difference between the Stokes and anti-Stokes scattering rate.

6.2. Parametric normal mode splitting

The above approximation is only adequate for weak driving such that $g_m \ll \kappa$ [198, 199]. To obtain an understanding of the mechanical susceptibility beyond this linear regime, we return to the linearized quantum Langevin equations (cf. Equations 6.1) and calculate the corresponding eigenfrequencies that determine the dynamics of the system. Though there exists an analytical solution, it is rather opaque and does not provide physical insight, so that we will use instead an approximation scheme appropriate for the parameter regime relevant for the observation of NMS and to attain ground state cooling. Along these lines, we focus in the following on: (*i*) the RSB regime ($\kappa \lesssim \Omega_m/2$) necessary for ground state cooling [198, 199, 194], (*ii*) optomechanical coupling $g_m \lesssim \Omega_m/2$, and (*iii*) $\delta^2 \ll \Omega_m^2$ ($\delta \equiv -\Delta - \Omega_m$, the frequency detuning from the lower sideband). For experiments operating in the deeply resolved sideband regime these constraints are typically met.

In the shifted representation – corresponding to Equation 6.1 – the relevant part of the parametric interaction in Hamiltonian H' is described by an effective dipole-like interaction term, i.e.

$$\hbar x_0 G \hat{a}_p^\dagger \hat{a}_p(\hat{a}_m + \hat{a}_m^\dagger) \to \frac{\hbar g_m}{2}(\hat{a}_p + \hat{a}_p^\dagger)(\hat{a}_m + \hat{a}_m^\dagger)$$

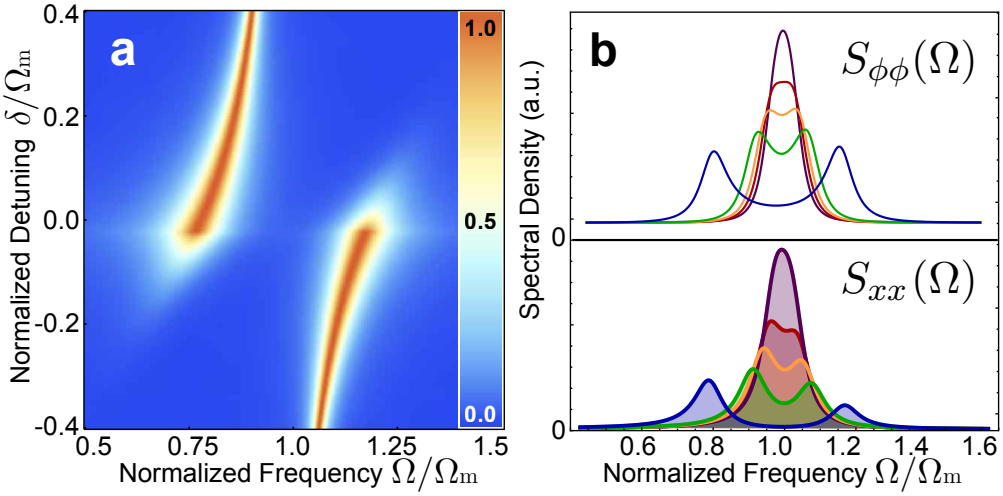

Figure 6.3.: Parametric normal mode splitting. (a) Normalized logarithm of the classical displacement spectrum (contribution $\propto \bar{n}_m$ in Equation 6.2) as a function of the normalized detuning from the lower sideband, plotted for coupling rate $g_m/\Omega_m = 0.4$ that exceeds the energy decay rate $\kappa/\Omega_m = 0.2$ by a factor two. Scanning the drive laser over the red sideband gives rise to an avoided crossing when the condition for resonant sideband cooling is met (i.e. $\delta = 0$). (b) The lower panel shows a series of mechanical displacement spectra for the coupling rates that are given by the dots in Figure 6.2 (i.e. $g_m/\kappa = \{0.6, 0.7, 0.8, 1.5, 2\}$). The curves in the upper panel correspond to the phase spectral density $S_{\phi\phi}(\Omega)$ that is recorded from the output fluctuations in a homodyne detection setting.

after neglecting the nonlinear term. This interaction term is analogous to the Jaynes-Cummings setting (with $\hat{a}_p \to \hat{\sigma}^-$) and naturally leads to resonance splitting when the modes have matching frequencies. When we neglect the off-resonant counter-rotating terms (CRT) $\propto \hat{a}_p^\dagger \hat{a}_m^\dagger$, $\hat{a}_p \hat{a}_m$, we obtain a simplified interaction

$$\frac{\hbar g_m}{2}(\hat{a}_p + \hat{a}_p^\dagger)(\hat{a}_m + \hat{a}_m^\dagger) \to \frac{\hbar g_m}{2}\left(\hat{a}_m^\dagger \hat{a}_p + \hat{a}_p^\dagger \hat{a}_m\right)$$

and the eigenvalues of the corresponding system of equations are readily calculated analytically (i.e., $\omega_\pm^{(0)}$ in Equation 6.4). The counter rotating terms that were neglected here are however known to induce a small frequency shift analogous to the Bloch-Siegert shift in atomic physics [216]. These CRT, which are responsible for the mixing between the creation and annihilation operators in the quantum Langevin equations 6.1, can be treated in perturbation theory within the parameter range defined by (*i*)-(*iii*). The first non-vanishing order in this perturbative expansion is quadratic in the CRT and yields a correction to the decoupled eigenvalues $\omega_\pm \approx \omega_\pm^{(0)} + \omega_\pm^{(2)}$ (note that we take $\Gamma_m = 0$ in $\omega_\pm^{(2)}$):

$$\omega_\pm^{(0)} = \Omega_m + \frac{\delta}{2} - i\frac{\kappa + \Gamma_m}{4} \pm \frac{1}{2}\sqrt{g_m^2 - (\kappa/2 - \Gamma_m/2 + i\delta)^2}\,, \tag{6.4}$$

$$\omega_\pm^{(2)} \approx -\frac{g_m^2/4}{2\Omega_m + \delta \pm \sqrt{g_m^2 - (\kappa/2 + i\delta)^2)}}\,. \tag{6.5}$$

Naturally, there is another pair of eigenfrequencies given by $-\omega_{\pm}^{*}$. In Figure 6.2, the real and imaginary parts of the eigenvalues are plotted. The inset shows the frequency shift ($\omega_{\pm}^{(2)}$) due to the CRT. If we choose the value $\delta = 0$ (i.e., $\Delta = -\Omega_m$) relevant for $\kappa \ll \Omega_m$ (see below) and neglect Γ_m, the square root term of $\omega_{\pm}^{(0)}$ leads to two regimes. While for $g_m < \kappa/2$ the term is fully imaginary and modifies the decay rate of the modes, for $g_m > \kappa/2$ it becomes real instead and the real parts of the eigenfrequencies exhibit the splitting that signals NMS (cf. Figure 6.3). The latter is associated to a mixing between the mechanical mode and the *fluctuation* around the steady-state of the resonator field. Classically, this *fluctuation* can be understood as a beat of the pump photons with the photons scattered on resonance, which leads to oscillations with frequency $|\Delta|$ in the intensity time-averaged over $2\pi/\omega_p$.

For $\kappa^2/4 \ll g_m^2$ the splitting ($\approx g_m$) is proportional to the square root of the mean cavity photon number (α^2). This is analogous to NMS in atomic physics where the splitting of the cavity resonance is proportional to the square root of the number of atoms coupled to the cavity mode [201]. When detecting the phase fluctuations in the transmitted light with a homodyne detection scheme, the signal at Ω_m splits (cf. Figure 6.3b), but the (suppressed) scattered light at the carrier frequency exhibits no splitting. It is important to note that the splitting in the displacement spectrum is not observed unless $g_m > \kappa/\sqrt{2}$, owed to the finite width of the peaks.
Due to the requirements on the cavity bandwidth and the detuning, the parameter regime in which NMS may appear implies cooling. In turn, for a positive detuning (which entails amplification) the observation of NMS is prevented by the onset of the parametric instability [179]. Therefore, a discussion of NMS cannot be decoupled from an analysis of the associated cooling. We also show below that the CRT in the interaction lead to the quantum limit of backaction cooling [199, 198].

6.2.1. Experimental observation of parametric normal mode splitting

Shortly after the publication of the results presented in the previous section (cf. reference [2]), parametric NMS was observed by Gröblacher and co-workers [210]. The authors grew a reflective mirror pad on a doubly clamp beam with a vibrational frequency of $\Omega_m = 2\pi \times 947\,\mathrm{kHz}$. The oscillating mirror formed one end of a 25 mm Fabry-Pérot cavity with a finesse of 14,000 corresponding to an energy decay rate of 215 kHz and thus being well within the RSB parameter regime. Using a strong driving laser beam of $\sim 10\,\mathrm{mW}$, the authors could achieve optomechanical coupling rates up to $g_m \approx 2\pi \times 460\,\mathrm{kHz}$ and observe optomechanical normal mode splitting.

Likewise Teufel and co-workers achieved strong coupling with an electromechanical device [211, 212]. The authors used a drum-like, deformable capacitor, coupled to a microwave resonator with resonance frequencies of $\Omega_m = 2\pi \times 10.69\,\mathrm{MHz}$ and $\omega_0 = 2\pi \times 7.5\,\mathrm{GHz}$ respectively. The microwave resonator feature a total decay rate of $\kappa = 2\pi \times 170\,\mathrm{kHz}$, which corresponds to a sideband resolution of $\Omega_m/\kappa \approx 63$.

As a result of the low loss rate, compared to the mechanical resonance frequency, normal mode splitting can be very well resolved in the system.
On the other hand we will show in the following section that the very same feature limits the cooling performance of the device.

6.3. Dynamical backaction cooling

In this section we use the approximate eigenfrequencies to perform contour integration on the normal ordered mechanical spectrum in order to obtain the final occupancy of the mechanical oscillator

$$n_f = \langle \hat{a}_m^\dagger(\tau)\hat{a}_m(0)\rangle\big|_{\tau=0} \,. \tag{6.6}$$

In this treatment we take both the thermal and the vacuum noise of the driving resonator into account. A finite value for $\bar{n}_p$ may be relevant for electromechanical systems, considering that 1 GHz$\hat{=}$50 mK [187, 191].
Within our approximation scheme we can introduce a formal parameter that tags the CRT and expand n_f in its powers. To zeroth order the poles are determined by the approximate eigenfrequencies $\omega_\pm^{(0)}, -\omega_\pm^{(0)*}$ given in Equation 6.4, and it is straightforward to evaluate $n_f^{(0)}$ (including Γ_m). To second order we use instead the poles $\omega_\pm^{(0)} + \omega_\pm^{(2)}, -\omega_\pm^{(0)*} - \omega_\pm^{(2)*}$. Subsequently, $n_f^{(2)}$ is expanded in the *small* parameters g_m/Ω_m, κ/Ω_m, and $|\delta|/\Omega_m$ up to second order with $\Gamma_m \to 0$. Both $n_f^{(0)}$ and $n_f^{(2)}$ do not contain terms linear in δ, allowing one to directly minimize the result with respect to δ by setting $\delta \to 0$. This yields

$$n_f^{(0)} = \bar{n}_m \frac{\Gamma_m}{\kappa} \frac{g_m^2 + \kappa^2}{g_m^2 + \Gamma_m\kappa} + \frac{g_m^2}{g_m^2 + \Gamma_m\kappa}\bar{n}_p \,, \tag{6.7}$$

$$n_f^{(2)} = \bar{n}_m \frac{\Gamma_m}{\kappa} \frac{g_m^2}{4\Omega_m^2} + \left(\bar{n}_p + \frac{1}{2}\right) \frac{\kappa^2 + 2g_m^2}{8\Omega_m^2} \,. \tag{6.8}$$

The final occupancy $n_f = n_f^{(0)} + n_f^{(2)}$ consists of three contributions. One is proportional to the occupancy of the thermal bath $\bar{n}_m$ and displays linear cooling for $\Gamma_m \ll g_m \ll \kappa$, i.e., $n_f \approx \frac{\Gamma_m}{g_m^2/\kappa}\bar{n}_m$. When g_m approaches κ, deviations from the linear cooling regime become apparent. Indeed, the final occupancy is *always limited* by $n_f \gtrsim \bar{n}_m \frac{\Gamma_m}{\kappa}$, which implies that the largest temperature reduction is bound by the cavity decay rate κ [1]. This is equivalent to the condition

$$Q_m > \bar{n}_m \frac{\Omega_m}{\kappa}$$

for ground state cooling. It is noted that operation in the deeply RSB regime is advantageous to avoid photon-induced heating [194], entailing that the condition on the mechanical Q_m is therefore more stringent.

[1] Note that $n_f^{(0)}$ follows from the classical rate equations for two resonant oscillators (frequency Ω_m) connected, respectively, to two reservoirs at temperatures T_m and $T_{\text{eff}} = T_m\Omega_m/\omega_p$ via

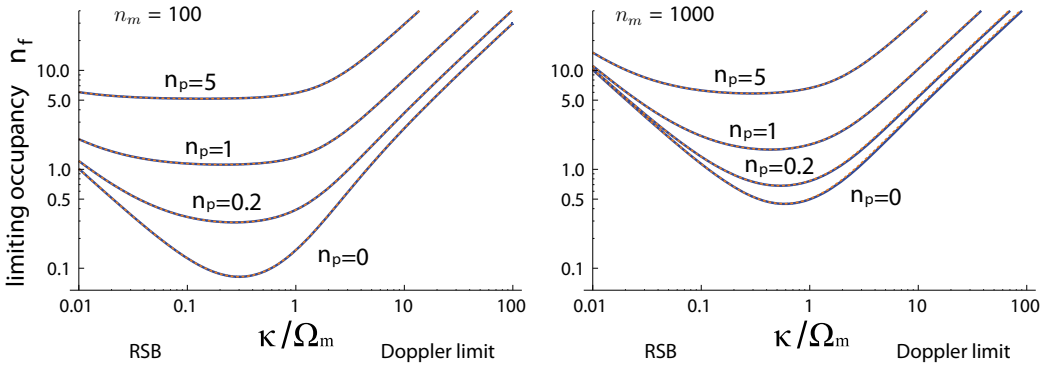

Figure 6.4.: Dynamical backaction cooling of a mechanical mode. The final occupancy of a dynamically cooled mechanical mode is plotted for different parameter settings. On the left hand side the initial thermal occupancy of $n_m = 100$ is in principle sufficient to cool the mechanics below one phonon to its quantum ground state. Here a finite "temperature" of the drive limits n_f. For a quantum limited drive, i.e., $n_p = 0$, the minimum is defined by the so called quantum limit $\kappa^2/16\Omega_m^2$. On the right hand side a higher initial temperature of the mechanics shows a different behavior. Here it is the cavity decay rate κ that sets the cooling limit via $n_f \geq n_m\Gamma_m/\kappa$. This is exemplified by the rise of n_f towards smaller values of κ/Ω_m, i.e., deeper in the RSB regime. It is interesting to note, that it any case there exists an optimal cavity bandwidth κ that allows for maximum cooling.

A second contribution is proportional to the finite occupancy of the driving circuit ($\bar{n}_p$) and corresponds to heating from thermal noise in its input. It implies that it is impossible to cool below the equilibrium occupation of the resonator. If we assume that the mechanical and electromagnetic baths are at the same temperature T_m, it entails $n_f \geq \bar{n}_m \frac{\Omega_m}{\omega_p}$. Last, there is a term in $n_f^{(2)}$ that is temperature-independent and corresponds to heating from quantum backaction noise. This term determines the quantum limit to the final occupancy and agrees with references [199, 198]. Interestingly, in the present analysis the quantum limit arises from the CRT. We note that the trade-off between the quantum limit and the cavity bandwidth limitation leads to an optimal value for κ. Consistent results are obtained with a covariance matrix approach [1].

Finally, we consider appreciable cooling ($n_f \ll \bar{n}_m$ so that we can take $\Gamma_m \to 0$ in the denominator of Equation 6.8) and optimize $n_f^{(0)} + n_f^{(2)}$ with respect to g_m, which yields

$$n_{\mathrm{opt}} \approx \bar{n}_m \frac{\Gamma_m}{\kappa} + \bar{n}_p + \frac{\kappa^2}{16\Omega_m^2} + \sqrt{\frac{\bar{n}_m \Gamma_m \kappa (\bar{n}_p + 1/2)}{\Omega_m^2}} \tag{6.9}$$

at the coupling rate

$$g_{\mathrm{opt}} = \sqrt[4]{4\bar{n}_m \Gamma_m \kappa \Omega_m^2 / [\bar{n}_p + 1/2 + \bar{n}_m \Gamma_m / \kappa]}.$$

rates Γ_m and κ ($\Gamma_m \ll \kappa$), and coupled via heat diffusion with a rate g_m^2/κ. In this picture, the deviation from linear cooling corresponds to heat diffusion from the cavity to the mechanical oscillator.

In the ground state cooling regime, the first three terms of Equation 6.9 always give the correct order of magnitude. Thus, a comparison of g_{opt} with the condition $g_m > \kappa/2$ implies that optimal ground state cooling leads to NMS only when the thermal noise (cf. first term in Equation 6.9) is at least comparable to the quantum backaction noise (cf. third term in Equation 6.9).

7. Multi cavity mode transducers

In the last chapter, we discussed the coupling between a mechanical oscillator and an optical cavity mode and showed how the motion of the mechanics can be manipulated via the light field. Here we extend these considerations to the question how the motion of the mechanical oscillator can actually be measured and how its spectrum is contained in the output fluctuations (e.g. phase and amplitude fluctuations) of the cavity. Indeed the photon shot noise of the light entering (and leaving) the cavity imposes a measurement imprecision, which can be expressed as an equivalent displacement spectral density $S_{xx}^{\mathrm{imp}}(\Omega)$. As a function of the input power, the measurement imprecision manifests a minimum – the so called standard quantum limit (SQL) – where the highest possible readout sensitivity is achieved. Beyond the SQL, the driving of the mechanics from shot noise dominates over the the noise background that is likewise set by photon shot noise.

In this chapter we present a quantum Langevin (QL) approach that describes multiple cavity modes and that allows us to separate the measurement imprecision by its different contributions. We apply the approach to a three resonance transducer (3RT) that relies on three optical resonances coupled to a single mechanical oscillator and where a resonant setting is established, when the spacing of the modes matches the resonance frequency of the mechanics. It is shown that the input power required to reach the SQL (or to reach a given sensitivity before the SQL) can be drastically reduced compared to a single resonance transducer (1RT). Cooling in a two mode scheme is also considered.

Finally we reassess the case of optomechanical cooling and show how the mechanical signal is transduced when the drive is detuned from resonance. In a compact presentation we summarize the most important result, namely that (i) the detuned readout of the motion does not constitute an ideal quantum measurement (according to Caves) such that the imprecision at the SQL is higher than for a resonant readout and (ii) that the ground state displacement uncertainty of the mechanics is established by the quantum properties of the light field.

The chapter starts with a presentation of the major results, reciting reference [3], which is followed by a derivation of the multi-mode quantum Langevin equations and the Gardiner-Collet input-output formalism extended to multiple modes. Next the Heisenberg-Langevin equations (HLE) are solved following a general treatment, which is complemented by its direct implementation in Mathematica code in Appendix E. Evaluation of the code enables the reader to recalculate the results of this chapter (as well as of reference [3]) and to explore the settings beyond their presentation here.

7.1. Theoretical analysis of mechanical displacement measurement using a multiple cavity mode transducer

High frequency nano- and micro-mechanical oscillators have received a high degree of attention recently. They have been used as sensitive detectors, e.g. for spin [217] or particle mass [218], but also carry an intrinsic interest in the study of small scale dissipation of mechanical systems [219], quantum limited motion detection [220], and backaction cooling of vibrational modes [176, 197, 196]. These studies have in common that a sensitive motion transduction is required, which can be implemented by parametric coupling to an optical, electrical, or microwave resonator. The ideal transducer should (i) have a high sensitivity and possibly operate at the standard quantum limit , and (ii) should operate at low power. The latter is experimentally advantageous, as high power may cause excess heating due to intrinsic losses. The former pertains to the minimum uncertainty in motion detection and arises from the trade off between measurement imprecision, inherent to the meter (i.e., detector shot noise), and (for linear continuous measurements) inevitable *quantum backaction* (QBA) [221, 222]. These processes are characterized by the displacement spectral density $\bar{S}_{xx}(\Omega)$ and the QBA force spectral density $\bar{S}_{FF}(\Omega)$.[1] For a parametric motion transducer, where a single cavity mode (with frequency ω_p and energy decay rate κ) is parametrically coupled to a mechanical oscillator [178], the spectral densities are given by

$$\begin{aligned} \bar{S}_{xx}(\Omega) &= \frac{\kappa^2 \hbar \omega_0}{64 G^2 P}\left(1+\frac{4\Omega^2}{\kappa^2}\right) \\ \bar{S}_{FF}(\Omega) &= \frac{16 \hbar G^2 P}{\kappa^2 \omega_0}\left(1+\frac{4\Omega^2}{\kappa^2}\right)^{-1}. \end{aligned} \tag{7.1}$$

Here P is the input power and the optomechanical coupling strength is determined by the cavity frequency shift due to mechanical displacement: $G = \frac{d\omega_0}{dx}$. Equations 7.1 satisfy $\sqrt{S_{xx}^{imp}(\Omega) S_{FF}^{qba}(\Omega)} \geq \hbar/2$, which is a consequence of the Heisenberg uncertainty principle [223]. The canonical way to lower the power to reach the SQL is to increase the cavity finesse, i.e., decreasing κ. However, Equation 7.1 reveals a fundamental deficiency: decreasing κ for fixed P only improves readout sensitivity as long as the mechanical signal (frequency Ω_m) lies within the cavity bandwidth, i.e., $\Omega_m < \kappa$, while for $\Omega_m > \kappa$ the displacement sensitivity experiences saturation. Physically this phenomenon is readily understood; the mechanical motion modulates the cavity field and creates motional sidebands at $\omega_0 \pm \Omega_m$, which constitute the readout signal. For $\kappa \ll \Omega_m$, i.e., in the resolved sideband regime (RSB), the sidebands (and therefore the signal) are suppressed. This regime has recently been subject to experimental investigation [194, 220]. Here we present a readout scheme where this fundamental limitation is overcome, by placing two auxiliary cavity resonances at $\omega_0 \pm \Omega_m$ around the central, driven resonance (cf. Fig. 7.1). This

[1] The bar denotes a symmetrized spectral density: $\bar{S}(\Omega) = 1/2\,(S(\Omega) + S(-\Omega))$.

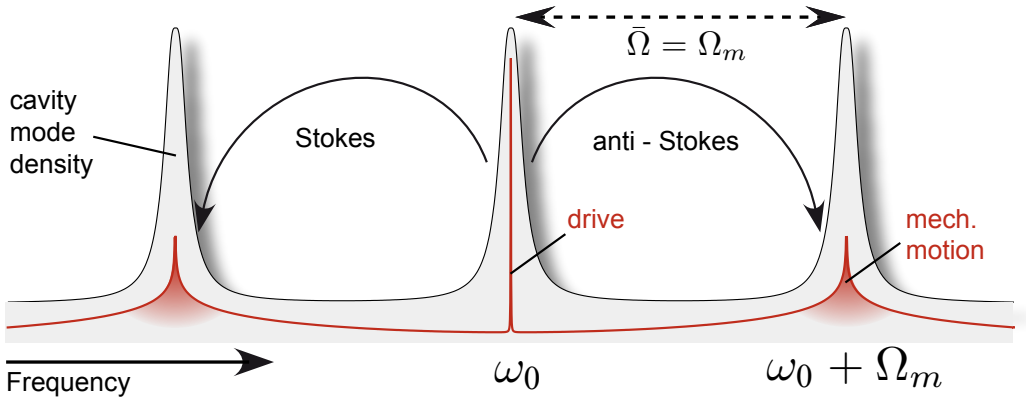

Figure 7.1.: Illustration of the triple mode transducer scheme. The motion of a mechanical mode that is linearly coupled to an optical cavity mode is translated into phase fluctuations at $\omega_p \pm \Omega_m$ when the cavity mode is driven on resonance. The effect can be viewed as Stokes and anti-Stokes scattering of pump photons. However, when the mechanical resonance frequency Ω_m exceeds the cavity linewidth κ, the scattering is strongly suppressed by the cavity cutoff. Introducing additional optical resonances at $\omega_p \pm \Omega_m$ can overcome this deficiency and permits resonant motional side band build-up. In the figure the red curve represents the optical spectrum with the narrow drive on resonance with the central mode and the sidebands reflecting the motion spectrum of the mechanical oscillator.

enables resonant side band build-up and causes a substantial decrease in the power required to reach the SQL. Moreover, we show that this scheme, when applied to the case of two resonances, can lead to quantum backaction interference, without the requirement of having a dissipative parametric coupling [224].

We start our analysis with a presentation of the theoretical framework, to describe multiple cavity modes parametrically coupled to a mechanical degree of freedom, which is characterized by its frequency Ω_m and effective mass m_{eff}. This model covers a wide range of experimental implementations on both nano- and microscale, as well as in the optical and electrical domain. The cavity features several equidistant modes at frequencies $\omega_k = \omega_0 + k \cdot \bar{\Omega}$ ($k \in \mathbb{Z}$), described by the annihilation(creation) operators $\hat{a}_k$ ($\hat{a}_k^\dagger$), where $\bar{\Omega}$ denotes the spacing between adjacent modes. A driving field at frequency ω_p (input power P) is coupled to the central cavity mode. Furthermore the optical modes are parametrically coupled to the mechanical degree of freedom, $\hat{a}_m$ ($\hat{a}_m^\dagger$) and zero point motion $x_0 = \sqrt{\hbar/2m_{\text{eff}}\Omega_{\text{m}}}$, via the interaction Hamiltonian [225]

$$\hat{H}_{\text{int}} = \hbar x_0 \sum_{k,l} G \hat{a}_k^\dagger \hat{a}_l (\hat{a}_m + \hat{a}_m^\dagger). \tag{7.2}$$

The geometric factor, coming from the mode overlap integral, is assumed (for simplicity) to be unity. Cavity damping is modeled by coupling the cavity modes to a harmonic oscillator bath via the damping Hamiltonian

$$\hat{H}_{\text{damp}} = i\hbar \sum_k \int_{-\infty}^{+\infty} d\omega \left[g_k^*(\omega) \hat{b}_\omega \hat{a}_k^\dagger - g_k(\omega) \hat{a}_k \hat{b}_\omega^\dagger \right]. \tag{7.3}$$

The bath operators obey the commutation relations $[\hat{b}_\omega, \hat{b}^\dagger_{\omega'}] = \delta(\omega - \omega')$. In the following we will consider a classical harmonic oscillator characterized by the position $\hat{q} = x_0(\hat{a}_m + \hat{a}^\dagger_m)$ and damping rate Γ_m. This treatment is justified, as we are solely interested in the transduction properties of the cavity, and the quantum backaction coming from the quantized nature of the field.

We eliminate the bath in the Markovian limit [226] setting $g_k(\omega) = \sqrt{\kappa}$. Surprisingly the damping Hamiltonian does not only couple the cavity modes to the dissipative bath, but also couples the modes among each other via the reservoir dynamics (cf. Equation 7.4). This off-resonant interaction is well known in laser theory (where it is responsible for Petermann excess noise [227]), but has (to the authors knowledge) never been applied to the context of opto- or electromechanics.
In the next step, we derive the Heisenberg-Langevin equations (HLE) for the optical modes, where the classical drive is eliminated by moving to a rotating frame at the drive frequency and subsequently transforming to the general quadrature fluctuations $\hat{X}_{k,\theta} \equiv e^{-i\theta}(\hat{a}_k - \langle\hat{a}_k\rangle) + e^{i\theta}(\hat{a}^\dagger_k - \langle\hat{a}^\dagger_k\rangle)$. We emphasize, that choosing one global rotating frame for all modes is essential, as it enables us to treat off-resonant interaction terms (to first order). These are known to account for quantum limits [2]. Explicitly the linearized HLE for the canonical quadrature fluctuations $\hat{X}_k = \hat{X}_{k,\theta=0}$ and $\hat{Y}_k = \hat{X}_{k,\theta=\pi/2}$ are

$$\begin{aligned}
\frac{d}{dt}\hat{X}_k &= -k\cdot\bar{\Omega}\hat{Y}_k - \frac{\kappa}{2}\sum_l \hat{X}_l + \sqrt{\kappa}\delta\hat{X}^{\text{in}}[t] \\
\frac{d}{dt}\hat{Y}_k &= k\cdot\bar{\Omega}\hat{X}_k - \frac{\kappa}{2}\sum_l \hat{Y}_l + g_m\hat{q}[t]/x_0 + \sqrt{\kappa}\delta\hat{Y}^{\text{in}}[t] \\
\frac{d^2}{dt^2}\hat{q} &= -\Gamma_m\frac{d}{dt}\hat{q} - \Omega_m^2\hat{q} + x_0 g_m\sum_l \hat{X}_l.
\end{aligned} \tag{7.4}$$

Solving for the canonical quadratures allows us to transform to the θ-dependent general quadrature. The global phase of the input field is chosen in the way that $\bar{\alpha} = \Sigma\langle\hat{a}_j\rangle$ and the optomechanical coupling rate $g_m = 2Gx_0\bar{\alpha}$ are real.[2] The noise operators in the HLE are δ-correlated: $\langle\delta\hat{X}^{\text{in}}[t]\delta\hat{X}^{\text{in}}[t']\rangle = \langle\delta\hat{Y}^{\text{in}}[t]\delta\hat{Y}^{\text{in}}[t']\rangle = \delta(t-t')$, $\langle\delta\hat{X}^{\text{in}}[t]\delta\hat{Y}^{\text{in}}[t']\rangle = \langle\delta\hat{Y}^{\text{in}}[t]\delta\hat{X}^{\text{in}}[t']\rangle^* = \imath\delta(t-t')$. We can account for intrinsic cavity loss by introducing a second loss channel in Equations 7.4, characterized by the internal loss rate κ_0. It will appear in the results as the degree of overcoupling $\eta_c = \kappa_0/\kappa_{\text{tot}}$, with κ_{tot} being the total cavity decay rate.[3] For multiple cavity modes, the output quadrature fluctuations are given by a generalized input-output relation [228]

$$\hat{X}^{\text{out}}_\theta + \hat{X}^{\text{in}}_\theta = \sqrt{\kappa}\sum_k \hat{X}_{k,\theta} \tag{7.5}$$

[2] This is always possible for a non-squeezed input field.
[3] In the limit of overcoupling, $\eta_c \to 1$.

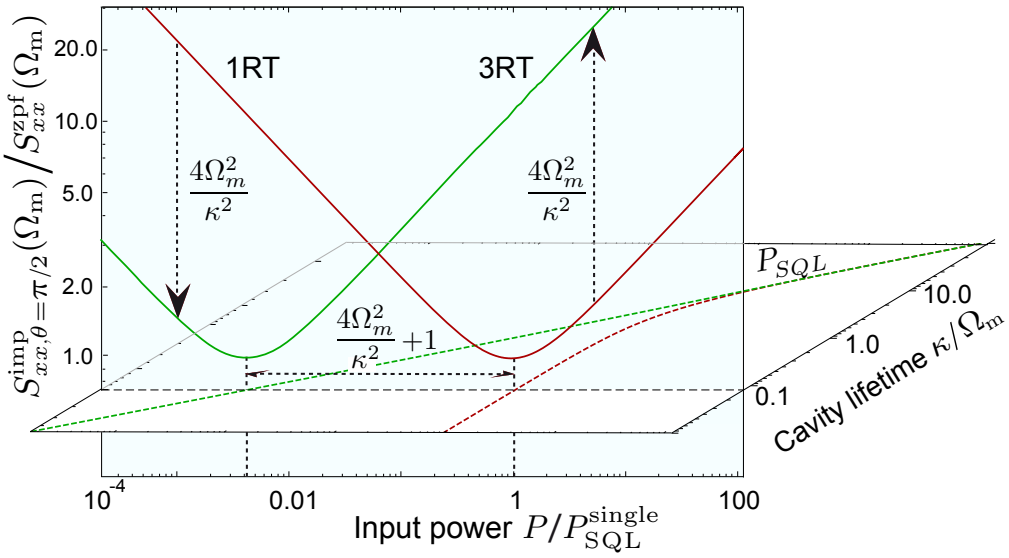

Figure 7.2.: The measurement displacement imprecision spectrum. The vertical plane shows the measurement imprecision $S^{imp}_{xx,\theta=\pi/2}(\Omega_m)$ (normalized to its value at the SQL $S^{imp}_{xx}\big|_{SQL}(\Omega_m) = \hbar|\chi_0(\Omega_m)|$). With increasing input power the shot noise background decreases until – beyond the SQL – quantum backaction starts to dominate and leads to an increase of measurement imprecision. In the resolved sideband regime (here $\kappa = \Omega_m/10$) the SQL is reached at lower input power when triple cavity mode transducer (3RT) is used instead of a single mode transducer (1RT). In the horizontal plane the power at the SQL is plotted as a function of the "sideband resolution" ($\propto \kappa/\Omega_m$). In the Doppler limit, where the three resonances of the 3RT overlap, the power to reach the SQL is the same in both cases, however at an overall higher level. We note that the dissipative coupling terms in Equation 7.4, which are treated in detail in section 7.2.2, ensure the correct description of overlapping cavity modes.

Triple mode transducer

Having introduced the theoretical model, we calculate the output spectrum of a cavity with three optical modes, spaced by the mechanical resonance frequency, i.e. $\bar{\Omega} = \Omega_m$. When the central resonance is driven, side bands at $\omega_0 \pm \Omega_m$, that encode for the mechanical motion, build up efficiently (cf. Figure 7.1) and signal to noise is enhanced.

From Eqs. 7.4 we calculate the quadrature fluctuations in Fourier space. Using the multi-mode input-output relation (Equation 7.5), the spectrum of the output fluctuations is derived. Importantly the off-resonant reservoir coupling terms ($\propto \kappa/2$ in Equations 7.4) preserve a flat shot noise spectrum for the decoupled ($g_m = 0$) cavity. The measurement noise spectrum $S^{imp}_{xx,\theta}(\Omega) = S_{xx,\theta}(\Omega) + |\chi_0(\Omega)|^2 S_{FF}(\Omega)$ is obtained by scaling the output fluctuations to the mechanical signal [229]. The classical motion of the mechanical oscillator, characterized by its bare susceptibility $\chi_0(\Omega)$, is not affected by the coupling, as dynamical backaction effects are absent

[230]. The shot noise background is given by

$$S_{xx,\theta}^{\text{triple}}(\Omega) = \frac{1}{\sin^2\theta}\frac{x_0^2\kappa}{\eta_c g_m^2}\left(1+\frac{4\Omega^2\left(\Omega_m^2-\Omega^2\right)^2}{\kappa^2\left(\Omega_m^2-3\Omega^2\right)^2}\right). \tag{7.6}$$

The sensitivity is maximized for $\theta = \pi/2$, implying that the information on the mechanical signal is encoded in the phase quadrature. Comparing $S_{xx,\theta}^{\text{triple}}(\Omega)$ to the single resonance transducer, we note that the transduction properties of a low frequency signal remain unchanged, i.e., $S_{xx,\theta}^{\text{single}}(0)/S_{xx,\theta}^{\text{triple}}(0) = 1$. However the sensitivity at the mechanical resonance frequency is dramatically increased

$$S_{xx,\theta}^{\text{single}}(\Omega_m)/S_{xx,\theta}^{\text{triple}}(\Omega_m) = 1+\frac{4\Omega_m}{\kappa^2}. \tag{7.7}$$

For systems that operate well into the RSB regime, such as toroidal microresonators [194] or superconducting microwave resonators [220], this factor is more than $\times 100$ and thus represents a major reduction. Based on the Heisenberg uncertainty principle for continuous position measurements, one expects that the enhanced sensitivity also implies an increased quantum backaction force spectral density. Physically these can be viewed as the beat of the carrier (at ω_0) with vacuum fluctuations at $\omega_0 + \Omega_{\text{m}}$, which resonantly heat the mechanical oscillator. The radiation pressure force fluctuations are given by

$$\delta\hat{F}^{\text{rp}}[\Omega] = \frac{\hbar g_m}{2x_0}\sum_k \hat{X}_k[\Omega]. \tag{7.8}$$

Indeed, in the same way, that the shot noise is reduced, the backaction force spectral density $S_{FF}^{\text{triple}}(\Omega)$ is increased, and the Heisenberg limit of the single resonance transducer is recovered.

$$\sqrt{\bar{S}_{xx,\theta=\pi/2}^{\text{triple}}(\Omega)\cdot\bar{S}_{FF}^{\text{triple}}(\Omega)} = \frac{\hbar}{2\sqrt{\eta_c}}. \tag{7.9}$$

We emphasize that the recovery of the Heisenberg limit is a consequence of the off-resonant coupling. Moreover, the triple transducer has the significant advantage over a single cavity mode transducer that the SQL is reached at substantially lower power: $P_{\text{SQL}}^{\text{single}}/P_{\text{SQL}}^{\text{triple}} \approx 4\Omega_m^2/\kappa^2$.[4] Moreover, the enhanced QBA itself can be a valuable resource. Indeed, many quantum optomechanical experiments rely on QBA to be the dominant force noise, such as in experiments relating to ponderomotive squeezing [231] or two beam entanglement [206].

Dual mode scheme

Within the framework of the multi-mode transducer theory, we can also consider the situation of two resonances, spaced by the mechanical resonance frequency [232,

[4] We note, that the mixing term $S_{xF,\theta}^{\text{triple}}(\Omega)$ is odd in Ω for $\theta = \pi/2$ and therefore disappears in the symmetrized spectrum.

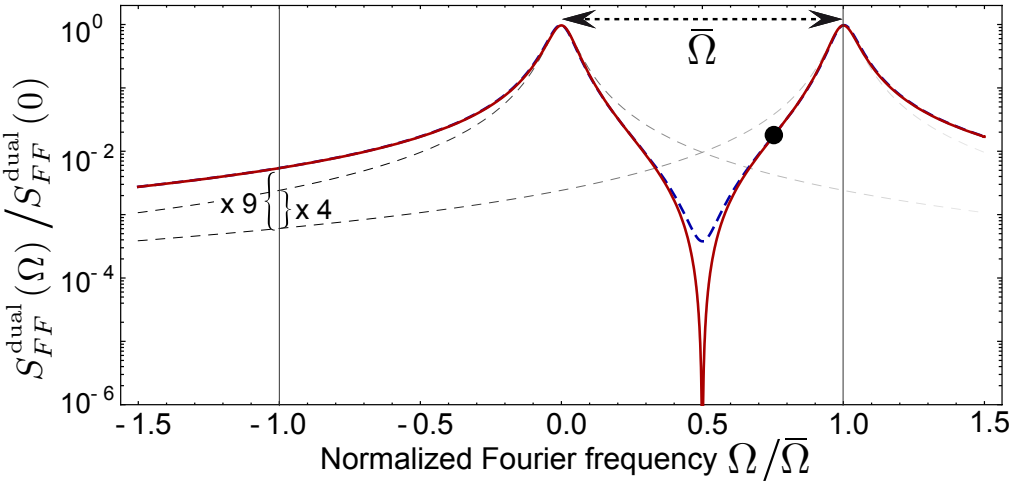

Figure 7.3.: The normalized quantum backaction force spectral density $S_{FF}^{\rm dual}(\Omega)/S_{FF}^{\rm dual}(+\Omega_m)$ (thick solid line) is plotted together with the result from a classical model (thick dashed line). The thin dashed lines correspond to the contributions from the single (uncorrelated) modes. The reservoir interaction between the modes leads to complete noise cancellation at $\Omega = \Omega_m/2$. Here pumping at $\Omega = 0$ (in a rotating frame at ω_p) leads to dynamic backaction cooling of the mechanical mode. The quantum limit is a result of the quantum backaction force spectral density and can be expressed as $S_{FF}^{\rm dual}(-\Omega_m)/S_{FF}^{\rm dual}(+\Omega_m)$. In the case of a single resonance this leads to the previously calculated $\kappa^2/16\Omega_m^2$. In the case of two resonance $S_{FF}^{\rm dual}(-\Omega_m)$ is $\times 9$ larger than for the single mode and the quantum limit is thus $9\kappa^2/16\Omega_m^2$. Interestingly the exists a complete extinction of quantum noise at a frequency exactly between the two optical resonances. We construct a case where $S_{FF}^{\rm dual}(-\tilde{\Omega_m})$ is evaluated at this root and imagine a mechanical oscillator with $\tilde{\Omega_m} = \Omega_m$. Driving the system nominally at 0.25 (indicated by the circle) creates exactly the situation where the quantum limit amounts to zero. A finite linewidth of the mechanical mode and the resulting overlap, lead however to a non-zero, i.e. power depended, limit.

233]. The situation differs from the triple mode scheme, as only the anti-Stokes process is resonantly enhanced by pumping the lower frequency mode. This results in net cooling of the mechanical degree of freedom, because every scattering process annihilates one phonon.[5] Then the response to an external force, e.g. a thermal Langevin force, a signal force, or quantum Langevin forces, is suppressed as a result of the damped mechanical motion. Consequently the transduction properties are not ideal.
Next, we calculate the QBA spectral density from Equation 7.8.

$$S_{FF}^{\rm dual}(\Omega) \;=\; \frac{\hbar^2}{x_0^2}\frac{g_m^2\kappa(\Omega_m-2\Omega)^2}{4(\Omega_m-\Omega)^2\Omega^2+\kappa^2(\Omega_m-2\Omega)^2} \tag{7.10}$$

Then an estimate for the final occupancy of the mechanical mode $n_f = \langle \hat{a}_m^\dagger \hat{a}_m \rangle$ is given by the quantum noise approach [222]. Unexpectedly, compared to the single resonance dynamical backaction cooling [199, 198], the quantum limit increases by

[5] On the other hand, pumping the higher frequency mode results in amplification.

a factor of $\times 9$.

$$\frac{n_f}{n_f+1} = \frac{S_{FF}^{\mathrm{dual}}(-\Omega_m)}{S_{FF}^{\mathrm{dual}}(+\Omega_m)}, \Rightarrow n_f \approx 9\,\frac{\kappa^2}{16\Omega_m^2} \tag{7.11}$$

This is understood from the constructive quantum noise interference at $\Omega = -\Omega_m$ (cf. Figure 7.3, $(\sqrt{1}+\sqrt{4})^2 = 9$). However, the QBA spectrum in Figure 7.3 reveals an additional, striking feature. At $\Omega = \Omega_m/2$ the *quantum noise exactly cancels*. This is a direct consequence of the reservoir coupling terms in Eqs. 7.4. Omitting these terms yields a *classical* interference pattern, shown by the thick dashed curve in Figure 7.3. The shape of the QBA spectrum suggests to tune the mode spacing to $\bar{\Omega} = 4\Omega_m$ and drive the cavity on the red wing of the upper resonance (cf. Figure 7.3, black circle). Then the heating term vanishes, i.e., $S_{FF}^{\mathrm{dual}}(-\Omega_m) = 0$ (in the rotating frame). However, an exact analysis, using a covariance approach [1], reveals that finite line width effects lead to a power dependent quantum limit, i.e. $n_f \approx 2g_m^2/\Omega_{\mathrm{m}}^2$. As the cooling rate saturates, when g_m approaches $\kappa/2$, one can find an upper limit for n_f by assuming $g_m < \kappa/2$ [2]. The same analysis for the canonical two mode cooling yields $n_f \approx (9\kappa^2 + 14g_m^2)/16\Omega_m^2$.

With respect to the transduction properties of the dual scheme we note, that in cooling experiments the QBA is not viewed as additional measurement noise (as for the 3RT), but contributes the signal itself. This is corroborated in the case of ground state cooling, where the field fluctuations conserve the zero point fluctuations of the mechanical oscillator, independently of its quantum nature.

Experimental implementation

The experimental challenge in the design of a multi-mode transducer lies in matching the cavity mode spacing with the resonance frequency of the mechanical oscillator without adding additional damping. The canonical setup is a Fabry-Pérot cavity where the free spectral range matches the resonance frequency of the harmonically suspended back mirror. However difficulties might arise from differing mode overlap integrals. These challenges can be circumvented in a more general way, adaptable to optical, electrical, and microwave domain.

As illustrated in Figure 7.4, three degenerate cavity modes $\{\hat{a}, \hat{b}, \hat{c}\}$ are coupled *in series* via the linear interaction $\hbar g_c \left[\hat{b}(\hat{a}^\dagger + \hat{c}^\dagger) + \hat{b}^\dagger(\hat{a} + \hat{c})\right]$. In the microwave domain, this interaction can be realized by coupling of three superconducting quarter or half wave resonators (via inductive or capacitive coupling as shown in Figure 7.4). In the optical domain, it can be achieved by coupling of degenerate cavity modes via partially transparent mirrors or evanescent field. In addition, only one mode ($\hat{c}$) is coupled to the mechanics by $\hat{H}_{\mathrm{int}}^{\mathrm{single}} = \hbar x_0 G\,\hat{c}^\dagger\hat{c}(\hat{a}_m + \hat{a}_m^\dagger)$. In the regime of strong mode coupling, when $g_c > \kappa$, the originally degenerate cavity modes exhibit normal mode splitting. The new cavity eigenmodes can then be represented in a basis of

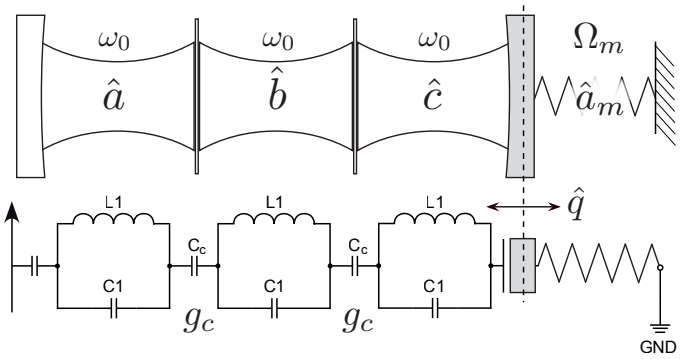

Figure 7.4.: Experimental schemes for the realization of three mode optomechanics. a) Three degenerate optical modes are coupled via semi-transparent mirrors. b) Three LC-oscillators (possibly microwave resonators) are capacitively coupled "in series". While mode $\hat{a}$ is connected to an external drive, i.e., a transmission line, mode $\hat{c}$ is parametrically coupled to a mechanical oscillator. When the coupling rate $g_c > \kappa$ exceeds the individual decay rate, the spectrum exhibits normal mode splitting.

dressed states $\{\hat{a}_0, \hat{a}_+, \hat{a}_-\}$ with eigenfrequencies $\{\omega_0, \omega_0 \pm \sqrt{2}g_c\}$.

$$\begin{pmatrix} \hat{a}_0 \\ \hat{a}_- \\ \hat{a}_+ \end{pmatrix} \propto \begin{pmatrix} 0 & -1 & 1 \\ -1/\sqrt{2} & 1/2 & 1/2 \\ 1/\sqrt{2} & 1/2 & 1/2 \end{pmatrix} \cdot \begin{pmatrix} \hat{a} \\ \hat{b} \\ \hat{c} \end{pmatrix} \tag{7.12}$$

$$\Rightarrow \begin{pmatrix} \hat{a} \\ \hat{b} \\ \hat{c} \end{pmatrix} \propto \begin{pmatrix} 0 & -\sqrt{2} & \sqrt{2} \\ -1 & 1 & 1 \\ 1 & 1 & 1 \end{pmatrix} \cdot \begin{pmatrix} \hat{a}_0 \\ \hat{a}_- \\ \hat{a}_+ \end{pmatrix} \tag{7.13}$$

The splitting $\sqrt{2}g_c$ can be matched to the mechanical resonance frequency by appropriately tuning the coupling rate. Transforming to the dressed state basis, one finds that the operator ($\hat{c} \propto \hat{a}_0 + \hat{a}_- + \hat{a}_+$) is proportional to the sum of the dressed state operators (cf. inverse of matrix in Equation 7.12). Replacing $\hat{c}$ in the parametric interaction $\hat{H}_{\text{int}}^{\text{single}}$ results in a multi-mode interaction as given by Equation 7.2. Indeed, a dual mode coupling of this kind has recently been demonstrated using toroidal microcavities [234] in this proposed way. Moreover, tunable mode splitting between counter propagating modes has also been achieved [235], making the experimental realization of this new class of high frequency transducers realistic.

7.2. General multi-mode formalism

In the last section we have given a comprehensive overview of properties of multi-mode cavity optomechanical system. The derivation is however more complex than suggested by the mere results, and we will therefore supply the full formalism here. First we devote a paragraph to operator definitions and relations, in order to define a convention for signs and factors of 2π. This is followed by the derivation of the multi-mode quantum Langevin equations and the multi-mode input-output formalism.

7.2.1. Definition of operator relations

We start with the definition of the Fourier transform, where the factor $(2\pi)^{-1}$ is included in the back transform.

$$\begin{aligned} f(\Omega) &= \int_{\mathbb{R}} dt\, e^{i\Omega t} f(t) \\ f(t) &= \int_{\mathbb{R}} \frac{d\Omega}{2\pi}\, e^{-i\Omega t} f(\Omega) \end{aligned}$$

Following this definition the Fourier transform of the derivative of a function $f(t)$, that vanishes in its limits (i.e. $\lim_{t\to\pm\infty} f(t) = 0$), is given by:

$$\int_{\mathbb{R}} dt\, e^{i\Omega t} \left(\frac{d}{dt} f(t)\right) = -i\Omega \cdot f(\Omega).$$

The definition is important to avoid sign error when eliminating time derivative by means of a Fourier transform.
Next we derive a couple of operator relations, namely for QL noise operators $\delta\hat{a}^\dagger$ and $\delta\hat{a}$, which stem from the coupling to a dissipative bath and preserve the commutation relations of the corresponding operator over time. Here the δ in front of the operator signal a noise operator with mean zero ($\langle\delta\hat{a}(t)\rangle = 0$). Rules that are also valid for general operators – such as transformation rules – will omit the δ. For all noise operators in this chapter we assume a delta correlation in time. Then the covariances given by

$$\begin{aligned} \left\langle \delta\hat{a}^\dagger(t)\delta\hat{a}(t')\right\rangle &= \bar{n}\cdot\delta(t-t') \\ \left\langle \delta\hat{a}(t)\delta\hat{a}^\dagger(t')\right\rangle &= (\bar{n}+1)\cdot\delta(t-t') \end{aligned}$$

Here the occupation number $\bar{n}$ of the heat bath can be viewed as a classical temperature. When the influence of quantum noise only is investigated, $\bar{n}$ is set to zero $\bar{n}\to 0$. Next we define the Fourier transform of the ladder operators and write the conjugation rules.

$$\begin{aligned} \hat{a}(\Omega) &= \int dt\, e^{i\Omega t}\hat{a}(t) \\ \hat{a}^\dagger(\Omega) &= \int dt\, e^{i\Omega t}\hat{a}^\dagger(t) \\ \Rightarrow [\hat{a}(\Omega)]^\dagger &= \hat{a}^\dagger(-\Omega) \\ \left[\hat{a}^\dagger(\Omega)\right]^\dagger &= \hat{a}(-\Omega) \end{aligned}$$

Then the expectation values in Fourier space are given by the expressions:

$$\begin{aligned} \left\langle \delta\hat{a}^\dagger(\Omega)\delta\hat{a}(\Omega')\right\rangle &= \int dt \int dt'\, e^{i\Omega t} e^{i\Omega' t'} \left\langle \delta\hat{a}^\dagger(t)\delta\hat{a}(t')\right\rangle \\ &= \bar{n}\int dt\, e^{i(\Omega+\Omega')t} \\ &= 2\pi\bar{n}\cdot\delta\left(\Omega+\Omega'\right) \\ \left\langle \delta\hat{a}(\Omega)\delta\hat{a}^\dagger(\Omega')\right\rangle &= 2\pi(\bar{n}+1)\cdot\delta\left(\Omega+\Omega'\right) \end{aligned}$$

Next we define the canonical amplitude and phase quadratures $\hat{X}(\Omega)$ and $\hat{Y}(\Omega)$. It is important to note that we did not include a prefactor $1/\sqrt{2}$, which is typically found in literature and which is certainly correct. Here the factor is omitted to facilitate the calculations. It is re-introduced as a fact $1/2$ when calculating noise spectra.

$$\begin{aligned} \hat{X}(\Omega) &= \hat{a}(\Omega) + \hat{a}^\dagger(\Omega) \\ \hat{Y}(\Omega) &= -i\left(\hat{a}(\Omega) - \hat{a}^\dagger(\Omega)\right) \\ \Rightarrow \left[\hat{X}(\Omega)\right]^\dagger &= \hat{X}(-\Omega) \\ \left[\hat{Y}(\Omega)\right]^\dagger &= \hat{Y}(-\Omega) \end{aligned}$$

The same definitions apply to the quadrature fluctuations in time domain.

$$\begin{aligned} \delta\hat{X}(t) &= \delta\hat{a}(t) + \delta\hat{a}^\dagger(t) \\ \delta\hat{Y}(t) &= -i\left(\delta\hat{a}(t) - \delta\hat{a}^\dagger(t)\right) \\ \Rightarrow 1/2\left\langle\delta\hat{X}(t)\delta\hat{X}(t')\right\rangle &= 1/2\left\langle\left(\delta\hat{a}(t) + \delta\hat{a}^\dagger(t)\right)\left(\delta\hat{a}(t') + \delta\hat{a}^\dagger(t')\right)\right\rangle \\ &= 1/2\left\langle\delta\hat{a}(t)\delta\hat{a}^\dagger(t')\right\rangle + 1/2\left\langle\delta\hat{a}^\dagger(t)\delta\hat{a}(t')\right\rangle \\ &= (\bar{n} + 1/2)\cdot\delta(t-t') \\ 1/2\left\langle\delta\hat{Y}(t)\delta\hat{Y}(t')\right\rangle &= (\bar{n} + 1/2)\cdot\delta(t-t') \end{aligned}$$

It is important to note that there exists a correlation between phase and frequency noise operators that is actually independent of the noise temperature.

$$\begin{aligned} \left\langle\delta\hat{X}(t)\delta\hat{Y}(t')\right\rangle &= -i/2\left\langle\left(\delta\hat{a}(t) + \delta\hat{a}^\dagger(t)\right)\left(\delta\hat{a}(t') - \delta\hat{a}^\dagger(t')\right)\right\rangle \\ &= i/2\left\langle\delta\hat{a}(t)\delta\hat{a}^\dagger(t')\right\rangle - i/2\left\langle\delta\hat{a}^\dagger(t)\delta\hat{a}(t')\right\rangle \\ &= i/2\cdot\delta(t-t') \\ \left\langle\delta\hat{Y}(t)\delta\hat{X}(t')\right\rangle &= -i/2\cdot\delta(t-t') \end{aligned}$$

Before elaborating on this property, we follow the scheme above and calculate the correlations between phase and amplitude noise operators in Fourier space.

$$\begin{aligned} 1/2\left\langle\delta\hat{X}(\Omega)\delta\hat{X}(-\Omega')\right\rangle &= 2\pi\,(\bar{n} + 1/2)\cdot\delta(\Omega - \Omega') \\ 1/2\left\langle\delta\hat{Y}(\Omega)\delta\hat{Y}(-\Omega')\right\rangle &= 2\pi\,(\bar{n} + 1/2)\cdot\delta(\Omega - \Omega') \\ 1/2\left\langle\delta\hat{X}(\Omega)\delta\hat{Y}(-\Omega')\right\rangle &= i\pi\cdot\delta(\Omega - \Omega') \\ 1/2\left\langle\delta\hat{Y}(\Omega)\delta\hat{X}(-\Omega')\right\rangle &= -i\pi\cdot\delta(\Omega - \Omega') \end{aligned}$$

It is important to note, that the correlations between phase fluctuations $\delta\hat{Y}(\Omega)$ and amplitude fluctuation $\delta\hat{X}(\Omega)$ are always odd in frequency and they are lost in the symmetrized spectrum. In our Mathematica algorithm in appendix E these terms

are marked with a parameter `K` that can be set to either zero or one, where zero corresponds to a symmetric spectrum. On the other hand it is exactly these "odd" frequency terms that signal quantum mechanical behavior such as sideband asymmetry [222]. For example, it is the spectral asymmetry of the quantum backaction force that gives rise to QBA heating. More over the non-zero QBA force density at a spectral frequency $\Omega = -\Omega_m$ is the cause for a non-zero quantum limit as it was derived in chapter 6.

7.2.2. Gardiner and Collet formalism for multiple cavity modes

In this section we extend the Gardiner-Collet input-output formalism to multiple cavity modes [226]. The derivation follows the canonical scheme, where dissipation is modeled by coupling to a heat bath of harmonic oscillators. Here we assume a frequency independent coupling constant between each cavity mode and the bath, which is equivalent to the Markov approximation. We will see, that the multi-mode io-formalism correctly deals with overlapping modes. It is noteworthy that the equations were derived before in the framework of lasers featuring non-orthogonal resonator modes, which leads to excess noise and linewidth broadening [236, 237]. Here we start with the Hamiltonian that is written as the sum of the system Hamiltonian, the thermal bath, and a damping Hamiltonian, which describes the interaction of the system with the bath.

$$\mathcal{H} = \mathcal{H}_{\text{sys}} + \mathcal{H}_{\text{bath}} + \mathcal{H}_{\text{damp}} \tag{7.14}$$

Explicitly we consider a system consisting of a number of non-interacting, orthogonal modes $\left\{a_n^\dagger, a_n\right\}$ with frequency ω_n. The heat bath is modeled by a continuum of harmonic oscillators.

$$\mathcal{H}_{\text{sys}} = \sum_{n=1}^{N} \hbar\omega_n \hat{a}_n^\dagger \hat{a}_n \tag{7.15}$$

$$\mathcal{H}_{\text{bath}} = \int_{-\infty}^{+\infty} d\omega\, \hbar\omega b^\dagger(\omega) b(\omega) \tag{7.16}$$

The very general interaction Hamiltonian describes the coupling of each cavity mode to the bath operators.

$$\mathcal{H}_{\text{damp}} = i\hbar \int_{-\infty}^{+\infty} d\omega \sum_{k=1}^{N} \left[g_k^*(\omega) b(\omega) \hat{a}_k^\dagger - g_k(\omega) \hat{a}_k b^\dagger(\omega) \right] \tag{7.17}$$

Then the equation of motion for the bath operators is defined as

$$\dot{b}(\omega) = -i\omega b(\omega) + \sum_{k=1}^{N} g_k(\omega) \hat{a}_k. \tag{7.18}$$

We nominally solve the differential equation for $t > t_0$ and $t < t_0$.

$$b(\omega) = e^{-i\omega(t-t_0)}b_0(\omega) + \int_{t_0}^{t} e^{-i\omega(t-t')} \sum_{k=1}^{N} g_k(\omega)\hat{a}_k(t')\, dt' \tag{7.19}$$

$$b(\omega) = e^{-i\omega(t-t_1)}b_1(\omega) - \int_{t}^{t_1} e^{-i\omega(t-t')} \sum_{k=1}^{N} g_k(\omega)\hat{a}_k(t')\, dt' \tag{7.20}$$

Then we derive the equation of motion for the system operator a_n and replace $b(\omega)$ in the contribution from the bath interaction.

$$\begin{aligned}
\dot{\hat{a}}_n &= -\frac{i}{\hbar}[\hat{a}_n, \mathcal{H}_{\text{sys}}] - \int_{-\infty}^{+\infty} d\omega\, g_n^*(\omega) b(\omega) \\
&= -\frac{i}{\hbar}[\hat{a}_n, \mathcal{H}_{\text{sys}}] - \int_{-\infty}^{+\infty} d\omega\, g_n^*(\omega) e^{-i\omega(t-t_0)} b_0(\omega) \qquad (7.21) \\
&\quad - \int_{-\infty}^{+\infty} d\omega\, g_n^*(\omega) \int_{t_0}^{t} dt'\, e^{-i\omega(t-t')} \sum_{k=1}^{N} g_k(\omega)\hat{a}_k(t') \qquad (7.22)
\end{aligned}$$

Now we assume that $g_n(\omega) \equiv \sqrt{\kappa_n/2\pi}$ is frequency independent. Further the input noise operator $\hat{a}_{in}(t)$ is defined.

$$\hat{a}_{in}(t) = \frac{-1}{\sqrt{2\pi}} \int_{-\infty}^{+\infty} d\omega\, e^{-i\omega(t-t_0)} b_0(\omega) \tag{7.23}$$

Then the equation of motion for $a_n(t)$ becomes:

$$\begin{aligned}
\dot{\hat{a}}_n &= -\frac{i}{\hbar}[\hat{a}_n, \mathcal{H}_{\text{sys}}] + \sqrt{\kappa_n}\hat{a}_{in}(t) - \sum_{k=1}^{N} \sqrt{\kappa_n \kappa_k} \int_{t_0}^{t} dt' \int_{-\infty}^{+\infty} \frac{d\omega}{2\pi}\, e^{-i\omega(t-t')} \hat{a}_k(t') \\
&= -\frac{i}{\hbar}[\hat{a}_n, \mathcal{H}_{\text{sys}}] + \sqrt{\kappa_n}\hat{a}_{in}(t) - \sum_{k=1}^{N} \sqrt{\kappa_n \kappa_k} \int_{t_0}^{t} dt'\, \delta(t-t')\hat{a}_k(t') \\
&= -\frac{i}{\hbar}[\hat{a}_n, \mathcal{H}_{\text{sys}}] - \sum_{k=1}^{N} \frac{\sqrt{\kappa_n \kappa_k}}{2} \hat{a}_k(t) + \sqrt{\kappa_n}\hat{a}_{in}(t) \qquad (7.24)
\end{aligned}$$

In the last line we have derived the Heisenberg-Langevin equations for multiple cavity modes, which was derived before in studies on excess noise [238, 228]. Strikingly, the modes are coupled to each other via the bath. What might seem completely unintuitive at first sight will become clear in an example in the following section. Here we continue with the derivation of the cavity output fluctuations, using the expression for the bath operator at $t > t_0$ and obtain in the same manner as before:

$$\dot{\hat{a}}_n = -\frac{i}{\hbar}[\hat{a}_n, \mathcal{H}_{\text{sys}}] + \sum_{k=1}^{N} \frac{\sqrt{\kappa_n \kappa_k}}{2} \hat{a}_k(t) - \sqrt{\kappa_n}\hat{a}_{out}(t) \tag{7.25}$$

Combining the input and output relations yields the Gardiner-Collet input-output formalism for multiple cavity modes.

$$\hat{a}_{in}(t) + \hat{a}_{out}(t) = \sum_{k=1}^{N} \sqrt{\kappa_k}\hat{a}_k(t) \tag{7.26}$$

Again we see that the cavity modes are combined in a single relation via the dissipative coupling.

7.2.3. Example: two orthogonal cavity modes

In the previous section we have derived the Heisenberg-Langevin equations for multiple, decoupled modes that are however connected to the same loss channel. The result implies that there exists a coupling via the dissipative bath, an intriguing fact, that we will elaborate on here. To this end we imagine an optical cavity with two modes that experience loss only through the output coupler described by the energy decay rate κ. Then we write the multi-mode HLE according to Equation 7.24.

$$\begin{aligned}\frac{d}{dt}\hat{a}_1(t) &= \left(-i\omega_1 - \frac{\kappa}{2}\right)\hat{a}_1(t) - \frac{\kappa}{2}\hat{a}_2(t) + \sqrt{\kappa}\hat{a}_{\text{in}}(t)\\ \frac{d}{dt}\hat{a}_2(t) &= \left(-i\omega_2 - \frac{\kappa}{2}\right)\hat{a}_2(t) - \frac{\kappa}{2}\hat{a}_1(t) + \sqrt{\kappa}\hat{a}_{\text{in}}(t)\end{aligned}$$

The modes are apparently coupled and their dynamics is described by the matrix $\mathbf{S}$.

$$\mathbf{S} = \begin{pmatrix} -i\omega_1 - \frac{\kappa}{2} & -\frac{\kappa}{2} \\ -\frac{\kappa}{2} & -i\omega_2 - \frac{\kappa}{2} \end{pmatrix} \tag{7.27}$$

We solve for the mode operators in Fourier space and find

$$\begin{pmatrix} \hat{a}_1 \\ \hat{a}_2 \end{pmatrix}(\Omega) = -\left[\mathbf{S} + i\Omega\mathbb{1}\right]^{-1}\sqrt{\kappa}\begin{pmatrix} \hat{a}_{\text{in}} \\ \hat{a}_{\text{in}} \end{pmatrix}[\Omega]$$

As both modes are subject to the same noise, the equation is straight for to solve. In resemblance to the input-output formalism in Equation 7.26 for multiple mode we calculate already the sum of the two modes.

$$\sqrt{\kappa}\left(\hat{a}_1 + \hat{a}_1\right)(\Omega) = -\left(\sum_{\text{all}}\left[\mathbf{S} + i\Omega\mathbb{1}\right]^{-1}\right)\kappa\hat{a}_{\text{in}}[\Omega]$$

Here the sum $\sum_{\text{all}}$ denotes the sum of all elements of the matrix. Finally we find the output fluctuations

$$\hat{a}_{\text{out}}[\Omega] = -\left\{\kappa\left(\sum_{\text{all}}\left[\mathbf{S} + i\Omega\mathbb{1}\right]^{-1}\right) + 1\right\}\hat{a}_{\text{in}}[\Omega] \equiv f_2(\Omega)\cdot\hat{a}_{\text{in}}[\Omega]$$

Using the rules defined in section 7.2.1 we find that

$$\hat{a}^{\dagger}_{\mathrm{out}}[\Omega] = f_2^*(-\Omega) \cdot \hat{a}^{\dagger}_{\mathrm{in}}[\Omega]$$

Then the output signal is given as

$$\left\langle \hat{a}_{\mathrm{out}}[\Omega]\hat{a}^{\dagger}_{\mathrm{out}}[\Omega'] \right\rangle = f_2(\Omega)f_2^*(-\Omega') \cdot \delta(\Omega + \Omega')2\pi(n+1)$$

and integration over $\int_{\mathbb{R}} d\Omega'/2\pi$ yields $|f_2(\Omega)|^2 = 1$. The spectrum of the output fluctuations therefore equals the spectrum of the input fluctuations. Of course this makes physical sense and one would not expect anything different, but we remind ourselves that the starting point of the calculation included the non-resonant coupling via the bath.

To gain some insight, we switch off the coupling terms in expression 7.27 and evaluate the problem again. This time we find $|f_2(\Omega)|^2 \neq 1$. Instead it yields 1 plus some complex term that is related to the cavity transmission spectrum. In fact the coupling terms describe the overlapping between two resonances and the coupling derives from the fact, that noise or fluctuations can enter both resonances at the same time. Indeed when the modes are well separated in frequency such that they are off resonance, the coupling terms only play a minor role. However, when there is a significant overlap or even congruence, the dissipative coupling terms maintain the balance.

It is interesting to consider a different possibility of describing multiple cavity modes. A straight forward method involves the complete decoupling of the modes by eliminating the corresponding terms and by using different, uncorrelated input noise operators. This might be justified as the input noise is also delta correlated in frequency space, but as soon as the resonances overlap, one runs into trouble. In particular the total noise level is not preserved.
The author has thought about the problem at length and came to the conclusion that such treatment is simply incorrect, even more when there is an elegant alternative at hand.

Next, we consider the case of a *lossy* cavity with an additional dissipative bath attached. We will show that the formalism can deal with a supplementary noise operator, which is uncorrelated with the input noise. To this end we introduce the parameter η_c, the degree of over coupling, which is defined as the ratio between the loss through the input coupler κ_{in} and the total energy loss rate.

$$\eta_c = \frac{\kappa_{\mathrm{in}}}{\kappa}$$

Correspondingly, the loss through the vacuum channel is described by the rate $\kappa_{\mathrm{vac}} = (1-\eta_c)\kappa$ and $\kappa_{\mathrm{in}} + \kappa_{\mathrm{vac}} = \kappa$.

$$\begin{aligned}\frac{d}{dt}\hat{a}_1(t) &= \left(-i\omega_1 - \frac{\kappa}{2}\right)\hat{a}_1(t) - \frac{\kappa}{2}\hat{a}_2(t) + \sqrt{\eta_c\kappa}\hat{a}_{\text{in}}(t) + \sqrt{(1-\eta_c)\kappa}\hat{a}_{\text{vac}}(t)\\ \frac{d}{dt}\hat{a}_2(t) &= \left(-i\omega_2 - \frac{\kappa}{2}\right)\hat{a}_2(t) - \frac{\kappa}{2}\hat{a}_1(t) + \sqrt{\eta_c\kappa}\hat{a}_{\text{in}}(t) + \sqrt{(1-\eta_c)\kappa}\hat{a}_{\text{vac}}(t)\end{aligned}$$

In brief, going through the exact same analysis as before, we find following expression for the output fluctuations

$$\begin{aligned}\hat{a}_{\text{out}}[\Omega] &= -\left\{\kappa\eta_c\left(\sum_{\text{all}}[\mathbf{S}+i\Omega\mathbb{1}]^{-1}\right)+1\right\}\hat{a}_{\text{in}}[\Omega]\\ &\quad -\kappa\sqrt{\eta_c(1-\eta_c)}\left(\sum_{\text{all}}[\mathbf{S}+i\Omega\mathbb{1}]^{-1}\right)\hat{a}_{\text{vac}}[\Omega]\\ &= \{\eta_c\,(f_2(\Omega)+1)-1\}\cdot\hat{a}_{\text{in}}[\Omega] + \left\{\sqrt{\eta_c(1-\eta_c)}\,(f_2(\Omega)+1)\right\}\cdot\hat{a}_{\text{vac}}[\Omega]\end{aligned}$$

We will not do the calculation here, but rather refer to the appendix E, where we introduce a powerful algorithm to calculate quadrature output fluctuations. The result however is not changed by the additional noise source and we find again $\int d\Omega'/2\pi\cdot\left\langle\hat{a}_{\text{out}}[\Omega]\hat{a}^\dagger_{\text{out}}[\Omega']\right\rangle = 1$.

7.3. Multi-mode cavity optomechanics

In this section we present a short, commented derivation of the quantum Langevin equations (QLE), for several optical modes interacting with a single mechanical oscillator. In particular we consider the case of three equidistant resonances, which was presented in section 7.1. Starting point of the analysis are the Hamiltonians $\hat{H}_0$ for the unperturbed fields and the free mechanical oscillator, and $\hat{H}_{drive}$ that describes the driving of the optical modes by an external, classical field at frequency ω_p with input power $P_{\text{in}} = \hbar\omega_p|s_+|^2$. Finally, the interaction with the mechanics is given by the well known parametric interaction Hamiltonian $\hat{H}_{int}$.

$$\hat{H}_0 = \sum_j \hbar\omega_j\hat{a}_j^\dagger\hat{a}_j + \hbar\Omega_m\hat{a}_m^\dagger\hat{a}_m \tag{7.28}$$

$$\hat{H}_{drive} = \hbar\sqrt{\kappa_{in}}(s_+e^{i\omega_p t+i\phi}\hat{a}_j + s_+^*e^{-i\omega_p t-i\phi}\hat{a}_j^\dagger) \tag{7.29}$$

$$\hat{H}_{int} = \sum_{j,k}\hbar G x_0\zeta_{jk}\hat{a}_j^\dagger\hat{a}_k(\hat{a}_m+\hat{a}_m^\dagger) \tag{7.30}$$

The strength of the optomechanical coupling is defined by the coupling parameter $G = \frac{d\omega_0}{dx}$, describing the linear change of the optical resonance frequency $\omega_0(x)$

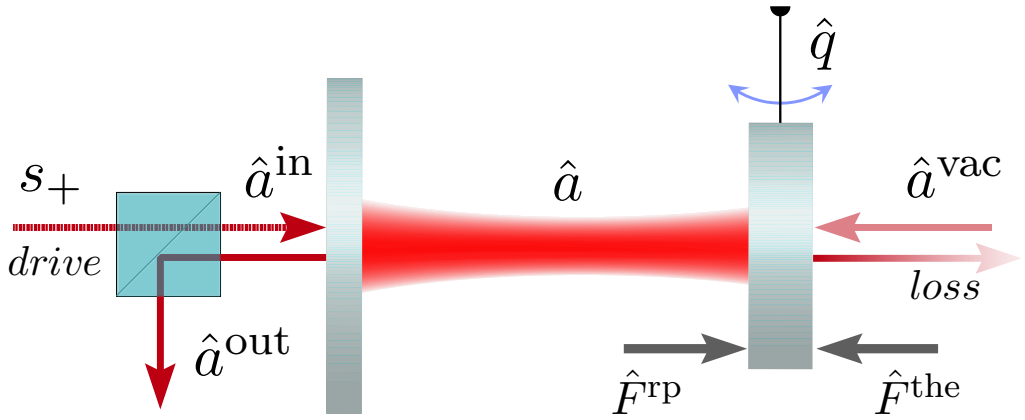

Figure 7.5.: Different noise sources and forces acting on the cavity field and the mechanical oscillator. On the left hand side of the cavity, the coupling mirror acts as a port for the classical (noise-free) driving field s_+ and as a dissipative channel for input noise $\hat{a}^{\text{in}}$. Moreover the output fluctuations $\hat{a}^{\text{out}}$ carry the information on the motion of the mechanics. The mirror on the right hand side represents a secondary dissipative channel that models cavity loss via coupling to vacuum fluctuations $\hat{a}^{\text{vac}}$. The output fluctuations that exit to the continuum do not appear in the calculations, and they represent a net loss of information. Finally the right hand side mirror is harmonically suspended and represents the mechanical oscillator, which is subject to a radiation pressure force $\hat{F}^{\text{rp}}$ and to external forces $\hat{F}^{\text{the}}$, which can be both, coherent or noisy, and shall not be specified further. It is however important to note that $\hat{F}^{\text{the}}$ is not correlated with any of the noises acting on the optical modes.

in response to a small mechanical displacement. Again, x_0 denotes the zero point fluctuations of the mechanical oscillator. A new parameter, exclusive to multi-mode interaction, is the geometric tensor ζ_{jk}, which accounts for the mode overlap between the optical modes, when interacting with the mechanics. In a first order picture one could view the tensor elements ζ_{jk} as overlap integrals, e.g., of the optical modes on a mirror surface. On second thought, it is probable that the actual shape of the mechanical displacement also needs to be taken into account and when we consider a finite speed of sound in the mirror material, the situation can become quite complex.
Here, for simplicity, we assume here that $\zeta_{jk} = 1\,\forall j,k$ and it was shown in Figure 7.4 how such situation can be tailored from hybridization of several modes. Moreover, it seems plausible that there normally exists some sort of overlap between multiple optical cavity modes and the mechanics ,i.e. $\zeta_{jk} > 0\,\forall j,k$. Therefore, setting all overlap parameters to one will grasp more of the physics of the system than setting some parameters to zero or introducing a questionable relation between them. Finally, the approximation is justified, because it is reversible and once the "simple" solution of the multi-mode optomechanical system is understood, we can easily change some parameters in the underlying interaction matrix and see what happens.

Dissipation in the coupled system is introduced via coupling to two dissipative baths, as it was presented in section 7.2.2. As it is illustrated in Figure 7.5, we assume two

loss channels that couple (i) to input noise $\hat{a}^{\text{in}}$ through the coupling port at the rate κ_{in}, and (ii) to vacuum fluctuations $\hat{a}^{\text{vac}}$ at the rate κ_{vac}, which models the intrinsic cavity loss. For these boundary conditions, we write the Langevin equations for the fields and the mechanical oscillator.

$$\begin{aligned}
\frac{d}{dt}\hat{a}_j &= -i\omega_j\hat{a}_j - \frac{\kappa}{2}\sum_k \hat{a}_k - iGx_0(\hat{a}_m + \hat{a}_m^\dagger)\left(\sum_l \hat{a}_l\right) && (7.31)\\
&\quad -i\sqrt{\kappa_{in}}s_+^* e^{-i\omega_p t - i\phi} + \sqrt{\kappa_{\text{vac}}}\hat{a}^{\text{vac}} + \sqrt{\kappa_{\text{in}}}\hat{a}^{\text{in}} && (7.32)\\
\frac{d}{dt}\hat{a}_m &= -i\Omega_m\hat{a}_m - \frac{\Gamma_m}{2}\hat{a}_m - iGx_0\left(\sum_l \hat{a}_l^\dagger\right)\left(\sum_j \hat{a}_j\right) + \sqrt{\Gamma_m}\hat{a}^{\text{the}}
\end{aligned}$$

Next, we move to a rotating frame with $\hat{a}_j \to \hat{a}_j e^{-i\omega_p t}$ and $\hat{a}^{\text{in/vac}} \to \hat{a}^{\text{in/vac}} e^{-i\omega_p t}$. We emphasize, that we chose the same rotating frame for all optical modes. Alternatively one could move to a rotating frame for each mode, as it is done for example in reference [233]. Unless one further simplifies the equations, such treatment renders the evaluation of the output spectrum more difficult, as the contribution of each mode needs to be queried at a different frequency. Equally important, such a method attributes an explicit time dependence to terms that we refer to as off-resonant terms (obviously with the intention to neglect them). Therefore, we chose one rotating frame for all modes and keep the off-resonant terms, because they can have important implications (cf. quantum limit of ground state cooling in chapter 6 as a result of the CRT). Here we denote the detuning of the optical modes by $\Delta_j = \omega_j - \omega_p$.

$$\begin{aligned}
\frac{d}{dt}\hat{a}_j &= -i\Delta_j\hat{a}_j - \frac{\kappa}{2}\sum_k \hat{a}_k - iGx_0(\hat{a}_m + \hat{a}_m^\dagger)\left(\sum_l \hat{a}_l\right) && (7.33)\\
&\quad -i\sqrt{\kappa_{in}}s_+^* e^{-i\phi} + \sqrt{\kappa_{\text{vac}}}\hat{a}^{\text{vac}} + \sqrt{\kappa_{\text{in}}}\hat{a}^{\text{in}} && (7.34)\\
\frac{d}{dt}\hat{a}_m &= -i\Omega_m\hat{a}_m - \frac{\Gamma_m}{2}\hat{a}_m - iGx_0\left(\sum_l \hat{a}_l^\dagger\right)\left(\sum_j \hat{a}_j\right) + \sqrt{\Gamma_m}\hat{a}^{\text{the}}
\end{aligned}$$

In the next step, we derive the steady states with $\langle\hat{a}_j\rangle = \alpha_j$ and $\langle\hat{a}_m\rangle = \beta$ and $\alpha \equiv \sum_j \alpha_j$. The static displacement of the mirror $\beta + \beta^*$, due to the radiation pressure of the pump field, is proportional to the intracavity power.

$$\beta = \frac{-iGx_0|\alpha|^2}{i\Omega_m + \Gamma_m/2} \Rightarrow \beta + \beta^* \approx -2\frac{Gx_0}{\Omega_m}|\alpha|^2 \qquad (7.35)$$

The global phase ϕ can be adjusted in a way that α is real. Then we shift the quantum Langevin equations (which is a unitary transformation [198]) and replace

$\hat{a}_j \to \alpha_j + \hat{a}_j$ and $\hat{a}_m \to \beta + \hat{a}_m$.

$$\begin{aligned}
\frac{d}{dt}\hat{a}_j &= -i\Delta_j\hat{a}_j - \frac{\kappa}{2}\sum_k \hat{a}_k - iGx_0(\hat{a}_m + \hat{a}_m^\dagger)\left(\sum_l \hat{a}_l\right) \\
&\quad +2i\frac{G^2x_0^2\alpha^2}{\Omega_m}\left(\sum_l \hat{a}_l\right) - iGx_0\bar{\alpha}(\hat{a}_m + \hat{a}_m^\dagger) + \sqrt{\kappa_{\text{vac}}}\hat{a}^{\text{vac}} + \sqrt{\kappa_{\text{in}}}\hat{a}^{\text{in}} \\
\frac{d}{dt}\hat{a}_m &= -i\Omega_m\hat{a}_m - \frac{\Gamma_m}{2}\hat{a}_m - iGx_0\left(\sum_l \hat{a}_l^\dagger\right)\left(\sum_j \hat{a}_j\right) \\
&\quad -iGx_0\bar{\alpha}\left(\sum_j \hat{a}_j + \hat{a}_j^\dagger\right) + \sqrt{\Gamma_m}\hat{a}^{\text{the}}
\end{aligned} \tag{7.36}$$

Calculating with the fluctuations only, allows linearization of the system and is sufficient for calculating the measurement imprecision as well as the fluctuations caused by the mechanical displacement. It is worthwhile however to discuss the global phase of the input light that we have used here to obtain a real steady state and which will eventually help us to get rid of the complex dimension. Indeed the phase adjustment is mathematically correct and it is also justified to lump a phase into the noise operators, which only corresponds to an adjustment of an arbitrary time in their definition (cf. Equation 7.23) and which will disappears anyways when the noise is evaluated. On the other hand the phase does play a role, when the spectrum of the output fluctuations is not observed directly, e.g., $\left\langle (\hat{a}^{\text{out}})^\dagger \hat{a}^{\text{out}} \right\rangle$ but rather its beat with a strong local oscillator. This correspond to an expression of the kind $\left\langle e^{-i\phi}\tilde{s}_+^* \hat{a}^{\text{out}} \right\rangle$, where the phase between the input and output fluctuation indeed is important from a theoretical point of view. In the experiment, however, this phase is typically adjustable via some delay and the problem is thus of pathological nature. We now define the optomechanical coupling rate g_m.

$$g_m = 2Gx_0\bar{\alpha}. \tag{7.37}$$

In literature one often encounters an alternative definition of the optomechanical coupling, namely $g = g_m/2$. For consistency with references [2] and [3] we stay with the g_m notation. We then write the final quantum Langevin equations for a multi-mode optomechanical setting.

$$\begin{aligned}
\frac{d}{dt}\hat{a}_j &= -i\Delta_j\hat{a}_j - \frac{\kappa}{2}\sum_k \hat{a}_k + i\frac{g_m^2}{2\Omega_m}\left(\sum_l \hat{a}_l\right) \\
&\quad -i\frac{g_m}{2}(\hat{a}_m + \hat{a}_m^\dagger) + \sqrt{\kappa_{\text{vac}}}\hat{a}^{\text{vac}} + \sqrt{\kappa_{\text{in}}}\hat{a}^{\text{in}} \\
\frac{d}{dt}\hat{a}_m &= -i\Omega_m\hat{a}_m - \frac{\Gamma_m}{2}\hat{a}_m \\
&\quad -i\frac{g_m}{2}\left(\sum_l \hat{a}_l + \hat{a}_l^\dagger\right) + \sqrt{\Gamma_m}\hat{a}^{\text{the}}
\end{aligned} \tag{7.38}$$

In the next step we transform the QLE the canonical quadrature fluctuations. Explicitly we define the amplitude and phase fluctuations as $\hat{X}_j = \hat{a}_j + \hat{a}_j^\dagger$ and $\hat{Y}_j = -i\left(\hat{a}_j - \hat{a}_j^\dagger\right)$. In contrast to most textbooks, we omitted a factor $1/\sqrt{2}$, which is done for convenience. When the spectral densities are evaluated later, the prefactor is re-inserted. Moreover we define the position and momentum quadratures of the mechanical oscillator quadratures by $\hat{q} = -\left(\hat{a}_m + \hat{a}_m^\dagger\right)$ and $\hat{p} = i\left(\hat{a}_m - \hat{a}_m^\dagger\right)$ (the changed sign compared to the definition of the field quadratures assigns a direction). The amplitude and phase noise operators are transformed according to the same rules. Here the abbreviations $\delta\hat{X}$ and $\delta\hat{Y}$ and they comprise input as well as vacuum noise and the prefactors $\sqrt{\kappa_{\mathrm{in/vac}}}$ (which changes the unit).

$$\begin{aligned}
\frac{d}{dt}\hat{X}_j &= \Delta_j\hat{Y}_j - \frac{\kappa}{2}\hat{X}_j - \frac{g_m^2}{2\Omega_m}\left(\sum_l \hat{Y}_l - \delta_{jl}\hat{Y}_j\right) + \delta\hat{X}[t] \qquad (7.39)\\
\frac{d}{dt}\hat{Y}_j &= -\Delta_j\hat{X}_j - \frac{\kappa}{2}\hat{Y}_j + \frac{g_m^2}{2\Omega_m}\left(\sum_l \hat{X}_l - \delta_{jl}\hat{X}_j\right) + g_m\hat{q} + \delta\hat{Y}[t]\\
\frac{d}{dt}\hat{q} &= \Omega_m\hat{p} - \frac{\Gamma_m}{2}\hat{q} + \delta\hat{q}[t]\\
\frac{d}{dt}\hat{p} &= -\Omega_m\hat{q} - \frac{\Gamma_m}{2}\hat{p} + g_m\left(\sum_l \hat{X}_l\right) + \delta\hat{p}[t]
\end{aligned}$$

We note that we were inconsistent in the derivation of the QLE with respect to the treatment of second order contributions. In the Equations 7.38 and 7.39 we kept terms that are $\propto g_m^2$ and should have been discarded due to their small influence but more importantly for consistency. They originate from the static mirror displacement and lead – in the resonant case – to a frequency offset $-\frac{g_m^2}{2\Omega_m}$, which was already included in the definition of the now effective detuning.[6] The other g_m^2-terms lead to a coupling between the modes and the are will be neglected throughout the analysis in this chapter. For an analysis of strong coupling and high intracavity power effects in multi-mode optomechanical setting it can be interesting to include these term and to estimate their influence. For example in the 3RT case they can contribute to a parametric instability due to asymmetric shifting of the resonance frequencies.

7.3.1. Optomechanical multi-mode equations of motion

In this section we derive the output quadrature fluctuations of a cavity coupled to a mechanical oscillator, which amounts in principle to solving Equation 7.26 (multi-mode IO-formalism) with the HL equations defined in 7.39. However to gain physical insight in the problem, we separate the output spectrum into contributions stemming from photon shot noise, quantum backaction, and an external (thermal)

[6] This can be done (and should be done), as the driving laser is *per se* locked to the resonance center.

force acting on the mechanics. Moreover we solve the equations in a very general way for an arbitrary number of optical modes, including an additional loss channel besides the output coupler. The final result is presented in a way that can directly be solved using the computer algebra program Mathematica. The corresponding code is supplied in Appendix E and we recommend switching between this chapter and the appendix or reading them in parallel.

We start the analysis with the definition of the the arbitrary field quadrature $\hat{X}_{j,\theta}$, where the index j corresponds to the "number" of the mode (i.e. $j \in \{1, \ldots, N\}$ for N optical modes) and θ is the quadrature angle.

$$\hat{X}_{j,\theta} = e^{-i\theta}\hat{a}_j + e^{i\theta}\hat{a}_j^\dagger = \cos(\theta)\hat{X}_j + \sin(\theta)\hat{Y}_j \tag{7.40}$$

According to the definition in the previous section, the phase quadrature is obtained when $\theta = \pi/2$ and the amplitude quadrature is recovered at $\theta = 0$. Adjusting the angle θ allows us to study any "mix" of the phase and amplitude quadrature. Again, in contrast to the textbook definition of the quadratures we have omitted a factor $1/\sqrt{2}$, which will be reinserted once the spectral densities are calculated.
With the above definition of the general quadrature, it is sufficient to solve the equations of motion for the canonical quadratures $\hat{X}_j$ and $\hat{Y}_j$. For an arbitrary number of modes it is convenient to introduce the quadrature vector $\vec{X}$.

$$\vec{X} = \left(\hat{X}_0, \hat{Y}_0, \ldots, \hat{X}_j, \hat{Y}_j, \ldots\right)^\mathsf{T}$$

It is important to note that the vector $\vec{X}$ only describes the optical modes. The mechanical degree of freedom will be considered separately at a later point. Next we define the noise acting on the optical modes. It was one of the major findings of section 7.2.2 that all optical modes are subject to the same noise sources and we therefore assign only one pair of input noise operators (i.e. $\hat{X}^{\text{in}}$ and $\hat{Y}^{\text{in}}$) as drive terms to the modes (compared to numbering them with some index j). To include cavity loss, we introduce a second pair of vacuum noise operator, $\hat{X}^{\text{vac}}$ and $\hat{Y}^{\text{vac}}$, that are not correlated with the input noise. One could argue whether the vacuum noise operators acting on different modes are also identical or whether one should assign different, uncorrelated operators to each mode. Such consideration could be motivated by a different spatial mode profile and loss through different scattering centers and they are certainly justified and make physical sense. Here however we will keep the calculation free from too much detail; once the formalism is established it will be relatively straight forward to introduce additional noise sources and loss channels.

The input noise and vacuum noise are coupled via the loss rates κ_{in} and κ_{vac}, respectively, such that the total energy decay rate is given as $\kappa = \kappa_{\text{in}} + \kappa_{\text{vac}}$. Then we write the total noise acting, e.g., on the amplitude quadratures as $\delta\hat{X}^{\text{noise}} = \sqrt{\kappa_{\text{in}}}\hat{X}^{\text{in}} + \sqrt{\kappa_{\text{vac}}}\hat{X}^{\text{vac}}$. Noise acting on the phase quadratures is defined in the same

way. In order to write compact equations and having regard to an efficient implementation later on, we introduce the auxiliary vector $\vec{T}_\theta$.

$$\begin{aligned} \vec{T}_\theta &= \{\cos(\theta), \sin(\theta), \ldots, \cos(\theta), \sin(\theta)\}^\intercal \\ \Rightarrow \vec{T}_0 &= \{1, 0, \ldots, 1, 0\}^\intercal \\ \Rightarrow \vec{T}_{\pi/2} &= \{0, 1, \ldots, 0, 1\}^\intercal \end{aligned} \tag{7.41}$$

The evaluation at 0 and $\pi/2$ is a trick that will be used to address amplitude and phase fluctuations in odd and even rows respectively. We can then define a noise vector $\delta\vec{X}$ that acts a inhomogeneity on the equations of motion of the canonical quadratures.

$$\begin{aligned} \delta\vec{X}^{\text{noise}} &= \vec{T}_0 \cdot \left(\sqrt{\eta_c\kappa}\,\hat{X}^{\text{in}} + \sqrt{(1-\eta_c)\kappa}\,\hat{X}^{\text{vac}}\right) \\ &\quad + \vec{T}_{\pi/2} \cdot \left(\sqrt{\eta_c\kappa}\,\hat{Y}^{\text{in}} + \sqrt{(1-\eta_c)\kappa}\,\hat{Y}^{\text{vac}}\right) \end{aligned} \tag{7.42}$$

Moreover we use the vector $\vec{T}_\theta$ to express the sum of the quadratures – as it appears in the IO-formalism 7.26 – in a compact way (cf. Equation 7.40).

$$\sum_j \hat{X}_{j,\theta}[\Omega] = \sum_j \cos(\theta)\hat{X}_j + \sin(\theta)\hat{Y}_j = \vec{T}_\theta^\intercal \cdot \vec{X}$$

The output fluctuations of the cavity of the cavity are give via the previously derived input-output formalism for multiple-cavity modes.

$$\begin{aligned} \hat{X}_\theta^{\text{out}} &= \left(\sum_j \sqrt{\kappa_{\text{in}}}\,\hat{X}_{j,\theta}\right) - \hat{X}_\theta^{\text{in}} \\ &= \sqrt{\eta_c\kappa}\,\vec{T}_\theta^\intercal \cdot \vec{X} - \hat{X}_\theta^{\text{in}} \\ &\equiv \hat{X}_{x,\theta} + \hat{X}_{F,\theta} + \hat{X}_{m,\theta} \end{aligned} \tag{7.43}$$

In the last line, the output fluctuations are written as the sum of three contributions. $\hat{X}_{x,\theta}$ are the fluctuations that are exclusively associated with the unperturbed cavity field. They reflect the measurement uncertainty due to photon shot noise and remain unchanged when the mechanical oscillator is decoupled from the cavity. $\hat{X}_{F,\theta}$ are the fluctuations arriving from quantum backaction in the measurement of the mechanical oscillators displacement. They amount to the (real) motion of the mechanical oscillator in response to optical noise. Finally $\hat{X}_{m,\theta}$ contains any mechanical motion that is not correlated with the field noise and which is here modeled by the thermal force $\hat{F}^{\text{the}}$. This might be an external signal, such as a cavity length

fluctuation due to gravitational waves, thermal noise, or quantum fluctuation of the mechanical oscillator. We keep it in the calculation to scale the output fluctuations to displacement fluctuations and to derive the transduction function.

Eventually it is our goal to calculate the output fluctuations of the cavity and to identify the contribution contributions that were just discussed.

$$S_{\theta\theta}^{\text{out}}(\Omega) = \int_{\mathbb{R}} \frac{d\Omega'}{2\pi} \langle \hat{X}_\theta^{\text{out}}[\Omega]\, \hat{X}_\theta^{\text{out}}[-\Omega'] \rangle \tag{7.44}$$

When the contribution of the mechanical signal is identified, e.g. $S_{\theta\theta}^{\text{out}}(\Omega) = \ldots + \lambda_\theta(\Omega) \cdot$ "real mechanical motion", we will scale the output fluctuations to obtain a displacement spectral density $S_{xx,\theta}^{\text{out}}(\Omega) = S_\theta^{\text{out}}(\Omega)/\lambda_\theta(\Omega)$.
To achieve this, we have to know the vector $\vec{X}$ containing the quadrature fluctuations, which will be calculated in the following paragraphs.

Full system including the mechanical oscillator

In this section, we set out to solve the quantum Langevin Equations 7.39. This can be done in two ways. In the a straight forward way, and in contrast to the previous definition, we can write the variables as a vector $\vec{X}_M = \left(\hat{X}_0, \hat{Y}_0, \ldots, \hat{X}_j, \hat{Y}_j, \ldots, \hat{q}, \hat{p}\right)^\intercal$ of $2N+2$ elements, which now also includes the mechanical degrees of freedom. Accordingly the noise vector $\delta\vec{X}_M^{\text{noise}}$ is defined.
As mentioned before, we rewrite the Langevin Equations 7.39 in matrix form and thereby defining the matrix $\mathbf{M}$. Then the QLE are rewritten and solved in a compact form.

$$\begin{aligned} \frac{d}{dt}\vec{X}_M &= \mathbf{M} \cdot \vec{X}_M + \delta\vec{X}_M^{\text{noise}} && (7.45) \\ \Rightarrow \vec{X}_M[\Omega] &= -\left[\mathbf{M} + i\Omega\mathbb{1}\right]^{-1} \cdot \delta\vec{X}_M^{\text{noise}}[\Omega] && (7.46) \\ &\equiv \tilde{\mathbf{M}}[\Omega] \cdot \delta\vec{X}_M^{\text{noise}}[\Omega] && (7.47) \end{aligned}$$

Now it is sufficient to take the first $2N$ elements of the vector $\vec{X}_M[\Omega]$ and to insert them into Equation 7.43 to obtain the desired output fluctuations $\hat{X}_\theta^{\text{out}}[\Omega]$ in a brute force manner. There is however a major drawback that comes with the result: (i) it is unnecessarily complex and difficult to simplify, as it includes the parameters from the mechanical oscillator and the optical fields, and (ii) moreover it lacks physical insight as it is not possible to separate, e.g. the photon shot noise from the radiation pressure contribution.

Reduced system with separate description of the mechanics

To overcome these difficulties we chose a more elegant approach and include the mechanical displacement $\hat{q}[t]$ as a parameter (without any further specification) in

the equations that describe only the optical modes. The motion of the mechanics includes however radiation pressure effects as well as any response to an external force.

$$\begin{aligned} \frac{d}{dt}\vec{X} &= \mathbf{S}\cdot\vec{X} + g_m\hat{q}[t]\cdot\vec{T}_{\pi/2} + \delta\vec{X}^{\text{noise}} \\ \Rightarrow \vec{X}[\Omega] &= -\left[\mathbf{S} - i\Omega\mathbb{1}\right]^{-1}\cdot\left(g_m\hat{q}[\Omega]\cdot\vec{T}_{\pi/2} + \delta\vec{X}^{\text{noise}}[\Omega]\right) \\ &\equiv \tilde{\mathbf{S}}[\Omega]\left(g_m\hat{q}[\Omega]\cdot\vec{T}_{\pi/2} + \delta\vec{X}^{\text{noise}}[\Omega]\right) \end{aligned}$$

Again we solved the system of equations in Fourier space via matrix inversion, but this time with two inhomogeneities. Already it is apparent which contributions of the output signal can be attributed to the mechanics and which are solely due to optical noise.

7.3.2. The photon shot noise spectral density

We go back to the input-output relation 7.43 and insert the solution vector for the field quadratures.

$$\begin{aligned} \hat{X}_\theta^{\text{out}}[\Omega] &= \left(\sum_j \sqrt{\eta_c\kappa}\,\hat{X}_{j,\theta}[\Omega]\right) - \hat{X}_\theta^{\text{in}}[\Omega] \\ &= \sqrt{\eta_c\kappa}\,\vec{T}_\theta^{\intercal}\cdot\vec{X}[\Omega] - \hat{X}_\theta^{\text{in}}[\Omega] && (7.48) \\ &= \sqrt{\eta_c\kappa}\,\vec{T}_\theta^{\intercal}\cdot\tilde{\mathbf{S}}[\Omega]\left(g_m\cdot\hat{q}[\Omega]\cdot\vec{T}_{\pi/2} + \delta\vec{X}^{\text{noise}}[\Omega]\right) - \hat{X}_\theta^{\text{in}}[\Omega] && (7.49) \\ &= \left\{\sqrt{\eta_c\kappa}\,\vec{T}_\theta^{\intercal}\cdot\tilde{\mathbf{S}}[\Omega]\cdot\delta\vec{X}^{\text{noise}}[\Omega] - \hat{X}_\theta^{\text{in}}[\Omega]\right\} && (7.50) \\ &\quad + \sqrt{\eta_c\kappa}\vec{T}_\theta^{\intercal}\cdot\tilde{\mathbf{S}}[\Omega]\cdot g_m\hat{q}[\Omega]\cdot\vec{T}_{\pi/2} && (7.51) \\ &\equiv \hat{X}_{x,\theta}[\Omega] + \lambda_\theta(\Omega)\hat{q}[\Omega] \end{aligned}$$

In line 7.50 we have separated the terms adding to $\hat{X}_\theta^{\text{out}}[\Omega]$ into a part the is proportional to the mechanical motion $\hat{q}[\Omega]$ and a second part that is depends only on noise operators directly acting on the cavity field and that we denote with $\hat{X}_\theta^{\text{out}}[\Omega]$ and which constitutes the first part of the sought solution.

Moreover we have defined the transduction function $\lambda_\theta(\Omega)$ that relates the motion of the oscillator the the output fluctuations $\hat{X}_\theta^{\text{out}}[\Omega]$. The θ-dependence indicates, that the mechanical signal is transduced differently to each quadrature. Indeed we will show that an optimal readout "angle" exists. The actual form of $\lambda_\theta(\Omega)$ can be written in a compact way

$$\lambda_\theta(\Omega) = \frac{g_m}{x_0}\sqrt{\eta_c\kappa}\,\vec{T}_\theta^{\intercal}\cdot\tilde{\mathbf{S}}[\Omega]\cdot\vec{T}_{\pi/2} \tag{7.52}$$

The transduction function provides the previously introduced scaling that is required to transform the output fluctuation spectrum to an equivalent displacement spectrum of the mechanics. To this end we introduced the zero point fluctuations x_0 in

the definition of $\lambda_\theta(\Omega)$, which corresponds effectively to a rescaling of the mechanical degrees of freedoms. In Appendix E the Mathematica code for the calculation of the transduction function is supplied.

Moreover we publish code to directly calculate the photon shot noise spectrum from the autocorrelation of $\hat{X}_{x,\theta}[\Omega]$ in Equation 7.50. In the following calculation we simplify the expression for the photon shot noise and rewrite it as a function of the noise operators, such that it resembles the Mathematica code in the appendix and elucidates its functioning.

$$\begin{aligned}\hat{X}_{x,\theta}[\Omega] &= \sqrt{\eta_c\kappa}\,\vec{T}_\theta^{\intercal}\cdot\tilde{\mathbf{S}}[\Omega]\cdot\delta\vec{X}^{\text{noise}}[\Omega]-\hat{X}_\theta^{\text{in}}[\Omega]\\ &= \sqrt{\eta_c\kappa}\,\vec{T}_\theta^{\intercal}\cdot\tilde{\mathbf{S}}[\Omega]\cdot\delta\vec{X}^{\text{noise}}[\Omega]-\cos(\theta)\cdot\hat{X}^{\text{in}}[\Omega]-\sin(\theta)\cdot\hat{Y}^{\text{in}}[\Omega]\end{aligned}$$

Next we insert the definition of the noise vector $\delta\vec{X}^{\text{noise}}[\Omega]$ (which was defined in expression 7.42) and sort the equation by the different noise contributions.

$$\begin{aligned}\hat{X}_{x,\theta}[\Omega] &= \sqrt{\eta_c\kappa}\,\vec{T}_\theta^{\intercal}\cdot\tilde{\mathbf{S}}[\Omega]\cdot\vec{T}_0\left(\sqrt{\eta_c\kappa}\hat{X}^{\text{in}}[\Omega]\right)-\cos(\theta)\cdot\hat{X}^{\text{in}}[\Omega]\\ &+\sqrt{\eta_c\kappa}\,\vec{T}_\theta^{\intercal}\cdot\tilde{\mathbf{S}}[\Omega]\cdot\vec{T}_{\pi/2}\left(\sqrt{\eta_c\kappa}\hat{Y}^{\text{in}}[\Omega]\right)-\sin(\theta)\cdot\hat{Y}^{\text{in}}[\Omega]\\ &+\sqrt{\eta_c\kappa}\,\vec{T}_\theta^{\intercal}\cdot\tilde{\mathbf{S}}[\Omega]\cdot\vec{T}_0\cdot\left(\sqrt{(1-\eta_c)\kappa}\hat{X}^{\text{vac}}[\Omega]\right)\\ &+\sqrt{\eta_c\kappa}\,\vec{T}_\theta^{\intercal}\cdot\tilde{\mathbf{S}}[\Omega]\cdot\vec{T}_{\pi/2}\cdot\left(\sqrt{(1-\eta_c)\kappa}\hat{Y}^{\text{vac}}[\Omega]\right)\end{aligned}$$

Finally we regroup the expression such that it can directly be solved using the Mathematica implementation in appendix E.

$$\begin{aligned}\hat{X}_{x,\theta}[\Omega] &= \left(\eta_c\kappa\,\vec{T}_\theta^{\intercal}\cdot\tilde{\mathbf{S}}[\Omega]\cdot\vec{T}_0-\cos(\theta)\right)\cdot\hat{X}^{\text{in}}[\Omega]+\\ &\left(\eta_c\kappa\,\vec{T}_\theta^{\intercal}\cdot\tilde{\mathbf{S}}[\Omega]\cdot\vec{T}_{\pi/2}-\sin(\theta)\right)\cdot\hat{Y}^{\text{in}}[\Omega]+\\ &\left(\kappa\sqrt{\eta_c(1-\eta_c)}\,\vec{T}_\theta^{\intercal}\cdot\tilde{\mathbf{S}}[\Omega]\cdot\vec{T}_0\right)\cdot\hat{X}^{\text{vac}}[\Omega]+\\ &\left(\kappa\sqrt{\eta_c(1-\eta_c)}\,\vec{T}_\theta^{\intercal}\cdot\tilde{\mathbf{S}}[\Omega]\cdot\vec{T}_{\pi/2}\right)\cdot\hat{Y}^{\text{vac}}[\Omega]\end{aligned}\tag{7.53}$$

We point to the appendix E where the code for the actual calculation is presented. In particular we give an example for the 1RT including vacuum noise (i.e., intrinsic cavity loss) and for the 3RT without vacuum noise. Simple exchange of the matrices that define the system shows however that in any case the output fluctuations are flat and represent the spectrum of the input noise.

$$S_{xx,\theta}(\Omega)=\frac{1}{2}\int_{\mathbb{R}}\frac{d\Omega'}{2\pi}\langle\hat{X}_{x,\theta}[\Omega]\,\hat{X}_{x,\theta}[-\Omega']\rangle=\bar{n}_{\text{in}}+\frac{1}{2}$$

This true as long as the temperature of the two dissipative heat baths (represented by their thermal occupation $\bar{n}_{\text{in}}$ and $\bar{n}_{\text{vac}}$) is equal, i.e. $\bar{n}_{\text{in}}=\bar{n}_{\text{vac}}$. Otherwise

the output spectrum reflects noise filtering through the cavity. In reality the most common case (in optics) will be a quantum limited laser source at the input with $\bar{n}_{\text{in}} = 0 = \bar{n}_{\text{vac}}$. This is typically different for electromechanics systems that rely on microwave resonators at GHz frequencies (1 GHz≙50 mK). Here our approach supplies the flexibility to quickly address these kinds of parameter regimes.

Moreover expression 7.53 clarifies how additional noise sources can be introduced. For example one can imagine some loss mechanism that acts exclusively on the first optical mode and is not correlated with other noises the system. Then one would introduce two more terms that are in principle the same as for the vacuum noise and label the noise operator, e.g., by $\hat{X}^{\text{scat1}}$ and $\hat{Y}^{\text{scat1}}$, and introduce the corresponding coupling rates. The first mode in our example is addressed by replacing the vectors $\vec{T}_0$ and $\vec{T}_{\pi/2}$ by vectors that only show a one in the corresponding field. It is the advantage of the approach that the equations are written in a concise and clean way that changes can readily be made and more complex systems can be explored.

7.3.3. The radiation pressure force spectrum

In this section we calculate the radiation pressure contribution $\hat{q}^{rp}$ contained in the mechanical signal $\hat{q}$. Naturally one obtains the mechanical signal from the matrix $\tilde{\mathbf{M}}[\Omega]$, where $\hat{q}[\Omega]$ is described in the $(2N+1)^{th}$ row. (We remind ourselves that $\tilde{\mathbf{M}}[\Omega]$ is the extended description of the optomechanical system, which includes the cavity modes as well as the mechanical oscillator.) Without further specifying $\tilde{\mathbf{M}}[\Omega]$ we can write

$$\hat{q}[\Omega] = \tilde{\mathbf{M}}_{2N+1} \cdot \delta\vec{X}_M[\Omega] \equiv \hat{q}^{rp}[\Omega] + \chi_{eff}(\Omega)\hat{F}^{\text{the}}[\Omega]. \tag{7.54}$$

Here the radiation pressure part contains all the parts that are proportional to noise operators acting on the optical field quadratures and the rest describes the response to external forces. We point out that the effective susceptibility χ_{eff}, which is also defined by $\tilde{\mathbf{M}}[\Omega]$, includes damping or heating effects that are also a response to the optical field. Yet its influence on the mechanical motion is not considered a radiation pressure signal here and it is thus not contained in $\hat{q}^{rp}$, because it originates from the classical and noise-free portion of the radiation pressure and is as such a deterministic (i.e., time reversible) contribution.

Here the effective susceptibility play a minor role and its knowledge is not required for most of the calculations. It is sufficient to know that $\chi_{eff}(\Omega)\hat{F}^{\text{the}}$ is describes the displacement of the mechanics. In a simplifying way one could say that the last chapter was about $\chi_{eff}(\Omega)$ and its integral, here we are interested in the light fluctuations that limit the resolution of the mechanical signal.

More importantly one could get the impression that in any case the full optomechanical system needs to be solved to obtain the expression for $\tilde{\mathbf{M}}_{2N+1}$ that describes the mechanical response to the radiation pressure. In this case we would have wasted

our time with the initial calculations that involve only the (much simpler) matrix $\tilde{\mathbf{S}}[\Omega]$ for the cavity modes. However strikingly we find that the first $2N$ entries of $\tilde{\mathbf{M}}_{2N+1}$ – exactly the ones that describe the radiation pressure contribution – can be expressed by the matrix $\tilde{\mathbf{S}}[\Omega]$ and the effective susceptibility $\chi_{eff}(\Omega)$ only.

$$\left(\tilde{M}_{2N+1,1},\ \ldots\ ,\tilde{M}_{2N+1,2N}\right) = \chi_{eff}(\Omega)\sum_{j=1}^{N} g_m \tilde{\mathbf{S}}_{2j-1} = g_m \chi_{eff}(\Omega)\vec{T}_0^{\intercal}\cdot\tilde{\mathbf{S}}[\Omega] \tag{7.55}$$

From Equation 7.55 we obtain an expression for the cavity length fluctuations due to radiation pressure and, as the effective susceptibility appears, we can directly infer the expression for the radiation pressure force fluctuations.

$$\begin{aligned}
\hat{q}^{rp}[\Omega] &= g_m\chi_{eff}(\Omega)\vec{T}_0^{\intercal}\cdot\tilde{\mathbf{S}}[\Omega]\cdot\delta\vec{X}[\Omega] \\
\Rightarrow \delta\hat{F}^{rp}[\Omega] &= \frac{\hbar g_m}{x_0}\vec{T}_0^{\intercal}\cdot\tilde{\mathbf{S}}[\Omega]\cdot\delta\vec{X}[\Omega] && (7.56)\\
&= \frac{\hbar g_m}{x_0}\,\vec{T}_0^{\intercal}\cdot\tilde{\mathbf{S}}[\Omega]\cdot\left(\sqrt{\kappa}\,\vec{T}_0\delta\vec{X}^{\mathrm{sum}}[\Omega]+\sqrt{\kappa}\,\vec{T}_{\pi/2}\delta\vec{Y}^{\mathrm{sum}}[\Omega]\right) && (7.57)
\end{aligned}$$

Notably the expression $\vec{T}_0^{\intercal}\cdot\tilde{\mathbf{S}}[\Omega]\cdot\delta\vec{X}$ is the sum over the amplitude fluctuations, a result, which one could have guessed as well. Moreover, in the last line, we do not differentiate between input noise and vacuum fluctuations,[7] which is reasonable when the dissipative heat baths have the same temperature. Again the expression is suited for direct evaluation with the Mathematica code in appendix E, where we provide examples for the three resonance transducer and the single mode optomechanical scheme with arbitrary detuning Δ.
Now we have obtained all the terms that contribute to the output fluctuations and we summarize the results the results.

$$\begin{aligned}
\hat{X}_\theta^{\mathrm{out}}[\Omega] &= \hat{X}_{x,\theta}[\Omega]+\hat{X}_{F,\theta}[\Omega]+\hat{X}_{m,\theta}[\Omega] && (7.58)\\
\hat{X}_{x,\theta}[\Omega] &= \sqrt{\eta_c\kappa}\,\vec{T}_\Theta^{\intercal}\cdot\tilde{\mathbf{S}}[\Omega]\cdot\delta\vec{X}[\Omega]-\hat{X}_\theta^{\mathrm{in}}[\Omega] && (7.59)\\
\hat{X}_{F,\theta}[\Omega] &= \lambda_\theta(\Omega)\chi_{eff}(\Omega)\hat{F}^{rp}[\Omega] && (7.60)\\
\hat{X}_{m,\theta}[\Omega] &= \lambda_\theta(\Omega)\chi_{eff}(\Omega)\hat{F}^{the}[\Omega] && (7.61)
\end{aligned}$$

In the following we will use these results to calculate the output spectrum, as well as the scaled imprecision spectrum that reflects the readout limitations of the transducer.

[7] The mechanical oscillator does not differentiate either.

Calculating the imprecision spectrum

In this paragraph we introduce the imprecision spectral density $S_\theta^{imp}(\Omega)$, which has the unit of a displacement sensitivity and is a function of the noise acting on the optical modes. The displacement imprecision is related to the output fluctuations via the absolute value square of the transduction function.

$$S_{\theta\theta}^{out}(\Omega) = |\lambda_\theta(\Omega)|^2 \, S_\theta^{imp}(\Omega) + |\lambda_\theta(\Omega)|^2 \, |\chi_{eff}(\Omega)|^2 \, S_{FF}^{the}(\Omega) \tag{7.62}$$

Then we can calculate $S_{xx,\theta}^{imp}(\Omega)$ from the scaled optical contributions of the output fluctuation spectrum.

$$\frac{\delta(\Omega+\Omega')}{2\pi} S_\theta^{imp}(\Omega) = \frac{\left\langle \left(\hat{X}_{x,\theta}[\Omega] + \hat{X}_{F,\theta}[\Omega] \right) \left(\hat{X}_{x,\theta}[-\Omega'] + \hat{X}_{F,\theta}[-\Omega'] \right) \right\rangle}{|\lambda_\theta(\Omega)|^2}. \tag{7.63}$$

Computing the expectation values, one obtains three terms, associated with different combinations of $\hat{I}_{x,\Theta}[\Omega]$ and $\hat{I}_{F,\Theta}[\Omega]$.

$$\begin{aligned} S_{xx,\theta}^{imp}(\Omega) &= S_{xx,\theta}(\Omega) + |\chi_{eff}(\Omega)|^2 \, S_{FF}(\Omega) && (7.64) \\ &\quad + \left\{ \chi_{eff}(\Omega) \, S_{xF,\theta}(\Omega) + \chi_{eff}^*(\Omega) \, S_{Fx,\theta}(\Omega) \right\} && (7.65) \end{aligned}$$

Here the photo shot noise spectral density $S_{xx,\theta}(\Omega)$ is the inverse of the susceptibility $|\lambda_\Theta(\Omega)|^2$ and $S_{FF}(\Omega)$ is the quantum backaction force spectral density.

$$S_{xx,\theta}(\Omega) = \frac{1}{2} \, |\lambda_\theta(\Omega)|^{-2} \tag{7.66}$$

In the the analysis of experimental data the equivalent shot noise spectral density is typically evaluated at $\Omega = \Omega_m$ to scale the whole (flat) noise background. Plotting $S_{xx,\theta}(\Omega)$ as a function of Ω also reflects the cavity transmission and gives the impression of a result that is not measured in the experiment. Moreover, when a calibration signal detuned from the mechanical resonance is applied, one needs verify whether is experiences a different sensitivity.
The quantum backaction contribution, which is more precisely a radiation pressure noise backaction, is explicitly given by the expression

$$S_{FF}(\Omega) = \frac{1}{2} \int_{\mathbb{R}} \frac{d\Omega'}{2\pi} \left\langle \hat{F}^{rp}[\Omega] \hat{F}^{rp}[-\Omega]' \right\rangle. \tag{7.67}$$

In contrast to the photon shot noise the imprecision coming from radiation pressure is restricted to the bandwidth defined by the mechanical oscillation. In fact it leads to a real world mechanical displacement and it is this false signal that limits the sensitivity. However there is a number of experiments that aim at the observation of radiation pressure and up to now it is typically the thermal noise of the mechanics that overwhelms the radiation pressure effect [239, 177, 240]. To this end we have proposed the triple mode transducer scheme in section 7.1, where the radiation pressure effect can be largely enhanced.

Finally there remains a mixing term that covers correlation between the photon shot noise and the radiation pressure. It does however not reflect a mechanical motion, but can rather be viewed as an interference effect. Moreover it is small and does not directly depend on the the coupling rate g_m as both S_{xF} and λ_θ are linear in g_m. Yet the mixing term can change with the coupling when the effective susceptibility features a coupling dependence, as it is the case for dynamic backaction cooling. The mixing term can also become negative, and we will show for the single mode transducer that it can manifest itself in the form of ponderomotive squeezing.

7.4. Detailed results for single mode transducer

In this section we apply the relations that were defined in the previous section to the case of the general single mode transducer. Here a single optical mode is coupled to a mechanical degree of freedom and the term general refers to an arbitrary detuning of the drive. The setting of a cavity with a movable mirror was subject to investigation before, also employing a QL approach and the input-output formalism [241, 242].
In contrast to these early results, we study the transduction properties of the single mode transducer when it is driven detuned from the resonance, in particular when the detuning matches the mechanical resonance and the mechanical mode is dynamically cooled. In this setting we notice one fundamental difference compared to the readout of the mechanical motion on resonance. While for a resonant drive the mechanical motion is exclusively encoded in a phase fluctuation, we find that in the detuned case the mechanical displacement is transduced equally to both quadratures. We will demonstrate that this has important implications on the sensitivity that can be reached.

Moreover we close the circle to the cooling studies of chapter 6 and calculate the energy spectrum of the mechanical oscillator. We will see that the ground state energy of the mechanics can be fully attributed to radiation pressure fluctuations of the optical field.
We start our beginning with the Heisenberg-Langevin equations as they are defined in Equations 7.39.

$$\begin{aligned}
\frac{d}{dt}\hat{X} &= -\Delta\hat{Y} - \frac{\kappa}{2}\hat{X} + \delta\hat{X}[t] \\
\frac{d}{dt}\hat{Y} &= \Delta\hat{X} - \frac{\kappa}{2}\hat{Y} + g_m\hat{q} + \delta\hat{Y}[t] \\
\frac{d}{dt}\hat{q} &= \Omega_m\hat{p} - \frac{\gamma}{2}\hat{q} + \delta\hat{q}[t] \\
\frac{d}{dt}\hat{p} &= -\Omega_m\hat{q} - \frac{\gamma}{2}\hat{p} + g_m\hat{X} + \delta\hat{p}[t].
\end{aligned} \tag{7.68}$$

Accordingly the full system is described by the matrix $\mathbf{M}_1$ and the quadrature vector $\vec{X}_M = \left(\hat{X}, \hat{Y}, \hat{q}, \hat{p}\right)^\mathsf{T}$, while the reduced system (which covers only the optical mode)

is represented by the matrix $\mathbf{S}_1$ and the corresponding vector $\vec{X} = \left(\hat{X}, \hat{Y}\right)^{\mathsf{T}}$.

$$\mathbf{M}_1 = \begin{pmatrix} -\frac{\kappa}{2} & -\Delta & 0 & 0 \\ \Delta & -\frac{\kappa}{2} & g_m & 0 \\ 0 & 0 & -\frac{\Gamma_m}{2} & \Omega_m \\ g_m & 0 & -\Omega_m & -\frac{\Gamma_m}{2} \end{pmatrix} \qquad \mathbf{S}_1 = \begin{pmatrix} -\frac{\kappa}{2} & -\Delta \\ \Delta & -\frac{\kappa}{2} \end{pmatrix}. \tag{7.69}$$

Then the inverted matrix $\tilde{\mathbf{S}}[\Omega]$, which describes the quadrature fluctuations in Fourier space, is written as

$$\frac{\tilde{\mathbf{S}}[\Omega]}{\chi_{cav}(\Omega)} = \begin{pmatrix} \frac{1}{2}(\kappa - 2i\Omega) & -\Delta \\ \Delta & \frac{1}{2}(\kappa - 2i\Omega) \end{pmatrix}. \tag{7.70}$$

Moreover we find the effective mechanical susceptibility and the cavity susceptibility (which is in fact the cavity transmission). In frequency units they are written as

$$\begin{aligned} \chi_{eff}(\Omega) &= \frac{\left(\Delta^2 + (\kappa/2 - i\Omega)^2\right)\Omega_m}{\Delta g_m^2 \Omega_m + \left(\Delta^2 + (\kappa/2 - i\Omega)^2\right)\left((\Gamma_m/2 - i\Omega)^2 + \Omega_m^2\right)} \\ \chi_{cav}(\Omega) &= \frac{1}{\Delta^2 + (\kappa/2 - i\Omega)^2}. \end{aligned}$$

Depending on the detuning Δ, the effective susceptibility describes amplification of damping of the mechanical motion, as well as a shift of the resonance frequency and it is essentially the same expression as in Equation 6.2.
Together with the vector $\vec{T}_\theta^{\mathsf{T}} = \{\cos(\theta), \sin(\theta)\}$, which we add for completeness, the quantities that were defined above are sufficient to calculate all of the important transduction properties. In the following we will not limit ourselves to the resolved sideband regime, except for the analysis of ground state cooling where $\Omega_m \gg \kappa$ is required.

Energy of the 1RT

Here, we calculate the energy of the mechanical oscillator in response to fundamental quantum backaction noise of the radiation pressure fluctuations. To this end we define an energy spectrum starting from the position and momentum fluctuations of the mechanical oscillator.

$$\begin{aligned} \frac{1}{4}\left(\langle q^2\rangle + \langle p^2\rangle\right) &= \frac{1}{2}\left(\langle a_m^\dagger a_m\rangle + \langle a_m a_m^\dagger\rangle\right) \\ &= \langle a_m^\dagger a_m\rangle + \frac{1}{2}\left[a_m^\dagger, a_m\right] \end{aligned} \tag{7.71}$$

Then the energy spectrum should represent the occupation number of the mechanical oscillator n_f plus half of the commutator. Especially the latter contribution is interesting, because it is a part that one would naturally associate with quantum properties of the mechanical oscillator. Here however we do not consider any

quantum Langevin noise operators that act on the mechanics to establish this commutator. We exclusively calculate the response to quantum backaction originating from quantum fluctuations of the light field.

$$\begin{aligned}\hat{q}^{rp}[\Omega] &= g_m \chi_{eff}(\Omega) \vec{T}_0^{\intercal} \cdot \tilde{\mathbf{S}}[\Omega] \cdot \delta\vec{X}[\Omega] \\ \hat{p}^{rp}[\Omega] &= g_m \frac{\Gamma_m/2 - i\Omega}{\Omega_m} \chi_{eff}(\Omega) \vec{T}_0^{\intercal} \cdot \tilde{\mathbf{S}}[\Omega] \cdot \delta\vec{X}[\Omega]\end{aligned}$$

Then the energy spectral density is defined, according to the outline in Equation 7.71, which is simplified when we replace the variances with the radiation pressure force spectral density.

$$\begin{aligned}\bar{S}_{FF}^{\text{energy}}(\Omega) &= \frac{\hbar\Omega_m}{2} \int_{\mathbb{R}} \frac{d\Omega'}{2\pi} \left[\frac{1}{2} \langle \hat{q}^{rp}[\Omega]\, \hat{q}^{rp}[-\Omega'] \rangle + \frac{1}{2} \langle \hat{q}^{rp}[\Omega]\, \hat{q}^{rp}[-\Omega'] \rangle \right] \\ &= \frac{\Omega_m x_0^2}{\hbar} \left(1 + \frac{\Gamma_m^2/4 + \Omega^2}{\Omega_m^2} \right) |\chi_{eff}(\Omega)|^2 \cdot \bar{S}_{FF}^{\text{single}}(\Omega) \qquad (7.72)\end{aligned}$$

In contrast to the previous chapter, we do not bother with an analytical solution, but instead perform a numerical integration of the spectrum and plot the solution for varying g_m in Figure 7.6. In panel (a) of the figure we can see that the half quantum of mechanical energy that is associated with the ground state is added by radiation pressure fluctuation already at a moderate coupling rate of $g_m \approx \kappa/20$. At the same time any quantum fluctuations originating from mechanical noise "hide" behind the effective susceptibility and are correspondingly suppressed. Consequently dynamic backaction cooling is most likely not suited to reveal the quantum nature of the mechanical oscillator. In panel (b) of Figure 7.6 we show a magnification of the area above one half quanta of the occupancy curve. Indeed there is a small difference that is exactly reproduced by the coupling dependent quantum limit (cf. Equation 6.8). Only towards ever stronger coupling one can sense a tiny deviation due to higher order terms.

In a way the result solves the problem, how to interpret the occupation number of a hybridized mode, namely whether the remaining energy quanta should be attributed to the mechanics or the optics. Here it becomes clear that the ground state fluctuations are purely a consequence of the quantum nature of the light field.

We can continue our analysis and take a look at the symmetry of the spectrum, in particular the asymmetric height of the mechanical sideband at $\pm\Omega_m$. Exchanging the symmetrized QBA spectrum against the full $\bar{S}_{FF}^{\text{single}} \rightarrow S_{FF}^{\text{single}}$ version ($\mathtt{K} \rightarrow \mathtt{1}$ in the algorithm), we find that even the sideband asymmetry that is expected to be found with a mechanical oscillator in the ground state is a result of quantum backaction.

In the end, when it comes down to possible practical applications, such as quantum computing or storage and manipulation of quantum states, the question whether the mechanical oscillator behaves as a quantum mechanical object or not, is little important. From a technical point of view the coherence time is more interesting,

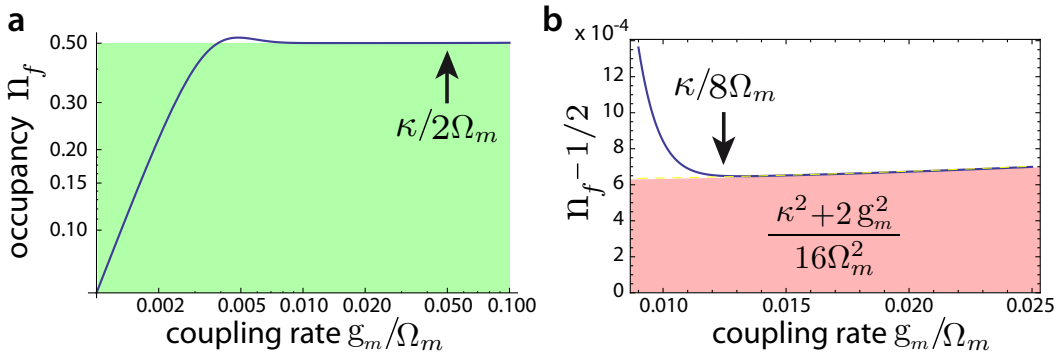

Figure 7.6.: The quantum backaction contribution to the ground state energy of the mechanical oscillator. The cavity energy decay rate is $\kappa = \Omega_m/10$. (a) The energy of the mechanical oscillator, driven only by quantum backaction of the cavity field, is plotted as a function of the coupling rate g_m and in terms of the phonon number. The curve is obtained from numerical integration of Equation 7.72, divided by the energy quantum $\hbar\Omega_m$. The arrow at $g_m = \kappa/2$ indicates the onset of normal mode splitting. Keeping in mind that the mechanics is represented by a purely classical susceptibility, it becomes apparent that the ground state uncertainty of the mechanical oscillator is indeed a consequence of the quantum nature of the light field. (b) The plot shows a magnified view of the left hand panel and highlights the offset between $n_f = 1/2$ and the actual occupancy. The shaded area correspond to the power dependent quantum limit derived in Equation 6.8 of the previous chapter, and thus draws the connection between the two approaches. Interestingly, the light pressure force already accounts for the quantum limit at a coupling rate of $\sim g_m = \kappa/8$, long before the optical and the mechanical mode hybridize.

in particular with regard to the question whether one can imprint a quantum state from the light field onto a mechanical object and then transfer this state to, e.g. a superconducting microwave cavity [213]. We will abort the discussion on the quantum mechanical properties of a macroscopic object here and maybe continue in the outlook section.

Transduction of the 1RT

We continue our analysis of the single mode transducer with the transduction function $\lambda_\theta^{single}(\Omega)$. In order to obtain a real quantity, we compute its absolute value square, which is in principle the inverse of the photon shot noise imprecision $S_{xx,\theta}(\Omega)$ (except for a factor $1/2$, due to out definition of the quadratures).

$$\begin{aligned}\left|\lambda_\theta^{single}(\Omega)\right|^2 &= \frac{g_m^2\eta_c}{x_0^2}\frac{2\kappa\left(4\Delta^2+\kappa^2+4\Omega^2\right)}{16\Delta^4+8\Delta^2\left(\kappa^2-4\Omega^2\right)+\left(\kappa^2+4\Omega^2\right)^2} \\ &\times\left(1+\mathrm{Cos}[2\theta-2\theta_{opt}]\cdot\sqrt{1-\frac{4\Delta^2\Omega^2}{\left(\Delta^2+\frac{\kappa^2}{4}+\Omega^2\right)^2}}\right).\end{aligned} \tag{7.73}$$

In the second line the transduction function was rewritten in a way that exposes its angle dependence. To this end we introduced an "optimal" readout angle θ_{opt},

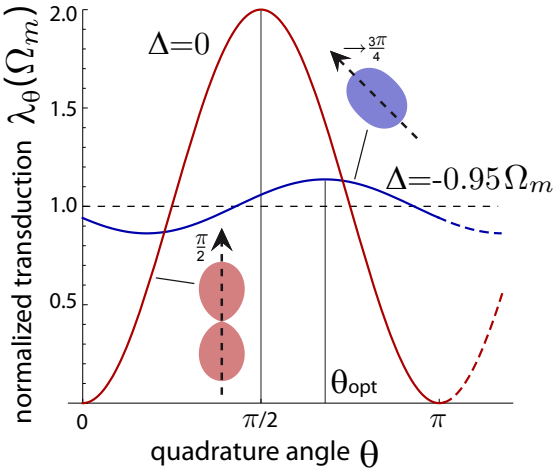

Figure 7.7.: The relative intensity of the mechanical signal in different quadratures. The figure shows the normalized sensitivity ($\propto 1/S_{xx,\theta}(\Omega)$) of the 1RT as a function of the measured quadrature, i.e., the angle θ. Readout at the mechanical resonance frequency $\Omega = \Omega_m$ and $\kappa = \Omega_m/4$. Curves for two values of the detuning Δ are plotted: (i) driving at resonance ($\Delta = 0$) and (ii) detuned from resonance for $\Delta = -0.95 \cdot \Omega_m$. When the detuning approaches $-\Omega_m$, and κ becomes $\ll \Omega_m$. The optimal readout angle θ_{opt} moves towards $3\pi/4$. In this case, the modulation amplitude becomes zero and the signal is correspondingly transduced into both quadratures.

where the transduction of the mechanical signal to a light fluctuation is maximized. The angle is of course a function of parameters such as the detuning and the exact dependence can be explored using the code example in appendix E. Here we focus on the general behavior.
When the cavity is driven on resonance (i.e., $\Delta = 0$), the optimal angle $\theta_{opt} = \pi/2$ corresponds to the phase quadrature and the square root term in Equation 7.73 is equal to one. On the other hand, in a detuned readout for $\Delta^2 \approx \Omega^2 \gg \kappa^2$, which is the case in resolved sideband cooling, the square root term becomes zero and the angle dependence vanishes. This is also the reason, why the actual expression for θ_{opt} only plays a minor role. In Figure 7.7 we plot the dependence of the transduction function on the readout angle. For resonant readout the transduction vanishes for $\theta = 0$, meaning that the mechanical motion does not induce amplitude fluctuation and the full signal is imprinted on the phase. When the laser is detuned from resonance the situation changes and the signature of the mechanical motion is found in both quadratures. At the same time the optimal angle shifts from $\pi/2 \to 3\pi/2$, which has however little impact as the amplitude of the modulation becomes small.

Physically, this finding suggests that independent of the recorded quadrature, one will only measure "half of the signal". On the other hand, we have only considered the influence of the angle dependent part of expression 7.73 and ignored the prefactor so far. In the following paragraph we study the overall measurement imprecision to gain an impression how the distribution of the mechanical information in both quadratures affects the uncertainty product.

Uncertainty product of the 1RT

In this paragraph we calculate the uncertainty product between the equivalent shot noise imprecision and the backaction force spectral density. We evaluate the code in appendix E and obtain an expression that resembles the angle dependent part of the transduction function 7.73.

$$\begin{aligned} S_{xx}^{single}(\Omega) \cdot S_{FF}^{single}(\Omega) &= \frac{\hbar^2}{4\eta_c} 2 \left[1 + \mathrm{Cos}[2\theta - 2\theta_{opt}] \cdot \sqrt{1 - \frac{4\Delta^2\Omega^2}{\left(\Delta^2 + \frac{\kappa^2}{4} + \Omega^2\right)^2}} \right]^{-1} \\ &\geq \frac{\hbar^2}{4\eta_c} \frac{2}{1 + \sqrt{1 - 4\Delta^2\Omega^2 / \left(\Delta^2 + \frac{\kappa^2}{4} + \Omega^2\right)^2}} \end{aligned}$$

In the second line we have chosen $\theta = \theta_{opt}$, such that the uncertainty product becomes minimal and sets a lower limit.For simplification we evaluate the statement for the phase quadrature at $\theta = \pi/2$ and obtain a less complex expression.

$$S_{xx}^{single}(\Omega) \cdot S_{FF}^{single}(\Omega)\Big|_{\theta \to \frac{\pi}{2}} = \frac{\hbar^2}{4\eta_c} \left(1 + \frac{\Delta^2}{\kappa^2/4 + \Omega^2} \right)$$

It becomes apparent that a resonant readout (i.e., $\Delta = 0$) can be considered as an ideal quantum measurement in the sense of Caves [243] as it is ideally limited by $\hbar/2$. However in the case that $\kappa \ll \Delta \approx \Omega$, which is encountered for dynamical backaction cooling in the RSB regime, an additional factor $\times 2$ appears and the SQL is given by

$$\sqrt{S_{xx}^{single}[\Omega] \cdot S_{FF}^{single}[\Omega]} \geq \frac{\hbar}{2} \cdot \sqrt{\frac{2}{\eta_c}}$$

The detuned readout of a mechanical oscillator therefore does not constitute an ideal quantum measurement, where the imprecision limit is set by $\hbar/2$. As the information about the oscillators motion is equally contained in the phase and amplitude quadrature, one necessarily loses half of the information during the readout, which is echoed by the additional factor $\sqrt{2}$ in the uncertainty product. Along the same line the factor η_c reflects the information that is lost through the vacuum channel. In particular this finding can become important, when the sensitivity of a measurement is expressed in terms of the Heisenberg uncertainty limit[244, 196].
Regarding the experimental readout technique the limitation can be overcome, when the motion of the mechanical oscillator is recorded with an auxiliary laser beam on the resonance center, while cooling is achieved with a strong detuned source.

The influence of the mixing term

Finally, we investigate the mixing term between photon shot noise and quantum backaction. As both contributions to the measurement imprecision originate from the same noise operators, one expects naturally a correlation. In contrast to the

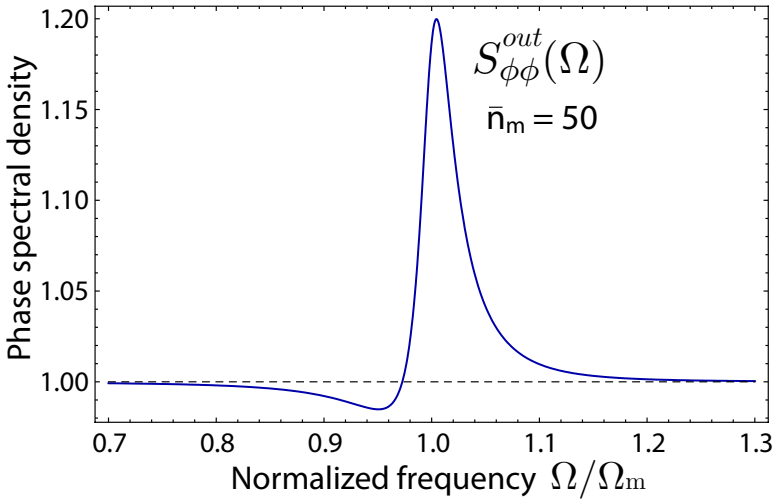

Figure 7.8.: Ponderomotive squeezing is a consequence of the mixing between the photon shotnoise and the backaction force $S_{xF,\theta}(\Omega)$. Here we plot the output phase fluctuations for the detuned single mode transducer, with an initial thermal occupation of $\bar{n}_m = 50$ phonons. One observes noise squashing below the photon shot noise level, slightly detuned from the mechanical resonance. Again the effect is linked to the quantum nature of the light and does not correspond to an actual squeezing of the mechanical motion. Ponderomotiv squeezing was recently observed by Brooks and co-workers [245]. We note that the imprecision spectrum of the amplitude fluctuations is "mirrored" around the mechanical resonance, and elevated noise is found in the frequency range where phase squashing takes place.

quantum backaction and imprecision spectra, the mixing terms are *a priori* independent of the the coupling rate g_m.

We remind ourselves that the mixing part $S_{xF,\theta}$ of the measurement imprecision is given by the expression

$$2\pi\,\delta(\Omega+\Omega')\,S_{xF,\theta}(\Omega) = \frac{\left\langle \hat{X}_{x,\theta}[\Omega]\hat{X}_{F,\theta}[-\Omega']\right\rangle}{\lambda^*_\theta(\Omega)}$$

And it contributes to the measurement imprecision in the following way.

$$\chi_{eff}(\Omega)\,S_{xF,\theta}(\Omega) + \chi^*_{eff}(\Omega)\,S_{Fx,\theta}(\Omega) = 2\cdot\Re\left[\chi_{eff}(\Omega)\,S_{xF,\theta}(\Omega)\right]$$

The latter is true, because switching the order of the quadrature fluctuation corresponds to changing the sign of their frequency arguments, such that $S_{Fx,\theta} = S^*_{xF,\theta}$. The full analytical expression of the mixing term is usually quite long, as it includes the effective mechanical susceptibility, and does not provide much physical insight. To get an impression of the influence of the mixing term, the plotted the full phase fluctuation spectrum in Figure 7.8.

Stripped of the effective susceptibility $\chi_{eff}(\Omega)$, we find the the following expression for the general single mode transducer

$$S^{single}_{xF,\theta}(\Omega) = \frac{e^{-i\theta}(-2i\Delta-\kappa+2i\Omega)\hbar}{4\Delta\cos(\theta)-2(\kappa-2i\Omega)\sin(\theta)}. \tag{7.74}$$

When the detuning Δ is set to zero, we obtain identical expressions for the 3RT and the 1RT.

$$S_{xF,\theta}^{triple}(\Omega) = S_{xF,\theta}^{single}(\Omega)\Big|_{\Delta=0} = \frac{\hbar}{2}(\mathrm{Cot}[\theta] - i). \tag{7.75}$$

Here, the highest sensitivity is achieved at $\theta = \pi/2$, where measurement uncertainty due to the mixing term is uneven in frequency $\chi_0(\Omega)S_{xF,\theta}^{triple}(\Omega) + \chi_0^*(\Omega)S_{Fx,\theta}^{triple}(\Omega) = \hbar\gamma\Omega|\chi_0(\Omega)|^2$. Therefore the term disappears in the symmetrized spectrum. This is, however, not the case for the detuned 1RT.

7.5. Outlook and Summary

In the last two chapters[8] we have, in detail, investigated one or more optical cavity modes coupled to a mechanical degree of freedom and we have presented an in depth analysis of dynamical backaction cooling of the mechanical oscillator – including the regime of strong coupling – as well as the transduction of the mechanical signal to the output fluctuations of the cavity.

In particular we found that for coupling rates $g_m > \kappa/2$, the optical and the mechanical mode hybridize which manifests as normal mode splitting (NMS) in the reflected signal. Intriguingly, this parameter regime was reached shortly after publication of the work and mode splitting was observed. Today NMS in optomechanical settings is regularly observed and it is at the basis of novel technical applications that require coherent energy (and information) exchange between the mechanics and the light field. With respect to dynamical backaction cooling we found that the strong coupling regime and in particular NMS, coincide with a saturation of the cooling rate.

Indeed, we could show that the final phonon occupation number of the mechanical oscillator can be separated in three terms of different physical origin: (i) the quantum limit, (ii) a limitation through a noisy drive that does not allow cooling below the thermal occupation of the drive source, and finally, (iii) the limitation through NMS, where the finite cavity decay rate prevents further reduction of thermal phonons. The final occupancy of the mechanics was presented up to second order – also taking a finite coupling rate into account – and the result was one-to-one utilized for the data analysis of the seminal ground state cooling work by Teufel and co-workers [196].

Moreover we investigated the transduction properties of cavity optomechanical settings that rely on multiple cavity modes, spaced by the mechanical resonance frequency. We found that the quantum backaction in a three mode scheme, with the central mode being driven, is greatly enhanced in the resolved sideband regime, and the SQL is reached at lower input power. Likewise, more efficient cooling can be

[8] Here we summarize the part on the theoretical work on cavity optomechanics, which covers chapters 6 and 7. For a detailed outlook and summary on the experimental part, we refer the reader to section 5.4.

achieved in a two mode scheme, where the lower frequency resonance is optically pumped.

Here, we followed two different formalisms to obtain our results, a covariance approach and a quantum Langevin approach, to calculate noise and imprecision spectra. As a treat for the reader and anyone who would like to follow up on the work, we expose our methods and publish not only the complete algorithm that was used to obtain the results of this work, but also its implementation. We emphasize that this is a rarely chosen strategy and reflects the confidence that we keep in our results. Moreover, we discuss the limitations and difficulties that arise, namely with the covariance approach.

Finally, we presented the essential results for the generic optomechanical system, consisting of a single optical field and a mechanical mode. The system has attracted an extraordinary amount of research during recent years, especially with respect to ground state cooling of the mechanics. In our analysis it becomes clear that the uncertainty associated with the motional ground state of the mechanical oscillator indeed reflects the quantum nature of the light that transduces the motion.

Appendix

A. WGM theory and Simulation of optical modes

A.1. Analytical WGM theory

In this paragraph we follow the instructional presentation of Teraoka *et al.* [96, 102], to introduce the analytical solutions of the wave equation for a microsphere geometry. The derivation of the equations has been published several times before and can be found, for example, in references [94, 95, 96, 97]. In order to provide a benefit to the reader, the equations for the mode intensity distribution, the resonance frequency, the mode volume, and other useful expression will be supplied directly in Mathematica notation. The code can be pasted to a Mathematica notebook to reproduce the figures and to recalculate the results.
The solutions to Equation 1.1 can be divided into waves of the electric type (TM polarization) and magnetic type (TE polarization), and by separation of variables, the explicit expressions for the electric field in spherical coordinates may be written as

$$\mathbf{E}^{\mathrm{TE}}_{lmq}(r,\vartheta,\varphi) = \frac{\exp(im\varphi)}{kr} S_{lq}(r)\mathbf{X}_{lm}(\vartheta) \tag{A.1}$$

$$\mathbf{E}^{\mathrm{TM}}_{lmq}(r,\vartheta,\varphi) = \frac{\exp(im\varphi)}{k^2\varepsilon(r)}\left[\frac{\partial}{r\partial r}T_{lq}(r)\mathbf{Y}_{lm}(\vartheta) + \frac{1}{r^2}T_{lq}(r)\mathbf{Z}_{lm}(\vartheta)\right] \tag{A.2}$$

$$\approx \frac{\exp(im\varphi)}{k^2r^2\varepsilon(r)} T_{lq}(r)\mathbf{Z}_{lm}(\vartheta). \tag{A.3}$$

Here, the mode numbers $\{l, m, q\}$ denote the polar, azimuthal, radial mode numbers, respectively, where m corresponds to the integer number of wavelengths fitting into the effective optical path of one round trip. At the same time $|m - l|$ and q are the number of intensity nodes in latitudinal and radial direction, respectively. In Figure A.2a the radial intensity distribution for modes with $q = 0$ and $q = 1$ is shown. In equations (A.1–A.3) the functions that depend on the polar angle ϑ are given by

$$\mathbf{X}_{lm}(\vartheta) = \frac{im}{\sin\vartheta} P_{lm}(\cos\vartheta)\,\hat{\mathbf{e}}_\vartheta - \frac{\partial}{\partial\vartheta} P_{lm}(\cos\vartheta)\,\hat{\mathbf{e}}_\varphi \tag{A.4}$$

$$\mathbf{Y}_{lm}(\vartheta) = \hat{\mathbf{e}}_r \times \mathbf{X}_{lm}(\vartheta) \tag{A.5}$$

$$\mathbf{Z}_{lm}(\vartheta) = l(l+1)\,P_{lm}(\cos\vartheta)\,\hat{\mathbf{e}}_r. \tag{A.6}$$

Here, $P_{lm}(\cos\vartheta)$ represent Legendre polynomials and $\{\hat{\mathbf{e}}_r, \hat{\mathbf{e}}_\vartheta, \hat{\mathbf{e}}_\varphi\}$ are the unity vectors in spherical coordinates. We note that the non-radial component of the TM wave in equation (A.2) is typically much smaller than the radial component and can be neglected when the mode energy and the electric field intensity are calculated.
We repeat that the spherical geometry of the resonator is established by the function

$\varepsilon(\mathbf{r})$, with

$$\varepsilon(\mathbf{r}) = \begin{cases} n_1^2 & \text{for } |\mathbf{r}| \leq R_{\text{sphere}} \\ n_2^2 & \text{for } |\mathbf{r}| > R_{\text{sphere}} \end{cases}$$

Here n_1 and n_2 are the refractive indices of silica and of the exterior, respectively.

Calculation of the radial part

While the analytical solutions to the angular parts are readily found after separation of variables, the radial part is defined through a more complex differential equation. In literature one finds different definitions that are eventually all equivalent, and it does not really matter, whether the solutions are Hankel functions or spherical Bessel functions. Here, we chose a compact representation that has the advantage that the eigenvalues/indices are whole numbers. With $z = n(r)\,kr$ the radial parts $S_{lq}(r)$ and $T_{lq}(r)$ of the solution (TE and TM) satisfy the differential equation

$$\left[\frac{\partial^2}{\partial z^2} - \frac{l(l+1)}{z^2} + 1\right] \begin{cases} S_l(z) & = 0 \\ T_l(z) & = 0 \end{cases} \tag{A.7}$$

The equation is solved by the functions $\{z \cdot j_l(z),\ z \cdot y_l(z)\}$, where j_l and $y_l$are spherical Bessel functions.
While equation A.7 represents the most compact description of the WGM radial part, it can also be rewritten in terms of an eigenvalue problem with an effective potential $U_{\text{eff}}(r)$, which provides additional insight on the physics of the problem [246].

$$\begin{aligned} \nabla \times (\nabla \times \Psi(\mathbf{r},t)) + \frac{\varepsilon(r)}{c^2}\frac{\partial^2}{\partial t^2}\Psi(\mathbf{r},t) &= 0 \\ \frac{\partial^2}{\partial r^2}\Psi(r,t) + \frac{\varepsilon(r)}{c^2}\frac{\partial^2}{\partial t^2}\Psi(r,t) + U_{\text{eff}}(r)\Psi(r,t) &= 0 \end{aligned}$$

With $\Psi(r,t) = \Psi(r)\,\exp(-i\omega t)$ we find

$$\frac{\partial^2}{\partial r^2}\Psi_{lq} - \underbrace{\left[\frac{l\,(l+1)}{r^2} - k_{lq}^2\,(\varepsilon(r)+1)\right]}_{U_{\text{eff}}(r)}\Psi_{lq} = \varepsilon(r)k_{lq}^2\Psi_{lq} \tag{A.8}$$

The effective potential thus consists of a radially decaying part $\propto r^{-2}$ and a step function $\propto 1/\varepsilon(r)$ at the interface. Together, the two contributions form an energy well that supports bound states. The finite height of the potential barrier $k^2(\varepsilon_{silica} - \varepsilon_{ex})$ limits the number of bound states. Consequently, only a finite number whispering gallery modes is supported. Moreover, tunneling through the potential barrier leads to whispering gallery loss that limits the optical Q factor. A detailed discussion is presented, e.g., in the thesis of T.J. Kippenberg [247].

Sticking to the compact form of the differential equation, the solutions inside and outside the sphere are given by linear superpositions of $r \cdot j_l$ and $r \cdot y_l$, but due to the requirements of normalization, a zero value at $r = 0$, and physical sense, only the combination below are valid.[1]

$$S_{lq}(r) = \begin{cases} (n_1 k_{lq} r) \cdot j_l(n_1 k_{lq} r) & , \text{for } r < a \\ A_l^{\mathrm{TE}} (n_2 k_{lq} r) \cdot y_l(n_2 k_{lq} r) & , \text{for } r \geq a \end{cases} \tag{A.9}$$

$$T_{lq}(r) = \begin{cases} (n_1 k_{lq} r) \cdot j_l(n_1 k_{lq} r) & , \text{for } r < a \\ A_l^{\mathrm{TM}} (n_2 k_{lq} r) \cdot y_l(n_2 k_{lq} r) & , \text{for } r \geq a \end{cases} \tag{A.10}$$

$$A_{lq}^{\mathrm{TE}} = A_{lq}^{\mathrm{TM}} = \frac{(n_1 k_{lq} a) \cdot j_l(n_1 k_{lq} a)}{(n_2 k_{lq} a) \cdot y_l(n_2 k_{lq} a)} \tag{A.11}$$

Here, the constants A_{lq}^{TE} and A_{lq}^{TM} are chosen, such that the continuity of the normal components of the electric field (for the TE wave) and of the electric displacement (for the TM wave) are ensured. Notably the term $\varepsilon^{-1}(r)$ appears in Equation A.2, such that the discontinuity of the normal component of the electric field at the interface is established by the above definition. However one will quickly notice, that the expressions of the radial parts for the TE and the TM waves are equivalent. The differences arise from the proper choice of the wavenumber k, which is defined via the continuity condition of the first derivative.

Calculation of the resonance frequency

The wavenumbers k_{lq} have to meet the requirement, that the first derivative is continuous at the interface. This yields two different conditions for the TE and TM mode (again because $\varepsilon(r)$ appears in Equation A.2). For the TE mode the relation

$$n_1 \left. \frac{\partial_z(z \cdot j_l(z))}{z \cdot j_l(z)} \right|_{z \to n_1 ka} = n_2 \left. \frac{\partial_z(z \cdot y_l(z))}{z \cdot y_l(z)} \right|_{z \to n_2 ka} \tag{A.12}$$

needs to be fulfilled, whilst for the TM mode the condition takes the following form:

$$\frac{1}{n_1} \left. \frac{\partial_z(z \cdot j_l(z))}{z \cdot j_l(z)} \right|_{z \to n_1 ka} = \frac{1}{n_2} \left. \frac{\partial_z(z \cdot y_l(z))}{z \cdot y_l(z)} \right|_{z \to n_2 ka} \tag{A.13}$$

The roots of these relations are plotted in Figure A.1, which illustrates that discrete values for the solution exist. A closed form analytical form of the discrete solutions does not exist, but an approximation is given by the Schiller expansion in reference [97]. An implementation of the series is given in the following section. Here, we will first demonstrate how to find the fundamental solutions numerically. We repeat that the following code can be pasted into a Mathematica notebook.

[1] In principle the continuity and normalization conditions can be fulfilled if $j_l(r)$ is chosen on the domain outside the sphere. The requirement of *physical sense* is however violated.

At the beginning of the calculation, we define the sphere radius a in μm, the (azimuthal) mode number M_{mode}, the refractive indices in silica (n_1) and water (n_2), and finally some initial values for the numerical root search algorithm that yields the resonance frequency (that correspond approximately to the zero crossings in Figure A.1). The notation here is chosen such that the numbers, i.e. z_**number**_TE, corresponds to the number of radial intensity nodes.

```
a=32.72;
Mmode=551;
n1=1.46071;
n2=1.33372;
\[Epsilon][r_]:=If[r<a,n1^2,n2^2];
z0TE=386; z0TM=386.5; z1TM=394.3;
```

Here, the mode number (as well as the initial values) appears from nowhere. In the following section we will present a way how to derive them in a deterministic fashion using the Schiller expansion. Next, we define some auxiliary functions that correspond to the left and right hand side of Equations A.12 and A.13.

```
Psi[l_,z_]:=(z*SphericalBesselJ[l,z]);
Chi[l_,z_]:=(z*SphericalBesselY[l,z]);
FracJ[l_,z_]:=(D[x*SphericalBesselJ[l,x],x]/.x->z)/(z*SphericalBesselJ[l,z]);
FracY[l_,z_]:=(D[x*SphericalBesselY[l,x],x]/.x->z)/(z*SphericalBesselY[l,z]);
```

We use these functions to calculate the resonant wave numbers of the TE00, TM00, and TM10 modes.

```
k0TE=(z/a)/.FindRoot[n1*FracJ[551,n1*z]-n2*FracY[551,n2*z],{z,z0TE}];
k0TM=(z/a)/.FindRoot[(1/n1)*FracJ[551,n1*z]-(1/n2)*FracY[551,n2*z],{z,z0TM}];
k1TM=(z/a)/.FindRoot[(1/n1)*FracJ[551,n1*z]-(1/n2)*FracY[551,n2*z],{z,z1TM}];
```

The equation possesses different solutions k_{lq}, corresponding to values of $q = 0, 1, 2, 3, \ldots$ and thus to different numbers of intensity nodes. To find the resonant wavenumbers corresponding to one or two intensity maxima, as they are frequently encountered in the experiment, one needs to supply "good" initial values for the numerical root search algorithm. Even small deviations can lead to unwanted radial mode numbers, because singularities and steep gradients may lead to overshoots in the search algorithm (cf. Figure A.1). We note that modes with the same lq mode numbers but different $(m - l)$ are frequency degenerate. Practically this degeneracy is lifted due to subtle eccentricity or non-spheriodicity, which can, e.g., be tuned by strain [248].
Here the units of the wavenumbers are $\mu\mathrm{m}^{-1}$ and multiplication with $3 \cdot 10^{14}/2\pi$ yields the resonance frequency. We note that the code above is easily modified to calculate the shift of the resonance frequency in response to a change of the refractive index of the exterior.

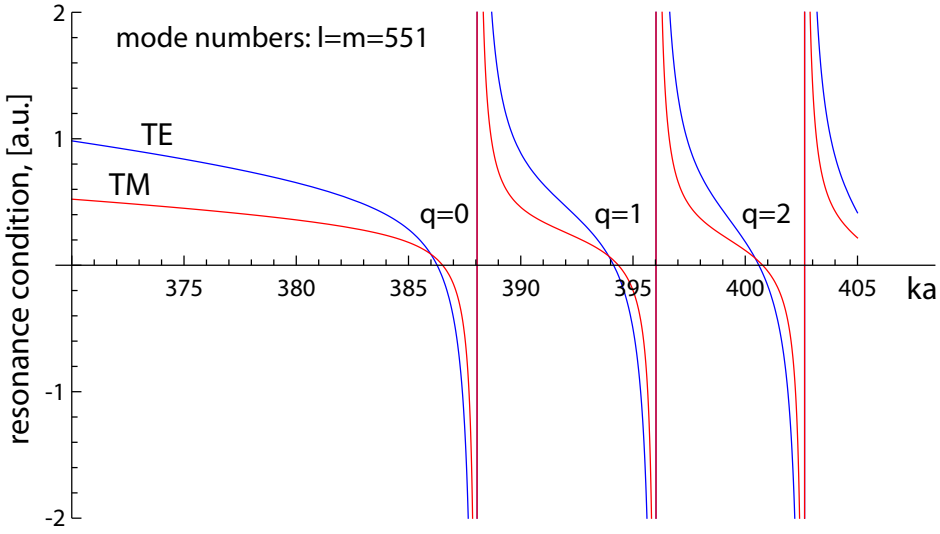

Figure A.1.: The resonance condition for TE and TM modes plotted as a function of ka (wave number times resonator radius). The curves represent the roots of the resonance condition A.12 and A.13 (left hand side minus right hand side). Every zero crossing corresponds to a mode with a different radial mode number q, which represents the number of radial field nodes. The resonance wavenumber and frequency of a specific mode is numerically found when choosing a starting value for ka close to the desired root.

Next we proceed with plotting the mode intensity distribution and start out with the calculation of the normalization constants A_{lq}^{TE} and A_{lq}^{TM} that ensure that the normal component of the dielectric displacement, i.e., $\propto T_{lq}(r)/r^2$ for the TM wave, and the tangential component of the electric field, i.e., $\propto S_{lq}(r)/r$ for the TE wave, are continuous.

```
A0TE=Psi[Mmode,n1*k0TE*a]/Chi[Mmode,n2*k0TE*a];
A0TM=Psi[Mmode,n1*k0TM*a]/Chi[Mmode,n2*k0TM*a];
A1TM=Psi[Mmode,n1*k1TM*a]/Chi[Mmode,n2*k1TM*a];
```

Now we can define the radial parts of the electric field according to the nomenclature of Equations A.1 and A.2. Here we also defined the derivative of the function $T_{lq}(r)$ that appears in expression A.2 and that can usually be neglected. With the code below, the reader is able to verify this claim.

```
S0[r_]:=If[r<a,Psi[Mmode,n1*k0TE*r],A0TE*Chi[Mmode,n2*k0TE*r]];

T0[r_]:=If[r<a,Psi[Mmode,n1*k0TM*r],A0TM*Chi[Mmode,n2*k0TM*r]];

T0p[r_]:=If[r<a,(D[x*SphericalBesselJ[Mmode,x],x]/.x->n2*k0TM*r),
A0TM*(D[x*SphericalBesselY[Mmode,x],x]/.x->n2*k0TM*r)];

T1[r_]:=If[r<a,Psi[Mmode,n1*k1TM*r],A1TM*Chi[Mmode,n2*k1TM*r]];

T1p[r_]:=If[r<a,(D[x*SphericalBesselJ[Mmode,x],x]/.x->n2*k1TM*r),
A1TM*(D[x*SphericalBesselY[Mmode,x],x]/.x->n2*k1TM*r)];
```

When calculating the electric field intensity, the absolute value square of the angular functions $\mathbf{X}_{lm}$ and $\mathbf{Z}_{lm}$ appear, which can become very large for higher values of l and m. It is convenient to express the integral over the 4π solid angle in a separate parameter W_{lm} that will be used for scaling.

$$W_{lm} = \int_0^{\pi} \sin\vartheta d\vartheta \int_0^{2\pi} d\varphi \, |\mathbf{X}_{lm}(\vartheta)|^2 = \frac{4\pi(l+m)!l(l+1)}{(l-m)!(2l+1)}$$

More over

$$\int_0^{\pi} \sin\vartheta d\vartheta \int_0^{2\pi} d\varphi \, |\mathbf{Z}_{lm}(\vartheta)|^2 = l(l+1)\, W_{lm}$$

The following code defines the value of the integral, as well as $|\mathbf{X}_{lm}(\vartheta)|^2$ and $|\mathbf{Z}_{lm}(\vartheta)|^2$.

```
Xsqrd[l_,m_,th_]:=m^2/Sin[th]^2*LegendreP[l,m,Cos[th]]^2+
D[LegendreP[l,m,Cos[x]],x]^2/.x->th;

Zsqrd[l_,m_,th_]:=(l*(l+1))^2*LegendreP[l,m,Cos[th]]^2;

W[l_,m_]:=4*Pi*(l+m)!*l*(l+1)/(l-m)!/(2*l+1);
```

Finally we can plot the radial parts of the electric field intensity for the TE00 and TM00 mode. The TM01 mode is plotted when exchanging $0 \to 1$ in the line coding for the TM00 mode.

```
Plot[{k0TE^2*(S0[r]/r)^2*Xsqrd[Mmode,Mmode,Pi/2]/W[Mmode,Mmode],
(T0[r]/r^2)^2*Zsqrd[Mmode, Mmode,Pi/2]/
W[Mmode,Mmode]/\[Epsilon][r]^2}, {r,a-4,a+2},PlotRange->All]
```

Normalization of the plots can be achieved, e.g., by scaling with the mode energy that is calculated in the next section. Then the curves resemble the ones in Figure A.2. Magnifying the intensity at the interface displays the previously discussed discontinuity. Notably the higher order TM mode ($q = 1$) features a larger evanescent fraction than the fundamental modes.

A.2. Simulations

In this section, we present the Mathematica code that was used for the calculation of the analytical single particle frequency shift for microspheres. In the first place, we define the refractive indices of the environment n_1, the microsphere n_2, and the particle n_p and name the sphere radius a in [μm]. Refractive indices for fused silica and water at the different wavelengths that we consider here, are listed in the table below.

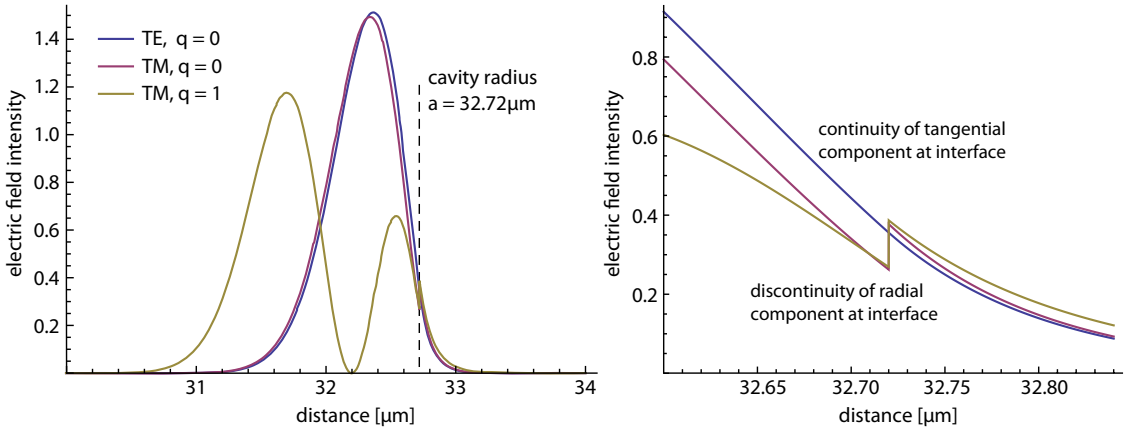

Figure A.2.: The field intensity distribution for different WGMs. (a) The normalized radial intensity distribution is plotted for the TE00, TM00, and TM01 mode. The right panel zooms in on the interface and highlights the discontinuity of the TM polarized modes.

$\lambda\,[\mathrm{nm}]$	$a\,[\mu\mathrm{m}]$	M_{mode}	z_0^{TE}	z_0^{TM}	z_1^{TM}
1311	30	**200**	143.8	144	149.5
1311	44	**294**	210.3	210.5	216.7
1311	51.6	**347**	247.4	246.6	254.2
1311	83.8	**567**	401.1	401.3	409.3
763	30	**346**	246	246.3	253
763	39	**453**	320.8	321	328.4
688	35	**452**	320	320.4	327.7
688	40	**517**	365.5	365.5	373.3
532	32.72	**551**	386	386.5	394

Table A.1.: Mode numbers and starting values for microsphere geometries used by Vollmer et al. in reference [37].

$\lambda\,[\mathrm{nm}]$	n_1	n_2
1311	1.4468	1.3234
763	1.45	1.33
688	1.45	1.33
532	1.46071	1.33372

The website **http://refractiveindex.info** gives access to a large database of refractive indices for different materials and wavelengths. Importantly the underlying sources for the data are properly cited. In the following we calculate mode geometries and resonance frequencies for microspheres of different radius and for different wavelength.

Derivation of the mode number using the Schiller expansion

As shown in the previous section, the resonance frequency can be found, following the illustrative way of guessing the mode number M_{mode}, plotting the resonance condition as in Figure A.1 and extracting starting values for the numerical root search. Here we present a different approach that is much faster and directly yields the correct mode number M_{mode} and the z_n^{TEM} starting values. To this we use the Schiller expansion [97] to calculate an approximate wavelength for a given mode number and polarization. We found that the best results are obtained when only the first three terms of the development are considered.

```
SchillerExpansion = nu/m - (p/Sqrt[m^2-1]) +
AiryAiZero[l]/(30*2^(2/3)*m*nu^(2/3))*(10*2^(1/3)*
((m^3*p*(3-2*p^2))/(m^2-1)^(3/2)-3*nu)+9*nu^(1/3)*AiryAiZero[l]);
```

Then, we can launch a root search for the desired wavelength (here in nm) and resonator dimension (again a is the radius in μm). The polarization in the example below has been set to TM by choice of the parameter $p = n_2^2/n_1^2$. For a TE mode the parameter p has to be replaced by $p = 1$. Then we compute the mode number M_{mode}.

```
wavelength = 532;
Mmode=Round[(nu/.FindRoot[(1000*2*Pi*n2*a/SchillerExpansion
/.{m->(n1/n2),p->(n2/n1)^2,l->1})==wavelength,{nu,300}])-0.5]
```

Higher order modes are calculated by setting the parameter l to the desired number of radial maxima. To find the starting values for the numerical search of the resonance frequency we rely again on the Schiller expansion and calculate the initial values $\left\{z_0^{\mathrm{TE}}, z_0^{\mathrm{TM}}, z_1^{\mathrm{TM}}\right\}$ for the wavenumber (in units of the inverse cavity radius $k \cdot a$) using the lines of code below.

```
z0TE=N[SchillerExpansion/n2/.{m->(n1/n2),p->1,nu->(Mmode+0.5),l->1}];
z0TM=N[SchillerExpansion/n2/.{m->(n1/n2),p->(n2/n1)^2,nu->(Mmode+0.5),l->1}];
z1TM=N[SchillerExpansion/n2/.{m->(n1/n2),p->(n2/n1)^2,nu->(Mmode+0.5),l->2}];
```

Then the resonant wavenumbers and frequencies are calculated using the following code.

```
k0TE=(z/a)/.FindRoot[n1*FracJ[Mmode,n1*z]-n2*FracY[Mmode,n2*z],{z,z0TE}];
k0TM=(z/a)/.FindRoot[(1/n1)*FracJ[Mmode,n1*z]-(1/n2)*FracY[Mmode,n2*z],{z,z0TM}];
k1TM=(z/a)/.FindRoot[(1/n1)*FracJ[Mmode,n1*z]-(1/n2)*FracY[Mmode,n2*z],{z,z1TM}];
```

λ [nm]	a [μm]	σ_{lat} [μm]	λ_r [nm]	V_s [μm^3]	V_{mode} [μm^3]
1311	30	2.131	311	3248	1815
1311	44	2.574	253	8619	3520
1311	51.6	2.777	238.5	12920	4653
1311	83.8	3.525	216	44398	11193
763	30	1.617	143	2481	924.3
763	39	1.836	134	4829	1476

Table A.2.: Evanescent field dimensions for different microsphere geometries used by Vollmer et al. in reference [37]. The values were used to obtain the frequency shifts in appendix B.

Calculating mode geometries

In this paragraph, we list the mode geometries for different toroid and microsphere geometries that were used by ourselves or competing groups. Moreover, we compare the analytical values to numbers that were obtained from simulations using finite element simulations with Comsol Multiphysics, which gives a good impression of the simulation error. The latter is important for toroidal geometries, as exact analytic solutions do not exist, and we have to rely on simulations.

We start by calculating the mode profiles of the microspheres used by Vollmer et al. in reference [37], which are discussed in detail in appendix B. The results are listed in Table A.2, and comparison with simulated values shows that the parameters, describing the geometry of the evanescent field, are reproduced with an error of $\lesssim 1\%$. The latitudinal extension σ_{lat} is well approximated by $\sigma_{lat} \approx R_{\text{major}}/\sqrt{M_{mode}}$ for mode numbers $M_{mode} > 100$.

For selected toroid geometries and wavelengths, the mode profile and the sensing mode volume were analytically calculated and simulated for a microsphere with a radius that matches the major radius of the toroid. We find that the The simulation overestimates the mode volume by $\sim 1.5\%$, the sensing mode volume however is underestimated by $\sim 9\%$. This is most likely due to the discontinuity of the electric field (for a TM mode) at the silica-water interface.

Using the values in the above tables, the electric field intensity of the evanescent field is easily written in its parametrized form.

$$|E(x,y,z)|^2 = V_s^{-1} \exp\left[-x^2/\sigma_{lat}^2\right] \exp\left[-z/\lambda_r\right] \tag{A.14}$$

In the case of a split mode, the intensity modulation along the y-direction is readily inserted by correction factor $\cos^2\left[M_{mode} \cdot (y/a)\right]$. In the chapter 3 such representation of the evanescent field was used to calculate to overlap of a lipid vesicle or a lipid pancake at random position with the evanescent field.

λ [nm]	a [μm]	σ_{lat} [nm]		λ_r [nm]	
688	35	1650 (1647)	**1009**	120 (121.4)	**118.0**
688	40	1762 (1759)	**1049**	117 (118.4)	**115.1**
532	32.72	1396 (1393)	**861.8**	86 (86.0)	**84.6**
		V_s [μm^3]		V_{mode} [μm^3]	
688	35	3494 (3212)	**1950.4**	1069 (1086)	**614.4**
688	40	4905 (4486)	**2647.0**	1364 (1383)	**755.3**
532	32.72	2774 (2515)	**1542.7**	701.7 (711.8)	**410.5**

Table A.3.: Geometric parameters for the fundamental modes of selected resonators, characterized by their major radius a and the wavelength λ. The table lists the latitudinal width and the exponential decay constant λ_r of the evanescent field. Moreover the mode volume V_{mode} and the sensing mode volume V_s are calculated. Here the **bold values** are obtained from a simulation of the toroidal geometry with a minor radius of 3.85 μm. The standard font values in the left column are obtained from the analytical calculation of the microsphere mode and the values in parentheses are simulated values for a microsphere. Apart from the sensing mode volume there is very good agreement between the analytical parameters and the simulated data.

Calculation of the single particle shift

Finally we use the knowledge of the mode profiles to calculate the maximum shift induced by a single particle. To this end we require the mode energy and thus the integral of the electric intensity over the entire volume, and the maximum value of the electric intensity outside the sphere. For the mode energy we re-assess reference [102] (and pay attention not to copy the minor mistake in equation (20)). Moreover we divide the integral by W_{lm}/k_0^4, as this is typically a very large value. In order to accelerate the numerical integration, we drop the derivative (as in equation A.3), which is typically a very minor approximation. Then we calculate the mode energy

```
Umode0TE=NIntegrate[k0TE^2*S0[r]^2*\[Epsilon][r],{r,a-6,a+2}];
Umode0TM=NIntegrate[Mmode*(Mmode+1)/r^2*T0[r]^2/\[Epsilon][r],{r,a-6,a+2}];
Umode1TM=NIntegrate[Mmode*(Mmode+1)/r^2*T1[r]^2/\[Epsilon][r],{r,a-6,a+2}];
```

at $r = a + 0.0001$. We add 0.1 nm to assure that we evaluate the function at the correct side of the discontinuity, even though this is normally not necessary.

```
E2max0TE=(k0TE^2*(S0[a+0.0001]/a)^2*Xsqrd[Mmode,Mmode,Pi/2]/W[Mmode,Mmode]);
E2max0TM=((T0[a+0.0001]/a^2)^2*Zsqrd[Mmode,Mmode,Pi/2]/W[Mmode,Mmode]/n2^4);
E2max1TM=((T1[a+0.0001]/a^2)^2*Zsqrd[Mmode,Mmode,Pi/2]/W[Mmode,Mmode]/n2^4);
```

the maximum evanescent intensity `E2max` yields the sensing mode volume V_s. Finally we compute the frequency shift induced by a 25 nm lipid vesicle with RI n_p. First we calculate the particle volume `Vp` in μm^3 for a membrane thickness of 4 nm; the RI contrast and the polarizability factor are included in the factor ξ (`Xi`).

```
np=1.46;
Vp=4*Pi/3*(25^3-21^3)*1*^-9;
Xi=(np^2-n2^2)*(2*np^2+n2^2)/np^2/(5+4*(21/25)^3);
Xi*Vp*E2max0TM/(2*Umode0TM)*5.6*^14
```

The resulting frequency shift is $\sim 365\,\mathrm{kHz}$, which is roughly a factor two smaller than one expects for a toroid. This is a direct consequence of the smaller mode confinement and thus smaller sensing volume of the microsphere.
The theoretical curves in the manuscript use a more refined geometric factor that includes the overlap integral between the particle and a parametrized version of the evanescent field.

B. Evaluation of published data with modified theory

In this appendix we survey the sensing results that were published by competing research groups, who work with high-Q WGM based sensors, and we will show that our modified theory – which was presented in section 1.3 – withstands their experimental findings. Here we concentrate on teams that have demonstrated single particle sensitivity using dispersive WGM based sensing methods, which are in principle the groups of Kerry Vahala at the California Institute of Technology, and Frank Vollmer together with Stephen Arnold (formerly Harvard University). The results of Lan Yang from Washington University, who records the frequency splitting in response to the adsorption of a single particle, rely on the scattering properties of the particle, rather than its dispersive properties and are not discussed here.

Results of Vollmer et al.

In this paragraph we discuss the results that were published by Vollmer et *al.* in the Proceeding of the National Academy of Science **105**(52):20701-20704,(2008) (reference [37]). The authors use microsphere resonators with different radii to detect single polystyrene beads with a radius of 250 nm and a refractive index of $n_p = 1.59$. The main point of the paper is, however, the detection of single Influenza A viruses. As the quality of the virus data is poor, it will not be discussed here, and we concentrate on the quantitative results given for the polystyrene beads.

We adapt Figure B.1 from the manuscript, where the authors plot the maximum frequency shifts that were obtained for resonators with different radii. The authors relate the frequency shift to the microsphere radius and find a dependency $\Delta\lambda_{\max} \propto$

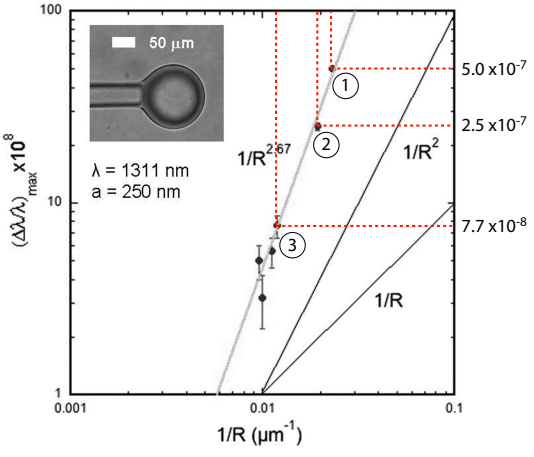

Figure B.1: Figure adapted from F. Vollmer *et al.* in PNAS **105**(52):20701-20704,(2008). The authors use silica microspheres with different radii R to measure the wavelength shift induced by polystyrene beads with a radius of $a = 250$ nm. Here the maximum wavelength shift is plotted against the inverse of the microsphere radius. For three measurements labeled $1 \to 3$, the wavelength shifts and sphere radii of 44.0 μm, 51.6 μm, and 83.8 μm were extracted from the graph. The values are listed in table B.1 and compared with theoretically expected numbers.

$R_{\mathrm{ms}}^{-2.67}$, similar to the relation that we obtained from simulations in section 3.1.[1] Here, we extract the data from the figure, and the values for the largest shifts are summarized in Table B.1. Then, we calculate the mode profiles for the corresponding microsphere geometries, both analytically and and numerically (the results are listed in appendix A.2) and compute the overlap with the 250 nm radius, solid polystyrene sphere. Using the single particle shift relation from section 3.5, we calculate the maximum expected frequency shift.

As an example, for a 44 μm microsphere resonator Vollmer and co-workers find a maximum relative wavelength shift of around $\Delta\lambda/\lambda \approx 5 \cdot 10^{-7}$. In their manuscript the authors supply (and use) two relations for data analysis: Equation (3) that yields the maximum wavelength shift as a function of the particle and the resonator radius, and Equation (4) which supposedly gives the particle radius, starting from a measured frequency shift.[2] There is, however, strong disagreement between the two relations, and the derivation of Equation (4) from Equation (3) is at least partially erroneous. In the end, the authors infer a radius of 211 nm that is slightly smaller than specified radius of 250 nm for the bead.[3] In Table B.1 we use Equation (3) of the manuscript to provide a theoretical value, as it seems to be more accurate.

	MS radius	$\Delta\lambda/\lambda$-shift	$\Delta\lambda/\lambda$-shift: Eqn. (3)	$\Delta\lambda/\lambda$-shift: Dobrindt
1	44.0 μm	5.0×10^{-7}	6.0×10^{-7} (+20.0%)	4.54×10^{-7} (−9.2%)
2	51.6 μm	2.51×10^{-7}	4.0×10^{-7} (+59.4%)	2.90×10^{-7} (+15.9%)
3	83.8 μm	7.65×10^{-8}	1.2×10^{-7} (+56.9%)	8.08×10^{-8} (+5.6%)

Table B.1.: Results of F. Vollmer *et al.* in PNAS, 105(52):20701-20704,(2008), which were extracted from the graph in Figure B.1. On the left hand side of the table, the experimental values are listed. On the right hand side the numbers are compared to the expected wavelength shift obtained from equation (3) in Vollmer et al. [37] and to the values resulting from the energy variation analysis. The numbers in parenthesis represent the deviation from the experimental values.

Moreover, we calculate the maximum frequency shift for the 44 μm resonator using the Teraoka relation from perturbation theory (cf. Equation 1.13), and we obtain an expected shift of $\Delta\lambda/\lambda = 1.8 \cdot 10^{-6}$, which is a factor$\sim$ 3.5 larger than the experimentally found value. Strikingly, with our modified theory that takes the full energy shift into account (cf. Equation 3.6), the expected shift is reduced by a factor $\div 3$, such that the final deviation is only −9.2%. We note that Equation (3) of the Vollmer manuscript has the interesting feature that the frequency shift for particles with a radius much larger than the evanescent decay length goes to zero.

[1] The different exponent, i.e., $R_{\mathrm{ms}}^{-2.67} \leftrightarrow R_{\mathrm{toroid}}^{-2.28}$, probably arises from the overlap of the bead with the evanescent field. For a smaller resonator the evanescent decay length is larger, such that the effect of the radius on the signal is larger compared to the situation in section 3.1, where only the peak intensity of the evanescent field is considered.

[2] The frequency shift is proportional to the particle volume, such that the conversion to a radius immediately divides the error by three.

[3] On the last page of their article, Vollmer et al. provide a table with measured wavelength shifts for particles of different size and the derived radius. Unfortunately the table contains errors, e.g. the radius in line two (which fits very well) is only obtained when a different wavelength (i.e. 1311 nm line one instead of 763 nm) is used.

Results of Lu et al.

In a second article on WGM based single particle sensing, Lu *et al.* use silica microtoroids to measure the frequency shift from single polystyrene beads with radii of 12.5 nm, 25 nm , and 50 nm [43]. Moreover, they report frequency shifts from single influenza viruses.
The results are, however, more difficult to follow, as the dimensions of the resonators are not mentioned in the manuscript. We therefore recalculate the expected frequency shifts for two resonators, with radii of $R = 35\,\mu$m and $R = 40\,\mu$m. In both cases the minor radius is $3.85\,\mu$m. At the wavelength of 688 nm, which was used by the authors, smaller resonators (that would yield a larger signal) are unlikely, as the radiation loss cutoff leads to a strong deterioration of the optical quality. In appendix A.2 the mode geometries and the sensing volumes for the chosen resonator sizes are listed. In particular we find inverse sensing mode volumes of $V_s^{-1} = 5.13 \times 10^{-4}\,\mu\text{m}^{-3}$ and $V_s^{-1} = 3.78 \times 10^{-4}\,\mu\text{m}^{-3}$, which are slightly smaller than the $V_s^{-1} = 6.42 \times 10^{-4}\,\mu\text{m}^{-3}$ for the resonator used for our single vesicle measurements.

Next, we adapt Figure B.2 (a) from the manuscript of Lu, where the authors show the maximum frequency shifts obtained during several measurements of polystyrene beads of different sizes. Moreover, a theoretical curve is plotted that agrees very well with the largest events for each particle size.
However, there are two curiosities about the Figure: on the one hand, the distribution of the data does not seem to follow the typical distribution, similar to what is plotted in panel (b). This might be owed to the fact, that only maximum shifts were recorded, such that large shifts are overrepresented in the figure. On the other hand, the theoretical curve is proportional to $\propto R^{2.70}$, even though the authors state in the text that they *"found it necessary to account for the actual field variation with the particle for the largest particle size"*. Integrating over a spherical particle in an exponentially decaying field yields however a law that is proportional to the particle radius cubed when the particle is much smaller than the decay length and grows only linear when the particle is much larger than the decay length. The effect of the transition should be visible in the theoretical curve.

We add the theoretical curves calculated for the $R = 35\,\mu$m and $R = 40\,\mu$m toroids to Figure B.2 (a) and find that the predicted frequency shifts ~ 1.5 and ~ 2 times smaller than the expected values from the authors. On the other hand, the curve for the $35\,\mu$m resonator fits the measured shifts for the larger particles reasonably well; the data points for the 12.5 nm particles are however clearly missed. This is also due to the bending of the curve towards smaller particle radii. In our model the curve is initially proportional to $\propto R^{2.93}$, decreasing towards $\propto R^{2.70}$ at a particle radius of 55 nm. For a particle much smaller than the decay length of the evanescent field (~ 100 nm), one expects that the signal grows with the particle volume, i.e., $\propto R^3$. The slope published by Lu *et al.* does not seem to consider this effect.

Moreover, it raises questions to obtain only 10 events from 51 distinct measurement runs as it is the case for the $R = 12.5$ nm polystyrene beads (cf. Figure B.2). The

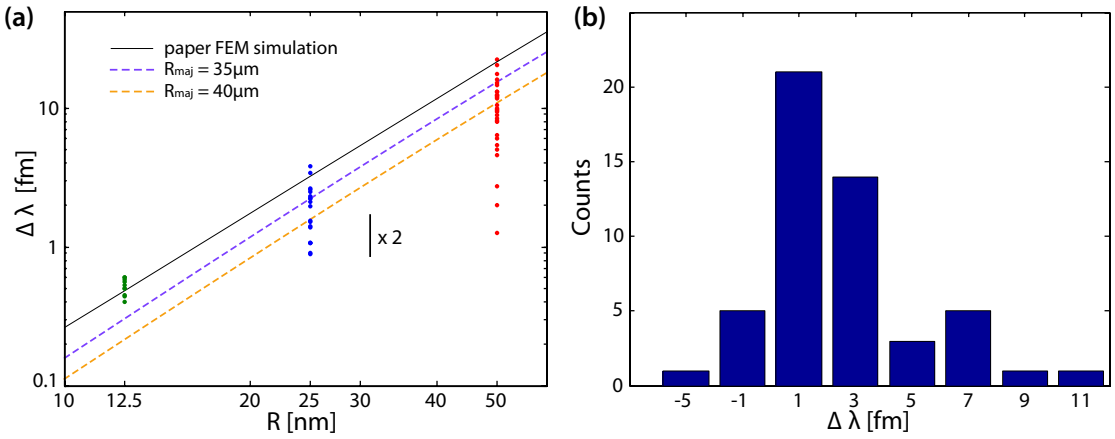

Figure B.2.: Two Figures adapted from T. Lu et al., PNAS, 108(15):5976-5979, (2011). (a) In the original paper the Figure is described with the wording: *"Measured wavelength-shift step sizes from many measurements using different microtoroids and bead sizes are compiled in [here (a)]. The data presented were compiled from* 51*,* 11*, and* 15 *distinct runs in which* 10*,* 25*, and* 43 *identifiable binding events were observed using* $R = 12.5\,\mathrm{nm}$ *(green cross),* $R = 25\,\mathrm{nm}$ *(blue cross), and* $R = 50\,\mathrm{nm}$ *(red cross) beads, respectively."* The solid line represents the maximum step size for a particle binding at the equator that was obtained by Lu *et al.* using finite element simulation. Here we added dashed lines, that correspond to the maximum shift, using the model that takes full particle polarization into account (cf. Equation 3.6) and assuming toroids with a major diameters of $70\,\mu\mathrm{m}$ and $80\,\mu\mathrm{m}$. For the larger particles, the $R_a = 35\,\mu\mathrm{m}$ line represents a relatively good fit to the data. Moreover, we note that the dashed lines display a slight curvature, which derives from the fact, that the model takes the finite decay length of the evanescent field into account. The curvature is not present in the theoretical curve of the original manuscript. (b) The wavelength step size histogram found for a measurement of Influenza A virus by Lu *et al.*. The measurement is not analyzed in the paper. Assuming a toroid with major radius of $40\,\mu\mathrm{m}$, a radius of 50 nm for the virus, and a refractive index of 1.5 for the virus, we obtain a maximum step size of 7.38 fm. Interestingly, for a non-split mode and monodisperse particles, theory predicts a histogram that features a peak at the position of the maximum step size, similar to what is observed in (b). This is due to the relatively broad intensity peak of the Gaussian field distribution in latitudinal direction, compared to the region of large field gradient, which makes a binding event close to the peak intensity more likely than a binding at, e.g. half intensity.

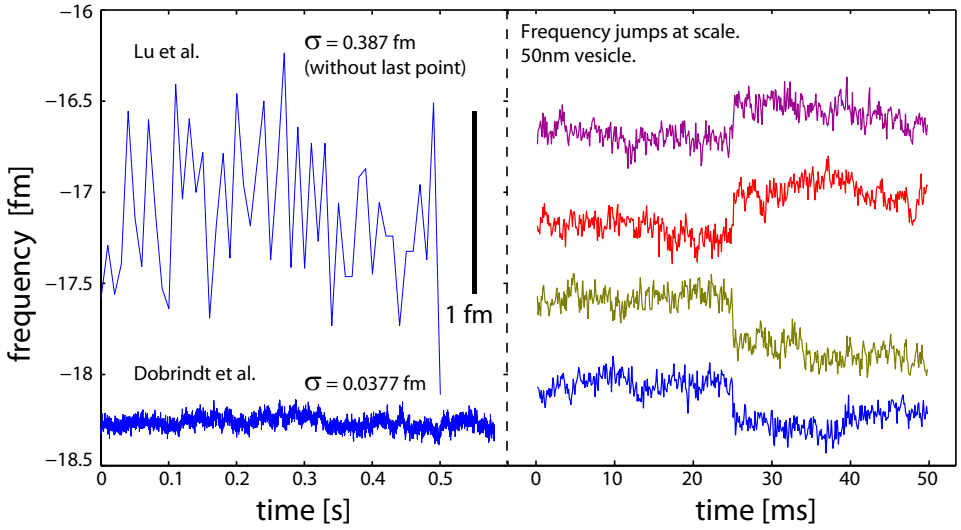

Figure B.3.: 10× improvement in frequency resolution. We extracted noise data from Lu *et al.* that did not undergo filtering and scaled our own noise floor (taken from Figure 5.1) to a femtometer scale. The time axis has also been correctly adapted. Moreover, we calculated the standard deviations σ, such that we can directly compare the performance. Indeed, we can show that the measurements presented in this thesis constitute a $\times 10$ improvement in frequency resolution. On the right hand side of the figure, we plot a selection of single vesicle frequency steps, however at a faster time scale. It becomes clear that the standard deviation σ or event $\sigma/\sqrt{2}$, as it was suggested by Lu, do not provide suited sensitivity measures for frequency step resolution.

authors claim a measurement uncertainty of $\sqrt{2}\sigma = 0.2\,\mathrm{fm}$ at a sampling rate of 100 Hz (private communication). In 51 measurements, each lasting around 200 s (which is a conservative estimate), one will statistically find around 11 frequency steps that exceed 0.6 fm, such that the smallest events can well be attributed to statistics. This estimate neglects the fact that a single exceptionally large value does not make a step, but the analysis shows that such a few events from a large number of measurements can well fall into the margin of error. Besides, the authors used a 3 point median filter for step enhancement.

In panel (b) of Figure B.2, we show the data of the single influenza A viruses measurement by Lu, which are not analyzed in the manuscript. Assuming a toroid radius of $R = 40\,\mu\mathrm{m}$ and a refractive index of 1.5 for protein, we calculate a theoretical maximum wavelength shift of 7.4 fm, which is in excellent agreement with the data and supports our model. For the $35\,\mu\mathrm{m}$ resonator a maximum shift of 10.0 fm is expected.

Finally, we extract a trace of noisy background from the Lu manuscript and compare it to the noise background, recorded during one of our measurement. In Figure B.3 we have scaled both curves to a femtometer scale, such that they can directly be compared. Indeed the factor $\times 10$ improvement in frequency resolution, which was, e.g., claimed in the abstract, is not just a striking value, but it is firmly linked to

experimental data.

In summary, we can state that the modified theoretical model, which takes the full energy shift induced by the particle into account, performs very well when re-evaluating published data.

C. Electronic setup

In this appendix we present a detailed layout of the electronic setup, which can serve as a blueprint for re-installation of teh system. Although the Pound-Drever-Hall lock itself is relatively simple, the devil is in the detail. Here we record the correction signal within the locking bandwidth ranging from DC to $\sim$ 100 kHz, which is sensitive to accoustic and electronic noise. In particular the prominent 50 Hz line and multiples are picked up easily from power supplies and via cross-talk, e.g. when cables pass behind the voltage transformers of electronic devices. To avoid low frequency noise, imortant coax cables are placed on the optical table, away from transformers and highvoltage cables. Moreover we can filter low frequency noise **directly** before demodulation, which is an additional advantage of the PDH scheme.

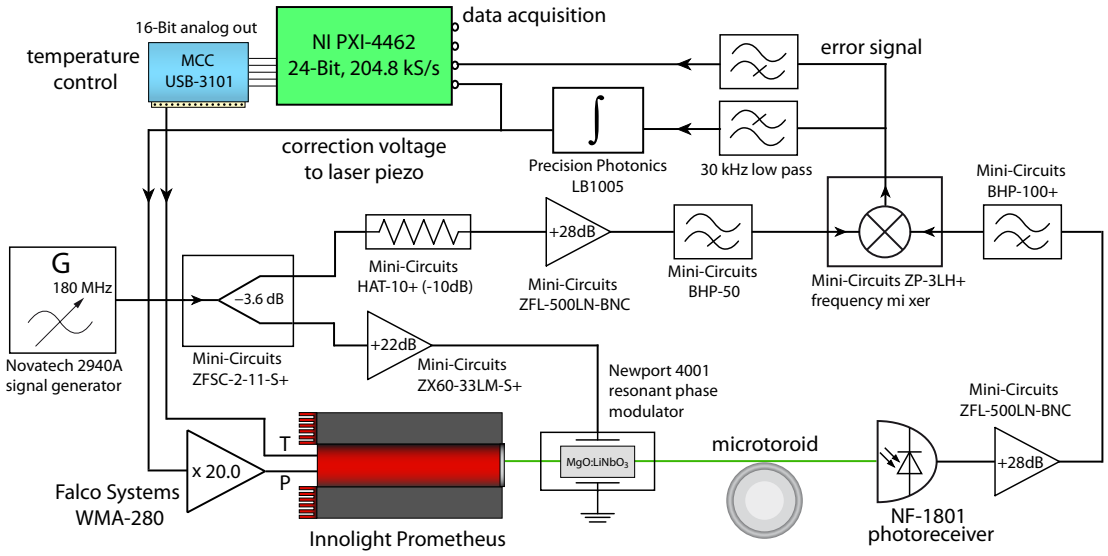

Figure C.1.: The layout of the electronic setup. The Novatech 2940A signal generator supplies a 180 MHz sinusoidal voltage (0 dBm) that is split and serves as an oscillator for modulation and demodulion. We note that both, the detected signal and the demodulation signal, undergo highpass filtering before demodulation at the frequency mixer. In this way low frequency electronic noise is efficiently blocked. The components were chosen with respect to matching entrance power levels and general low noise properties. In particular the installation of the Falco WMA-280 power amplifier for amplification of the correction signal acting on the laser piezo actuator (P), lead to a substantial reduction of electronic noise in the signal. A slow and coarse frequency correction is applied via the temperature of the laser crystal (T).

Noise is also easily picked up by the optical fibers, especially when 630 nm single mode fibers are used at a wavelength of 532 nm. In this case the poalrization of the light – and thus the coupling to the resonator and the slope of the error signal – is

especially susceptible to fiber bending and vibrations. Here we put a dense foam material inside a plastic channel for cable management and then use a sharp knife to cut about two thirds through the foam along the channel. An optical fiber that is placed in the slit is protected against vibration and bending. In fact we installed such fiber channel on our optical table, leading from the fiber port to the flow cell device.

Most components that we used in the electronic setup were bought from the company Minicircuits and different types of mixers, power dividers, and amplifiers where tested until an optimum configuration was found.[1] It is however important to note that the 30 kHzlow pass filter behind the electronic mixer is a simple home built first order filter. The Minicircuits filter usually have a higher order and lead to a phase delay long before the cutoff frquency. For example, the popular 1.9 MHz low pass filter already shows a $\pi/2$ phase shift at ~ 300 kHz. When such a filter is used on the error signal in a PDH lock, it leads to a corrupted phase and thus to a poor performance of the lock. On the other hand home built filters are problematic at high frequencies and in critical applications it is advantageous to combine, e.g., a 30 kHz first order low pass with a 1.9 MHz higher order Minicircuits low pass filter.

[1] This does not mean that improvement is not possible.

D. Covariance matrix approach

This appendix we present an implementation of the Heisenberg-Langevin equations to calculate and solve the covariance matrix [226, 249]. The implementation uses the language of the computer algebra program Mathematica and the code is formatted in a way that it can directly be copied and pasted to Mathematica notebooks.

The formalism is kept very general and does not differentiate between mechanical and optical modes. To provide a tangible example we use the code to compute all the relevant cooling limits for the single cavity mode case as they were described in chapter 6.

We start with a matrix $\mathbb{M}_N$ that describes the coupled mode equations of N modes. The rows of $\mathbb{M}_N$ contain the equations of motion of

$$\vec{v}_N = \left\{\hat{a}_1, \hat{a}_1^\dagger, \hat{a}_2, \hat{a}_2^\dagger, \ldots, \hat{a}_N, \hat{a}_N^\dagger\right\}^{\mathrm{T}}$$

and the dimension of $\mathbb{M}_N$ is accordingly $2N$. Moreover the system is subject to noise, which is represented by the inhomogeneity $\delta\vec{v}_N[t]$ and that will be specified later.

$$\frac{d}{dt}\vec{v}_N(t) = \mathbb{M}_N \cdot \vec{v}_N(t) + \delta\vec{v}_N[t]$$

It is our goal to obtain a matrix $\mathbb{C}_N$ that describes the equation of motion of the expectation values of all possible operator combinations, e.g., $\langle\hat{a}_1\hat{a}_2\rangle(t)$ or $\left\langle\hat{a}_1^\dagger\hat{a}_1\right\rangle$. The dimension of $\mathbb{C}_N$ is given by the total number of combinations.

$$\dim\{\mathbb{C}_N\} = 2N^2 + N$$

The problem here is mostly about operator ordering and in the first place we are defining a rule that assigns a row in the matrix to each combination of operators. We start with indexing the operators:

$$\begin{array}{rccccccc} \text{operator}: & \hat{a}_1 & \hat{a}_1^\dagger & \hat{a}_2 & \hat{a}_2^\dagger & \ldots & \hat{a}_n^\dagger \\ & \downarrow & \downarrow & \downarrow & \downarrow & & \downarrow \\ \text{index}: & 1 & 2 & 3 & 4 & \ldots & 2n \end{array}$$

Next we index the rows of $\mathbb{C}_n$ that shall be referred to by the index j. To cover all possible operator combinations, we proceed modewise and cover the correlation between the operators of one mode. Also we impose normal ordering on the operator products, which will become important later, when commutator have to be obeyed. The first three lines of $\mathbb{C}_N$ are always reserved for the first mode: $\left\{\left\langle\hat{a}_1^\dagger\hat{a}_1\right\rangle, \langle\hat{a}_1\hat{a}_1\rangle, \left\langle\hat{a}_1^\dagger\hat{a}_1^\dagger\right\rangle\right\}$. The next three lines describe the operator products of the second mode, following the same ordering, such that the first $3N$ lines of $\mathbb{C}_N$ are reserved for products within one mode. The next block in $\mathbb{C}_N$ describes the products between the first two modes: $\left\{\left\langle\hat{a}_1^\dagger\hat{a}_2\right\rangle, \left\langle\hat{a}_1\hat{a}_2^\dagger\right\rangle, \langle\hat{a}_1\hat{a}_2\rangle, \left\langle\hat{a}_1^\dagger\hat{a}_2^\dagger\right\rangle\right\}$. It is a valid question, whether operators such as $\hat{a}_1^\dagger$ and $\hat{a}_2$ still commute, when their equations of motion are coupled. The dimension of the covariance matrix:

```
DimCovar[m_]:=2*m^2+m;
```

Next we define a couple of routines that relate the index pairs of operators to a row in $\mathbb{C}_N$ that describes the motion of the corresponding covariance.

```
BlockIndex[n_,m_]:=IntegerPart[(n-3*m-1)/4+1];
qIndex[n_,m_]:=IntegerPart[3/2+Sqrt[2*BlockIndex[n,m]-7/4]];
IndexPair[n_,m_]:={BlockIndex[n,m]-(qIndex[n,m]-1)*(qIndex[n,m]-2)/2,qIndex[n,m]};
OpIndex[k_]:={IntegerPart[(k-1)/2]+1,Mod[k-1,2]};
SubIndexEven[s_,k_]:=If[(s==1 && k==0)||(s==0 && k==1),0,If[(s==0 && k==0),1,2]];
SubIndexOdd[s_,k_]:=If[(s==1 && k==0),0,If[(s==0 && k==1),1,If[(s==0 && k==0),2,3]]];
Block3Mat={{1,0},{0,0},{1,1}};
Block4Mat={{1,0},{0,1},{0,0},{1,1}};
```

And finally we build a couple of routines that relate the index pairs of operators to a row in $\mathbb{C}_N$ and vice versa.

```
OpPairToIndex[j_,m_]:={tj=OpIndex[j[[1]]];tk=OpIndex[j[[2]]];
If[tj[[1]]==tk[[1]],
3*(tj[[1]]-1)+SubIndexEven[tj[[2]],
tk[[2]]]+1,
3*m+4*((Max[tj[[1]],tk[[1]]]-1)*(Max[tj[[1]],tk[[1]]]-2)/2+Min[tj[[1]],tk[[1]]]-1)
+SubIndexOdd[tj[[2]],tk[[2]]]+1]}[[1]];

IndexToOpPair[n_,m_]:=If[n<=3*m,te=IntegerPart[(n-1)/3]+1;
2*{te,te}-{1,1}+Block3Mat[[n-3*(te-1)]],
2*IndexPair[n,m]-{1,1}+Block4Mat[[n-3*m-4*(BlockIndex[n,m]-1)]]];

Commutation[j_,m_]:={tj=OpIndex[j[[1]]];tk=OpIndex[j[[2]]];If[(tj[[1]]==tk[[1]])&&
(tj[[2]]==0)&&(tk[[2]]==1),1,0]}[[1]];
```

We show an example to demonstrate the functioning of the routines defined above. As such we take the case of three bosonic fields, i.e., $N = 3$, which results in 6 operator equation of motion and the dimension of the covariance matrix is correspondingly 21.

```
DimCovar[3]
Out[...]= 21
```

The index j therefore runs from $1 \to 21$. We take a look at the operator product described by the rows of $\mathbb{C}_N$, using the previously defined function `IndexToOpPair`:

```
Table[IndexToOpPair[n,3],{n,1,21}]
Out[...]= {{2,1},{1,1},{2,2},{4,3},{3,3},{4,4},{6,5},{5,5},{6,6},{2,3},{1,4},
{1,3},{2,4},{2,5},{1,6},{1,5},{2,6},{4,5},{3,6},{3,5},{4,6}}
```

This illustrates the ordering rule defined above and allows us to find the operator belonging to a certain line of the covariance matrix. In particular, if the first two fields were to describe optical modes and the third one corresponded to a mechanical mode, the mechanical occupation would be given by line 7 of the covariance matrix, which describes $\left\langle \hat{a}_3^\dagger \hat{a}_3 \right\rangle$, combining the operators with indices 6 and 5.
Lastly we define a rule to create a transformation matrix that is used to rotate the covariance matrix, such that it describes the quadratures of the complex operator products. This eliminates the complex dimension from the equation and removes a redundant multi-dimensionality. The matrix is block-diagonal and consists of sub-matrices that rotate the blocks of the covariance matrix.

```
MakeTransformMatrix[m_]:={md={};ld={};ud={};
For[j=1,j<=m,j++,AppendTo[md,{1,1,-I}];AppendTo[ld,{0,I,0}];AppendTo[ud,{0,1,0}];];
For[j=1,j<=m*(m-1)/2,j++,AppendTo[md,{1,-I,1,-I}];
AppendTo[ld,{I,0,I,0}];AppendTo[ud,{1,0,1,0}];];
(DiagonalMatrix[Flatten[md]]+DiagonalMatrix[Delete[Flatten[ld],DimCovar[m]],-1]
+DiagonalMatrix[Delete[Flatten[ud],DimCovar[m]],1])}[[1]];
```

Practical example: 2 modes

In the last section we have defined all the routines that are required to build a covariance matrix from a matrix that describes the (linear) equations of motion of arbitrary quantum fields. Here we give an example for one optical mode ($\hat{a}$) that is coupled to a mechanical mode ($\hat{b}$) via the coupling rate g_m (i.e. coupling $\hbar\left(\hat{a}+\hat{a}^\dagger\right)\left(\hat{b}+\hat{b}^\dagger\right)$. Then the motion is described by the matrix $\mathbf{M}_2$.

```
M2:=
{{-\[Kappa]/2+I*\[CapitalDelta],0,-I*Subscript[g,m]/2,-I*Subscript[g,m]/2},
{0,-I*\[CapitalDelta]-\[Kappa]/2,I*Subscript[g,m]/2,I*Subscript[g,m]/2},
{-I*Subscript[g,m]/2,-I*Subscript[g,m]/2,
-Subscript[\[CapitalGamma],m]/2-I*Subscript[\[CapitalOmega],m],0},
{I*Subscript[g,m]/2,I*Subscript[g,m]/2,0,
-Subscript[\[CapitalGamma],m]/2+I*Subscript[\[CapitalOmega],m]}};
MatrixForm[M2]
```

Pasting the code to Mathematica and evaluating the input yields the matrix that describes the equation of motion of the two fields.

$$\mathrm{M2} = \begin{pmatrix} i\Delta - \frac{\kappa}{2} & 0 & -\frac{ig_m}{2} & -\frac{ig_m}{2} \\ 0 & -i\Delta - \frac{\kappa}{2} & \frac{ig_m}{2} & \frac{ig_m}{2} \\ -\frac{ig_m}{2} & -\frac{ig_m}{2} & -\frac{\Gamma_m}{2} - i\Omega_m & 0 \\ \frac{ig_m}{2} & \frac{ig_m}{2} & 0 & -\frac{\Gamma_m}{2} + i\Omega_m \end{pmatrix} \tag{D.1}$$

As before, Δ is the detuning of the drive from resonance, Ω_m is the mechanical resonance frequency, κ and Γ_m are the decay rates of the modes, and g_m describes

the optomechanical coupling. We use an outer For-loop to walk through the rows of the covariance matrix `CVM` a subsequently fill up the entries. First we create the vector `oi` that contains the operator pairs described by `CVM`.

```
SMat := M2;

fields = Dimensions[SMat][[1]]/2;

nV = Table[0, {n, 1, DimCovar[fields]}];
CVM = DiagonalMatrix[nV];

For[n = 1, n <= DimCovar[fields], n++, oi = IndexToOpPair[n, fields];
For[j = 1, j <= 2*fields, j++, oit = {j, oi[[2]]};
CVM[[n,OpPairToIndex[Sort[oit],fields]]]+=SMat[[oi[[1]],j]];
nV[[n]]+=Commutation[oit, fields]*SMat[[oi[[1]], j]];];
For[j = 1, j <= 2*fields, j++, oit = {oi[[1]], j};
CVM[[n,OpPairToIndex[Sort[oit],fields]]]+=SMat[[oi[[2]],j]];
nV[[n]] += Commutation[oit, fields]*SMat[[oi[[2]], j]];];];

transMat = MakeTransformMatrix[fields];

CVMq := FullSimplify[transMat.CVM.Inverse[transMat]];
nVq := FullSimplify[transMat.nV];
```

Evaluating the code above yields the covariance matrix of the quadratures.

CVMq =

$$\begin{pmatrix}
-\kappa & 0 & 0 & 0 & 0 & 0 & 0 & -\frac{g_m}{2} & 0 & \frac{g_m}{2} \\
0 & -\kappa & 2\Delta & 0 & 0 & 0 & 0 & g_m & 0 & -g_m \\
0 & -2\Delta & -\kappa & 0 & 0 & 0 & g_m & 0 & g_m & 0 \\
0 & 0 & 0 & -\Gamma_m & 0 & 0 & 0 & \frac{g_m}{2} & 0 & \frac{g_m}{2} \\
0 & 0 & 0 & 0 & -\Gamma_m & -2\Omega_m & 0 & -g_m & 0 & -g_m \\
0 & 0 & 0 & 0 & 2\Omega_m & -\Gamma_m & g_m & 0 & g_m & 0 \\
0 & 0 & \frac{g_m}{2} & 0 & 0 & \frac{g_m}{2} & \frac{1}{2}(-\kappa-\Gamma_m) & -\Delta-\Omega_m & 0 & 0 \\
g_m & \frac{g_m}{2} & 0 & -g_m & -\frac{g_m}{2} & 0 & \Delta+\Omega_m & \frac{1}{2}(-\kappa-\Gamma_m) & 0 & 0 \\
0 & 0 & -\frac{g_m}{2} & 0 & 0 & -\frac{g_m}{2} & 0 & 0 & \frac{1}{2}(-\kappa-\Gamma_m) & \Delta-\Omega_m \\
g_m & \frac{g_m}{2} & 0 & g_m & \frac{g_m}{2} & 0 & 0 & 0 & -\Delta+\Omega_m & \frac{1}{2}(-\kappa-\Gamma_m)
\end{pmatrix}$$

Moreover the vector `nVq` contains all the constants that were obtain from operator commutations and that represent the quantum nature of the fields. Interestingly the

$$\mathrm{nVq} = \{0, 0, 0, 0, 0, 0, 0, 0, 0, g_m\} \tag{D.2}$$

```
LinearSolve[ CVMq /. {Subscript[\[CapitalGamma], m] -> 0,
\[CapitalDelta] -> -Subscript[\[CapitalOmega], m]}, -nVq][[ 4]] // FullSimplify
```

Here we query the entry fourth entry of the solution vector, which corresponds to the excess mechanical occupation due to quantum noise $\left\langle \hat{a}_m^\dagger \hat{a}_m \right\rangle$

$$\frac{\kappa^4 - 2\kappa^2 g_m^2 + 4\left(\kappa^2 + 2g_m^2\right)\Omega_m^2}{16\Omega_m^2\left(\kappa^2 - 4g_m^2 + 4\Omega_m^2\right)} \quad \begin{matrix} g_m = 0 \\ \longrightarrow \end{matrix} \quad \frac{\kappa^2}{16\Omega_m^2} \tag{D.3}$$

As g_m is limited by $\kappa/2$ in a physically meaningful situation, it can be neglected in the above equation. The actual development of the expression in the small quantities $g_m$and κ

```
Series[%,{\[Kappa],0,2},{Subscript[g,m],0,2}]// FullSimplify
```

yields the power dependent quantum limit in Equation 6.8 and which is plotted in Figure 7.6.

To obtain the cooling limit imposed by the cavity decay rate, we modify the noise vector and include the classical noise contribution from the heat bath coupled to the mechanics.

$$\mathrm{nVq} = \{0, 0, 0, \Gamma_m n_m, 0, 0, 0, 0, 0, 0\} \tag{D.4}$$

```
nVq = {0, 0, 0, Subscript[\[CapitalGamma], m] nm, 0, 0, 0, 0, 0, 0};

LinearSolve[ CVMq /. {
\[CapitalDelta] -> -Subscript[\[CapitalOmega], m]}, -nVq][[ 4]] // FullSimplify
```

In the above derivation we explicitly kept the mechanical dissipation rate Γ_m, which was set to zero in the previous example. The resulting expression is a rather lengthy fraction that requires additional simplification. To this end we factorize the nominator end denominator separately and keep only terms proportional to Ω_m^6. This is justified because $\kappa, g_m \ll \Omega_m$. Then we obtain the much simpler fraction

$$n_f = \Gamma_m n_m \frac{g_m^2 + \kappa\left(\kappa + \Gamma_m\right)}{\left(\kappa + \Gamma_m\right)\left(g_m^2 + \kappa\Gamma_m\right)} \approx n_m \frac{\Gamma_m}{\kappa} \frac{g_m^2 + \kappa^2}{g_m^2 + \kappa\Gamma_m}$$

This is exactly the result in reference [2], which was used for data analysis by Teufel et al. [196].

Lastly we study the influence of a noisy driving field on the final occupancy of the mechanical oscillator, which is achieved by setting the quadrature noise vector to

$$\mathrm{nVq} = \{\kappa n_p, 0, 0, 0, 0, 0, 0, 0, 0, 0\}\,. \tag{D.5}$$

This is because the first line of the covariance matrix `CVM` describes the occupancy of the optical mode $\langle \hat{a}^\dagger \hat{a} \rangle$. Here the mechanical decay rate is again set to zero, because its influence at zero coupling, i.e. $g_m \to 0$, can always be neglected compared to κ.

```
nVq = {\[Kappa] np, 0, 0, 0, 0, 0, 0, 0, 0, 0};

LinearSolve[ CVMq /. {Subscript[\[CapitalGamma], m] -> 0,
\[CapitalDelta] -> -Subscript[\[CapitalOmega], m]}, -nVq][[ 4]] // FullSimplify
```

We obtain a solution that can again be simplified by development up to second order in κ and g_m.

$$\begin{aligned} n_f &= \frac{n_p\left(\kappa^4+12\kappa^2\Omega_m^2+32\Omega_m^4-2g_m^2\left(\kappa^2+12\Omega_m^2\right)\right)}{8\Omega_m^2\left(\kappa^2-4g_m^2+4\Omega_m^2\right)} \\ &\approx n_p+n_p\frac{\kappa^2/2+g_m^2}{4\Omega_m^2} \end{aligned}$$

This reproduces the result of reference [2] and shows that it is never possible to cool the mechanical oscillator below the occupation of the optical drive.
To gain better understanding for the system it is a good exercise to solve for the optical occupation number in line 1 of `CVM` and to watch how the noise in the optical field increases with stronger cooling.

Important questions to be raised

Before creating any confusion, we emphasize that the above results are to the best of our knowledge correct. They have been derived using different approaches (cf. chapter 6) and they were experimentally confirmed by Teufel and co-workers [196, 212].
However there are two curiosities that we want to address, the first of which has already been mentioned, i.e. the question whether the field operator continue to commute even when they are not orthogonal anymore. The second question concerns the quantum nature of the mechanical oscillator. In the final result of the chapter 6 calculation one obtains a noise term $\propto (n_p + 1/2)$, where the $1/2$ leads to the so called quantum limit of $\kappa^2/16\Omega_m^2$. This gives the impression as if the quantum limit were a consequence exclusively of the quantum nature of the photon field. Moreover we have shown in chapter 7 that the quantum contribution of the vacuum noise operators acting on the mechanics goes to zero in back-action cooling because of its power independence. In the quantum Langevin approach the quantum nature of the field operators is not *a priori* imposed via commutation relations that are carved in stone, but the commutation rules are established via properly defined vacuum noise operators. Therefore the origin of a particular effect is more apparent and the quantum limit – even the ground state uncertainty of $1/2$ – can be related solely to radiation pressure fluctuations and thus to the quantum nature of the light. In this case no judgment about the quantum nature of the mechanics is possible.

In contrast, for the covariance matrix approach that is presented here, it seems as if the commutators of the mechanics and optics shared the responsibility for the quantum limit and that each contributed $g_m/2$ to the inhomogeneity in the vector `nVq`. One could thus be tempted to switch of the commutator of the mechanical mode here to simulate classical behavior and to see what happens. Indeed this would violate the rules of the game. The commutation of the operators during

the assembly of the covariance matrix, e.g., $[\hat{a}_1(t), \hat{a}_2(t)]_{t\to\infty} = 0$, only works when the original commutation rules are the same for all players. Otherwise complicated commutators have to be considered and even complex terms show up in the vector `nVq` that are a consequence of broken symmetry.
In a similar fashion the photon shot noise in chapter 7, which nicely evaluates to $1/2 + n$, independent of the number of contributing modes, will take a complex, pathological form when the quantum nature of one optical field is switched off, while being kept for the others.

In summary we conclude that the covariance approach provides a compact and fast way to compute steady state covariances of complex systems. The physical meaning that can be associated with the solution remains however limited. The physical intuition will be satisfied in the following appendix where a different approach based on the quantum Langevin equations is presented. In this case it is the vacuum noise operators that introduce the quantum nature to the problem and that sustain the commutation relations of the physical quantities. The approach is in a sense more rigorous as it allows us to separate the contributions to the noise and imprecision.

E. Heisenberg-Langevin approach

In this appendix we present the algorithm that was used to calculate the caviy output noise spectral densities from the quantum Langevin equations. It was already mentioned a couple of times in chapter 7 that the power of the algorithm is based on the ability to include a number of correlated and uncorrelated noise sources following a deterministic scheme, which eventually helps to prevent mistakes. Therefore the code can be used to efficiently calculate and simplify complicated spectra. As an arbitrary example we take a look at the mixing term $S_{xF,\theta}$.

$$S_{xF,\theta}(\Omega) \sim \int \frac{d\Omega'}{2\pi} \left\langle \hat{X}_{x,\theta}[\Omega] \hat{X}_{F,\theta}[-\Omega'] \right\rangle$$

Both operators, $\hat{X}_{x,\theta}[\Omega]$ and $\hat{X}_{F,\theta}[\Omega]$, linearly depend on a number of different noise operators and the "evaluation by hand" of the equation above becomes very time consuming. Here we take Mathematica's `AngleBracket`-operator $\langle \cdot, \cdot \rangle$, which is a bilinear function of two arguments, and define it in a way that it automatically treats quadrature noise operators according to the rules defined in section 7.2.1. For this to work, we introduce a unique representation for quadrature noise operators that redefines Mathematica's `CircleTimes`-operator ($\otimes$) with a capital $\mathtt{X}_\mathtt{s}$ or $\mathtt{Y}_\mathtt{s}$ (neccesarily including a subscript) at its right hand side according to following rule.

$$\begin{aligned} (\mathtt{x}) \otimes \mathtt{X}_\mathtt{s} &\rightarrow \{\mathtt{x}, \mathtt{s}, 1, \mathtt{Random[Real]}\} \\ (\mathtt{x}) \otimes \mathtt{Y}_\mathtt{s} &\rightarrow \{\mathtt{x}, \mathtt{s}, -1, \mathtt{Random[Real]}\} \end{aligned}$$

The Mathematica operator expression is automatically converted to a list, where the first element is the argument to the left hand side of the $\otimes$, the second element contains the subscipt, which names the noise source (e.g. `in` for noise entering through the input channel), the third element is either 1 or -1 to identify amplitude and phase noise, and lastly there is a random number that makes the list unique.
The code that defines the $\otimes$ operator in Mathematica, as well as the `AngleBracket`-operator, is listed below. It can directly be pasted into a Mathematica notebook. For this tutorial to work, we found it neccesary to define the $\otimes$-operator twice for each quadrature. The first two definitions cope with a subscript representation, which prints as $\mathtt{X}_\mathtt{s}$ and is entered by typing `X`, then `Ctrl` + `m`, then `s` in Mathematica. When pasting the code from this pdf, however, the subscript is often represented as `Subscript[X, s]`, which is taken care of in the two additional defining lines of the $\otimes$-operator.

```
MakeExpression[RowBox[{x_,"\[CircleTimes]",SubscriptBox["Y",n_]}],
StandardForm]:=MakeExpression[RowBox[{"ToString[{",x,",",n,",",1,",
```

```
Random[Real]},InputForm]"}],StandardForm];

MakeExpression[RowBox[{x_,"\[CircleTimes]",SubscriptBox["X",n_]}],
StandardForm]:=MakeExpression[RowBox[{"ToString[{",x,",",n,",",-1,",
Random[Real]},InputForm]"}],StandardForm];

MakeExpression[RowBox[{x_,"\[CircleTimes]",RowBox[{"Subscript","[",RowBox[
{"Y",",",n_}],"]"}]}],StandardForm]:=MakeExpression[RowBox[{"ToString[
{",x,",",n,",",1,",Random[Real]},InputForm]"}],StandardForm];

MakeExpression[RowBox[{x_,"\[CircleTimes]",RowBox[{"Subscript","[",RowBox[
{"X",",",n_}],"]"}]}],StandardForm]:=MakeExpression[RowBox[{"ToString[
{",x,",",n,",",-1,",Random[Real]},InputForm]"}],StandardForm];

\[Nu]Y[a_,b_,s_]:=If[a*b>0,1+2*Subscript[n,s],If[a>0&&b<0,
-I*Subscript[\[CapitalKappa],s],I*Subscript[\[CapitalKappa],s]]];

comm[a_,b_]:=If[x=ToExpression[a];y=ToExpression[b];x[[2]]===y[[2]],
\[Nu]Y[x[[3]],y[[3]],x[[2]]]*(y[[1]]/.\[CapitalOmega]->-\[CapitalOmega])*x[[1]],0];

AngleBracket[a_,b_]:=Distribute[f[a,b]]/.f->comm//Expand//FullSimplify;
```

Next we address the syntax and functioning of the `AngleBracket`-operator $\langle\cdot,\cdot\rangle$. When we enter a complex expression that depending on many noise operators, according to the noise representation defined by the $\otimes$-operator, it is immediately broken down to a sum of the lists that represent the noise and the argument. The `AngleBracket`-operator now calls the `Distribute`-function, such that – according to the bilinear nature of the operator – one ends up with a sum of `AngleBracket`s with only one noise argument on each side.

These are then evaluated according to the rules in section 7.2.1, which are here implemented in the `comm`-function. Importantly the frequency variable of the argument must be denoted by capital omega Ω, such that the algorithm can automatically switch signs when required by the rules. The index of the noise, the letter s in the above example, "names" different operators and has to match for corresponding phase and amplitude noise. Below we give some examples that show how the operators work and that have NO PHYSICAL MEANING.

$$\begin{aligned}
\langle(1+\Omega)\otimes X_s,(2\Omega)\otimes X_s\rangle &= -2\Omega(1+\Omega)(1+2n_s)\\
\langle(1+\Omega)\otimes Y_s,(2\Omega)\otimes Y_s\rangle &= -2\Omega(1+\Omega)(1+2n_s)\\
\langle(1+\Omega)\otimes X_s,(2\Omega)\otimes Y_s\rangle &= -2i\Omega(1+\Omega)K_s\\
\langle(1+\Omega)\otimes X_s+(2\Omega)\otimes Y_s,(2\Omega)\otimes Y_s\rangle &= 4\Omega^2(1+2n_s)-2i\Omega(1+\Omega)K_s\\
\langle(1+\Omega)\otimes X_s+(2\Omega)\otimes Y_s,(\dots)\otimes Y_k\rangle &= 0
\end{aligned}$$

For the correlations between amplitude and phase noise, e.g. in line three and four, a marker K_s appears, which should be set to either one or zero. (The letter is `\[CapitalKappa]` and not `K`.) For $K_s\to 0$ a physical spectrum is automatically symmetrized (which is not true for the carelessly chosen example), while $K_s\to 1$ results in the full "quantum" spectrum that cover effects like sideband assymmetry.

The symmetry considerations are adressed on the first pages of reference [222].
In the last line the noise index on the right hand side was changed and – by definition – noises with different indices are not correlated such that the whole statement gives zero. After having evaluated the code that defines the operators, one can paste and evaluate the code for the examples above.

```
\[LeftAngleBracket] (1+\[CapitalOmega])\[CircleTimes]Subscript[X,s],
(2\[CapitalOmega])\[CircleTimes]Subscript[X,s] \[RightAngleBracket]
\[LeftAngleBracket] (1+\[CapitalOmega])\[CircleTimes]Subscript[Y,s],
(2\[CapitalOmega])\[CircleTimes]Subscript[Y,s] \[RightAngleBracket]
\[LeftAngleBracket] (1+\[CapitalOmega])\[CircleTimes]Subscript[X,s],
(2\[CapitalOmega])\[CircleTimes]Subscript[Y,s] \[RightAngleBracket]
\[LeftAngleBracket] (1+\[CapitalOmega])\[CircleTimes]Subscript[X,s]+
(2\[CapitalOmega])\[CircleTimes]Subscript[Y,s],
(2\[CapitalOmega])\[CircleTimes]Subscript[Y,s] \[RightAngleBracket]
\[LeftAngleBracket] (1+\[CapitalOmega])\[CircleTimes]Subscript[X,s]+
(2\[CapitalOmega])\[CircleTimes]Subscript[Y,s],
(2\[CapitalOmega])\[CircleTimes]Subscript[Y,k] \[RightAngleBracket]
```

In the following we calculate the major results found for the triple mode transducer and the general single mode transducer. The author encourages the reader to play with the code and the parameters to see how the result changes.

E.1. Three mode transducer

Before starting with the calculations of this section, the code that defines the three mode matrix S_3 needs to be defined. It is found in a supplementary paragraph at the very end of this appendix. Moreover we start with a calculation where cavity loss is not present an noise enters only through the input coupler. An additional vacuum loss channel is introduced in the next section that covers the single mode transducer (1RT). For the calcluation of the triple mode transducer with a lossy cavity it is sufficient to exchange the matrix and the `T`-vector in the code of the 1RT, namely `Sw1` $\rightarrow$ `Sw3` and `T1` $\rightarrow$ `T3`.

Calculation of the photon shot noise

In this paragraph we demonstrate how to calculate the photon shot noise for the three resonance transducer. Before pasting the code below, the matrix Sw_3 and the vector $T_3(\theta)$ need to defined. Apart from that the code is identical to the definition of the shot noise fluctuations in equation 7.53.

```
Xx3=(\[Kappa]*T3[\[Theta]].Sw3.T3[0]-
Cos[\[Theta]])\[CircleTimes]Subscript[X,in] +
(\[Kappa]*T3[\[Theta]].Sw3.T3[Pi/2]- Sin[\[Theta]])\[CircleTimes]Subscript[Y,in];

(1/2)*\[LeftAngleBracket] Xx3,Xx3 \[RightAngleBracket]/.{
Subscript[\[CapitalKappa],in]->\[CapitalKappa]}//FullSimplify
```

Calculation of the backaction force spectral density

We use the previously defined matrices and vectors to directly implement equation 7.57. We exclude however the prefactor $\sqrt{\kappa}\hbar g_m/x_0$, whose square will be mulitplied with the result. Stripped from this prefactor, the expression for the radiation pressure force in our notation breaks down to

$$(T_3(0)\cdot \mathrm{Sw}_3\cdot T_3(0))\otimes X_1 + (T_3(0)\cdot \mathrm{Sw}_3\cdot T_3(\pi/2))\otimes Y_1$$

In the code example below we calculate the radiation pressure force spectral density.

```
XF3=(T3[0].Sw3.T3[0])\[CircleTimes]Subscript[X,1]+
(T3[0].Sw3.T3[Pi/2])\[CircleTimes]Subscript[Y,1];

SFF3 = (1/2)*\[LeftAngleBracket] XF3,XF3
\[RightAngleBracket]/.Subscript[n,1]->0
```

$$S_{\mathrm{FF}}(\Omega) = \frac{\kappa\hbar^2 g_m^2}{x_0^2}\frac{2\left(\Omega_m^2-3\Omega^2\right)^2}{\kappa^2\left(\Omega_m^2-3\Omega^2\right)^2+4\Omega^2\left(\Omega_m^2-\Omega^2\right)^2}$$

The calculation for the one or two resonance case is the very same, only the vector and the matrix need to be renamed. Here we do not differentiate between the different loss channels, as the noise operators are uncoorrelated and enter the exactly same way. If one were to include them separately, the loss rates would at up and one obtains the same result as if one directly had used the total loss rate (as we did here).

Calculation of the transduction function

In this paragraph we calculate the last missing piece, the transduction function $\lambda(\theta)$.

$$\begin{aligned}\lambda_\theta(\Omega) &= \frac{g_m}{x_0}\sqrt{\eta_c\kappa}\,\vec{T}_\theta^{\mathsf{T}}\cdot\tilde{\mathbf{S}}[\Omega]\cdot\vec{T}_{\pi/2}\\ &\to \frac{g_m}{x_0}\sqrt{\eta_c\kappa}\,[T_3(\theta)\cdot \mathrm{Sw}_3\cdot T_3(\pi/2)]\end{aligned}$$

Then the implementation is straight forward.

```
lambda3=T3[\[Theta]].Sw3.T3[Pi/2] // FullSimplify
```

$$\lambda_3(\theta) = \frac{g_m}{x_0}\sqrt{\eta_c\kappa}\frac{2i\left(\Omega_m^2-3\Omega^2\right)\sin(\theta)}{2\Omega\left(\Omega_m^2-\Omega^2\right)+\kappa\left(\Omega_m^2-3\Omega^2\right)}$$

We calculate the absolute value of the
Here it is convenient to replace $\Omega\to-\Omega$ in $\lambda_3(\theta)$ to obtain its complex conjugate.

```
Sxx3=(1/2)/(lambda3*(lambda3/.\[CapitalOmega]->
-\[CapitalOmega]))//FullSimplify

Sxx3*SFF3
```

(given by the omitted prefactors) and minimized for $\theta = \pi/2$. This finding confirms that the mechanical signal is transduced to the phase quadrature.

E.2. The very general single mode case

Evaluating the code below, we define the matrices $\mathbf{S}_1$ (`S1`), $\tilde{\mathbf{S}}_1[\Omega]$ (`Sw1`), and the vector $\vec{T}_\theta$ (`T1`) for the general single mode transducer.

```
S1 := {{-\[Kappa]/2, \[CapitalDelta]}, {-\[CapitalDelta], -\[Kappa]/2}}
Sw1 := -Inverse[S1 + I*\[CapitalOmega]*IdentityMatrix[2]] //FullSimplify
T1[\[Theta]_] := {Cos[\[Theta]], Sin[\[Theta]]};
```

Next we define the photon shot noise $\hat{X}_{x,\theta}[\Omega]$ and implement the exact analogon to expression 7.53, which we denote `xX` here. In the second step we calculate the photon shot noise spectrum $1/2\,\langle \mathtt{xX} \cdot \mathtt{xX} \rangle$, where the replacement rules set the symmetry tags to an arbitrary value `K`. Likewise the thermal occupancy of both reservoirs is set to the value `n`, i.e. $\mathtt{n}_{\mathtt{in}} \to \mathtt{n}$ and $\mathtt{n}_{\mathtt{vac}} \to \mathtt{n}$. Differing occupancies will alter the result.

```
Xx1 =
(\[Kappa]*Subscript[\[Eta],c]*T1[\[Theta]].Sw1.T1[0]-
Cos[\[Theta]])\[CircleTimes]Subscript[X,in]+
(\[Kappa]*Subscript[\[Eta],c]*T1[\[Theta]].Sw1.T1[Pi/2]-
Sin[\[Theta]])\[CircleTimes]Subscript[Y,in]+
(\[Kappa]*Sqrt[Subscript[\[Eta],c]*(1-Subscript[\[Eta],c])]*
T1[\[Theta]].Sw1.T1[0])\[CircleTimes]Subscript[X,vac]+
(\[Kappa]*Sqrt[Subscript[\[Eta],c]*(1-Subscript[\[Eta],c])]*
T1[\[Theta]].Sw1.T1[Pi/2])\[CircleTimes]Subscript[Y, vac];

(1/2)*\[LeftAngleBracket] Xx1,Xx1 \[RightAngleBracket]/.{
Subscript[\[CapitalKappa],vac]->\[CapitalKappa],
Subscript[\[CapitalKappa],in]->\[CapitalKappa],
Subscript[n, vac] -> n, Subscript[n, in] -> n}//Expand //FullSimplify
```

The result yields flat photon shot noise as one would expect. It is interesting however to play with the temperatures of the dissipative baths, which are represented by the noise occupation numbers $\mathtt{n}_{\mathtt{in}}$ and $\mathtt{n}_{\mathtt{vac}}$.
Next we calculate the transduction function, the equivalent shot noise, and

```
lambda1 = T1[\[Theta]].Sw1.T1[Pi/2];

Sxx1 = (1/2)/(lambda1*(lambda1/.\[CapitalOmega]-> -\[CapitalOmega]));

XF1 = (T1[0].Sw1.T1[0])\[CircleTimes]Subscript[X,1]+
(T1[0].Sw1.T1[Pi/2])\[CircleTimes]Subscript[Y,1];

SFF1 = (1/2)*\[LeftAngleBracket] XF1,XF1 \[RightAngleBracket]

Sxx1*SFF1 /.{Subscript[n, 1]->0,Subscript[\[CapitalKappa],1]->0,
\[Theta]->Pi/2}//FullSimplify
```

The result for S_{xx} still needs to be multiplied with $x_0^2/g_m^2\kappa\eta_c$, while S_{FF} comes with a prefactor $\kappa\hbar^2 g_m^2/x_0^2$, such that the result is again given in units of $\hbar^2/4$.

The definition of the three mode matrix

In this paragraph the matrix that describes three cavity modes S_3 is defined. In the definion below, the "small" coupling term $\propto g_m^2$ are included and tagged with an ϵ. Before evaluation the parameter has to be set to either 0 or 1. Here we set $\epsilon \to 0$ when calculating the inverted matrix Sw_3.

```
S3 :=
{{-\[Kappa]/2,Subscript[\[CapitalDelta],1],-\[Kappa]/2,-\[Epsilon]*Subscript[g,m]^2/2,
-\[Kappa]/2,-\[Epsilon]*Subscript[g,m]^2/2},{-Subscript[\[CapitalDelta],1],-\[Kappa]/2,
\[Epsilon]*Subscript[g,m]^2/2,-\[Kappa]/2,\[Epsilon]*Subscript[g,m]^2/2,-\[Kappa]/2},
{-\[Kappa]/2,-\[Epsilon]*Subscript[g,m]^2/2,-\[Kappa]/2,Subscript[\[CapitalDelta],2],
-\[Kappa]/2,-\[Epsilon]*Subscript[g,m]^2/2},{\[Epsilon]*Subscript[g, m]^2/2,-\[Kappa]/2,
-Subscript[\[CapitalDelta],2],-\[Kappa]/2,\[Epsilon]*Subscript[g,m]^2/2,-\[Kappa]/2},
{-\[Kappa]/2,-\[Epsilon]*Subscript[g,m]^2/2,-\[Kappa]/2,-\[Epsilon]*Subscript[g,m]^2/2,
-\[Kappa]/2,Subscript[\[CapitalDelta],3]},{\[Epsilon]*Subscript[g,m]^2/2,-\[Kappa]/2,
\[Epsilon]*Subscript[g,m]^2/2,-\[Kappa]/2,-Subscript[\[CapitalDelta],3],-\[Kappa]/2}};

Sw3 :=
-Inverse[(S3 /.{Subscript[\[CapitalDelta],1]->0,
Subscript[\[CapitalDelta],2]->-1,Subscript[\[CapitalDelta],3]->1,
\[Epsilon]->0})+I*\[CapitalOmega]*IdentityMatrix[6]]// FullSimplify

T3[\[Theta]_] :=
{Cos[\[Theta]],Sin[\[Theta]],Cos[\[Theta]],Sin[\[Theta]],Cos[\[Theta]],Sin[\[Theta]]};
```

The matrices can be inspected using the `MatrixForm`-command.

Bibliography

[1] I. Wilson-Rae, N. Nooshi, J. Dobrindt, T. J. Kippenberg, and W. Zwerger. Cavity-assisted back action cooling of mechanical resonators. *New Journal of Physics*, 10:095007, 2008. viii, 107, 116

[2] J. M. Dobrindt, I. Wilson-Rae, and T. J. Kippenberg. Parametric Normal-Mode splitting in cavity optomechanics. *Physical Review Letters*, 101(26):263602, dec 2008. viii, ix, 105, 112, 116, 127, 170, 171

[3] J. M. Dobrindt and T. J. Kippenberg. Theoretical analysis of mechanical displacement measurement using a multiple cavity mode transducer. *Physical Review Letters*, 104(3):033901, jan 2010. viii, ix, 109, 127

[4] J. M. Dobrindt, E. Rodrigo Teixeira da Silva, C. Alves, C. Oliveira, F. Nallet, E. Andreoli de Oliveira, and L. Navailles. Anisotropic brownian motion in ordered phases of DNA fragments. *The European Physical Journal E: Soft Matter and Biological Physics*, 35(1):1–11, 2012. viii, 69

[5] J. M. Dobrindt, B. Nickel, E. Gavartin, S. Krysiak, J. O. Rädler, and T. J. Kippenberg. Time-resolved, label-free sensing of single lipid vesicles using high-Q microresonators. submitted to Nature Nanotechnology. viii, ix

[6] Jeffrey N. Anker, W. Paige Hall, Olga Lyandres, Nilam C. Shah, Jing Zhao, and Richard P. Van Duyne. Biosensing with plasmonic nanosensors. *Nature Materials*, 7(6):442–453, 2008. 3, 12, 13

[7] Jeffrey T. Finer, Robert M. Simmons, and James A. Spudich. Single myosin molecule mechanics: piconewton forces and nanometre steps. *Nature*, 368(6467):113–119, mar 1994. 2

[8] Erwin Neher and Bert Sakmann. Single-channel currents recorded from membrane of denervated frog muscle fibres. *Nature*, 260(5554):799–802, apr 1976. 2

[9] Yongki Choi, Issa S. Moody, Patrick C. Sims, Steven R. Hunt, Brad L. Corso, Israel Perez, Gregory A. Weiss, and Philip G. Collins. Single-molecule lysozyme dynamics monitored by an electronic circuit. *Science*, 335(6066):319–324, January 2012. 2, 11, 14, 95

[10] J. C. Bergquist, Randall G. Hulet, Wayne M. Itano, and D. J. Wineland. Observation of quantum jumps in a single atom. *Physical Review Letters*, 57(14):1699–1702, oct 1986. 2

[11] Frank Diedrich and Herbert Walther. Nonclassical radiation of a single stored ion. *Physical Review Letters*, 58(3):203–206, jan 1987. 2

[12] T. Hirschfeld. Optical microscopic observation of single small molecules. *Applied Optics*, 15(12):2965–2966, dec 1976. 2

[13] E. Brooks Shera, Newton K. Seitzinger, Lloyd M. Davis, Richard A. Keller, and Steven A. Soper. Detection of single fluorescent molecules. *Chemical Physics Letters*, 174(6):553–557, nov 1990. 2

[14] William B. Whitten, J. Michael Ramsey, Stephen Arnold, and Burt V. Bronk. Single-molecule detection limits in levitated microdroplets. *Analytical Chemistry*, 63(10):1027–1031, 1991. 2

[15] W. E. Moerner and L. Kador. Optical detection and spectroscopy of single molecules in a solid. *Physical Review Letters*, 62(21):2535–2538, may 1989. 2, 3, 11

[16] M. Orrit and J. Bernard. Single pentacene molecules detected by fluorescence excitation in a p-terphenyl crystal. *Physical Review Letters*, 65(21):2716–2719, nov 1990. 2, 3

[17] Eric Betzig and Robert J. Chichester. Single molecules observed by near-field scanning optical microscopy. *Science*, 262(5138):1422–1425, nov 1993. 2

[18] D. M. Eigler and E. K. Schweizer. Positioning single atoms with a scanning tunnelling microscope. *Nature*, 344(6266):524–526, apr 1990. 2, 3

[19] G. Binnig, H. Rohrer, Ch. Gerber, and E. Weibel. Surface studies by scanning tunneling microscopy. *Physical Review Letters*, 49(1):57–61, jul 1982. 2

[20] B. C. Stipe, M. A. Rezaei, and W. Ho. Single-molecule vibrational spectroscopy and microscopy. *Science*, 280(5370):1732–1735, 1998. 3

[21] W. E Moerner and Michel Orrit. Illuminating single molecules in condensed matter. *Science*, 283(5408):1670–1676, dec 1999. 3

[22] S. Weiss. Fluorescence spectroscopy of single biomolecules. *Science*, 283(5408):1676–1683, 1999. 3

[23] Michael J Rust, Mark Bates, and Xiaowei Zhuang. Sub-diffraction-limit imaging by stochastic optical reconstruction microscopy (STORM). *Nature Methods*, 3(10):793–796, jan 2006. 3

[24] Abraham J. Qavi, Adam L. Washburn, Ji-Yeon Byeon, and Ryan C. Bailey. Label-free technologies for quantitative multiparameter biological analysis. *Analytical and Bioanalytical Chemistry*, 394(1):121–135, feb 2009. 4, 13, 73

[25] Celine I.L. Justino, Teresa A. Rocha-Santos, Armando C. Duarte, and Teresa A. Rocha-Santos. Review of analytical figures of merit of sensors and biosensors in clinical applications. *TrAC Trends in Analytical Chemistry*, 29(10):1172–1183, nov 2010. 4

[26] Jiří Homola, Sinclair S. Yee, and Günter Gauglitz. Surface plasmon resonance sensors: review. *Sensors and Actuators B: Chemical*, 54(1–2):3–15, jan 1999. 4

[27] Monya Baker. Making membrane proteins for structures: a trillion tiny tweaks. *Nature Methods*, 7(6):429–434, jun 2010. 4

[28] Heather K. Hunt and Andrea M. Armani. Label-free biological and chemical sensors. *Nanoscale*, 2(9):1544–1559, sep 2010. 5

[29] Tomoyuki Yoshie, Lingling Tang, and Shu-Yu Su. Optical microcavity: Sensing down to single molecules and atoms. *Sensors*, 11(2):1972–1991, February 2011. 7

[30] Demetri Psaltis, Stephen R. Quake, and Changhuei Yang. Developing optofluidic technology through the fusion of microfluidics and optics. *Nature*, 442(7101):381–386, jul 2006. 7

[31] Kevin A. Arpin, Agustin Mihi, Harley T. Johnson, Alfred J. Baca, John A. Rogers, Jennifer A. Lewis, and Paul V. Braun. Multidimensional architectures for functional optical devices. *Advanced Materials*, 22(10):1084–1101, 2010. 7, 13

[32] K. J. Vahala. Optical microcavities. *Nature*, 424(6950):839–846, 2003. 7

[33] F. Vollmer, D. Braun, A. Libchaber, M. Khoshsima, I. Teraoka, and S. Arnold. Protein detection by optical shift of a resonant microcavity. *Applied Physics Letters*, 80(21):4057–4059, may 2002. 9, 72

[34] Frank Vollmer, Stephen Arnold, Dieter Braun, Iwao Teraoka, and Albert Libchaber. Multiplexed DNA quantification by spectroscopic shift of two microsphere cavities. *Biophysical Journal*, 85(3):1974–1979, sep 2003. 9, 10

[35] S. Arnold, M. Khoshsima, I. Teraoka, S. Holler, and F. Vollmer. Shift of whispering-gallery modes in microspheres by protein adsorption. *Optics Letters*, 28(4):272–274, feb 2003. 9

[36] D. Keng, S. R. McAnanama, I. Teraoka, and S. Arnold. Resonance fluctuations of a whispering gallery mode biosensor by particles undergoing brownian motion. *Applied Physics Letters*, 91(10):103902–103902–3, sep 2007. 9, 78

[37] F. Vollmer, S. Arnold, and D. Keng. Single virus detection from the reactive shift of a whispering-gallery mode. *Proceedings of the National Academy of Sciences*, 105(52):20701–20704, dec 2008. 9, 20, 43, 45, 52, 62, 153, 155, 158, 159

[38] Frank Vollmer and Stephen Arnold. Whispering-gallery-mode biosensing: label-free detection down to single molecules. *Nature Methods*, 5(7):591–596, jan 2008. 9

[39] S. Arnold, D. Keng, S. I. Shopova, S. Holler, W. Zurawsky, and F. Vollmer. Whispering gallery mode carousel - a photonic mechanism for enhanced nanoparticle detection in biosensing. *Optics Express*, 17(8):6230–6238, apr 2009. 9, 19, 62, 63, 64

[40] Miguel A Santiago-Cordoba, Svetlana V Boriskina, Frank Vollmer, and Melik C Demirel. Nanoparticle-based protein detection by optical shift of a resonant microcavity. *Applied Physics Letters*, 99(7):073701–073701–3, aug 2011. 9

[41] Andrea M Armani, Rajan P Kulkarni, Scott E Fraser, Richard C Flagan, and Kerry J Vahala. Label-Free, Single-Molecule detection with optical microcavities. *Science*, 317(5839):783–787, aug 2007. 9

[42] S. Arnold, S. I. Shopova, and S. Holler. Whispering gallery mode bio-sensor for label-free detection of single molecules: thermo-optic vs. reactive mechanism. *Optics Express*, 18(1):281–287, jan 2010. 9

[43] Tao Lu, Hansuek Lee, Tong Chen, Steven Herchak, Ji-Hun Kim, Scott E Fraser, Richard C Flagan, and Kerry Vahala. High sensitivity nanoparticle detection using optical microcavities. *Proceedings of the National Academy of Sciences*, 108(15):5976–5979, apr 2011. 9, 20, 45, 52, 62, 160

[44] Jiangang Zhu, Sahin Kaya Özdemir, Yun-Feng Xiao, Lin Li, Lina He, Da-Ren Chen, and Lan Yang. On-chip single nanoparticle detection and sizing by mode splitting in an ultrahigh-Q microresonator. *Nature Photonics*, 4(1):46–49, dec 2009. 9, 60, 61

[45] Woosung Kim, Sahin Kaya Özdemir, Jiangang Zhu, Lina He, and Lan Yang. Demonstration of mode splitting in an optical microcavity in aqueous environment. *Applied Physics Letters*, 97(7):071111–071111–3, aug 2010. 9

[46] Lina He, Sahin Kaya Özdemir, Jiangang Zhu, and Lan Yang. Ultrasensitive detection of mode splitting in active optical microcavities. *Physical Review A*, 82(5):053810, nov 2010. 9

[47] Lina He, Sahin Kaya Özdemir, Jiangang Zhu, Woosung Kim, and Lan Yang. Detecting single viruses and nanoparticles using whispering gallery microlasers. *Nature Nanotechnology*, 6(7):428–432, jun 2011. 9, 43

[48] Adam L. Washburn and Ryan C. Bailey. Photonics-on-a-chip: recent advances in integrated waveguides as enabling detection elements for real-world, lab-on-a-chip biosensing applications. *The Analyst*, 136(2):227, 2011. 9

[49] Yuze Sun and Xudong Fan. Optical ring resonators for biochemical and chemical sensing. *Analytical and Bioanalytical Chemistry*, 399(1):205–211, 2011. 9

[50] W. Bogaerts, P. De Heyn, T. Van Vaerenbergh, K. De Vos, S. Kumar Selvaraja, T. Claes, P. Dumon, P. Bienstman, D. Van Thourhout, and R. Baets. Silicon microring resonators. *Laser & Photonics Reviews*, 6(1):47–73, 2012. 9

[51] T. Claes, J.G. Molera, K. De Vos, E. Schacht, R. Baets, and P. Bienstman. Label-Free biosensing with a Slot-Waveguide-Based ring resonator in silicon on insulator. *Photonics Journal, IEEE*, 1(3):197 –204, sep 2009. 9, 10

[52] Carlos A. Barrios, Maria Jose Banuls, Victoria Gonzalez-Pedro, Kristinn B. Gylfason, Benito Sanchez, Amadeu Griol, A. Maquieira, H. Sohlström, M. Holgado, and R. Casquel. Label-free optical biosensing with slot-waveguides. *Optics Letters*, 33(7):708–710, apr 2008. 9

[53] C.A. Barrios, K.B. Gylfason, B. Sanchez, A. Griol, H. Sohlström, M. Holgado, and R. Casquel. Slot-waveguide biochemical sensor. *Optics Letters*, 32(21):3080–3082, 2007. 9

[54] C.-Y. Chao, W. Fung, and L.J. Guo. Polymer microring resonators for biochemical sensing applications. *IEEE Journal on Selected Topics in Quantum Electronics*, 12(1):134–142, 2006. 9

[55] A. Ramachandran, S. Wang, J. Clarke, S.J. Ja, D. Goad, L. Wald, E.M. Flood, E. Knobbe, J.V. Hryniewicz, S.T. Chu, D. Gill, W. Chen, O. King, and B.E. Little. A universal biosensing platform based on optical micro-ring resonators. *Biosensors and Bioelectronics*, 23(7):939–944, feb 2008. 9

[56] Adam L. Washburn, Matthew S. Luchansky, Adrienne L. Bowman, and Ryan C. Bailey. Quantitative, Label-Free detection of five protein biomarkers using multiplexed arrays of silicon photonic microring resonators. *Anal. Chem.*, 82(1):69–72, 2009. 9

[57] Adam L Washburn, L Cary Gunn, and Ryan C Bailey. Label-free quantitation of a cancer biomarker in complex media using silicon photonic microring resonators. *Analytical Chemistry*, 81(22):9499–9506, nov 2009. PMID: 19848413. 9

[58] Siyka I Shopova, Hongying Zhou, Xudong Fan, and Po Zhang. Optofluidic ring resonator based dye laser. *Applied Physics Letters*, 90(22):221101–221101–3, may 2007. 9

[59] Ian M White, Hesam Oveys, Xudong Fan, Terry L Smith, and Junying Zhang. Integrated multiplexed biosensors based on liquid core optical ring resonators and antiresonant reflecting optical waveguides. *Applied Physics Letters*, 89(19):191106–191106–3, nov 2006. 9

[60] Katrin Kneipp, Yang Wang, Harald Kneipp, Lev T. Perelman, Irving Itzkan, Ramachandra R. Dasari, and Michael S. Feld. Single molecule detection using Surface-Enhanced raman scattering (SERS). *Physical Review Letters*, 78(9):1667–1670, mar 1997. 9, 10

[61] S. M. Nie and S. R. Emery. Probing single molecules and single nanoparticles by surface-enhanced raman scattering. *Science*, 275(5303):1102–1106, 1997. 9, 10

[62] Katrin Kneipp, Harald Kneipp, Irving Itzkan, Ramachandra R. Dasari, and Michael S. Feld. Surface-enhanced non-linear raman scattering at the single-molecule level. *Chemical Physics*, 247(1):155–162, aug 1999. 9

[63] Katrin Kneipp, Harald Kneipp, V. Bhaskaran Kartha, Ramasamy Manoharan, Geurt Deinum, Irving Itzkan, Ramachandra R. Dasari, and Michael S. Feld. Detection and identification of a single DNA base molecule using surface-enhanced raman scattering (SERS). *Physical Review E*, 57(6):R6281–R6284, June 1998. 10

[64] P. G. Etchegoin and E. C. Le Ru. A perspective on single molecule SERS: current status and future challenges. *Physical Chemistry Chemical Physics*, 10(40):6079, 2008. 10

[65] A. Gupta, D. Akin, and R. Bashir. Single virus particle mass detection using microresonators with nanoscale thickness. *Applied Physics Letters*, 84(11):1976–1978, mar 2004. 10, 11

[66] Kenzo Maehashi and Kazuhiko Matsumoto. Label-free electrical detection using carbon nanotube-based biosensors. *Sensors*, 9(7):5368–5378, July 2009. 10

[67] Jiri Homola. Surface plasmon resonance sensors for detection of chemical and biological species. *Chem. Rev.*, 108(2):462–493, 2008. 10

[68] Irene Ament, Janak Prasad, Andreas Henkel, Sebastian Schmachtel, and Carsten Sönnichsen. Single unlabeled protein detection on individual plasmonic nanoparticles. *Nano Lett.*, 12(2):1092–1095, 2012. 10, 13

[69] Qimin Quan, Ian B. Burgess, Sindy K. Y. Tang, Daniel L. Floyd, and Marko Loncar. High-Q, low index-contrast polymeric photonic crystal nanobeam cavities. *Optics Express*, 19(22):22191–22197, oct 2011. 10, 12

[70] A. Gaiduk, M. Yorulmaz, P. V Ruijgrok, and M. Orrit. Room-Temperature detection of a single molecule's absorption by photothermal contrast. *Science*, 330(6002):353–356, oct 2010. 11

[71] Michele Celebrano, Philipp Kukura, Alois Renn, and Vahid Sandoghdar. Single-molecule imaging by optical absorption. *Nature Photonics*, 5(2):95–98, jan 2011. 11

[72] J.l. Arlett, E.b. Myers, and M.l. Roukes. Comparative advantages of mechanical biosensors. *Nature Nanotechnology*, 6(4):203–215, 2011. 11

[73] Blake N. Johnson and Raj Mutharasan. Biosensing using dynamic-mode cantilever sensors: A review. *Biosensors and Bioelectronics*, 32(1):1–18, February 2012. 11

[74] K. Jensen, Kwanpyo Kim, and A. Zettl. An atomic-resolution nanomechanical mass sensor. *Nature Nanotechnology*, 3(9):533–537, 2008. 11

[75] M. S. Hanay, S. Kelber, A. K. Naik, D. Chi, S. Hentz, E. C. Bullard, E. Colinet, L. Duraffourg, and M. L. Roukes. Single-protein nanomechanical mass spectrometry in real time. *Nature Nanotechnology*, 2012. 11

[76] Eric Stern, James F. Klemic, David A. Routenberg, Pauline N. Wyrembak, Daniel B. Turner-Evans, Andrew D. Hamilton, David A. LaVan, Tarek M. Fahmy, and Mark A. Reed. Label-free immunodetection with CMOS-compatible semiconducting nanowires. *Nature*, 445(7127):519–522, feb 2007. 11, 72

[77] Brian Cunningham, Peter Li, Bo Lin, and Jane Pepper. Colorimetric resonant reflection as a direct biochemical assay technique. *Sensors and Actuators B: Chemical*, 81(2–3):316–328, jan 2002. 11

[78] Jon Olav Grepstad, Peter Kaspar, Olav Solgaard, Ib-Rune Johansen, and Aasmund S. Sudbø. Photonic-crystal membranes for optical detection of single nano-particles, designed for biosensor application. *Optics Express*, 20(7):7954–7965, mar 2012. 11

[79] Marko Lončar, Axel Scherer, and Yueming Qiu. Photonic crystal laser sources for chemical detection. *Applied Physics Letters*, 82(26):4648–4650, jun 2003. 12

[80] Mindy R. Lee and Philippe M. Fauchet. Two-dimensional silicon photonic crystal based biosensing platform for protein detection. *Optics Express*, 15(8):4530–4535, apr 2007. 12

[81] M.G. Scullion, A. Di Falco, and T.F. Krauss. Slotted photonic crystal cavities with integrated microfluidics for biosensing applications. *Biosensors and Bioelectronics*, 27(1):101–105, sep 2011. 12

[82] Andreas Otto. Excitation of nonradiative surface plasma waves in silver by the method of frustrated total reflection. *Zeitschrift fÃŒr Physik A Hadrons and Nuclei*, 216(4):398–410, 1968. 12

[83] Bo Liedberg, Claes Nylander, and Ingemar Lunström. Surface plasmon resonance for gas detection and biosensing. *Sensors and Actuators*, 4(0):299–304, 1983. 12

[84] Peter Zijlstra, Pedro M. R. Paulo, and Michel Orrit. Optical detection of single non-absorbing molecules using the surface plasmon resonance of a gold nanorod. *Nature Nanotechnology*, apr 2012. 13

[85] Todd M Squires, Robert J Messinger, and Scott R Manalis. Making it stick: convection, reaction and diffusion in surface-based biosensors. *Nature Biotechnology*, 26(4):417–426, 2008. 13, 51

[86] Jonathan S. Daniels and Nader Pourmand. Label-Free impedance biosensors: Opportunities and challenges. *Electroanalysis*, 19(12):1239–1257, 2007. 13

[87] Heather K. Hunt, Carol Soteropulos, and Andrea M. Armani. Bioconjugation strategies for microtoroidal optical resonators. *Sensors*, 10(10):9317–9336, oct 2010. 13, 66

[88] Simona Scarano, Marco Mascini, Anthony P.F. Turner, and Maria Minunni. Surface plasmon resonance imaging for affinity-based biosensors. *Biosensors and Bioelectronics*, 25(5):957–966, jan 2010. 13, 66

[89] Jiří Homola. Present and future of surface plasmon resonance biosensors. *Analytical and Bioanalytical Chemistry*, 377(3):528–539, 2003. 13

[90] Lindsay M Freeman, Su Li, Yasaman Dayani, Hong-Seok Choi, Noah Malmstadt, and Andrea M Armani. Excitation of cy5 in self-assembled lipid bilayers using optical microresonators. *Applied Physics Letters*, 98(14):143703–143703–3, apr 2011. 13

[91] Christoph Herold, Grzegorz Chwastek, Petra Schwille, and Eugene P. Petrov. Efficient electroformation of supergiant unilamellar vesicles containing cationic lipids on ITO-Coated electrodes. *Langmuir*, 28(13):5518–5521, apr 2012. 13, 47

[92] S. I Shopova, R. Rajmangal, S. Holler, and S. Arnold. Plasmonic enhancement of a whispering-gallery-mode biosensor for single nanoparticle detection. *Applied Physics Letters*, 98(24):243104–243104–3, jun 2011. 14, 65

[93] V. R. Dantham, S. Holler, V. Kolchenko, Z. Wan, and S. Arnold. Taking whispering gallery-mode single virus detection and sizing to the limit. *Applied Physics Letters*, 101(4):043704–043704–4, July 2012. 14

[94] A. N. Oraevsky. Whispering-gallery waves. *Quantum Electronics*, 32:377–400, 2002. 15, 147

[95] Steven Johnson and John Joannopoulos. Block-iterative frequency-domain methods for maxwell's equations in a planewave basis. *Optics Express*, 8(3):173–190, jan 2001. 15, 147

[96] Iwao Teraoka, Stephen Arnold, and Frank Vollmer. Perturbation approach to resonance shifts of whispering-gallery modes in a dielectric microsphere as a probe of a surrounding medium. *Journal of the Optical Society of America B*, 20(9):1937–1946, 2003. 15, 147

[97] S. Schiller. Asymptotic-expansion of morphological resonance frequencies in mie scattering. *Applied Optics*, 32(12):2181–2185, 1993. 15, 147, 149, 154

[98] M. L Gorodetsky and A. E Fomin. Geometrical theory of whispering-gallery modes. *IEEE Journal of Selected Topics in Quantum Electronics*, 12(1):33–39, feb 2006. 15, 43

[99] M. Oxborrow. Traceable 2-d finite-element simulation of the whispering-gallery modes of axisymmetric electromagnetic resonators. *IEEE Transactions on Microwave Theory and Techniques*, 55(6):1209 –1218, June 2007. 15

[100] Feynman, Richard. *The Feynman Lectures on Physics 2 Volume II - Mainly Electromagnetism and Matter*. Massachusetts, Addison-Wesley Publishing Company 1977, January 1977. 18

[101] Armin Wachter and Henning Hoeber. *Repetitorium Theoretische Physik*. Springer Berlin Heidelberg, 1 edition, September 1998. 18

[102] Iwao Teraoka and Stephen Arnold. Theory of resonance shifts in TE and TM whispering gallery modes by nonradial perturbations for sensing applications. *Journal of the Optical Society of America B*, 23(7):1381–1389, jul 2006. 18, 19, 147, 156

[103] J. C. Knight, G. Cheung, F. Jacques, and T. A. Birks. Phase-matched excitation of whispering-gallery-mode resonances by a fiber taper. *Optics Letters*, 22(15):1129–1131, 1997. 25

[104] Ming Cai, Oskar Painter, and Kerry J. Vahala. Observation of critical coupling in a fiber taper to a Silica-Microsphere Whispering-Gallery mode system. *Physical Review Letters*, 85(1):74, jul 2000. 25

[105] S. M. Spillane, T. J. Kippenberg, O. J. Painter, and K. J. Vahala. Ideality in a Fiber-Taper-Coupled microresonator system for application to cavity quantum electrodynamics. *Physical Review Letters*, 91(4):043902, jul 2003. 25

[106] U. Fano. Effects of configuration interaction on intensities and phase shifts. *Physical Review*, 124:1866–1878, 1961. 27

[107] Albert Schliesser. *Cavity Optomechanics and Optical Frequency Comb Generation with Silica Whispering-Gallery-Mode Microresonators*. PhD thesis, Ludwig-Maximilians-Universität München, 2009. 29

[108] Pascal Del'Haye. *Optical Frequency Comb Generation in Monolithic Microresonators*. PhD thesis, Ludwig-Maximilians-Universität München, 2011. 29

[109] Thomas J. Kane and Robert L. Byer. Monolithic, unidirectional single-mode Nd:YAG ring laser. *Optics Letters*, 10(2):65–67, February 1985. 32

[110] Drever, Hall, Kowalski, Hough, Ford, Munley, and Ward. Laser phase and frequency stabilization using an optical resonator. *Applied Physics B*, 31:97–105, 1983. 34

[111] Eric D. Black. An introduction to pound–drever–hall laser frequency stabilization. *American Journal of Physics*, 69:79–87, 2001. 34, 35

[112] Fritz Riehle. *Frequency Standards: Basis and Applications*. Wiley-VCH, 2004. 34, 76

[113] Hermann A. Haus. *Waves and Fields in Optoelectronics*. Prentice-Hall, 1983. 36

[114] Vernon Miyamoto and Walther Stoeckenius. Preparation and characteristics of lipid vesicles. *Journal of Membrane Biology*, 4(1):252–269, 1971. 46, 47, 48

[115] A.D. Bangham and R.W. Horne. Negative staining of phospholipids and their structural modification by surface-active agents as observed in the electron microscope. *Journal of Molecular Biology*, 8(5):660, 1964. 46

[116] David W. Deamer. From "banghasomes" to liposomes: A memoir of alec bangham, 1921–2010. *The FASEB Journal*, 24(5):1308–1310, jan 2010. 46

[117] Grazia Sessa and Gerald Weissmann. Phospholipid spherules (liposomes) as a model for biological membranes. *Journal of Lipid Research*, 9(3):310–318, jan 1968. 46, 47

[118] James R. C. Whyte and Sean Munro. Vesicle tethering complexes in membrane traffic. *Journal of Cell Science*, 115(13):2627–2637, jan 2002. 46

[119] Thomas C Südhof and James E Rothman. Membrane fusion: Grappling with SNARE and SM proteins. *Science*, 323(5913):474–477, jan 2009. 46

[120] Yongling Zhu, Jian Xu, and Stephen F. Heinemann. Two pathways of synaptic vesicle retrieval revealed by Single-Vesicle imaging. *Neuron*, 61(3):397–411, feb 2009. 46, 47

[121] Sunil P. Gandhi and Charles F. Stevens. Three modes of synaptic vesicular recycling revealed by single-vesicle imaging. *Nature*, 423(6940):607–613, jun 2003. 46

[122] Philip R Evans and David J Owen. Endocytosis and vesicle trafficking. *Current Opinion in Structural Biology*, 12(6):814–821, dec 2002. 46

[123] Nadja Jung, Martin Wienisch, Mingyu Gu, James B Rand, Sebastian L Müller, Gerd Krause, Erik M Jorgensen, Jürgen Klingauf, and Volker Haucke. Molecular basis of synaptic vesicle cargo recognition by the endocytic sorting adaptor stonin 2. *The Journal of Cell Biology*, 179(7):1497–1510, dec 2007. 46

[124] Yee-Hung M Chan and Steven G Boxer. Model membrane systems and their applications. *Current Opinion in Chemical Biology*, 11(6):581–587, December 2007. 47, 67

[125] D. Needham and E. Evans. Structure and mechanical properties of giant lipid (DMPC) vesicle bilayers from 20.degree.C below to 10.degree.C above the liquid crystal-crystalline phase transition at 24.degree.C. *Biochemistry*, 27(21):8261–8269, oct 1988. 47

[126] Aurélien Roux, Katherine Uyhazi, Adam Frost, and Pietro De Camilli. GTP-dependent twisting of dynamin implicates constriction and tension in membrane fission. *Nature*, 441(7092):528–531, apr 2006. 47

[127] Aurélien Roux, Gerbrand Koster, Martin Lenz, Benoit Sorre, Jean-Baptiste Manneville, Pierre Nassoy, and Patricia Bassereau. Membrane curvature controls dynamin polymerization. *Proceedings of the National Academy of Sciences*, 107(9):4141–4146, feb 2010. 47

[128] M. Bally, A. Gunnarsson, L. Svensson, G. Larson, V. P. Zhdanov, and F. Höök. Interaction of single viruslike particles with vesicles containing glycosphingolipids. *Physical Review Letters*, 107(18):188103, oct 2011. 47

[129] Vladimir P. Torchilin. Recent advances with liposomes as pharmaceutical carriers. *Nature Reviews Drug Discovery*, 4(2):145–160, jan 2005. 47

[130] Jeffrey G. Linhardt. *Applications of lipid vesicles: drug delivery systems and templates for nanometer and micron sized structures*. PhD thesis, University of Massachusetts Amherst, 2001. 47

[131] Shao-Ling Huang. Liposomes in ultrasonic drug and gene delivery. *Advanced Drug Delivery Reviews*, 60(10):1167–1176, jun 2008. 47

[132] Margaret N. Holme, Illya A. Fedotenko, Daniel Abegg, Jasmin Althaus, Lucille Babel, France Favarger, Renate Reiter, Radu Tanasescu, Pierre-Léonard Zaffalon, André Ziegler, Bert Müller, Till Saxer, and Andreas Zumbuehl. Shear-stress sensitive lenticular vesicles for targeted drug delivery. *Nature Nanotechnology*, 7(8):536–543, 2012. 47

[133] Miglena I. Angelova and Dimiter S. Dimitrov. Liposome electroformation. *Faraday Discussions of the Chemical Society*, 81:303, 1986. 47

[134] L.A Bagatolli, T Parasassi, and E Gratton. Giant phospholipid vesicles: comparison among the whole lipid sample characteristics using different preparation methods: A two photon fluorescence microscopy study. *Chemistry and Physics of Lipids*, 105(2):135–147, apr 2000. 47

[135] D. G. Hunter and B. J. Frisken. Effect of extrusion pressure and lipid properties on the size and polydispersity of lipid vesicles. *Biophysical Journal*, 74(6):2996–3002, jun 1998. 48, 53

[136] A. J. Jin, Daniel Huster, Klaus Gawrisch, and Ralph Nossal. Light scattering characterization of extruded lipid vesicles. *European Biophysics Journal*, 28(3):187–199, mar 1999. 48, 53, 71

[137] Bronwyn Jean Battersby, Rudo Grimm, Stefan Huebner, and Gregor Cevc. Evidence for three-dimensional interlayer correlations in cationic lipid-DNA complexes as observed by cryo-electron microscopy. *Biochimica et Biophysica Acta (BBA) - Biomembranes*, 1372(2):379–383, July 1998. 48

[138] Marieke Kranenburg and Berend Smit. Phase behavior of model lipid bilayers. *The Journal of Physical Chemistry B*, 109(14):6553–6563, apr 2005. 49, 82

[139] Jens M. Dobrindt. Single particle events observed as discrete jumps of a wgm resonance. *http://youtu.be/ypiQX1L5KXY*, 2012. 50

[140] J. Rädler, H. Strey, and E. Sackmann. Phenomenology and kinetics of lipid bilayer spreading on hydrophilic surfaces. *Langmuir*, 11(11):4539–4548, 1995. 58

[141] Ilya Reviakine and Alain Brisson. Formation of supported phospholipid bilayers from unilamellar vesicles investigated by atomic force microscopy. *Langmuir*, 16(4):1806–1815, 2000. 58, 67

[142] Holger Schönherr, Joseph M. Johnson, Peter Lenz, Curtis W. Frank, and Steven G. Boxer. Vesicle adsorption and lipid bilayer formation on glass studied by atomic force microscopy. *Langmuir*, 20(26):11600–11606, 2004. 58

[143] Siewert J. Marrink and Alan E. Mark. The mechanism of vesicle fusion as revealed by molecular dynamics simulations. *J. Am. Chem. Soc.*, 125(37):11144–11145, 2003. 58

[144] Travers H. Anderson, Younjin Min, Kim L. Weirich, Hongbo Zeng, Deborah Fygenson, and Jacob N. Israelachvili. Formation of supported bilayers on silica substrates. *Langmuir*, 25(12):6997–7005, 2009. 58, 67

[145] D. S. Weiss, V. Sandoghdar, J. Hare, V. Lefevreseguin, J. M. Raimond, and S. Haroche. Splitting of high-q mie modes induced by light backscattering in silica microspheres. *Optics Letters*, 20(18):1835–1837, 1995. 60

[146] P. C. Weber, D. H. Ohlendorf, J. J. Wendoloski, and F. R. Salemme. Structural origins of high-affinity biotin binding to streptavidin. *Science*, 243(4887):85–88, 1989. 66

[147] Dinesh Shenoy, Wei Fu, Jane Li, Curtis Crasto, Graham Jones, Charles DiMarzio, Srinivas Sridhar, and Mansoor Amiji. Surface functionalization of gold nanoparticles using hetero-bifunctional poly(ethylene glycol) spacer for intracellular tracking and delivery. *International Journal of Nanomedicine*, 1(1):51–57, March 2006. PMID: 16467923 PMCID: PMC1351208. 66

[148] Yuri L. Bunimovich, Young Shik Shin, Woon-Seok Yeo, Michael Amori, Gabriel Kwong, and James R. Heath. Quantitative Real-Time measurements of DNA hybridization with alkylated nonoxidized silicon nanowires in electrolyte solution. *J. Am. Chem. Soc.*, 128(50):16323–16331, 2006. 66

[149] Carol E Soteropulos, Heather K Hunt, and Andrea M Armani. Determination of binding kinetics using whispering gallery mode microcavities. *Applied Physics Letters*, 99(10):103703–103703–3, sep 2011. 67

[150] E. Sackmann. Supported membranes: Scientific and practical applications. *Science*, 271(5245):43–48, jan 1996. 67

[151] Ralf P. Richter, Rémi Bérat, and Alain R. Brisson. Formation of solid-supported lipid bilayers: An integrated view. *Langmuir*, 22(8):3497–3505, April 2006. 67

[152] Stéphane Mornet, Olivier Lambert, Etienne Duguet, and Alain Brisson. The formation of supported lipid bilayers on silica nanoparticles revealed by cryo-electron microscopy. *Nano Letters*, 5(2):281–285, February 2005. 67

[153] Adrienne A. Brian and Harden M. McConnell. Allogeneic stimulation of cytotoxic t cells by supported planar membranes. *Proceedings of the National Academy of Sciences*, 81(19):6159–6163, 1984. 67

[154] Adam Cohen Simonsen and Luis A. Bagatolli. Structure of spin-coated lipid films and domain formation in supported membranes formed by hydration. *Langmuir*, 20(22):9720–9728, 2004. 67

[155] D. Axelrod, D.E. Koppel, J. Schlessinger, E. Elson, and W.W. Webb. Mobility measurement by analysis of fluorescence photobleaching recovery kinetics. *Biophysical Journal*, 16(9):1055–1069, September 1976. 69

[156] D. M. Soumpasis. Theoretical analysis of fluorescence photobleaching recovery experiments. *Biophysical Journal*, 41(1):95–97, January 1983. 69

[157] Margaret R. Horton, Christian Reich, Alice P. Gast, Joachim O. Rädler, and Bert Nickel. Structure and dynamics of crystalline protein layers bound to supported lipid bilayers. *Langmuir*, 23(11):6263–6269, May 2007. 69

[158] Marion B Hochrein, Christian Reich, Bärbel Krause, Joachim O Rädler, and Bert Nickel. Structure and mobility of lipid membranes on a thermoplastic substrate. *Langmuir: The ACS Journal of Surfaces and Colloids*, 22(2):538–545, jan 2006. PMID: 16401100. 69

[159] Y. Gambin, R. Lopez-Esparza, M. Reffay, E. Sierecki, N. S. Gov, M. Genest, R. S. Hodges, and W. Urbach. Lateral mobility of proteins in liquid membranes revisited. *Proceedings of the National Academy of Sciences of the United States of America*, 103(7):2098–2102, February 2006. 69

[160] Christian Reich, Margaret R. Horton, Bärbel Krause, Alice P. Gast, Joachim O. Rädler, and Bert Nickel. Asymmetric structural features in single supported lipid bilayers containing cholesterol and GM1 resolved with synchrotron x-ray reflectivity. *Biophysical Journal*, 95(2):657–668, July 2008. 70

[161] Viktor Peikov and Zoltan A. Schelly. Modeling of the electric Field–Induced birefringence of vesicles. *J. Phys. Chem. B*, 108(26):9357–9363, 2004. 70

[162] Pasut Ratanabanangkoon, Michael Gropper, Rudolf Merkel, Erich Sackmann, and Alice P. Gast. Mechanics of Streptavidin-Coated giant lipid bilayer vesicles: A micropipet study. *Langmuir*, 19(4):1054–1062, 2003. 70

[163] Jerry Tsai, Robin Taylor, Cyrus Chothia, and Mark Gerstein. The packing density in proteins: standard radii and volumes. *Journal of Molecular Biology*, 290(1):253–266, jul 1999. 71

[164] D. Huster, A.J. Jin, K. Arnold, and K. Gawrisch. Water permeability of polyunsaturated lipid membranes measured by 17O NMR. *Biophysical Journal*, 73(2):855–864, aug 1997. 71

[165] Shulei Zhao and W. M. Reichert. Influence of biotin lipid surface density and accessibility on avidin binding to the tip of an optical fiber sensor. *Langmuir*, 8(11):2785–2791, November 1992. 72

[166] Thomas Kodadek. Protein microarrays: prospects and problems. *Chemistry & Biology*, 8(2):105–115, February 2001. 73

[167] Xudong Fan, Ian M. White, Siyka I. Shopova, Hongying Zhu, Jonathan D. Suter, and Yuze Sun. Sensitive optical biosensors for unlabeled targets: A review. *Analytica Chimica Acta*, 620:8–26, jul 2008. 75

[168] Elke Haustein and Petra Schwille. Fluorescence correlation spectroscopy: Novel variations of an established technique. *Annual Review of Biophysics and Biomolecular Structure*, 36(1):151–169, 2007. 77

[169] Milestone 10 : Nature Milestones in Light Microscopy. http://www.nature.com/milestones/milelight/full/milelight10.html. 77

[170] Janos Vörös. The density and refractive index of adsorbing protein layers. *Biophysical Journal*, 87(1):553–561, jul 2004. 79

[171] Erik G. Brandt. *Molecular Dynamics Simulations of Fluid Lipid Membranes*. PhD thesis, Kungliga Tekniska Högskolan (KTH) Stockholm, 2011. 82

[172] Richard F. Voss and John Clarke. Flicker (1/f) noise: Eqilibrium temperature and resistance fluctuations. *Physical Review B*, 13:556–573, 1976. 83, 89

[173] Michael L. Gorodetsky and Ivan S. Grudinin. Fundamental thermal fluctuations in microspheres. *Journal of the Optical Society of America B*, 21(4):697–705, apr 2004. 87, 88, 90

[174] Ieee standard definitions of physical quantities for fundamental frequency and time metrology – random instabilities. Technical Report IEEE Std 1139-1999, IEEE Standards Coordinating Committee 27 on Time and Frequency, 1999. 90

[175] A. D. O'Connell, M. Hofheinz, M. Ansmann, Radoslaw C. Bialczak, M. Lenander, Erik Lucero, M. Neeley, D. Sank, H. Wang, M. Weides, J. Wenner, John M. Martinis, and A. N. Cleland. Quantum ground state and single-phonon control of a mechanical resonator. *Nature*, 464(7289):697–703, March 2010. 98

[176] T. J. Kippenberg and K. J. Vahala. Cavity optomechanics: Back-Action at the mesoscale. *Science*, 321(5893):1172–1176, aug 2008. 99, 100, 110

[177] Menno Poot and Herre S.J. van der Zant. Mechanical systems in the quantum regime. *Physics Reports*, 511(5):273–335, feb 2012. 99, 136

[178] V. B. Braginsky. *Measurement of Weak Forces in Physics Experiments*. University of Chicago Press, 1977. 99, 110

[179] T. J. Kippenberg, H. Rokhsari, T. Carmon, A. Scherer, and K. J. Vahala. Analysis of Radiation-Pressure induced mechanical oscillation of an optical microcavity. *Physical Review Letters*, 95(3):033901, jul 2005. 99, 105

[180] O. Arcizet, P.-F. Cohadon, T. Briant, M. Pinard, and A. Heidmann. Radiation-pressure cooling and optomechanical instability of a micromirror. *Nature*, 444(7115):71–74, feb 2006. 99, 100, 103

[181] S. Gigan, H. R. Böhm, M. Paternostro, F. Blaser, G. Langer, J. B. Hertzberg, K. C. Schwab, D. Bäuerle, M. Aspelmeyer, and A. Zeilinger. Self-cooling of a micromirror by radiation pressure. *Nature*, 444(7115):67–70, feb 2006. 99, 100

[182] A. Schliesser, P. Del'Haye, N. Nooshi, K. J. Vahala, and T. J. Kippenberg. Radiation pressure cooling of a micromechanical oscillator using dynamical backaction. *Physical Review Letters*, 97(24):243905, dec 2006. 99, 100, 103

[183] I. Wilson-Rae, P. Zoller, and A. Imamoglu. Laser cooling of a nanomechanical resonator mode to its quantum ground state. *Physical Review Letters*, 92(7):075507, 2004. 99

[184] L. Tian and P. Zoller. Coupled Ion-Nanomechanical systems. *Physical Review Letters*, 93(26):266403, dec 2004. 99, 101

[185] A. Naik, O. Buu, M. D. LaHaye, A. D. Armour, A. A. Clerk, M. P. Blencowe, and K. C. Schwab. Cooling a nanomechanical resonator with quantum back-action. *Nature*, 443(7108):193–196, sep 2006. 99

[186] M. D. LaHaye, O. Buu, B. Camarota, and K. C. Schwab. Approaching the quantum limit of a nanomechanical resonator. *Science*, 304:74–77, 2004. 99

[187] K. R. Brown, J. Britton, R. J. Epstein, J. Chiaverini, D. Leibfried, and D. J. Wineland. Passive cooling of a micromechanical oscillator with a resonant electric circuit. *Physical Review Letters*, 99(13):137205, 2007. 99, 106

[188] D. G. Blair, E. N. Ivanov, M. E. Tobar, P. J. Turner, F. van Kann, and I. S. Heng. High sensitivity gravitational wave antenna with parametric transducer readout. *Physical Review Letters*, 74(11):1908–1911, mar 1995. 99

[189] A. D. Armour, M. P. Blencowe, and K. C. Schwab. Entanglement and decoherence of a micromechanical resonator via coupling to a Cooper-Pair box. *Physical Review Letters*, 88(14):148301, mar 2002. 99

[190] Ivar Martin, Alexander Shnirman, Lin Tian, and Peter Zoller. Ground-state cooling of mechanical resonators. *Physical Review B*, 69(12):125339, mar 2004. 99

[191] C. A. Regal, J. D. Teufel, and K. W. Lehnert. Measuring nanomechanical motion with a microwave cavity interferometer. *Nature Physics*, 4(7):555–560, 2008. 99, 106

[192] M. I. Dykman. Heating and cooling of local and quasilocal vibrations by a nonresonance field. *Sov Phys-solid state*, 20:1306, 1978. 99

[193] Tobias J. Kippenberg and Kerry J. Vahala. Cavity opto-mechanics. *Opt. Express*, 15:17172–17205, 2007. 100

[194] A. Schliesser, R. Rivière, G. Anetsberger, O. Arcizet, and T. J. Kippenberg. Resolved-sideband cooling of a micromechanical oscillator. *Nature Physics*, 4(5):415–419, 2008. 100, 103, 106, 110, 114

[195] J. D. Teufel, J. W. Harlow, C. A. Regal, and K. W. Lehnert. Dynamical backaction of microwave fields on a nanomechanical oscillator. *Physical Review Letters*, 101(19):197203, nov 2008. 100

[196] J. D. Teufel, T. Donner, Dale Li, J. W. Harlow, M. S. Allman, K. Cicak, A. J. Sirois, J. D. Whittaker, K. W. Lehnert, and R. W. Simmonds. Sideband cooling of micromechanical motion to the quantum ground state. *Nature*, 475(7356):359–363, jul 2011. 100, 110, 142, 144, 170, 171

[197] Jasper Chan, T. P. Mayer Alegre, Amir H. Safavi-Naeini, Jeff T. Hill, Alex Krause, Simon Gröblacher, Markus Aspelmeyer, and Oskar Painter. Laser cooling of a nanomechanical oscillator into its quantum ground state. *Nature*, 478(7367):89–92, October 2011. 100, 110

[198] I. Wilson-Rae, N. Nooshi, W. Zwerger, and T. J. Kippenberg. Theory of ground state cooling of a mechanical oscillator using dynamical backaction. *Physical Review Letters*, 99:093901, 2007. 100, 101, 103, 105, 107, 115, 126

[199] Florian Marquardt, Joe P. Chen, A. A. Clerk, and S. M. Girvin. Quantum theory of Cavity-Assisted sideband cooling of mechanical motion. *Physical Review Letters*, 99(9):093902, 2007. 100, 101, 102, 103, 105, 107, 115

[200] D. J. Wineland and W. M. Itano. Laser cooling of atoms. *Physical Review A*, 20(4):1521–1540, 1979. 100

[201] R. J. Thompson, G. Rempe, and H. J. Kimble. Observation of normal-mode splitting for an atom in an optical cavity. *Physical Review Letters*, 68(8):1132–1135, feb 1992. 100, 105

[202] C. Weisbuch, M. Nishioka, A. Ishikawa, and Y. Arakawa. Observation of the coupled exciton-photon mode splitting in a semiconductor quantum microcavity. *Physical Review Letters*, 69(23):3314–3317, dec 1992. 100

[203] A. Wallraff, D. I. Schuster, A. Blais, L. Frunzio, R.-S. Huang, J. Majer, S. Kumar, S. M. Girvin, and R. J. Schoelkopf. Strong coupling of a single photon to a superconducting qubit using circuit quantum electrodynamics. *Nature*, 431(7005):162–167, sep 2004. 100

[204] J. P. Reithmaier, G. Sęk, A. Löffler, C. Hofmann, S. Kuhn, S. Reitzenstein, L. V. Keldysh, V. D. Kulakovskii, T. L. Reinecke, and A. Forchel. Strong coupling in a single quantum dot–semiconductor microcavity system. *Nature*, 432(7014):197–200, nov 2004. 100

[205] J. I. Cirac, R. Blatt, A. S. Parkins, and P. Zoller. Preparation of fock states by observation of quantum jumps in an ion trap. *Physical Review Letters*, 70(6):762–765, feb 1993. 100

[206] Stefano Mancini, Vittorio Giovannetti, David Vitali, and Paolo Tombesi. Entangling macroscopic oscillators exploiting radiation pressure. *Physical Review Letters*, 88(12):120401, mar 2002. 101, 114

[207] D. Vitali, S. Gigan, A. Ferreira, H. R. Böhm, P. Tombesi, A. Guerreiro, V. Vedral, A. Zeilinger, and M. Aspelmeyer. Optomechanical entanglement between a movable mirror and a cavity field. *Physical Review Letters*, 98(3):030405, jan 2007. 101, 102

[208] M. Wallquist, K. Hammerer, P. Zoller, C. Genes, M. Ludwig, F. Marquardt, P. Treutlein, J. Ye, and H. J. Kimble. Single-atom cavity QED and optomicromechanics. *Physical Review A*, 81(2):023816, feb 2010. 101

[209] U Akram, N Kiesel, M Aspelmeyer, and G J Milburn. Single-photon opto-mechanics in the strong coupling regime. *New Journal of Physics*, 12(8):083030, aug 2010. 101

[210] Simon Gröblacher, Klemens Hammerer, Michael R. Vanner, and Markus Aspelmeyer. Observation of strong coupling between a micromechanical resonator and an optical cavity field. *Nature*, 460(7256):724–727, aug 2009. 101, 105

[211] Miles Blencowe. Quantum mechanics: A light sounding drum. *Nature*, 471(7337):168–169, mar 2011. 101, 105

[212] J. D. Teufel, Dale Li, M. S. Allman, K. Cicak, A. J. Sirois, J. D. Whittaker, and R. W. Simmonds. Circuit cavity electromechanics in the strong-coupling regime. *Nature*, 471(7337):204–208, mar 2011. 101, 105, 171

[213] E. Verhagen, S. Deléglise, S. Weis, A. Schliesser, and T. J. Kippenberg. Quantum-coherent coupling of a mechanical oscillator to an optical cavity mode. *Nature*, 482(7383):63–67, feb 2012. 101, 140

[214] M. Bhattacharya and P. Meystre. Trapping and cooling a mirror to its quantum mechanical ground state. *Physical Review Letters*, 99(7):073601, 2007. 101, 103

[215] Thomas Corbitt, Christopher Wipf, Timothy Bodiya, David Ottaway, Daniel Sigg, Nicolas Smith, Stanley Whitcomb, and Nergis Mavalvala. Optical dilution and feedback cooling of a Gram-Scale oscillator to 6.9 mK. *Physical Review Letters*, 99(16):160801, oct 2007. 103

[216] F. Bloch and A. Siegert. Magnetic resonance for nonrotating fields. *Physical Review*, 57(6):522–527, mar 1940. 104

[217] D. Rugar, R. Budakian, H. J. Mamin, and B. W. Chui. Single spin detection by magnetic resonance force microscopy. *Nature*, 430(6997):329–332, jul 2004. 110

[218] A. K. Naik, M. S. Hanay, W. K. Hiebert, X. L. Feng, and M. L. Roukes. Towards single-molecule nanomechanical mass spectrometry. *Nature Nanotechnology*, 4(7):445–450, 2009. 110

[219] G. A. Steele, A. K. Huttel, B. Witkamp, M. Poot, H. B. Meerwaldt, L. P. Kouwenhoven, and H. S. J. van der Zant. Strong coupling between Single-Electron tunneling and nanomechanical motion. *Science*, 325(5944):1103–1107, aug 2009. 110

[220] J. D Teufel, T. Donner, M. A Castellanos-Beltran, J. W Harlow, and K. W Lehnert. Nanomechanical motion measured with precision beyond the standard quantum limit. *Nature Nanotechnology*, 4:820 – 823, jun 2009. 110, 114

[221] Carlton M. Caves. Quantum limits on noise in linear amplifiers. *Physical Review D*, 26(8):1817–1839, oct 1982. 110

[222] A. A. Clerk, M. H. Devoret, S. M. Girvin, Florian Marquardt, and R. J. Schoelkopf. Introduction to quantum noise, measurement, and amplification. *Reviews of Modern Physics*, 82(2):1155–1208, April 2010. 110, 115, 120, 175

[223] V. B. Braginsky and F.Y. Khalili. *Quantum Measurement*. Cambridge University Press, 1992. 110

[224] Florian Elste, S. M. Girvin, and A. A. Clerk. Quantum noise interference and backaction cooling in cavity nanomechanics. *Physical Review Letters*, 102(20):207209, may 2009. 111

[225] C. K. Law. Interaction between a moving mirror and radiation pressure - a hamiltonian-formulation. *Physical Review A*, 51(3):2537–2541, 1995. 111

[226] C. W. Gardiner and P. Zoller. *Quantum Noise*. Springer, 2000. 112, 120, 166

[227] A. E. Siegmann. Excess spontaneous emission in non-hermitian optical systems. i. laser amplifiers. *Physical Review A*, 39:1253, 1989. 112

[228] Carlos Viviescas and Gregor Hackenbroich. Field quantization for open optical cavities. *Physical Review A*, 67(1):013805, jan 2003. 112, 121

[229] M. T Jaekel and S Reynaud. Quantum limits in interferometric measurements. *Europhysics Letters (EPL)*, 13(4):301–306, oct 1990. 113

[230] William Kells and Erika D'Ambrosio. Considerations on parametric instability in Fabry–Perot interferometer. *Physics Letters A*, 299(4):326–330, jul 2002. 114

[231] P. Verlot, A. Tavernarakis, T. Briant, P. F. Cohadon, and A. Heidmann. Scheme to probe optomechanical correlations between two optical beams down to the quantum level. *Physical Review Letters*, 102:103601, 2009. 114

[232] V.B. Braginsky, S.E. Strigin, and S.P. Vyatchanin. Parametric oscillatory instability in Fabry–Perot interferometer. *Physics Letters A*, 287(5–6):331–338, sep 2001. 115

[233] A. B. Matsko, D. V. Strekalov, and N. Yu. Sensitivity of terahertz photonic receivers. *Physical Review A*, 77(4):043812, apr 2008. 115, 126

[234] K. Vahala, M. Herrmann, S. Knünz, V. Batteiger, G. Saathoff, T. W. Hänsch, and Th Udem. A phonon laser. *Nature Physics*, 5(9):682–686, 2009. 117

[235] G. Anetsberger, O. Arcizet, Q. P. Unterreithmeier, R. Rivière, A. Schliesser, E. M. Weig, J. P. Kotthaus, and T. J. Kippenberg. Near-field cavity optomechanics with nanomechanical oscillators. *Nature Physics*, 5(12):909–914, 2009. 117

[236] Gregor Hackenbroich, Carlos Viviescas, and Fritz Haake. Quantum statistics of overlapping modes in open resonators. *Physical Review A*, 68:063805, 2003. 120

[237] K. Petermann. Calculated spontaneous emission factor for double-heterostructure injection lasers with gain-induced waveguiding. *IEEE Journal of Quantum Electronics*, 15:566–570, 1979. 120

[238] P. J. Bardroff and S. Stenholm. Quantum langevin theory of excess noise in lasers. *Physical Review A*, 61:023806, 2000. 121

[239] Kater W. Murch, Kevin L. Moore, Subhadeep Gupta, and Dan M. Stamper-Kurn. Observation of quantum-measurement backaction with an ultracold atomic gas. *Nat Phys*, 4(7):561–564, jul 2008. 136

[240] T. Caniard, T. Briant, P. Cohadon, M. Pinard, and A. Heidmann. Ultrasensitive optical measurement of thermal and quantum noises. *Optics and Spectroscopy*, 103(2):225–230, 2007. 136

[241] S. Mancini and P. Tombesi. Quantum-noise reduction by radiation pressure. *Physical Review A*, 49(5):4055–4065, 1994. Part B. 137

[242] C. Fabre, M. Pinard, S. Bourzeix, A. Heidmann, E. Giacobino, and S. Reynaud. Quantum-noise reduction using a cavity with a movable mirror. *Physical Review A*, 49(2):1337–1343, 1994. 137

[243] C. M. Caves, K. S. Thorne, R. W. P. Drever, V. D. Sandberg, and M. Zimmermann. On the measurement of a weak classical force coupled to a quantum-mechanical oscillator .1. issues of principle. *Reviews of Modern Physics*, 52(2):341–392, 1980. 0034-6861. 142

[244] R. Rivière, S. Deléglise, S. Weis, E. Gavartin, O. Arcizet, A. Schliesser, and T. J. Kippenberg. Optomechanical sideband cooling of a micromechanical oscillator close to the quantum ground state. *Physical Review A*, 83(6):063835, jun 2011. 142

[245] Daniel W. C. Brooks, Thierry Botter, Sydney Schreppler, Thomas P. Purdy, Nathan Brahms, and Dan M. Stamper-Kurn. Non-classical light generated by quantum-noise-driven cavity optomechanics. *Nature*, 488(7412):476–480, August 2012. 143

[246] Andrey B. Matsko and Vladimir S. Ilchenko. Optical resonators with whispering-gallery modes – part i: Basics. *IEEE Journal of Selected Topics in Quantum Electronics*, 12:3–14, 2006. 148

[247] Tobias J. Kippenberg. *Nonlinear Optics in Ultra-high-Q Whspering -Gallery Optical Microcavities*. PhD thesis, California Institute of Technology, 2004. 148

[248] V. S. Ilchenko, P. S. Volikov, V. L. Velichansky, F. Treussart, V. Lefèvre-Seguin, J.-M. Raimond, and S. Haroche. Strain-tunable high-Q optical microsphere resonator. *Optics Communications*, 145:86–90, 1998. 150

[249] D. F. Walls and G.J. Milburn. *Quantum Optics*. Springer, New York, 1994. 166

Danke

Abschließend möchte ich mich bei all den Leuten bedanken, die mich in den letzen Jahren begleitet haben und die ihren Anteil am Gelingen dieser Arbeit haben. Konsequenterweise überträgt sich die Vermischung von Wissenschaft und Privatem aus dem realen Leben auch in diesen Abschnitt.

Zuallererst danke ich **Prof. Tobias Jan Kippenberg** dafür, dass ich in seiner Gruppe Lernen und Forschen durfte, und dass er mit seinen Ideen und seinem Elan diese Arbeit möglich gemacht hat. Ich habe viel von TJK gelernt, nicht nur mit Blick auf wissenschaftliches Arbeiten, sondern auch darin seine Ziele mit äußerster Hingabe und Motivation zu verfolgen und zum Erfolg zu führen.

Des Weiteren bedanke mich bei **Prof. Hänsch** für die Begutachtung dieser Arbeit und vor allem auch dafür, dass ich als Teil seiner Gruppe am MPQ und auf Ringberg Seminaren den unmittelbaren Kontakt zur Spitzenforschung erfahren durfte.

Auch bei **Prof. Rädler** bedanke ich mich für die Begutachtung der Doktorarbeit und zusammen mit **Dr. Bert Nickel** für die anhaltene Zusammenarbeit und den Kontakt zur Soft Matter Gruppe (e.g., in Antholz).

Bei **Dr. Ronald Holzwarth** und **Dr. Michael Mei** bedanke ich mich sehr für die freundliche Aufnahme bei Menlosystems und die hervorragenden Bedingungen während der Zeit des Zusammenschreibens.

Je remercie les **Dr. Laurence Navailles** et **Frédéric Nallet** de m'avoir introduit au monde scientifique au CRPP et pour avoir continué le travail sur la diffusion d'ADN.

Für administrative Unterstützung und unerschöpfliche Geduld mit "time sheets" und Abrechnungen möchte ich mich bei **Christina Becker**, **Frau Herrman**, **Frau Gschwendtner**, **Hélène Laurens** und **Patricia Marti-Rochat** bedanken.

Ich danke **Rike** für viele Dinge, aber am meisten dafür, dass sie mich während der "heißen" Phase des Zusammenschreibens unterstützt und auch ertragen hat.

Besonderer Dank geht an **Emanuel Gavartin** für die gute Zeit im Labor. Des Weiteren danke ich den anderen Gruppenmitgliedern des **K-lab**, namentlich **Bastian Schröter**, **Georg Anetsberger**, **Rémi Rivière**, **Xiaoqing Zhou**, **Pascal Del'Haye**, **Tobias Herr**, **Pierre Verlot**, **Olivier Arcizet**, **Stefan Weis**, **Christine Wang**, **Samuel Deléglise**, **Albert Schliesser**, **Johannes Beck** und **Klaus Hartinger**, für die Zeit des gemeinsamen Arbeitens, Spaßhabens und manchmal auch Leidens.

Aus vielen der Kollegen sind über die Jahre Freunde geworden und gemeinsame Aktivitäten beschränkten sich nicht nur auf das Labor, sondern dehnten sich auf

die Isar, in die Alpen, bis an den Gardasee aus. Deshalb möchte ich mich hier auch bei den anderen Menschen bedanken, die diese Zeit zu einer schönen Zeit gemacht haben und die den Namen nach **Thomas**, **Markus**, **Dunja**, **Conny**, **Aida**, **Lisa**, **Ruth**, **Christina, Caro**, **Andi**, (nochmal) **Christina,** und **Bronto** heißen. Speziell herausheben möchte ich noch meine Mitbewohnerinnen **Julia**, **Friederike**, **Dani** und **Doreen**, auch weil sie meine Macken so tapfer ertragen, und schließlich geht ein dickes Klopf-klopf-bumm-bumm an **Biggi**, **Micha**, **Martin** und den Rest der **MPC**.

Enfin, j'aimerais remercier **Anne** pour s'être investie dans notre tandem Franco-Allemand qui marchait si bien, et **Roland**, **Verena**, **Jana**, **Anne-Lise**, **Benoît**, **Nicolas** et **Peru** pour avoir rendu mon séjour Suisse si agréable, et duquel je garderai toujours de beaux souvenirs.